

MEASUREMENTS AND SEARCHES FOR NEW PHYSICS IN
DIBOSON PROCESSES WITH THE DØ DETECTOR

by

ALEXEY V. FERAPONTOV

B.S., Moscow State University, 2002

M.S., Moscow State University, 2004

AN ABSTRACT OF A DISSERTATION

submitted in partial fulfillment of the
requirements for the degree

DOCTOR OF PHILOSOPHY

Department of Physics
College of Art and Sciences

KANSAS STATE UNIVERSITY

Manhattan, Kansas

2009

Abstract

This dissertation describes a comprehensive study of the $Z\gamma \rightarrow ee\gamma/\mu\mu\gamma/\nu\bar{\nu}\gamma$ process. The data have been collected with the DØ detector at the Fermilab Tevatron $p\bar{p}$ collider with the center-of-mass energy of 1.96 TeV, and correspond to up to 3.6 fb^{-1} of integrated luminosity. Firstly, in this study we perform a measurement of the $Z\gamma$ production cross section. The measured cross sections in both $\ell\ell\gamma$ ($\ell = e$ or μ) and $\nu\bar{\nu}\gamma$ channels are the most precise cross sections measured at hadron colliders to date, and they agree within uncertainties with the theoretical calculations to the next-to-leading order. We claim the first observation of the $Z\gamma \rightarrow \nu\bar{\nu}\gamma$ process at hadron colliders at 5.1 standard deviations statistical significance.

We also conduct a search for anomalous $Z\gamma$ processes. Such anomalous $Z\gamma$ processes, where a Z boson couples to a photon, result in an increased cross section and an enhancement of the production of high-energetic photons. Thus, an observation of this kind might possibly indicate the presence of new physics. Having found no excess of data over the SM expectations, we set the most restrictive 95% C.L. limits on the anomalous trilinear $Z\gamma\gamma$ and $ZZ\gamma$ gauge couplings (ATGC) at hadron colliders to date: $|h_{30}^\gamma| < 0.033$, $|h_{40}^\gamma| < 0.0017$, $|h_{30}^Z| < 0.033$, and $|h_{40}^Z| < 0.0017$, which mark almost three times improvement over the most recent results published to date. Three out of four current limits improve on the LEP limits, and are the tightest limits on ATGC in the world.

Finally, we performed a search for narrow vector and scalar resonances that decay to $Z\gamma$. Many extensions of the SM predict such resonances, thus making this search a test of the gauge sector of the SM. We found no significant deviation of data from the SM predictions, and hence we set 95% C.L upper limits on the production cross section of the resonances.

MEASUREMENTS AND SEARCHES FOR NEW PHYSICS IN
DIBOSON PROCESSES WITH THE DØ DETECTOR

by

ALEXEY V. FERAPONTOV

B.S., Moscow State University, 2002

M.S., Moscow State University, 2004

A DISSERTATION

submitted in partial fulfillment of the
requirements for the degree

DOCTOR OF PHILOSOPHY

Department of Physics
College of Art and Sciences

KANSAS STATE UNIVERSITY

Manhattan, Kansas

2009

Approved by:

Major Professor
Yurii Y. Maravin

Abstract

This dissertation describes a comprehensive study of the $Z\gamma \rightarrow ee\gamma/\mu\mu\gamma/\nu\bar{\nu}\gamma$ process. The data have been collected with the DØ detector at the Fermilab Tevatron $p\bar{p}$ collider with the center-of-mass energy of 1.96 TeV, and correspond to up to 3.6 fb^{-1} of integrated luminosity. Firstly, in this study we perform a measurement of the $Z\gamma$ production cross section. The measured cross sections in both $\ell\ell\gamma$ ($\ell = e$ or μ) and $\nu\bar{\nu}\gamma$ channels are the most precise cross sections measured at hadron colliders to date, and they agree within uncertainties with the theoretical calculations to the next-to-leading order. We claim the first observation of the $Z\gamma \rightarrow \nu\bar{\nu}\gamma$ process at hadron colliders at 5.1 standard deviations statistical significance.

We also conduct a search for anomalous $Z\gamma$ processes. Such anomalous $Z\gamma$ processes, where a Z boson couples to a photon, result in an increased cross section and an enhancement of the production of high-energetic photons. Thus, an observation of this kind might possibly indicate the presence of new physics. Having found no excess of data over the SM expectations, we set the most restrictive 95% C.L. limits on the anomalous trilinear $Z\gamma\gamma$ and $ZZ\gamma$ gauge couplings (ATGC) at hadron colliders to date: $|h_{30}^\gamma| < 0.033$, $|h_{40}^\gamma| < 0.0017$, $|h_{30}^Z| < 0.033$, and $|h_{40}^Z| < 0.0017$, which mark almost three times improvement over the most recent results published to date. Three out of four current limits improve on the LEP limits, and are the tightest limits on ATGC in the world.

Finally, we performed a search for narrow vector and scalar resonances that decay to $Z\gamma$. Many extensions of the SM predict such resonances, thus making this search a test of the gauge sector of the SM. We found no significant deviation of data from the SM predictions, and hence we set 95% C.L upper limits on the production cross section of the resonances.

Table of Contents

Table of Contents	v
List of Figures	ix
List of Tables	xv
Acknowledgements	xviii
Dedication	xix
1 Introduction	1
2 Theoretical Model	4
2.1 The Standard Model	4
2.2 Theory of $Z\gamma$ Processes	6
2.2.1 Diboson physics	6
2.2.2 $Z\gamma$ phenomenology	8
2.2.3 Higher order and QCD corrections	11
2.2.4 Theories beyond the SM	13
2.2.5 Previous studies	14
3 The Tevatron Collider and the Upgraded DØ Detector	16
3.1 The Accelerator Chain	16
3.1.1 Pre-accelerator	16
3.1.2 Linac	16
3.1.3 Booster	17
3.1.4 Main Injector	18
3.1.5 Tevatron	18
3.2 The DØ Detector	19
3.2.1 Coordinate system and useful variables	20
3.2.2 Silicon microstrip tracker	22
3.2.3 Central fiber tracker	24
3.2.4 Solenoid	27
3.2.5 Preshower detectors	27
3.2.6 Calorimeter	30
3.2.7 Intercryostat detector	32
3.2.8 Luminosity monitor	33
3.2.9 Muon system	34

3.2.10	Trigger	36
3.2.10.1	Level 1 trigger	38
3.2.10.2	Level 2 trigger	40
3.2.10.3	Level 3 trigger	42
3.2.11	Data acquisition system	43
4	Data Analysis Techniques	45
4.1	Track Reconstruction	45
4.1.1	Alternative Algorithm	45
4.1.2	Histogramming Track Finder	47
4.2	Electromagnetic Object Reconstruction	47
4.3	Jet Reconstruction	52
4.4	Muon Reconsruction	53
4.5	Vertex Reconstruction	57
4.6	Missing Transverse Energy	58
5	Measurement of the $Z\gamma$ Cross Section	59
5.1	$Z\gamma \rightarrow ll\gamma$ Cross Section	60
5.1.1	Data samples	60
5.1.2	Monte Carlo samples	64
5.1.2.1	QCD corrections	65
5.1.2.2	The $D\bar{O}$ detector simulation	66
5.1.2.3	PDF uncertainty	67
5.1.3	Data selection	68
5.1.3.1	$Z \rightarrow ee$ selection	68
5.1.3.2	$Z \rightarrow \mu\mu$ selection	70
5.1.3.3	Photon identification	72
5.1.3.4	Selected data	73
5.1.4	Photon identification efficiency	74
5.1.5	Electron identification efficiency and $Z\gamma \rightarrow ee\gamma$ acceptance and efficiencies	80
5.1.5.1	Kinematic and geometrical acceptance	80
5.1.5.2	Single-electron trigger efficiency	81
5.1.5.3	Electron preselection efficiency	82
5.1.5.4	Electron H-matrix efficiency	82
5.1.5.5	Spatial track match efficiency	85
5.1.5.6	Summary of the $Z\gamma \rightarrow ee\gamma$ efficiency studies	87
5.1.6	Muon identification efficiency and $Z\gamma \rightarrow \mu\mu\gamma$ acceptance and efficiencies	89
5.1.6.1	Kinematic and geometrical acceptance	90
5.1.6.2	Muon trigger efficiency	91
5.1.6.3	Summary of the $Z\gamma \rightarrow \mu\mu\gamma$ efficiency studies	91
5.1.7	Backgrounds	92
5.1.8	Cross section calculation	96

5.1.9	Observed distributions	99
5.2	$Z\gamma \rightarrow \nu\bar{\nu}\gamma$ Cross Section	99
5.2.1	Data samples	99
5.2.2	Monte Carlo samples, QCD corrections and PDF uncertainty	104
5.2.3	Event selection	106
5.2.3.1	Photon identification	106
5.2.3.2	EM pointing algorithm	108
5.2.3.3	Kinematic cuts	111
5.2.4	Summary of the $Z\gamma \rightarrow \nu\bar{\nu}\gamma$ efficiency studies	115
5.2.5	Backgrounds	117
5.2.6	Cross section calculation	121
5.2.7	Observed distributions	122
5.2.8	Statistical significance of the measurements	123
5.3	Number of neutrino generations measurement	127
6	Setting Limits on Anomalous Trilinear Gauge Boson Couplings	131
6.1	Anomalous Couplings Limits in the Electron and Muon Mode	132
6.2	Anomalous Couplings Limits in the Neutrino Mode	133
6.3	Combined Anomalous Couplings Limits	135
6.4	Limits on CP-violating Couplings	139
6.5	Comparison between the Tevatron and LEP limits	140
7	Search For a Narrow Resonance Decaying into $Z\gamma$	143
7.1	Particle Models	143
7.1.1	Scalar Particle	144
7.1.2	Vector Particle	145
7.2	Monte Carlo Samples	145
7.3	Event Selection	146
7.3.1	Photon transverse energy and dilepton invariant mass cuts optimization	146
7.3.2	Muon correction	147
7.3.3	High mass inefficiency	148
7.4	Acceptance and Efficiencies	149
7.5	Backgrounds	149
7.5.1	Interferences	151
7.6	Analysis	152
7.6.1	Observed data	152
7.6.2	Limits setting software	153
7.6.2.1	Results	154
8	Summary	160
8.1	Large Extra Dimensions	161
8.2	Future Prospects	162

List of Figures

2.1	Examples of Feynman diagrams for (a) tree level interaction and (b) one-loop interaction.	7
2.2	Standard model Feynman diagrams describing $Z\gamma \rightarrow \ell\ell\gamma$ production: (a) and (b) describe initial state radiation; (c) and (d) describe final state radiation.	9
2.3	(a), (b) Feynman diagrams of anomalous $Z\gamma \rightarrow \ell\ell\gamma$ production; (c) general $ZV\gamma$ vertex.	10
2.4	$Z\gamma \rightarrow \nu\bar{\nu}\gamma$ cross section as a function of the anomalous couplings (a) h_{30}^γ , (b) h_{30}^Z , (c) h_{30}^γ , and (d) h_{40}^Z . For each case all other couplings are set to their SM values (zero). The minimum on the plots corresponds to the SM point. The distributions are obtained from the simulation of the $Z\gamma \rightarrow \nu\bar{\nu}\gamma$ process, but show the same behavior for other Z boson decay modes.	12
2.5	Photon transverse momentum spectra for the SM and anomalous $Z\gamma$ production. The distributions are obtained from the simulation of the $Z\gamma \rightarrow \nu\bar{\nu}\gamma$ process, but show the same behavior for other Z boson decay modes.	13
3.1	Fermilab's accelerator chain.	17
3.2	The DØ detector side-view.	20
3.3	The DØ detector coordinate system.	21
3.4	The pseudorapidity as a function of the polar angle for four values of θ	22
3.5	The central tracking system side-view.	23
3.6	3-D view of the silicon microstrip tracker.	23
3.7	Cross section of the SMT barrel.	25
3.8	Two layers of each of the CFT cylinders.	26
3.9	Waveguides of the CFT.	26
3.10	Schematic side-view of the solenoidal magnet.	27
3.11	Cross section of the preshower detectors scintillator strips.	28
3.12	Forward preshower detector segment exploded view.	29
3.13	3-D view of the DØ calorimeter.	30
3.14	Side view of the calorimeter cell.	32
3.15	Side view of the DØ calorimeter.	33
3.16	Side view of the luminosity monitor.	34
3.17	Exploded view of the muon system drift tubes.	36
3.18	Exploded view of the muon system trigger scintillation counters.	37
3.19	Overview of the DØ trigger system.	38
3.20	Block diagram of Level 1 and Level 2 trigger systems.	40
3.21	Schematic view of the DØ detector data acquisition system.	44

4.1	Schematic view of the calorimeter isolation.	49
5.1	Gauge bosons cross sections.	59
5.2	K -factor as a function of photon E_T obtained from NLO $Z\gamma$ Baur generator for the standard model $Z\gamma \rightarrow \ell\ell\gamma$ process.	66
5.3	Invariant mass of two selected electrons (CC-CC and CC-EC topologies combined).	69
5.4	Invariant mass of the dimuon system.	71
5.5	The ratio of the MC truth energy to the reconstructed one for 100 GeV photons in ϕ -fiducial volume and those reconstructed in the intercryostat gaps. Significant loss of energy for the latter photons can hide potential signal of the anomalous $Z\gamma$ production; therefore, we require photons to be in ϕ -fiducial region only.	74
5.6	Overall efficiency of the photon selection criteria as a function of modphi. Black dash-and-dotted lines show the standard fiducial boundaries.	75
5.7	Invariant mass of the dilepton system vs. invariant mass of dilepton and a photon system.	76
5.8	Event display of a $Z\gamma \rightarrow ee\gamma$ event. Upper row: (left) as seen from the front in the $x - y$ plane, muon spectrometer layers are shown; (right) calorimeter lego plot. Lower row: (left) side view ($z - y$ plane); (right) $r - \phi$ view with hits in the tracker, reconstructed tracks, and three EM showers in the calorimeter (red).	77
5.9	Event display of a $Z\gamma \rightarrow \mu\mu\gamma$ event. Upper row: (left) as seen from the front in the $x - y$ plane, muon spectrometer layers are shown; (right) calorimeter lego plot. Lower row: (left) side view ($z - y$ plane); (right) $r - \phi$ view with hits in the tracker, reconstructed tracks one EM shower in the calorimeter (red), and reconstructed muon candidates (green).	78
5.10	(a) Efficiency, ϵ_γ , of the photon reconstruction vs. photon transverse energy in CC. (b) Efficiencies in $Z \rightarrow ee$ data and Monte Carlo, and their ratio fitted to a zero degree polynomial (red horizontal line).	79
5.11	Electron preselection efficiency dependencies as a function of (a) E_T , (b) η_{Det} , (c) ϕ and (d) phimod. Red dots and blue squares correspond to the CC and EC region probes, respectively.	83
5.12	Preselection efficiency η_D dependencies for probe electrons transverse energy ranges (a) $15 \text{ GeV} < E_T < 25 \text{ GeV}$ and (b) $E_T > 25 \text{ GeV}$. Red dots and blue squares correspond to the CC and EC region probes, respectively.	84
5.13	H-matrix efficiency dependencies as functions of (a) E_T , (b) η_{Det} , (c) ϕ and (d) phimod. Red dots and blue squares correspond to CC and EC region probes, respectively.	85
5.14	H-matrix efficiency η_D dependencies for four probe electrons transverse energy ranges (a) $15 \text{ GeV} < E_T < 25 \text{ GeV}$, (b) $25 \text{ GeV} < E_T < 35 \text{ GeV}$, (c) $35 \text{ GeV} < E_T < 45 \text{ GeV}$, and (d) $E_T > 45 \text{ GeV}$. Red dots and blue squares correspond to CC and EC region probes, respectively.	86

5.15	Spatial track matching efficiency dependences as functions of (a) E_T , (b) η_{Det} , (c) ϕ and (d) phimod. Red dots and blue squares correspond to CC and EC region probes, respectively.	88
5.16	Spatial track matching efficiency η_D dependences for six z vertex ranges (a) $-100 \text{ cm} < z_v < 100 \text{ cm}$, (b) $z_v < -40 \text{ cm}$, (c) $-40 \text{ cm} < z_v < -10 \text{ cm}$, (d) $-10 \text{ cm} < z_v < 10 \text{ cm}$, (e) $10 \text{ cm} < z_v < 40 \text{ cm}$, (f) $z_v > 40 \text{ cm}$. Red dots and blue squares correspond to CC and EC region probes, respectively.	89
5.17	(a) Rate for an EM-like jet to satisfy photon identification criteria. No subtraction from the direct photon contribution is made. (b) Photon purity in CC region. (c) Rate, f , for an EM-like jet to satisfy photon selection criteria. Contribution from direct photons is subtracted.	93
5.18	First row: photon E_T spectrum in data, Monte Carlo (two points in the grid of anomalous coupling points) and QCD background in the electron (left) and muon (right) channels. Second row: di-electron (left) and dimuon (right) mass distributions in data, MC and QCD background. Third row: di-electron and photon (left), and dimuon and photon (right) mass distributions in data, MC and QCD background. All MC distributions are normalized to the integrated luminosity.	100
5.19	First row: photon E_T spectrum (left) and dilepton invariant mass distribution (right) in data, Monte Carlo and QCD background for the electron and muon channels combined. Second row: dilepton and photon mass distribution in data, Monte Carlo and QCD background for the electron and muon channels combined. All MC distributions are normalized to the integrated luminosity.	101
5.20	K -factor as a function of photon E_T obtained from the NLO $Z\gamma$ Baur generator: (a) no jet veto is applied, (b) jets with $p_T > 14 \text{ GeV}/c$ are vetoed, (c) jets with $p_T > 15 \text{ GeV}/c$ are vetoed (the cut, used in this current analysis), and (d) jets with $p_T > 16 \text{ GeV}/c$ are vetoed.	105
5.21	K -factor as a function of photon E_T for various cuts on the jet transverse momentum.	106
5.22	Photon core efficiency (from γ +jet MC) and scale factors for Run IIa (left) and Run IIb (right) samples. The uncertainty on the scale factors comes from the systematic uncertainties on the efficiency fits for electrons in data and MC. We also apply 1% (1.5%) additional uncertainty to the electron fits in data (MC) due to the background subtraction procedure. For more information, please see DØ Notes 4976 and 5761.	109
5.23	CPS match efficiency (from γ +jet MC) and scale factors for Run IIa (left) and Run IIb (right) samples. The uncertainty on the scale factors comes from the systematic uncertainties on the efficiency fits for electrons in data and MC. We also apply 1% (1.5%) additional uncertainty to the electron fits in data (MC) due to the background subtraction procedure. For more information, please see DØ Notes 4976 and 5761.	110
5.24	Anti-track match efficiency for Run IIb sample (from γ +jet MC).	111

5.25	Event display of a $Z\gamma \rightarrow \nu\bar{\nu}\gamma$ event. Upper row: (left) as seen from the front in the $x - y$ plane, muon spectrometer layers are shown; (right) calorimeter lego plot. Lower row: (left) side view ($z - y$ plane), very little activity in the tracker and calorimeter is seen; (right) $r - \phi$ view with hits in the tracker, four reconstructed tracks, one EM shower in the calorimeter, and \cancel{E}_T balancing this energy deposit.	116
5.26	The e/γ , non-collision and misidentified jets DCA distributions (inserts). The fit of the linear sum of the three DCA templates to the DCA distribution in the final photon sample (main plots). Left - Run IIa, right - Run IIb.	119
5.27	Photon E_T spectrum in Run IIa (left) and Run IIb (right) data, Monte Carlo (two points in the grid of anomalous coupling points) and sum of backgrounds. MC distributions are normalized to the integrated luminosity. The shaded band represents the 1 standard deviation (s.d.) systematic and statistical uncertainty on the Monte Carlo signal plus background. Last bin is the overflow bin.	123
5.28	Photon E_T spectrum in combined Run IIa and Run IIb data, Monte Carlo (two points in the grid of anomalous coupling points) and sum of backgrounds. MC distributions are normalized to the integrated luminosity. The shaded band represents the 1 s.d. systematic and statistical uncertainty on the Monte Carlo signal plus background. Last bin is the overflow bin.	124
5.29	Photon z vertex, \cancel{E}_T , $phimod$, η and ϕ distributions in Run IIa and Run IIb data and PMCS output (without the background component overlaid).	125
5.30	Photon z vertex, \cancel{E}_T , $phimod$, η and ϕ distributions in combined Run IIa and Run IIb data and PMCS output (without the background component overlaid).	126
5.31	Distribution of number of background events, $newN_{bkg}$, and number of observed events, N_{obs} , (example, only 1M entries) for the background-only hypothesis (left) for all pseudo-experiments, and the combined cross section distribution for the background-only hypothesis (right). The red (blue) line represents the combined cross section measured in data (expected from theory).	127
5.32	Distribution of number of Run IIa background events, $newN_{bkg}$, number of signal events, $newN_{sig}$, and number of observed events, N_{obs} , for the signal-plus-background hypothesis (left) for all pseudo-experiments, and the combined cross section distribution for the signal-plus-background hypothesis (right). The red line represents the Run IIa cross section measured in data.	128
5.33	Distribution of number of Run IIb background events, $newN_{bkg}$, number of signal events, $newN_{sig}$, and number of observed events, N_{obs} , for the signal-plus-background hypothesis (left) for all 1M pseudo-experiments, and the combined cross section distribution for the signal-plus-background hypothesis (right). The red line represents the Run IIb cross section measured in data.	129
6.1	Fitting function general behavior as a function of h_{30} and h_{40}	133

6.2	Negative value of log likelihood of all 775 fits of photon E_T spectrum from Monte Carlo $Z\gamma\gamma$ (left) and $ZZ\gamma$ (right) simulation and QCD background to the data for $\Lambda = 1.2$ TeV.	134
6.3	Two-dimensional contour (ellipse) and one-dimensional limits (ticks on the cross) of 95% C.L. on CP-conserving anomalous $Z\gamma\gamma$ (left) and $ZZ\gamma$ (right) couplings. Dashed straight lines indicate the unitarity limits for $\Lambda = 1.2$ GeV. Red dots represent the anomalous couplings grid.	134
6.4	Negative value of log likelihood of fits of E_T spectrum from Monte Carlo $Z\gamma\gamma$ (left) and $ZZ\gamma$ (right) simulation and backgrounds to the data for $\Lambda = 1.5$ TeV in the combined neutrino and electron plus muon channel.	137
6.5	Two-dimensional contours (ellipses) and one-dimensional limits (ticks on the crosses) of 95% C.L. on CP-conserving anomalous $Z\gamma\gamma$ (left) and $ZZ\gamma$ (right) couplings in the combined neutrino and electron plus muon channel. Dashed straight lines indicate the unitarity limits for $\Lambda = 1.5$ TeV. Both two-dimensional contours are inside the unitarity boundaries. Red dots represent the anomalous couplings grid.	137
6.6	Kinematic distributions comparison between the CP-conserving and CP-violating pair of couplings. The values of couplings are: $h_{30}^Z = h_{10}^Z = 0.02$, $h_{40}^Z = h_{20}^Z = -0.003$	140
6.7	Kinematic distributions comparison between the CP-conserving and CP-violating pair of couplings. The values of couplings are: $h_{30}^Z = h_{10}^Z = 0.09$, $h_{40}^Z = h_{20}^Z = 0.005$	141
7.1	Feynman diagrams for the leading order processes which produce $Z\gamma$ candidates: (a) SM initial state radiation (ISR), (b) SM final state radiation (FSR), (c) $q\bar{q}$ pair annihilation into a V particle (obtained from MADGRAPH, adapted to produce a vector particle decaying into $Z\gamma$), and (d) Higgs production and decay (PYTHIA).	144
7.2	Total efficiencies of the $X \rightarrow Z\gamma$ process as a function of the resonance mass. Here, X denotes either a vector or a scalar resonance.	150
7.3	Ratio of the vector resonance production phase space (\hat{s}, \hat{t}) and the SM $Z\gamma$ process phase space. Each phase space is normalized to its cross section.	152
7.4	Invariant mass of the dilepton system vs. invariant mass of dilepton and a photon candidates.	153
7.5	Invariant dilepton plus photon mass spectrum for $\ell\ell\gamma$ data (dots), SM $Z\gamma$ background (dashed line histogram), Z +jet background (dash-dot line histogram) and Monte Carlo signal plus background associated with a scalar particle of 200 GeV/ c^2 (left) and 300 GeV/ c^2 (right) decaying into $Z\gamma$ (solid line). The shaded band represents the 1 s.d. systematic and statistical uncertainty on the Monte Carlo signal plus background.	155

7.6	Invariant dilepton plus photon mass spectrum for $\ell\ell\gamma$ data (dots), SM $Z\gamma$ background (dashed line histogram), Z +jet background (dash-dot line histogram) and Monte Carlo signal plus background associated with a vector particle of 200 GeV/ c^2 (left) and 300 GeV/ c^2 (right) decaying into $Z\gamma$ (solid line). The shaded band represents the 1 s.d. systematic and statistical uncertainty on the Monte Carlo signal plus background.	156
7.7	The cross section times branching fraction at 95% C.L. limit for a vector particle that decays into $Z\gamma$ as a function of the vector resonance mass. The two shaded bands represents the 1 s.d. (dark) and 2 s.d. (light) uncertainties on the expected limit.	157
7.8	The cross section times branching fraction at 95% confidence level limit for a scalar particle that decays into $Z\gamma$ as a function of the scalar particle mass. The two shaded bands represents the 1 s.d. (dark) and 2 s.d. (light) uncertainties on the expected limit.	157
7.9	$C_{qq}^2 \cdot C_{Z\gamma}^2$ at 95% C.L. limit for a vector particle that decays into $Z\gamma$ as a function of the vector particle mass.	158
7.10	Signal events for a vector particle that decays into $Z\gamma$ if the cross section times branching fraction is right below our 95% C.L. limit as a function of the vector particle mass.	158
7.11	Signal events for a scalar particle that decays into $Z\gamma$ if the cross section times branching fraction is right below our 95% C.L. limit as a function of the scalar particle mass.	159

List of Tables

2.1	Summary of gauge bosons and fundamental forces.	5
2.2	Summary of leptons.	5
2.3	Summary of quarks.	6
2.4	Summary of previous 95% C.L. limits on anomalous $ZZ\gamma$ and $Z\gamma\gamma$ couplings.	15
4.1	Muon types.	55
4.2	Muon quality. Here, N_A^w (N_{BC}^w) is the number of wire hits in the A-layer (BC-layers), N_A^{sc} (N_{BC}^{sc}) is the number of scintillator hits in the A-layer (BC-layers), and χ_{loc}^2 is the criterion of the local fit convergence.	56
5.1	Summary of Run IIa triggers used in the electron channel.	62
5.2	Summary of Run IIa triggers used in the muon channel.	63
5.3	Summary of integrated luminosity in the electron channel.	64
5.4	Summary of integrated luminosity in the muon channel.	64
5.5	Summary of the “OR’ed” calorimeter-only single-electron trigger efficiencies.	82
5.6	Summary of efficiencies for the electron channel.	90
5.7	Summary of muon trigger efficiencies.	91
5.8	Summary of the components for the $Z\gamma \rightarrow ee\gamma$ cross section calculation.	96
5.9	Summary of the components for the $Z\gamma \rightarrow \mu\mu\gamma$ cross section calculation.	96
5.10	Summary of the uncertainties of the $Z\gamma \rightarrow \ell\ell\gamma$ cross section for the electron CC-CC, electron CC-EC, and muon channels.	98
5.11	Summary of Run IIa triggers used in the neutrino channel.	102
5.12	Summary of Run IIb triggers used in the neutrino channel.	103
5.13	Integrated luminosity of the data sets.	103
5.14	Summary of efficiencies of the kinematic cuts.	114
5.15	Summary of efficiencies for the neutrino channel.	115
5.16	Summary of backgrounds.	120
5.17	Summary of the components for the $Z\gamma \rightarrow \nu\bar{\nu}\gamma$ production cross section calculation.	121
5.18	Summary of the uncertainties of the $Z\gamma \rightarrow \nu\bar{\nu}\gamma$ cross section for the Run IIa and Run IIb data sets.	122
5.19	Summary of the components to the calculation of the cross section for $Z\gamma \rightarrow \ell\ell\gamma$ decay for the photon $E_T > 90$ GeV.	130
6.1	Summary of the 95% C.L. one-dimensional anomalous couplings limits.	138
6.2	Comparison between the CP-conserving and CP-violating pair of couplings. The values of couplings are: $h_{30}^Z = h_{10}^Z = 0.02$, $h_{40}^Z = h_{20}^Z = -0.003$	139

6.3	Comparison between the CP-conserving and CP-violating pair of couplings. The values of couplings are: $h_{30}^Z = h_{10}^Z = 0.09$, $h_{40}^Z = h_{20}^Z = 0.005$	139
6.4	The 95% C.L. one-dimensional limits on the anomalous trilinear gauge couplings: combination of four LEP collaborations results, and current limits from the DØ experiment at the Tevatron.	142
7.1	Optimization cuts on $M_{\ell\ell}$ and photon E_T for different particles/masses. $S/\sqrt{S+B}$ optimization does not include the cut on three-body ($M_{\ell\ell\gamma}$) mass, which is highly correlated with these cuts.	147
7.2	Dilepton plus photon invariant mass resolution. The fourth column shows an improvement in the dimuon plus photon invariant mass resolution after the Z mass constraint has been applied.	149
7.3	Summary of the components used to estimate number of SM $Z\gamma$ background events.	151
7.4	Summary of background events.	151

Acknowledgements

There are many people around me that I am thankful to. It is simply impossible to remember everyone, so I apologize to those people I have not included into the acknowledgment. First of all, I am grateful to my parents who always supported my craving for knowledge. Raised in a family of physics engineers, I had no hesitations when it was time for me to choose the field of study at the university. They also supported my intention to transfer to Kansas State graduate school, despite of the fact that it was some 5,500 miles away from home. My parents deserve this thesis to be dedicated to them.

I would like to thank my advisor Yurii Maravin for his constant support, help, patience, and motivation. It was a pleasure to work under his supervision, and that resulted in a number of papers we could publish together. He taught me how to take a chunk of data and transform a collection of numbers into a fine physics analysis. I learned a lot from him, and I'm sure this knowledge will help me in my professional career. Moreover, Yurii was and is one of my best friends, and I hope to keep in touch with him after the graduation.

I am grateful to Kansas State University faculty members: Tim Bolton, Noel Stanton, Larry Weaver, Glenn Horton-Smith, for their helpful advices and support. I am also thankful to my physics group colleagues at KSU – Lado Samushia, Keti Kaadze, Irakli Chakaberia, Irakli Svintradze, Mahsana Ahsan, Mansoor Shamim, Mark Smith, Deepak Shrestha, and Jasmine Foster. And, of course, I would like to thank my friends at KSU – Eric Moon, Chrissy Williams, Matt Berg, Fran Mateycik, Jackie and Mike Chini, Nora Johnson, Sean and Dyan McBride, Irina Bocharova, Olga Firsova (and many others!) for sharing great time offcampus. Without them my life in Kansas would not be that memorable.

I would like to express my gratitude to my colleagues at Fermilab – Vesna Cuplov, Drew Alton, Yurii Maravin, Yuri Gershtein, and Edgar Carrera for their constant help and expertise in the physics analyses we have performed together. I believe, we formed a wonderful professional group, whose mutual work lead to interesting and important results (many of

which are world's best!), publications, and collaboration-wide innovative techniques. Special thanks to the members of two Editorial Boards – Electroweak EB, chaired by Greg Landsberg, and New Phenomena EB, chaired by Elemer Nagy, for their patience in reviewing our analyses, fruitful discussions, and positive feedback. And, of course, I am very thankful to all my DØ colleagues that I have closely worked with through all these years at Fermilab (to mention all their names would easily take two or three pages). I would also like to mention the current and ex-conveners of the groups I have been a member of: the DØ Photon/EM ID group and Dmitri Bandurin, Oleksiy Atramentov, Yurii Maravin, and Maiko Takahashi; the Electroweak physics group and Tim Bolton, Heidi Schellman, and Junjie Zhu; the Trigger Board and Marco Verzocchi, Rick Jesik, Sabine Lammers, and Liang Li; the Diboson group and Adam Lyon, Jadranka Sekaric, Tom Diehl, and Andrew Askew. Working inside these groups allowed me to understand physics and the detector in much more details.

I would like to thank my supervisors at the Institute for High Energy Physics in Protvino – Sergei Denisov and Sergei Erin. They introduced me to the field, and I started my career in experimental high energy physics under their supervision.

I am thankful to my Russian friends at Fermilab, that always remind me of my Motherland – Russian Fermilab staff, current and ex-members of the Protvino IHEP, Dubna JINR, and Saint-Petersburg PNPI groups. Among them are Dmitri Sidorov, Yuri Sinkin, and Leonid Mikhalev (with them I also shared the undergraduate years at Moscow State University), Andrey Shchukin, Sergei Efremov, Georgy Golovanov, Sergey Kulikov, Sergey Koshkarev, Andrey Sidorov, and Natalie Miklyukh.

Finally, I would like to express a special gratitude to my girlfriend Kelly McMinn and her family members who admitted me into their family, and inspired and supported me far away from my home. Their doors have always been open for me. Kelly has encouraged me to start graduate school here, in the United States, and she has always been patient with me when I had to work overtime or on weekends. I would also like to devote a part of this thesis to her, as my graduation marks a step to another exciting period of our life.

Dedication

To my parents, Nina and Valeri Ferapontov.

Chapter 1

Introduction

High energy physics, or particle physics, is a branch of physics that studies properties and interactions between elementary particles. The current knowledge of fundamental particles and their interactions is summarized in a so-called *standard model* (SM), briefly described in the next Chapter.

The basics of the SM have been formed in the 60's, when S. Glashow found a way to unify the weak and electromagnetic interactions, and A. Salam and S. Weinberg incorporated the Higgs mechanism into the theory [1, 2]. After the discovery of neutral currents [3] in 1973, and the direct observation of the much anticipated Z and W bosons [4–7] 10 years later in 1983, the SM has acquired its popularity among the physicists around the world. It is a truly beautiful theory and is a product of titanic efforts of both theorists and experimentalists.

Up to date, the SM has been experimentally tested in major laboratories, and no deviations from the theoretical expectations have been found. However, despite its tremendous success, the SM is not a complete theory for many reasons. First of all, the SM appears to have too many intrinsic constants (21 in total), most of which are empirical and unrelated. This makes the SM rather inelegant. Also, the SM falls short in explaining some of the fundamental problems:

- How can gravity be included in the SM, and why is it such a weak force at the accessible energy scales? Why is the Planck energy scale (when gravity becomes strong enough) of 10^{19} GeV so different from the electroweak scale (100 GeV)?

- Why do neutrinos have mass? What mechanism is responsible for that?
- What is the origin of matter/antimatter asymmetry? Why are we living in the “matter” world?
- What is dark matter? Is the hypothetical graviton a dark matter candidate? What is dark energy?
- Does Higgs boson exist? If not, how can the electroweak symmetry breaking mechanism be explained without it?
- Are there more than four space-time dimensions? What is the size of these extra dimensions?
- Are there symmetries other than those incorporated in the SM? Does supersymmetry exist?

These questions and many others, that lack answers, stimulate the ongoing efforts in search for a more general model of fundamental particles and their interactions – a model, that would give answers to the questions described above. However, we do not know the threshold of the validity of the SM in its current form. Hence, new laboratories are being built, new energy frontiers are being explored, new theories that might shed the light on the fundamental problems are being developed. And we all hope that these efforts will help us understand how our Universe has been formed and how it evolved.

This dissertation contains the results of a comprehensive and thorough study of the associated production of photons and Z bosons, aimed to test the electroweak sector of the SM and possibly find hints for physics beyond the SM. Photons, that possess both wave and particle properties, are among the “oldest” objects in the Universe. Thus, studying photons and their properties in great detail might help us go back in time to the early stages of the Universe. In addition, analyses with photons in the final state are very interesting and rather challenging, as photons in the particle detectors can easily be misidentified as other objects,

such as electrons (positrons) and streams of charged and neutral particles, often referred to as jets. Adding yet another gauge boson to the final state even further complicates the analyses, challenging physicists' skills. But the game is worth a candle, as studying diboson production allows for the thorough tests of the SM and might indicate the presence of new phenomena (see Section 2.2.1).

This work is organized as follows: Chapter 2 contains the description of the theoretical aspects of the analyses and the motivation for the searches. An overview of the Fermilab's collider chain and the detailed description of the main parts of the DØ detector is given in Chapter 3. The methods and algorithms used to identify physics objects in the detector are described in Chapter 4. Chapter 5 contains the results of the $Z\gamma$ cross section measurement in the charged leptons and neutrino channels. A comparison between main kinematic distributions, as well as the methods used to set limits on the strength of the couplings between Z bosons and photons, is given in Chapter 6. Chapter 7 contains the results of the search for the resonance $Z\gamma$ production in the charged leptons channel, and upper limits on the production cross section of such resonances. Finally, main physics results of this work are summarized in Chapter 8.

Chapter 2

Theoretical Model

2.1 The Standard Model

The standard model (SM) of particle physics is a model that describes interactions between the building blocks of the Universe - the fundamental elementary particles. Within the SM framework all particles are divided into two types: bosons and fermions. The latter have half-integer spin and hence obey the Fermi-Dirac statistics. Fermions are the constituent matter of the visible Universe. To the contrary, bosons have integer spins and follow the Bose-Einstein statistics. Gauge bosons, such as Z , W^\pm , photons, and gluons, serve as the fundamental forces mediators. There are three fundamental forces in the SM: strong, weak and electromagnetic (EM). Each force is described by its own gauge group: strong – $SU(3)$, weak – $SU(2)$, and electromagnetic – $U(1)$. The SM is a gauge theory governed by all three groups: $SU(3) \times SU(2) \times U(1)$. The combination of $SU(2) \times U(1)$ describes the electroweak interactions. These forces and their mediators are summarized in Table 2.1 (see, *e.g.* Ref. [8]). Gravity is the only known force that is not included into the SM. The hypothetical particle, *graviton*, is its mediator and has yet to be observed.

The fundamental fermions are divided into two types, or families – leptons and quarks, and then are further divided into three generations. Each generation consists of total 8 fermions, including their antiparticles. Tables 2.2 and 2.3 summarize the properties of all three generations of leptons and quarks, respectively. Quarks also have an additional prop-

Table 2.1: *Summary of gauge bosons and fundamental forces.*

Gauge boson	Mass, (GeV/ c^2)	Charge	Symmetry group	Force	Acts on
<i>gluon</i> , g	0	0	SU(3)	strong	color charge
<i>photon</i> , γ	0	0	U(1)	EM	electric charge
W^\pm	80.40	$\pm 1e$	SU(2)	weak	flavor
Z	91.19	0	SU(2)	weak	flavor

Table 2.2: *Summary of leptons.*

Lepton	Mass, (MeV/ c^2)	Charge	Acting force
e	0.511	$-1e$	weak and EM
ν_e	$< 2.2 \times 10^{-6}$	0	weak
μ	105.65	$-1e$	weak and EM
ν_μ	< 0.17	0	weak
τ	1776.84	$-1e$	weak and EM
ν_τ	< 15.5	0	weak

erty called *color*. The mediators of the strong interaction, gluons, are doubly colored. Since gluons have the color charge, they interact with each other. The theory that describes interactions between colored particles is called *quantum chromodynamics* (QCD). The strong interactions can change the color of the quarks, but cannot change their flavor. An interesting property of the strong interactions is that a single quark cannot be isolated from other quarks (the so-called *confinement*). However, quarks can form other colorless particles by means of the strong color couplings. This process is known as *hadronization*, and the “new” particles that consist of quarks are called *hadrons*. There are two types of hadrons: mesons (comprised of a quark and an antiquark) and baryons (made of three quarks or three antiquarks of all three colors). An examples of the former are pions, kaons, *etc*; and protons and neutrons are examples of the baryons.

One of the biggest puzzles of high energy physics is a mechanism that makes particles have different masses. Such a mixture of massive and massless particles can be explained in a number of ways, one of which is realized in introducing another particle into the SM – a Higgs boson (H). Higgs boson (spin zero) is a hypothetical particle which has not

Table 2.3: *Summary of quarks.*

Lepton	Mass, (GeV/ c^2)	Charge
u	0.003	$2/3e$
d	0.006	$-1/3e$
c	1.3	$2/3e$
s	0.1	$-1/3e$
t	175	$2/3e$
b	4.3	$-1/3e$

been observed yet. It is a force mediator of another field – a Higgs field. Elementary particles interact with Higgs bosons, and through these interactions particles acquire their mass (including the Higgs boson itself, as it is allowed to self-interact). The so-called *spontaneous electroweak symmetry breaking*, or the *Higgs mechanism* [9], explains the difference between essentially massless photons and gluons and massive W and Z bosons. The searches for the Higgs boson have been conducted at all major laboratories in the world, however it has not been discovered yet. The latest experimental results allow one to exclude the Higgs boson at 95% confidence level (C.L.) with masses below 114 GeV/ c^2 [10] and a 170 GeV/ c^2 SM Higgs boson [11]. The direct observation of the Higgs boson in the mass range between 115 GeV/ c^2 and 180 GeV/ c^2 will be an important test of the validity of the SM.

2.2 Theory of $Z\gamma$ Processes

2.2.1 Diboson physics

The searches for the W and Z gauge bosons have been performed in all major high energy laboratories in the world since the day they have been predicted. Their discovery in 1983 at the UA1 and UA2 experiments [4–7] at the CERN Super Proton Synchrotron has been a major success and the triumph of the SM. The properties of the gauge bosons and their decay modes have been studied in great details. For about 70% of the time both W and Z bosons decay to hadrons (quarks and their combinations, excluding the t quark due to its

large mass). For about 30% (10%) of the time W (Z) bosons decay to a charged lepton (e , μ and τ) and its neutrino (or a pair of charged leptons). And for about 20% of the time the Z boson decays invisibly, into a pair of neutrinos. Unlike massive gauge bosons, a photon is essentially a stable particle. The couplings of the gauge bosons to fundamental fermions have been predicted by the SM and have been measured with high accuracy.

The symmetry transformations of the gauge groups that govern the SM also allow gauge bosons to self-interact, *i.e.* couple to other gauge bosons with some restrictions. These restrictions are that the allowed self-interactions at the tree level are between charged and neutral gauge bosons. A tree level interaction or decay is defined as a process in which particles interact with each other directly, and the Feynman diagram for that process looks like a tree (see Fig. 2.1(a)). Another possible case of interaction is the loop interaction with diagrams involving an exchange of virtual particles that recombine into new components (see Fig. 2.1(b)). Just as in case of the couplings between gauge bosons and fundamental fermions, the couplings between gauge bosons have also been precisely predicted by the SM. However, due to the rarity of diboson processes, the gauge bosons self-interaction couplings (often referred to as *trilinear gauge couplings*) have been studied in much less details.

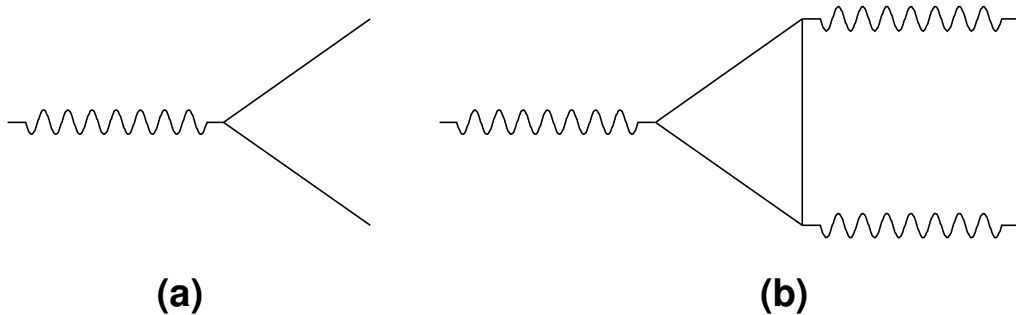


Figure 2.1: Examples of Feynman diagrams for (a) tree level interaction and (b) one-loop interaction.

It is worth mentioning that diboson final states are important decay modes for the

predicted Higgs boson (*e.g.* $H \rightarrow \gamma\gamma$, $H \rightarrow WW$, $H \rightarrow ZZ$, *etc.*) and for hypothetical new phenomena particles (*e.g.* $Z' \rightarrow Z\gamma$). Hence, extensive and thorough studies of gauge boson production can not only provide important tests of the gauge sector of the SM, but also possibly lead to a discovery of particles which are not predicted by the SM.

2.2.2 $Z\gamma$ phenomenology

As shown in Section 2.2.1, a Z boson and a photon do not self-interact at the tree level in the SM. This means that the trilinear gauge $Z\gamma\gamma$ and $ZZ\gamma$ couplings are zero in the SM. The allowed diagrams of the SM $Z\gamma \rightarrow \ell\ell\gamma$ (here, ℓ is an electron or a muon) processes are shown in Fig. 2.2. The processes when a photon is emitted by one of the interacting partons are called the initial state radiation (ISR), and are shown in Figs. 2.2(a) and (b). The final state radiation (or the radiative decay) processes when a photon is emitted by one of the leptons in the final state are shown in Figs. 2.2(c) and (d). In this dissertation, we collectively refer to all these processes as $Z\gamma \rightarrow \ell\ell\gamma$ in the charged leptonic channel. As neutrinos do not carry the electric charge, and hence do not interact by means of the electromagnetic force, only initial state radiation diagrams shown in Figs. 2.2(a) and (b) contribute to the $Z\gamma \rightarrow \nu\bar{\nu}\gamma$ final state. The tree level diagrams of the $Z\gamma$ processes forbidden in the SM (*anomalous* $Z\gamma$ production) are presented in Fig. 2.3. These diagrams form the complete set of the Feynman diagrams of the processes with two leptons and a photon in the final state.

The most general parameterization of interaction between a Z boson and a photon is expressed by constructing the Lorentz- and gauge-invariant $ZV\gamma$ vertex, shown in Fig. 2.3(c). Here, V can be either a Z boson or a photon. The shaded circle hides various tree level and loop contributions to the $ZV\gamma$ coupling (see Section 2.2.4) making the description of the $ZV\gamma$ coupling model-independent. This most general coupling can be parameterized by four complex coupling parameters as shown in Refs. [12, 13]. The $ZZ\gamma$ vertex function (see Fig. 2.3(c) for the notation) is defined in Eq. 2.1.

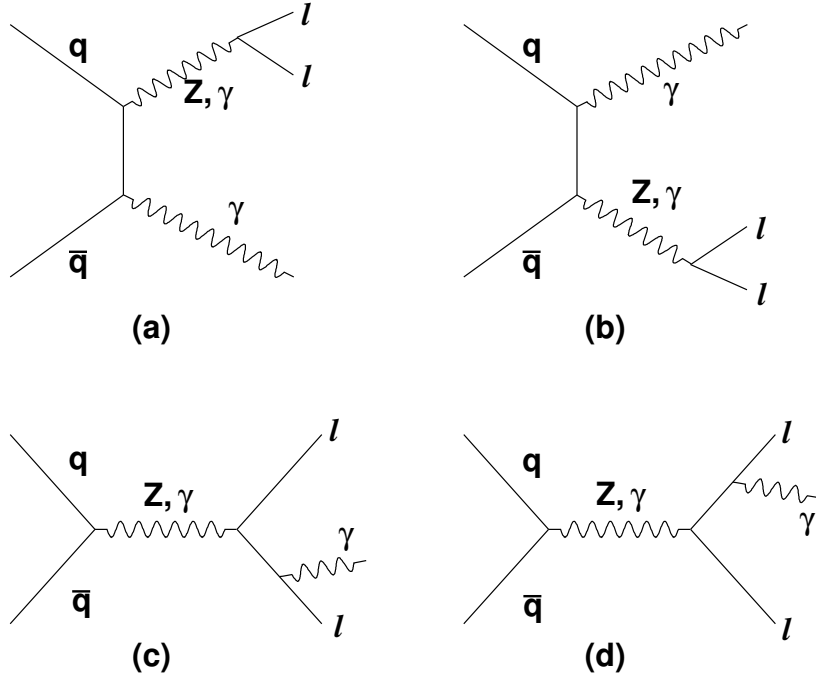


Figure 2.2: Standard model Feynman diagrams describing $Z\gamma \rightarrow \ell\ell\gamma$ production: (a) and (b) describe initial state radiation; (c) and (d) describe final state radiation.

$$\begin{aligned}
\Gamma_{ZZ\gamma}^{\alpha\beta\mu}(q_1, q_2, P) = & \frac{P^2 - q_1^2}{m_Z^2} (h_1^Z (q_2^\mu g^{\alpha\beta} - q_2^\alpha g^{\mu\beta}) + \\
& \frac{h_2^Z}{m_Z^2} P^\alpha [(P \cdot q_2) g^{\mu\beta} - q_2^\mu P^\beta] + \\
& h_3^Z \epsilon^{\mu\alpha\beta\rho} q_{2\rho} + \frac{h_4^Z}{m_Z^2} P^\alpha \epsilon^{\mu\beta\rho\sigma} P_\rho q_{2\sigma}), \tag{2.1}
\end{aligned}$$

here, m_Z is the Z boson mass and $\epsilon^{\mu\alpha\beta\rho}$ is the 4-D totally asymmetric tensor. The $Z\gamma\gamma$ vertex function can be obtained from Eq. 2.1 by the following substitution:

$$\frac{P^2 - q_1^2}{m_Z^2} \rightarrow \frac{P^2}{m_Z^2}, \text{ and } h_i^Z \rightarrow h_i^\gamma \text{ for } i = 1, \dots, 4. \tag{2.2}$$

Eqs. 2.1, 2.2 give us the definition of the couplings between a Z boson and a photon, h_i^V ($V = Z$ or γ). These couplings are dimensionless functions of the squared momenta of

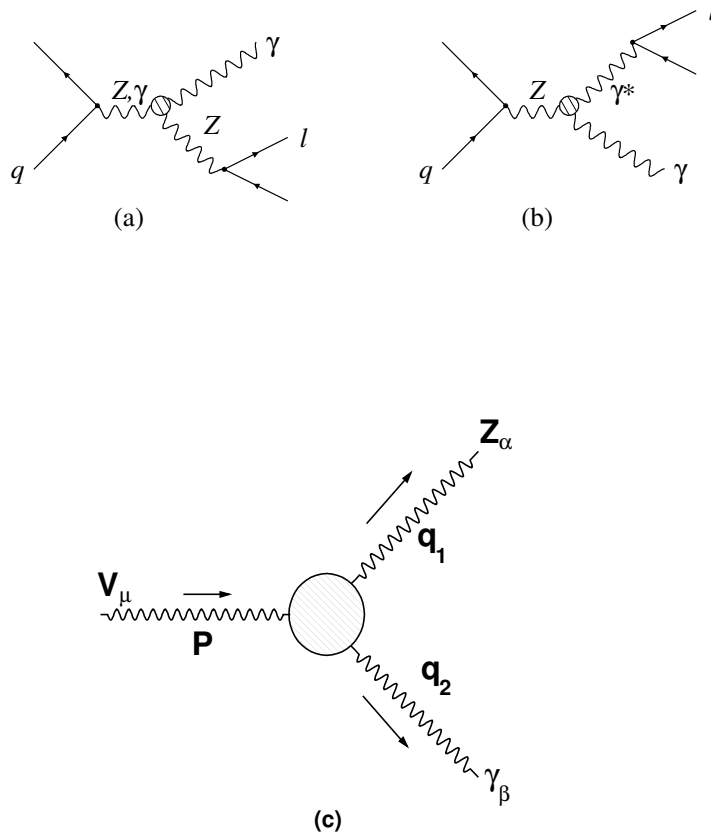


Figure 2.3: (a), (b) Feynman diagrams of anomalous $Z\gamma \rightarrow \ell\ell\gamma$ production; (c) general $ZV\gamma$ vertex.

the bosons in the trilinear $ZV\gamma$ vertex (see Fig. 2.3(c)). All couplings violate the C -parity, and couplings h_3^V and h_4^V violate the P -parity. Hence, h_1^V and h_2^V (h_3^V and h_4^V) couplings are CP -violating (CP -conserving). The couplings have to vanish at large values of q_1^2 , q_2^2 , and P^2 . For the $Z\gamma$ production values of q_1^2 and q_2^2 are restricted to $q_1^2 \approx m_Z^2$ and $q_2^2 = 0$, respectively. However, in cases when P^2 increases up to the squared center-of-mass energy (\hat{s}) values, this leads to the production of photons with extremely high transverse energy and an increase of the $Z\gamma$ cross section, eventually leading to the violation of the partial wave

unitarity of the $ff \rightarrow Z\gamma$ process. Here, f represents quarks or gluons that form protons and antiprotons. Hence, the inverse \hat{s} dependence has to be included into the couplings form-factor [12, 13]:

$$h_i^{Z,\gamma} = \frac{h_{i0}^{Z,\gamma}}{(1 + \hat{s}/\Lambda^2)^n}. \quad (2.3)$$

In this equation Λ is a form-factor scale, meaning a characteristic energy scale above which the SM processes start receiving non-negligible contributions from new phenomena processes. In accordance with Refs. [12, 13], h_{i0}^V are the low energy approximations of couplings, and $n = 3$ for h_1^V and h_3^V , and $n = 4$ for h_2^V and h_4^V . At the Tevatron $q\bar{q}$ center-of-mass energy of up to 2 TeV, a good starting value for Λ is on the order of 1 TeV.

Once introduced into the theory, the anomalous $ZV\gamma$ couplings (given the partial-wave unitarity) result in the $Z\gamma$ cross section increase (see Fig. 2.4) and in an excess of the production of photons with high values of the transverse energy (see Fig. 2.5). Observation of anomalously high gauge boson production could possibly indicate new physics.

2.2.3 Higher order and QCD corrections

As stated in Section 2.2.2, all couplings h_i^V vanish at the tree level within the SM framework. The h_3^V and h_4^V (CP -conserving) couplings receive contribution from the QED processes at the one-loop level. It has been shown, that these corrections are of the order of $\mathcal{O}(\alpha)$, and for h_3^V the value of the correction is [12]:

$$2.2 \times 10^{-4} \leq h_3^Z \leq 2.5 \times 10^{-4} \quad (2.4)$$

The corrections on the couplings due to the QED processes are by far smaller than the sensitivity that we expect from the experiment, and will be neglected in this work. However, the situation is different with the QCD corrections ($\mathcal{O}(\alpha_s)$). Virtual and soft gluon radiation diagrams contribute to the tree level diagrams shown in Figs. 2.2, 2.3. The magnitude of the QCD corrections to the leading order (LO) calculations depends on the experiment, center-of-mass-energy, set of requirements imposed in the analysis, *etc.*. Typical value of the correction is on the order of 20%–50%, but can be as large as a factor of 2.2 [13]. The QCD

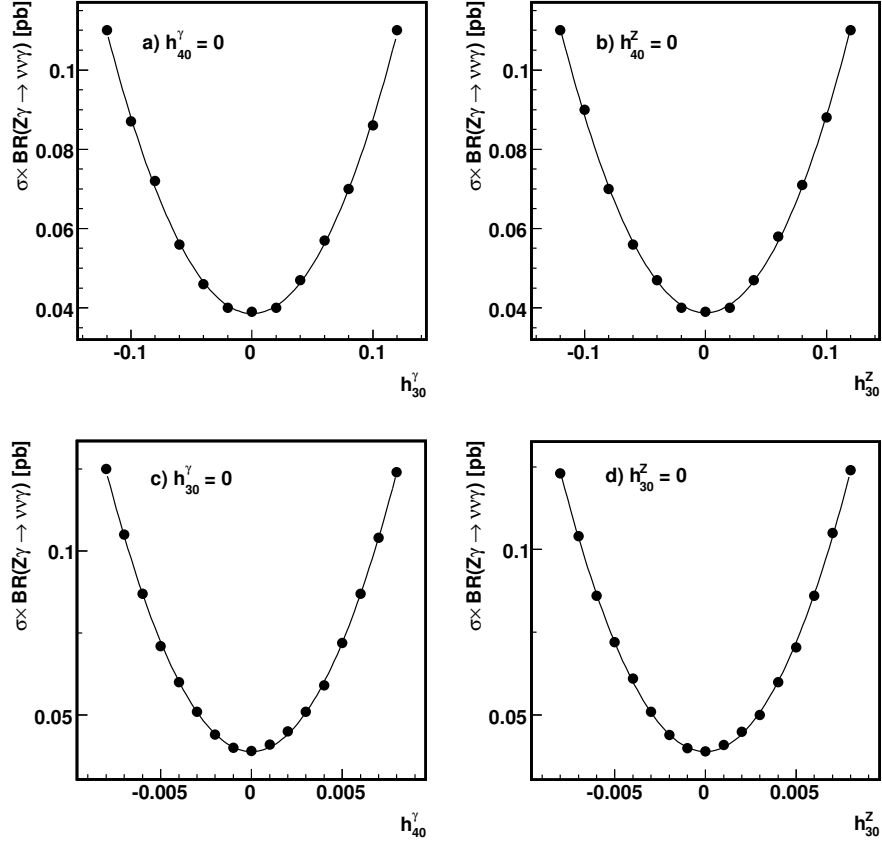


Figure 2.4: $Z\gamma \rightarrow \nu\bar{\nu}\gamma$ cross section as a function of the anomalous couplings (a) h_{30}^γ , (b) h_{30}^Z , (c) h_{40}^γ , and (d) h_{40}^Z . For each case all other couplings are set to their SM values (zero). The minimum on the plots corresponds to the SM point. The distributions are obtained from the simulation of the $Z\gamma \rightarrow \nu\bar{\nu}\gamma$ process, but show the same behavior for other Z boson decay modes.

corrections not only increase the LO cross section but also change the shape of the photon transverse momentum spectrum, and hence must be taken into account in the search for the anomalous $Z\gamma$ production. The next-to-leading order (NLO) QCD corrections are available only for the LO initial state radiation processes, and thus the generator (*NLO Baur* [13]) that involves these corrections is of the limited use. However, as it will be shown in Chapter 5, the NLO corrections are taken into account by applying the E_T -dependent K -factor (obtained from the NLO Baur generator) to the LO photon transverse momentum spectrum.

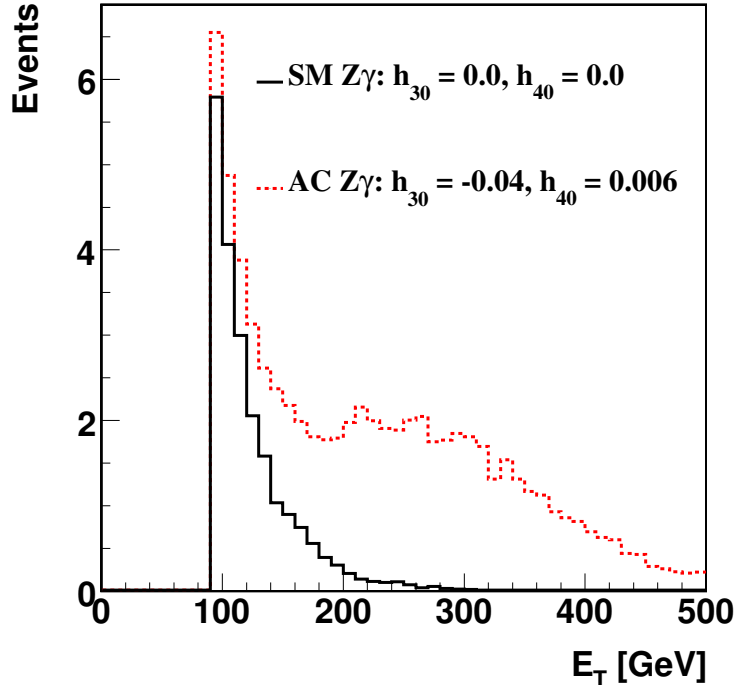


Figure 2.5: Photon transverse momentum spectra for the SM and anomalous $Z\gamma$ production. The distributions are obtained from the simulation of the $Z\gamma \rightarrow \nu\bar{\nu}\gamma$ process, but show the same behavior for other Z boson decay modes.

2.2.4 Theories beyond the SM

There are several theories that predict anomalously strong $ZV\gamma$ couplings. The most developed ones to date are the minimal supersymmetric standard model [14] (MSSM) and the theory that predicts the compositeness of the Z boson [15, 16].

In the MSSM model, heavy SUSY particles in one-loop diagrams (see *e.g.* Fig. 2.1(b)) can enhance the strength of the couplings between Z boson and a photon. The expected values of the anomalous couplings in the MSSM model are on the order of $\mathcal{O}(10^{-2})$ [17]. To date, SUSY particles have not been observed yet.

The composite Z boson theory states that a Z boson is not a solid particle, but consists of point-like hypothetical particles: *preon* and *antipreon*. Preons couple to photons, and hence the trilinear $ZV\gamma$ vertex is a consequence of the radiation of photon(s) by the preon.

The magnitude of the anomalous couplings is predicted to be on the order of $\mathcal{O}(0.1) - \mathcal{O}(1)$ [17]. As in the case of the MSSM, the compositeness of the Z boson, as well as fundamental fermions, has not been observed.

2.2.5 Previous studies

In the past, studies of the $Z\gamma$ production have been performed by the CDF [18–20] and DØ [20–24] collaborations at the Tevatron collider, as well as the LEP collider by the ALEPH [25], DELPHI [26], L3 [27, 28] and OPAL [29] collaborations. The most recent combination of LEP results can be found elsewhere [30, 31]. The most recent 95% C.L. on one-dimensional trilinear gauge couplings from these experiments are summarized in Table 2.4. DELPHI collaboration has updated the analysis [32] recently, but these results are not combined with the results from other three LEP experiments, and hence are not included in Table 2.4.

Table 2.4: Summary of previous 95% C.L. limits on anomalous $ZZ\gamma$ and $Z\gamma\gamma$ couplings.

Experiment	$ZZ\gamma$ Limits	$Z\gamma\gamma$ Limits
ALEPH	$-0.28 < h_3^Z < h_3^Z < 0.19, -0.10 < h_4^Z < 0.15$	$-0.069 < h_3^\gamma < 0.037, -0.020 < h_4^\gamma < 0.045$
DELPHI	$-0.32 < h_3^Z < h_3^Z < 0.18, -0.12 < h_4^Z < 0.18$	$-0.047 < h_3^\gamma < 0.047, -0.032 < h_4^\gamma < 0.030$
L3	$-0.23 < h_3^Z < h_3^Z < 0.11, -0.08 < h_4^Z < 0.16$	$-0.062 < h_3^\gamma < -0.014, -0.004 < h_4^\gamma < 0.045$
OPAL	$-0.29 < h_3^Z < h_3^Z < 0.14, -0.09 < h_4^Z < 0.19$	$-0.16 < h_3^\gamma < 0.00, 0.01 < h_4^\gamma < 0.13$
LEP-II combined	$-0.20 < h_3^Z < 0.07, -0.05 < h_4^Z < 0.12$	$-0.049 < h_3^\gamma < -0.008, -0.002 < h_4^\gamma < 0.034$
CDF	$ h_{30}^Z < 0.083, h_{40}^Z < 0.0047$	$ h_{30}^\gamma < 0.084, h_{40}^\gamma < 0.0047$
D0	$ h_{30}^Z < 0.21, h_{40}^Z < 0.019$	$ h_{30}^\gamma < 0.22, h_{40}^\gamma < 0.019$

Chapter 3

The Tevatron Collider and the Upgraded DØ Detector

The Fermilab Tevatron [33, 34] is currently the world's highest energy collider operating with protons and antiprotons at the center-of-mass energy of $\sqrt{s} = 1.96$ TeV. Bunches of protons and antiprotons are accelerated to the energies of 980 GeV each in a circular ring and collide at two interaction points, located in the middle of two detectors: CDF and DØ.

3.1 The Accelerator Chain

A complex machine is needed in order to accelerate the massive particles to energies of almost 1 TeV. The Fermilab's accelerator chain consists of several consecutive accelerators described in this Section and shown in Fig. 3.1.

3.1.1 Pre-accelerator

The first stage of the acceleration complex is the Cockcroft-Walton accelerator. The hydrogen gas is ionized to produce negative hydrogen ions, and the high positive voltage is used to accelerate the ions to the energy of 750 keV.

3.1.2 Linac

The 750 keV hydrogen ions then enter a linear accelerator (linac), in which the oscillating electric fields in the radio frequency (RF) cavities accelerate the ions to 400 MeV. With the

FERMILAB'S ACCELERATOR CHAIN

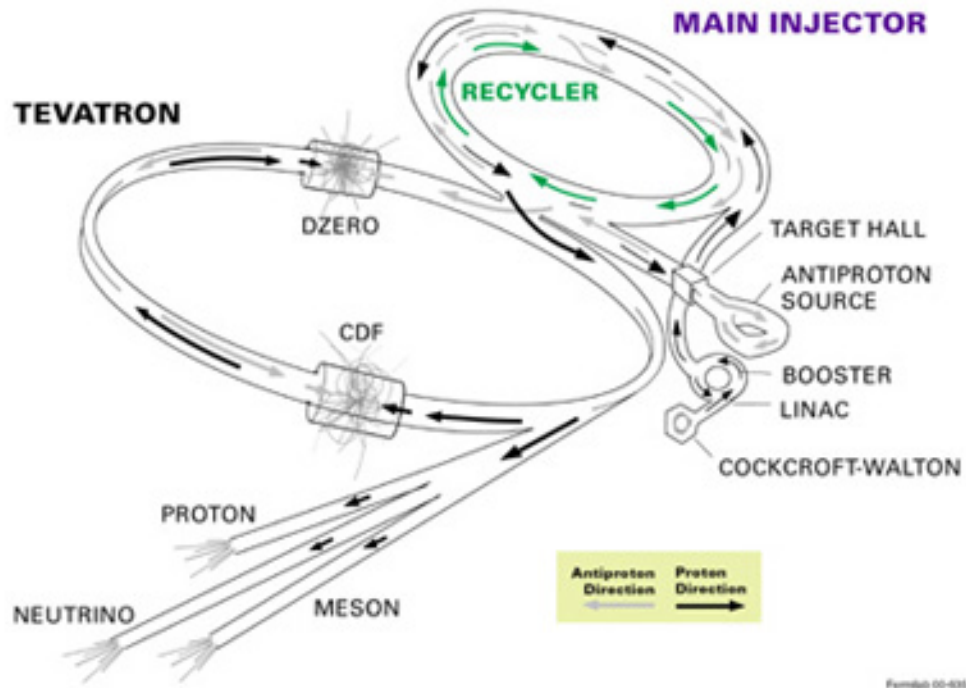


Figure 3.1: Fermilab's accelerator chain.

length of the linac of about 150 meters, the acceleration gradient is roughly 2.7 MeV per meter. The ions then pass through a thin carbon foil at the end of the linac, that strips off two electrons from the ions, and leaves only protons.

3.1.3 Booster

The protons from the linac then enter the Booster, a circular accelerator that uses magnets to keep the protons in a circular orbit. With each of about 20,000 revolutions protons pass through the electric field that gradually boosts their energy until the protons reach the energy of about 8 GeV.

3.1.4 Main Injector

The Main Injector (MI) plays a number of important roles in the accelerator chain. It receives 8 GeV protons from the Booster and accelerates them to 120 GeV; some portion of these protons is sent to the antiproton factory, the Antiproton Source. The protons at the Antiproton Source collide with a nickel target, producing antiprotons accompanied by secondary particles. About 50 thousand protons is needed to produce one antiproton. Antiprotons are then collimated and stored in the Accumulator ring, that passes them to the MI. 120 GeV protons and antiprotons in the MI are accelerated to 150 GeV, and are injected into the Tevatron ring for the final stage of the acceleration and collisions. The MI also houses the Antiproton Recycler, that stores the \bar{p} from the Tevatron to re-inject them back.

3.1.5 Tevatron

36 bunches of protons and antiprotons each consisting of more than 10^{10} particles are injected into the Tevatron ring in the opposite direction and are accelerated to the energy of 980 GeV each, traveling at almost the speed of light. Powerful dipole magnets bend the particles trajectories in the beam pipe to keep them in the circular orbits, and the quadrupole magnets are used to focus the beams and compress them to about 30 microns in radius. Both types of magnets are cooled down to the temperature of liquid helium to sustain the multi-thousand amperes currents flowing through their coils. With the circumference of the Tevatron ring of 6.28 km, the proton and antiproton bunches collide in the two high-luminosity interaction points every 396 ns. The low beta magnets installed at both ends of the two collider detectors are used to focus the beams and create the collisions in the middle of the detectors: the Collider Detector at Fermilab (CDF) and the DØ detector.

The instantaneous luminosity [8] is the measure of the collision rate per unit area per unit time, usually measured in $\text{cm}^{-2}\text{s}^{-1}$. It is proportional to the number of particles in two colliding bunches, n_1 and n_2 , the collision rate, f , and inversely proportional to the

overlapping transverse area of the beams, $\sigma_x\sigma_y$:

$$\mathcal{L} = f \frac{n_1 n_2}{4\pi\sigma_x\sigma_y}. \quad (3.1)$$

The highest achieved instantaneous luminosity to date at the Tevatron is roughly $360 \times 10^{30} \text{ cm}^{-2}\text{s}^{-1}$, and is the world's highest instantaneous luminosity ever achieved at the hadron colliders. The integrated luminosity is defined as the instantaneous luminosity summed over time, and is measured in units of cm^{-2} , or more commonly, in inverse barns, b^{-1} . One inverse barn corresponds to 10^{-24} cm^{-2} . The analyses described in this dissertation make use of up to 4 fb^{-1} of integrated luminosity.

3.2 The DØ Detector

The DØ detector [35] is a full scale multi-purpose hermetic detector designed to work with high-intensity Tevatron beams. Its dimensions are approximately $18 \text{ m} \times 12 \text{ m} \times 10 \text{ m}$. The side-view of the detector with all the main components is shown in Fig. 3.2.

The interaction point in the middle of the detector is surrounded by the tracking system, consisting of the silicon microstrip tracker (SMT), central fiber tracker (CFT), and 2 T superconducting solenoid. The main purpose of the tracking system is to provide momentum measurements and vertexing. Outside the central tracker there are two preshower detectors and a calorimeter (both central and forward), that measure the energy of most particles, as well as aid in determining the direction of the electromagnetic (EM) showers. The outer subsystem of the DØ detector is the muon system, comprised of wire drift tubes, scintillation trigger counters and 1.8 T toroidal magnet. The purpose of the muon system is to trigger the muon candidates and measure their properties. Two plastic scintillator arrays located between the tracking system and the forward calorimeter cryostats are used to measure the instantaneous luminosity of the colliding beams.

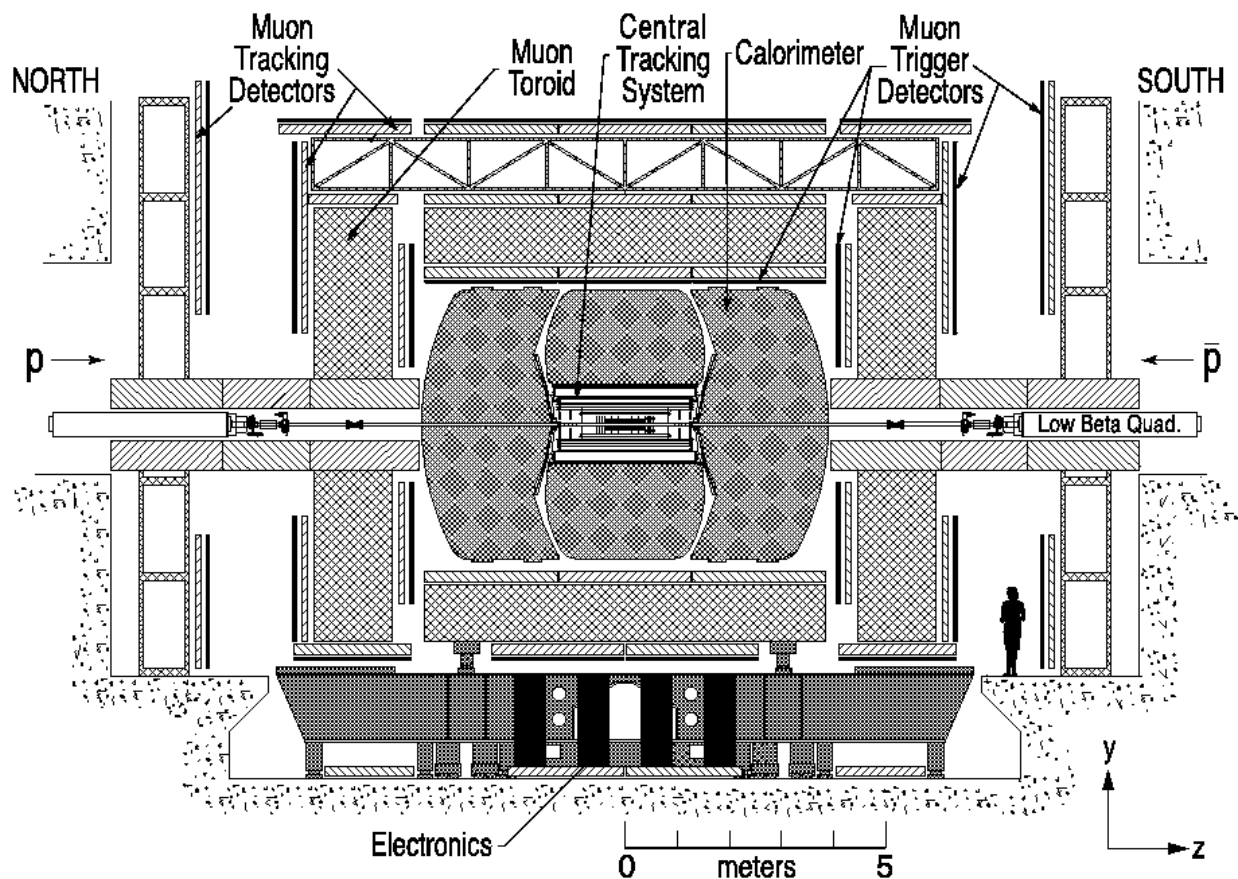


Figure 3.2: The $D\bar{O}$ detector side-view.

3.2.1 Coordinate system and useful variables

The $D\bar{O}$ detector coordinate system is shown in Fig. 3.3 and is defined in such a way, that the protons move along the z -axis and the antiprotons move in the opposite direction. The center of the detector is used as the zero point of the coordinate system. The z coordinate is defined as the distance along the beam line, with the y -axis pointing upwards. Azimuthal angle, ϕ , is measured with respect to the x -axis of the detector in the $x - y$ plane (also called $r - \phi$ plane, where r is the perpendicular distance in the direction away from the beam pipe), and varies from 0 to 2π :

$$\phi = \tan^{-1} \left(\frac{p_y}{p_x} \right). \quad (3.2)$$

The polar angle, θ , is measured with respect to the z -axis in the $z - y$ plane. In addition

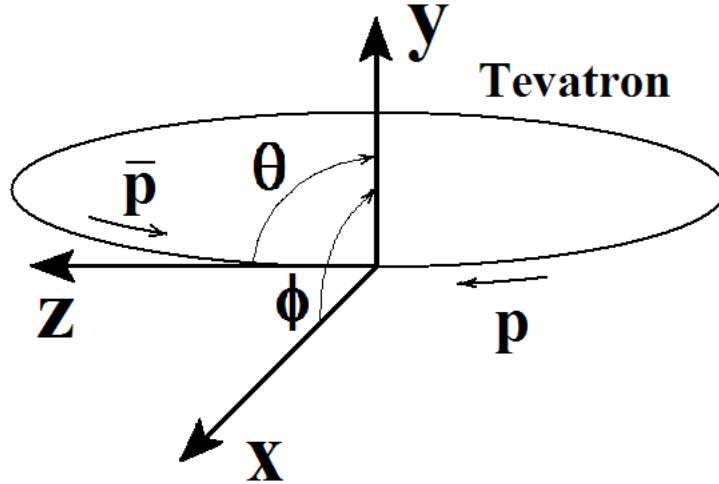


Figure 3.3: *The DØ detector coordinate system.*

to these basic variables, at DØ we use other important variables defined below. The rapidity, y (see, *e.g.* Ref. [8]), is another way to measure the motion of the particle and is defined as:

$$y = \frac{1}{2} \ln \frac{E + p_L}{E - p_L} = \tanh^{-1}(\beta_L), \quad (3.3)$$

where E is the energy of the particle, p_L is the longitudinal component of the momentum along the z -axis, and β_L is the longitudinal component of the speed of the particle relative to the speed of light. When the momentum of the particle is large enough to neglect the mass of the particle, rapidity transforms into another variable, called *pseudorapidity* (η):

$$\eta = \frac{1}{2} \ln \frac{|\vec{p}| + p_L}{|\vec{p}| - p_L} = -\ln \left[\tan \left(\frac{\theta}{2} \right) \right], \quad (3.4)$$

where \vec{p} is the total momentum of the particle. As seen from the definitions, rapidity and pseudorapidity are dimensionless functions, and the main advantage of their usage (compared to the polar angle) is that the difference in the rapidity of two particles is independent of the Lorentz boost along the beam axis. The pseudorapidity dependence on the polar angle is shown in Fig. 3.4. The region with values of $\eta \leq 1.1$ is called central.

The transverse energy and momentum, E_T and p_T , of particles after the collision are

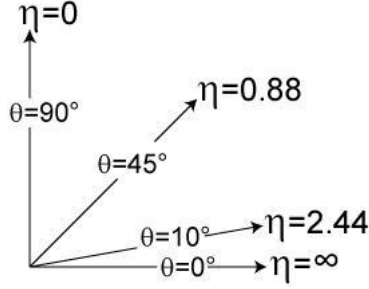


Figure 3.4: *The pseudorapidity as a function of the polar angle for four values of θ .*

defined as:

$$E_T = E \sin\theta, \text{ and } p_T = \sqrt{p_x^2 + p_y^2}. \quad (3.5)$$

There are useful relations between the components of the total momentum and the angles listed below:

$$p_x = p_T \cos\phi, \quad p_y = p_T \sin\phi, \quad p_z = p_T/\tan\theta. \quad (3.6)$$

Another Lorentz boost invariant variable is the spatial separation of two particles, ΔR , defined as:

$$\Delta R = \sqrt{\Delta\phi^2 + \Delta\eta^2}, \quad (3.7)$$

where $\Delta\phi$ and $\Delta\eta$ are the differences of the corresponding variables of two particles.

3.2.2 Silicon microstrip tracker

The central tracker side-view is shown in Fig. 3.5. The silicon microstrip tracker (SMT) is the closest to the beam pipe component of the central tracking system. The beam pipe at $D\emptyset$ is made of beryllium with an outer diameter of 38.1 mm, wall thickness of 0.508 mm and length of 2.37 m. The three-dimensional (3-D) view of the SMT is shown in Fig. 3.6.

The SMT consists of thin layers of silicon arranged in readout layers, and oriented either parallel or perpendicular to the beam pipe. This is done in an effort to make charged tracks from the collision as perpendicular to the SMT sensors as possible.

The principle of the silicon detector work is based on the ionizing action of the charged particles, when they pass through the doped silicon. Electron-hole pairs, produced by

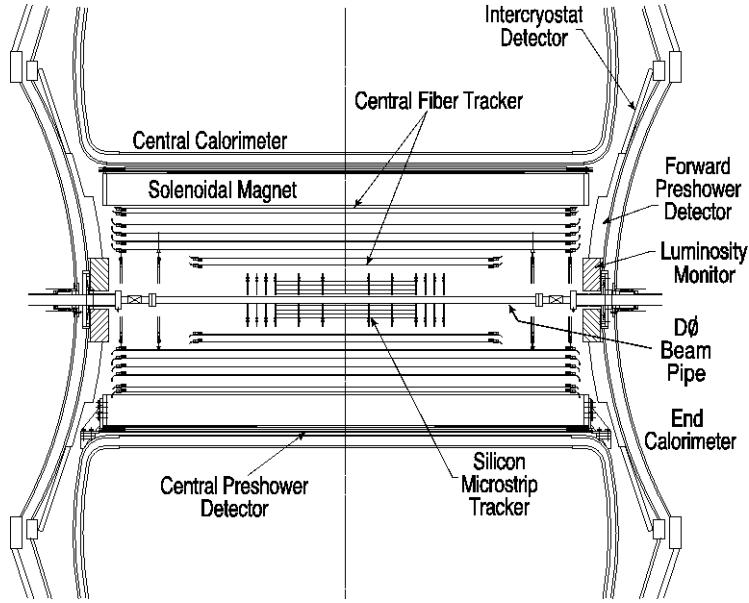


Figure 3.5: *The central tracking system side-view.*

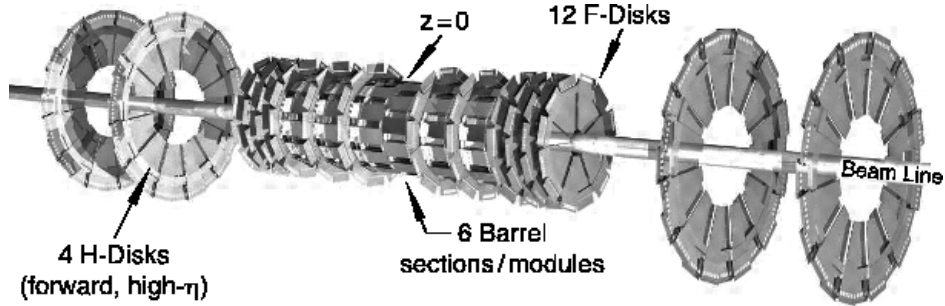


Figure 3.6: *3-D view of the silicon microstrip tracker.*

the particle, travel to the electrodes by the influence of the electric field. The charge is accumulated by the capacitor arrays and is further read out. The amount of charge is the measure of the energy of the incident particle.

The SMT consists of several modules: six barrels and twelve F-disks in the central region, and four H-disks in the forward region. The inner (outer) radii of the barrels, F-disks and H-disks are: 2.7 (10.5) cm, 2.6 (10.0) cm, and 9.5 (26.0) cm, respectively. Each barrel has four readout layers. Layers 1 and 2 consist of twelve so-called *ladders*, and layers 3 and 4 consist of twenty four ladders. A ladder is a silicon wafer, oriented axially. The strips in the

ladders can be oriented either axially, or at angles (stereo strips) with respect to the beam line. The cross section of the barrel with the ladders assembly is shown in Fig. 3.7. The centers of barrels are located at $|z| = 6.2, 19.0$ and 31.8 cm. At the higher $|z|$, each barrel is capped with an F-disk. All F-disks are assembled of twelve wedge-shaped double-sided silicon wafers. The remaining three F-disks on each side of the z -axis are combined into a single unit with small gaps between the disks. The centers of the F-disks are located at $|z| = 12.5, 25.3, 38.2, 43.1, 48.1,$ and 53.1 cm. The large-diameter H-disks consist of twenty four double-sided wedges, and are located at $|z| = 100.4$ and 121.0 cm. Such a large distance of the H-disks from the interaction point allows reconstruction of tracks with small angles to the beam pipe. Combining all ladders and wedges, there are total of 912 readout modules with 792,576 signal channels. With the H-disks, the SMT provides precise tracking and vertexing with pseudorapidities up to $|\eta| < 3$. Typical resolution of the track position measurement is on the order of $10 \mu\text{m}$. The SMT is kept at temperatures below 5°C to minimize the damage to the silicon.

The Layer 0 detector is a silicon detector installed between the beam pipe and the barrels of the SMT during the Summer 2006 shutdown. It has a single-layer barrel structure with axially oriented silicon wafers. Unlike the SMT, due to limited space the Layer 0 readout electronics is not mounted on the sensors, but receives the analog signal through the cables. The main purpose of the Layer 0 detector is to improve the resolution of the impact parameter.

3.2.3 Central fiber tracker

The central fiber tracker (CFT) is the subsystem that comes after the SMT. It is made of scintillation fibers, $835 \mu\text{m}$ in diameter. The fiber has a scintillation core covered by two claddings to achieve the total internal reflection inside the fiber. The scintillation fibers are mounted in two layers - an axial layer and a stereo layer oriented at $\pm 3^\circ$ angle in ϕ (the so-called u and v layers), arranged in ribbons each having 256 fibers (see Fig. 3.8). These

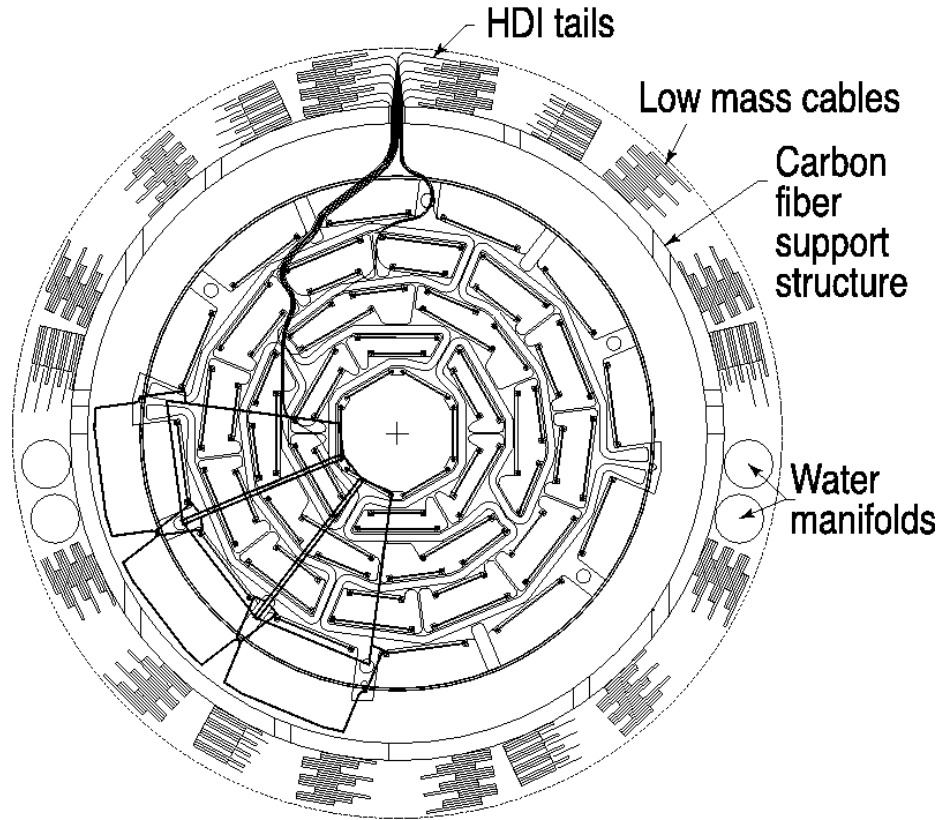


Figure 3.7: *Cross section of the SMT barrel.*

layers form eight concentric cylinders, the first and the last one being 20 cm and 52 cm in diameter, respectively. The two innermost cylinders are 1.66 m long, and the other six are 2.52 m long. Such a design allows the large-diameter SMT H-disks to be inside the CFT cylinders.

The principle of the fiber detector work is based on the emittance of photons by charged particles when they pass the scintillation fiber. The peak emission wavelength of the fibers used in CFT is approximately 540 nm. One of the scintillation fibers ends is coated with aluminum so most of the light is collected by the clear waveguides on the other end (see Fig. 3.9). The photons from the scintillation fibers are then carried by the waveguides to the silicon avalanche photodetectors, or the visible light photon counters (VLPC), which convert the photons into the electric signals. The VLPCs are kept at 9 K for high efficiency

and low noise. With the position of each fiber known to better than $50 \mu\text{m}$, the spatial resolution of the CFT is on the order of $100 \mu\text{m}$. The CFT covers the pseudorapidity range of up to $|\eta| < 1.7$

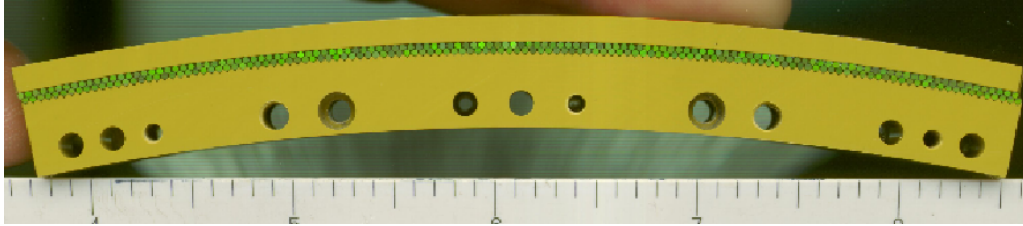


Figure 3.8: *Two layers of each of the CFT cylinders.*

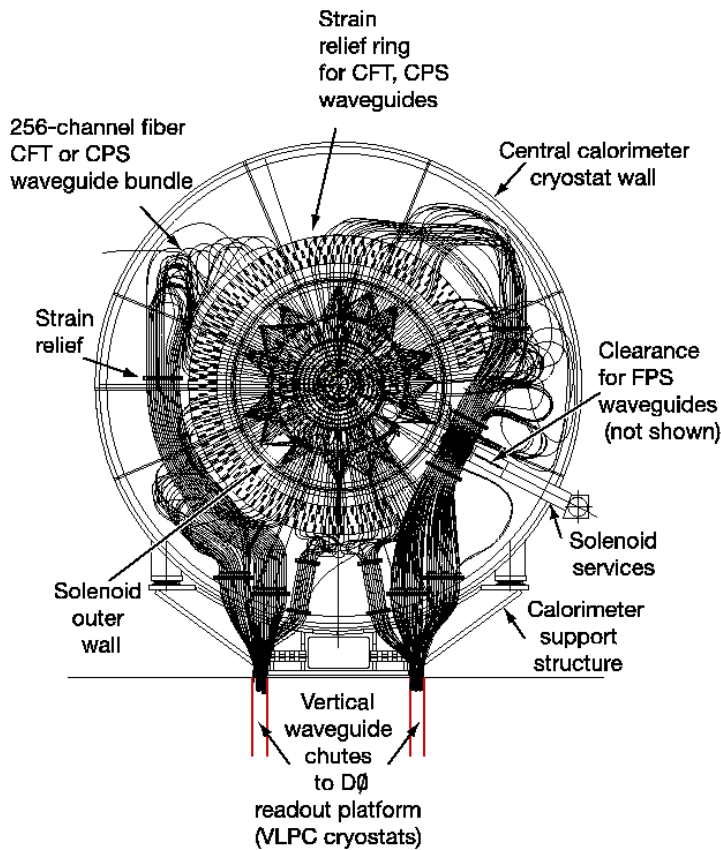


Figure 3.9: *Waveguides of the CFT.*

3.2.4 Solenoid

The outer part of the central tracking system is the superconducting 2 T solenoid (Fig. 3.10). The solenoid is enclosed in the cryostat 2.73 m long, and 1.4 m in diameter, and is cooled by liquid helium to sustain the operating current of 4,749 A. The thickness of the solenoid is 0.87 radiation lengths (X_0) at $\eta = 0$. The design of the solenoid allows one to achieve a uniform magnetic field in the inner volume of the solenoid with the magnetic field lines parallel to the beam line. The magnetic field in the tracking system allows measurement of the charged particles' momentum, curvature of the track, and the charge to transverse momentum ratio.

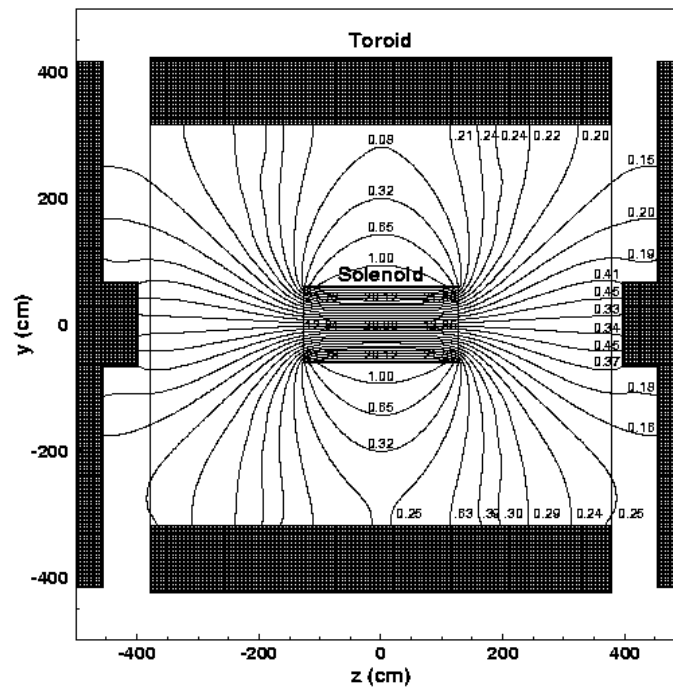


Figure 3.10: Schematic side-view of the solenoidal magnet.

3.2.5 Preshower detectors

The preshower detectors (PS) possess features of both calorimeter and tracking devices. They can be used as a tool to improve the matching between calorimeter showers and

tracks reconstructed in the central tracker. The preshower detectors are also important for the photon identification, as the information about the position of the cluster in the PS is used in the pointing algorithm. This allows one not only to reconstruct the pointed vertex of the photon candidate and estimate how far the photon candidate was produced from the beam line in the $r - \phi$ plane, but also to estimate and suppress the backgrounds. Level 1 trigger also uses the energy and position measurement information from the PS. And moreover, this information can be used to correct the energy deposited in the calorimeter for the losses in the solenoid, unaccounted material, cables, *etc.*

The preshower detectors are divided into the central (CPS) and two forward (FPS) sections. Both CPS and FPS are made of triangular strips of extruded plastic scintillator with $835 \mu\text{m}$ -diameter wavelength shifting fibers (WLS) in the middle of each strip, as shown in Fig. 3.11. The layout geometry of the strips allows no dead space between the strips, and in most cases the charged particle crosses more than one strip, which results in the improved measurement of the track position. The scintillator strips are wrapped in mylar

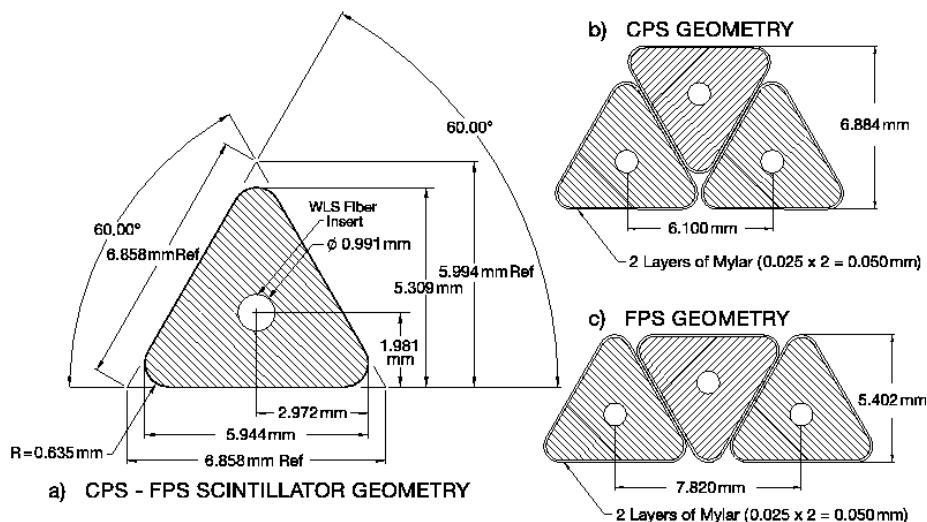


Figure 3.11: *Cross section of the preshower detectors scintillator strips.*

for optical isolation, and both ends of the strips are painted white. The light produced by charged particles in the scintillator strips is guided by the WLS to the CFT waveguides and

further to the same VLPCs used in the CFT readout system.

The CPS is located between the solenoid and the central calorimeter. There is a lead radiator of approximately one radiation length before the CPS, covering $|\eta| < 1.3$. The CPS has three layers of scintillator strips arranged in three concentric cylindrical layers. Each layer is built of 1,280 strips. The strips in layers are arranged as follows: the strips in the innermost layer are axially oriented, while the stereo strips in the second and third layers are oriented at angles of 23.774° (u layer) and 24.016° (v layer) to the axial layer. Such a geometry allows reconstruction of 3-D clusters in the central preshower. Each layer is divided into eight octant modules.

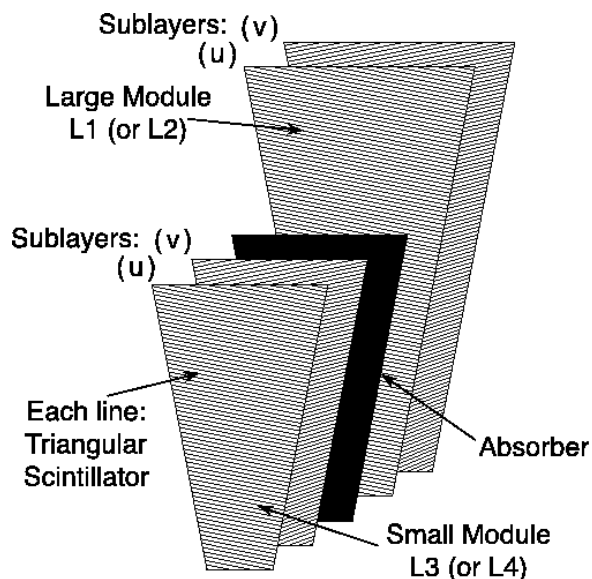


Figure 3.12: *Forward preshower detector segment exploded view.*

The two FPS detectors are situated on the calorimeter endcaps. The FPS consists of two trapezoidal layers separated by $2 X_0$ lead-steel absorber, as shown in Fig. 3.12. Each layer consists of an u and v stereo sublayers. The innermost layer, closest to the interaction region, is called the minimum ionizing particle (MIP) layer, and the other one is called the shower layer. The charged particles after the collision produce minimum ionizing signals in the MIP layer, while electromagnetic particles after showering in the absorber will deposit

their energy in the shower layer. As in case of the CPS, the stereo orientation of the sublayers allow 3-D measurement of the position and the energy of the clusters. The FPS is divided into eight segments with total coverage of $1.5 < |\eta| < 2.5$.

3.2.6 Calorimeter

The $D\emptyset$ calorimeter is a liquid argon/uranium sampling calorimeter. It provides measurements of the incident particle energy, as well as the shape of this energy deposit in the calorimeter cells for particle identification. The 3-D view of calorimeter is shown in Fig. 3.13.

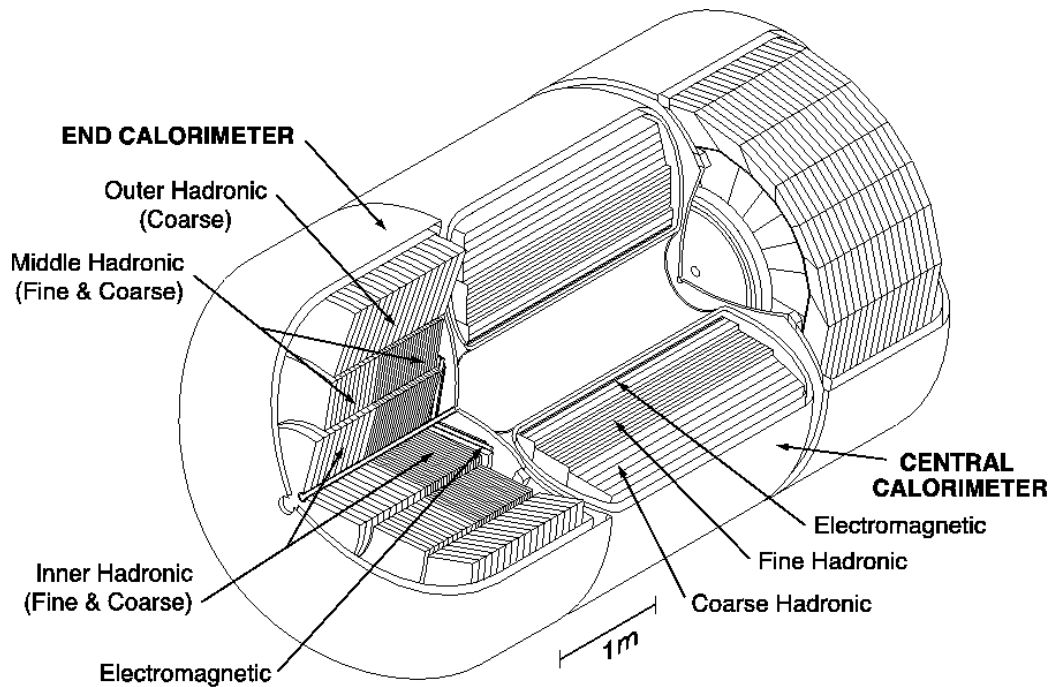


Figure 3.13: 3-D view of the $D\emptyset$ calorimeter.

A typical sampling calorimeter consists of alternating layers of absorber and active medium. Particles entering the calorimeter interact with the absorber and initiate showers of secondary particles. Electromagnetic (EM) showers are produced by the particles that interact mostly via electromagnetic force. The development of the EM shower is governed by the production of electron-positron pairs and bremsstrahlung. Hadronic (HAD) showers

are initiated by hadrons, either charged or neutral. The development of the hadronic shower is governed by interactions between the particle and the nuclei via strong force. In addition to pure hadronic showers, charged hadrons also produce EM showers, so typical hadronic shower is a combination of both. In both EM and HAD cases, the charged particles then ionize the active medium. Electric charge from ionization is collected by the high voltage pads, and is proportional to the energy deposited in the active medium. Usually, the EM showers are detected with higher efficiency, than the HAD showers. This effect is known as *noncompensation*, and leads to a non-linear hadronic response as a function of energy. This can be prevented by either decreasing the EM calorimeter sensitivity, or increasing the HAD calorimeter sensitivity. At DØ, compensation is achieved by using the uranium absorbers in the EM and fine HAD sections of the calorimeter.

The DØ calorimeter is spatially divided into the central calorimeter (CC), with the pseudorapidity coverage of $|\eta| < 1.1$, and two endcap calorimeters (EC) with $1.3 < |\eta| < 4.0$. Longitudinally the calorimeter is divided into the EM section of high granularity, and two HAD sections - fine and coarse. All three calorimeters are enclosed into separate cryostats and cooled down to 90 K with liquid helium.

The EM section of the calorimeter both in CC and EC is divided into four layers of different thickness. In the CC these layers are 1.4, 2.0, 6.8, and 9.8 X_0 thick. In the EC they are 1.6, 2.6, 7.9, and 9.3 X_0 thick. The depleted uranium absorbers are 3 mm and 4 mm thick in the CC and EC, respectively. The total thickness of the EM calorimeter is 20 X_0 (21.4 X_0) in the CC (EC). The maximum of EM showers is located in the third layer of the EM calorimeter, hence this layer has a finer granularity, $\Delta\eta \times \Delta\phi = 0.05 \times 0.05$, compared to 0.1×0.1 in three other layers.

The fine HAD part of the central calorimeter has three layers of 1.3, 1.0, and 0.76 absorption lengths (λ_A), and the coarse HAD single layer is 3.2 λ_A thick. In the EC the inner hadronic section has four layers of 1.1 λ_A (0.9 λ_A) in the fine (middle) part. The inner coarse hadronic section is 4.1 λ_A and 4.4 λ_A , respectively. The outer hadronic section is

$6.0 \lambda_A$ thick. Copper is used as an absorber material in the central HAD calorimeter, while stainless steel is used in the endcap HAD calorimeter.

The ionization charge in the calorimeter is read out from the signal boards in cells. A typical cell of the DØ calorimeter is shown in Fig. 3.14. A 1 unit cell consists of the grounded absorber, a positively charged signal pad and a liquid argon gap. The ionization electrons (fast component of the shower) drift to the signal pad, from which the charge is sent into the readout chain. The calorimeter cells are further arranged in readout towers (see Fig. 3.15) with $\Delta\eta \times \Delta\phi = 0.2 \times 0.2$ for trigger purposes.

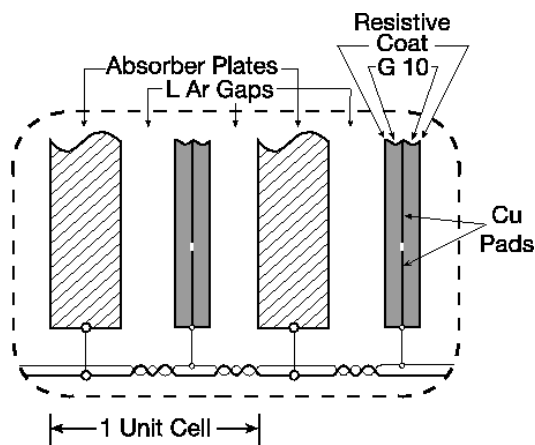


Figure 3.14: *Side view of the calorimeter cell.*

The average liquid argon gap in the cell is 2.3 mm, which results, together with the high voltage of approximately 2.0 kV, in the electron drift time of 450 ns. This drift time is larger than the beam crossing time of 396 ns, which means that the signal from the previous event is still being integrated when the next collision occurs. To account for that as well as for the pile-up (multiple interactions in one collision), the baseline subtraction (BLS) is used.

3.2.7 Intercryostat detector

Separate cryostats for all three calorimeters result in an incomplete coverage in the $0.8 < |\eta| < 1.4$ region. Also, as there is significant amount of the unsampled material, the energy

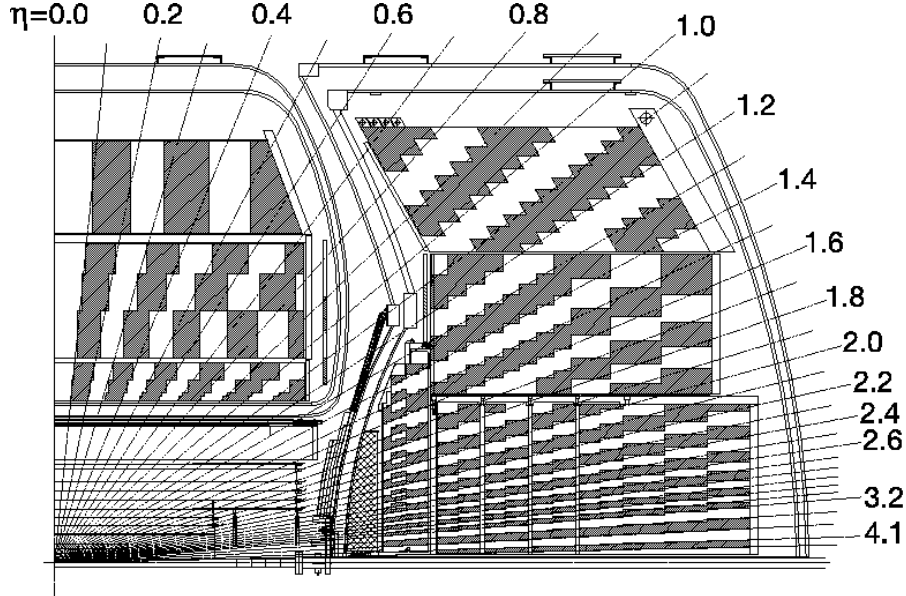


Figure 3.15: Side view of the $D\emptyset$ calorimeter.

resolution in this pseudorapidity range is more poor. To account for that, additional sampling layers are installed there, forming the so-called *intercryostat detector* (ICD). The ICD is divided into eight $\Delta\eta \times \Delta\phi = 0.3 \times 0.4$ octants (tiles), each consisting of twelve 0.1×0.1 trapezoidal subtiles. In addition, single calorimeter cell structures are installed in front of the first layer of uranium absorbers, forming the so-called *massless gaps*.

3.2.8 Luminosity monitor

The amount of data collected with the $D\emptyset$ detector is proportional to the number of inelastic $p\bar{p}$ collisions. The luminosity monitor (LM) is the device that measures the rate of these collisions. The LM is shown in Fig. 3.16, and is located in front of each endcap calorimeter at $|z| = 140$ cm. Each LM consists of twenty four trapezoidal optically isolated plastic scintillators and photomultiplier tubes, which are oriented along the beam axis. The LM covers the pseudorapidity range of $2.7 < |\eta| < 4.4$. The luminosity is evaluated to the

formula:

$$\mathcal{L} = f \frac{\bar{N}_{LM}}{\sigma_{LM}}, \quad (3.8)$$

where f is the beam crossing frequency, \bar{N}_{LM} is the average number of inelastic $p\bar{p}$ collisions per event, and σ_{LM} is the effective cross section for the luminosity monitor. \bar{N}_{LM} is corrected for the multiplicity of the $p\bar{p}$ collisions per event, and σ_{LM} is corrected for the inefficiency and acceptance of the luminosity monitor. To suppress the beam halo backgrounds that result in an overestimated \bar{N}_{LM} , the time-of-flight is measured for particles that hit the South and North LM scintillator arrays, t_- and t_+ . Then the z position of the interaction point, z_v , can be estimated from the formula:

$$z_v = \frac{c}{2} (t_- - t_+) \quad (3.9)$$

By requiring $|z_v| < 100$ cm, the halo background becomes negligible, so the estimate of the \bar{N}_{LM} is realistic.

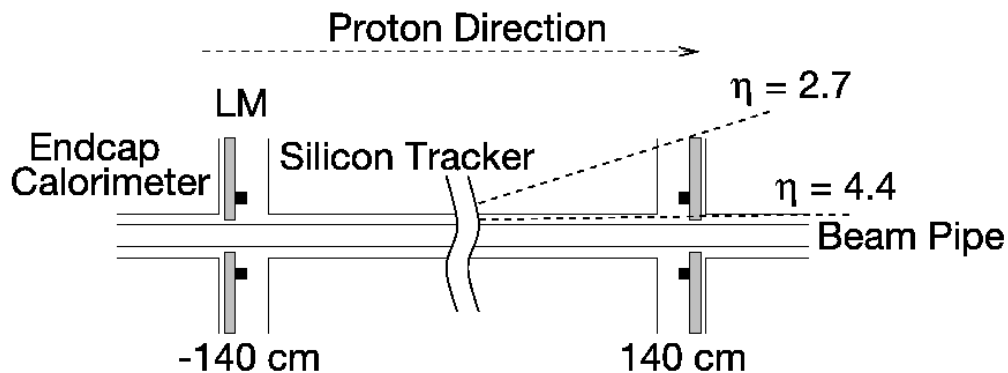


Figure 3.16: Side view of the luminosity monitor.

3.2.9 Muon system

Calorimeters are “destructive” devices, meaning that incident particles are destroyed by interactions with the calorimeter material, and the showers initiated by these particles are fully contained in the calorimeter volume. The only SM particles that penetrate the calorimeter

and leave it unharmed are neutrinos and muons. Neutrinos escape the detection, but the muons can be detected with the muon spectrometer – the outmost subsystem of the DØ detector. The muon system consists of scintillation counters (for trigger purposes and time measurement), wire drift tubes (for position measurement) and 1.8 T toroidal magnets. The magnetic field bends the muon candidates trajectories allowing for local momentum measurement in addition to the momentum measurement using the central tracker. In addition, the iron yokes of the toroids suppress the punch-through particles (mostly jets with very high energy) and very soft muons.

The central muon system, covering $|\eta| < 1.0$, and the forward muon system ($1.0 < |\eta| < 2.0$), share the same principles but are built using different components. Each of them is divided into three layers – A, B, and C – with an A-layer being the innermost one. An iron toroid is placed between the A-layer and B-layer. All three layers in the forward region consist of scintillation counters (FSC) and mini-drift tubes (MDT). The forward muon system also includes shielding around the beam pipe to suppress the backgrounds from the beam halo and protect the detector from excessive radiation. All three layers in the central muon system consist of proportional drift tubes (PDT), and only layers A and B have trigger scintillation counters ($A\phi$ counters). The A-layer (B- and C-layer) have four (three) planes of drift tubes. The scintillation counters are arranged in a single-layer structures. In total, there are 13 (12) combined drift chambers and scintillation counters signal layers in the forward (central) muon system. The average number of hits in the forward (central) muon system is slightly higher than 13 (12) due to the fact that some angled tracks can have more than one hit per plane in the drift tubes. The acceptance in the bottom A-layer is reduced by the calorimeter support structure. The drift chambers of the muon system are shown in Fig. 3.17, and the scintillation counters are shown in Fig. 3.18.

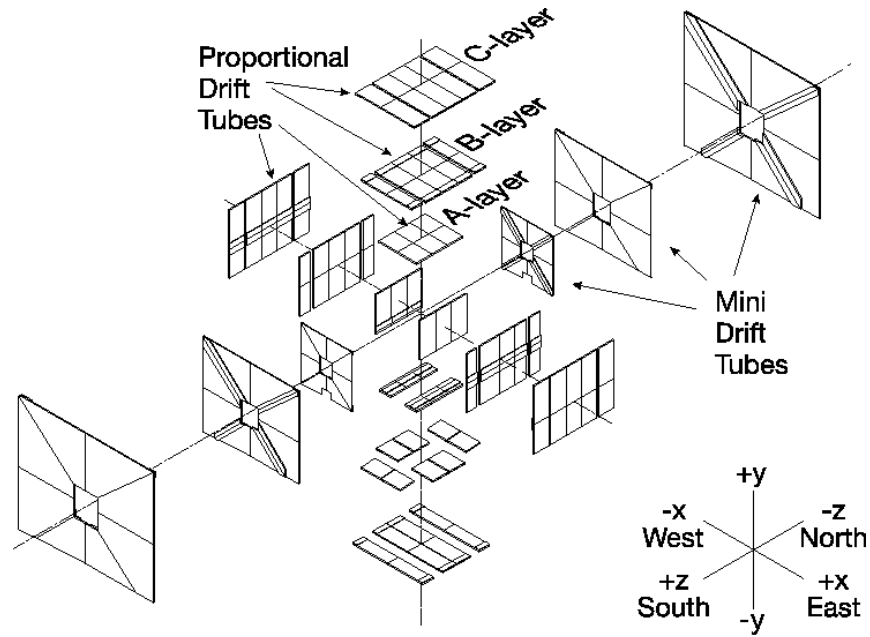


Figure 3.17: *Exploded view of the muon system drift tubes.*

3.2.10 Trigger

The time between beam crossings at the Tevatron is 396 ns, which means that there might be up to 2.5 million collisions per second. Not every bunch crossing is filled and results in a collision, so on average collisions at DØ occur at a rate of approximately 1.7 MHz. With an average amount of information that fully describes an event being on the order of 200 kB, the detector produces more than 300 GB of data per second. In addition, not every collision produces events that are interesting to physicists. Hence, it is important to quickly analyze the collisions, and acquire and write to tape only those events that contain potentially interesting candidates. This is done using a three-level DØ trigger system that works in accordance with a predefined strategy and filters the events. This strategy has been developed taking into account the signatures of hard scatter events: a presence of high- p_T tracks, leptons or jets. Also, a large amount of missing transverse energy, displaced vertices, *etc.*, might indicate potentially interesting physics. A set of particular three-level conditions is called a trigger.

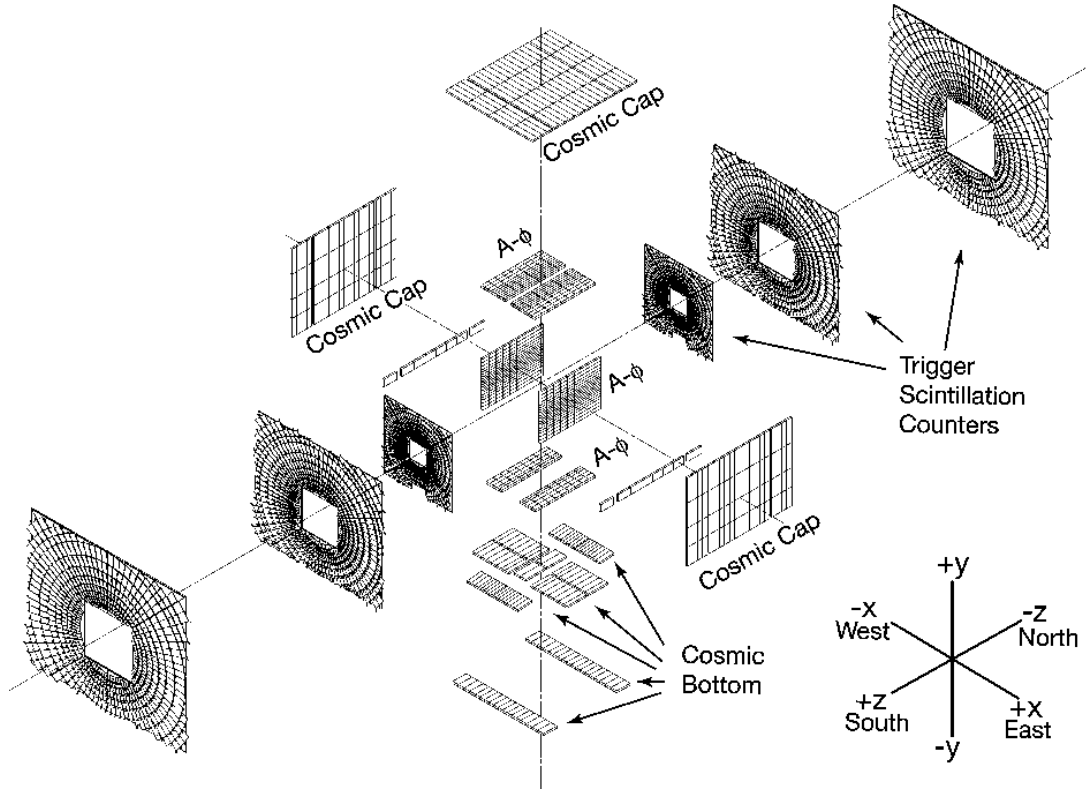


Figure 3.18: *Exploded view of the muon system trigger scintillation counters.*

The Level 1 (L1) filter is based on the hardware and firmware properties of an event from various subdetectors. The L1 reduces the rate to approximately 2 kHz. A set of prescales might be applied to individual triggers or groups of triggers depending on the instantaneous luminosity and the bandwidth of that trigger. A prescale of ten means that on average only each tenth triggered event will be randomly selected. Level 2 (L2) accepts events that passed L1 requirements. The 2 kHz L2 input rate is low enough to make decisions of the usefulness of the event based on both hardware quantities and results of simple software algorithms. The output rate of L2 is ≈ 1 kHz. Level 3 (L3) accepts events that passed L2 conditions. A number of computers (called a *farm*) run more sophisticated algorithms and perform a fast reconstruction of events. Events that pass L3 requirements are written to tape for offline reconstruction. The resulting rate to tape is on average 100-150 Hz. The structure of the $D\bar{O}$ trigger system is shown in Fig. 3.19.

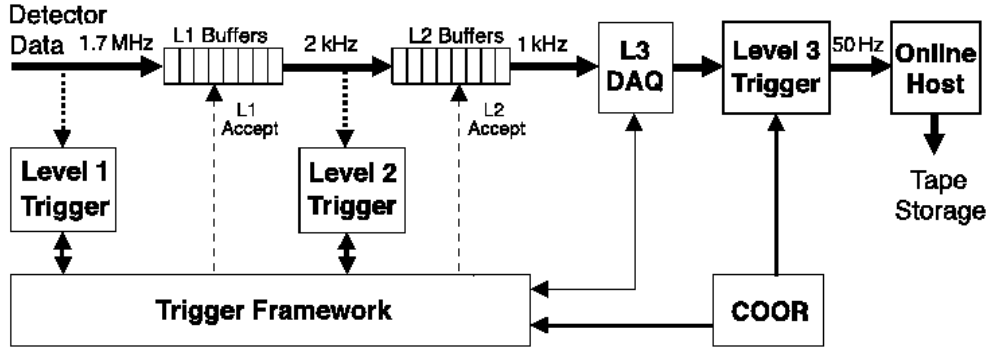


Figure 3.19: Overview of the $D\bar{O}$ trigger system.

A set of triggers is combined into a trigger list. As bandwidth of triggers depends on the instantaneous luminosity, the trigger lists have to be defined for different ranges of the instantaneous luminosity to fit into the specifications of each of the three trigger levels. In addition, with the detector and reconstruction software upgrades, trigger lists have to be re-optimized.

3.2.10.1 Level 1 trigger

The Level 1 trigger system communicates with all the subsystems of the $D\bar{O}$ detector (except the SMT), as shown in Fig. 3.20. All L1 decisions are made at the hardware level. The L1 analyzes every collision and thus has to be very fast. In order to minimize the dead time all events are buffered, and L1 trigger decisions have to arrive at the trigger framework (TFW) in $3.5 \mu\text{s}$. The TFW collects the information from each of the L1 trigger systems and passes the events of interest to the L2 trigger. Its other functions include prescaling, coordination of trigger vetoes, communication between the front-end electronics and the trigger control computer, *etc.* The L1 trigger systems are divided into calorimeter (L1Cal), tracker (L1CTT), and muon (L1Muon) triggers:

- The L1 central track trigger (L1CTT) uses the information about the position of axial hits in the CFT and CPS to search for tracks in the event. The full 360° circle in the $r - \phi$ plane is divided into 80 sectors of 4.5° . In each sector hits in the CFT are

compared to 20,000 predefined track equations in four p_T bins (1.5–3, 3–5, 5–10, and >10 GeV/ c). The track candidates which are found by this algorithm are then sorted, counted, and checked for matching with the CPS clusters. If no other tracks are found in the same or two adjacent 4.5° sectors, the track candidate is called isolated. Then the trigger terms with this information are passed to the TFW for the L1CTT decision. A similar algorithm finds tracks in the forward region, using the information about the position of the hits in the FPS layers. Its own L1 terms are sent to the TFW for the decision. The stereo CPS subsystem is not included into the L1 decision chain, however this information can be used at L2. Data from the FPS system are also used at L2 and L3. The L1CTT output is also sent to the L1 muon trigger system for matching the muon candidates to the tracks in the central tracking system.

- As mentioned in Section 3.2.6, the L1 calorimeter trigger (L1Cal) uses a sum of four EM and HAD calorimeter towers (total of $\Delta\eta \times \Delta\phi = 0.2 \times 0.2$ forming a *trigger tower*) energy deposits to form L1 calorimeter trigger terms. The tower energies are converted into the transverse energy, E_T , and the total transverse energy in four towers is calculated. In Run IIa the L1Cal terms were calculated using the threshold reference algorithm, when a number of trigger towers with E_T greater than a certain threshold was calculated. In Run IIb, the E_T of the trigger tower is compared to the threshold set by various trigger terms. In addition, the trigger tower can be tested whether most of the energy is contained in its EM section. A typical example of the L1Cal term is “CSWEM(1,19,3.2)”. The requirements are that there exists at least one EM object with $E_T > 19$ GeV with $|\eta| < 3.2$. Further, L1Cal trigger term can be combined with the L1CTT term, forming L1CalTrack trigger. A typical example of such a term is “CTK(E,1,10.,13.,W,X,X)”, which requires one CTT track with $p_T > 10$ GeV/ c matched to an electron with $E_T > 13$ GeV, without any preshower or isolation requirement and within $|\eta| < 1.6$. The L1Cal decisions are sent to the TFW.
- The L1 muon trigger (L1Muon) uses the hits from both wire drift tubes and scintil-

lation counters, and L1CTT trigger information for matching purposes. At L1, up to 480 CTT tracks can be compared to hits in roughly 60,000 muon channels, finding the best match. Central tracks matched to the hits in the A-layer (both A- and B-layer) form loose (tight) muon trigger terms. In addition, muon trigger terms can be formed using the information solely from the muon chambers by matching hits in two or three scintillation counters to the hits in the wire chambers. A typical muon trigger term is “mu1p13wtlx_TTK(1,10.)”, which requires one muon in the wide region ($|\eta| < 1.6$) meeting tight scintillator and loose wire requirements matched to a CTT track with $p_T > 13 \text{ GeV}/c$. The L1Muon decision is then passed to the TFW.

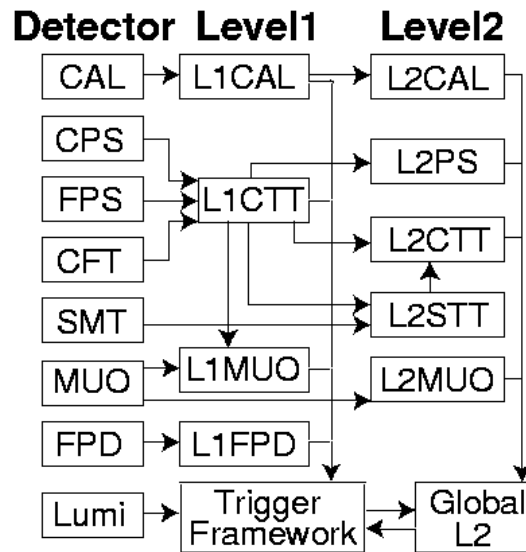


Figure 3.20: Block diagram of Level 1 and Level 2 trigger systems.

3.2.10.2 Level 2 trigger

The Level 2 trigger accepts the events that passed the L1 trigger. This input rate is about 2 kHz with the maximum design input rate of 10 kHz. In addition to the L1 output, L2 uses information from the front-end electronics. At L2, time allotted for a decision allows to use simple software algorithms, in addition to the firmware terms, when forming the L2 trigger

terms. These algorithms are able to make rough models of objects like electrons, photons, muons, and jets. The L2 trigger is divided into several triggers:

- The L2 central track trigger (L2CTT) and L2 silicon track trigger (L2STT) systems acquire a list of tracks from the L1CTT, and L2STT also receives the information about the hits in the SMT. The finer spatial resolution of the SMT detector improves the online p_T determination of the tracks found in the CFT. The L2STT output is sent to L2CTT for the calculation of the azimuthal angle at the third layer of the EM calorimeter and the isolation of the track.
- The L2 calorimeter (L2Cal) trigger system is used to identify jets and EM objects (electrons and photons), and calculate the transverse energy carried away by non-detectable particles (missing transverse energy, \cancel{E}_T). EM objects (jets) are identified by L2Cal as 3×3 (5×5) towers centered on the seed tower. The seed tower is any calorimeter tower with $E_T > 1$ GeV (2 GeV) in the EM section of the calorimeter (EM+HAD sections). The absolute value of the \cancel{E}_T is calculated as the vector sum of all trigger towers E_T using information from L1Cal.
- The L2 preshower trigger system (L2PS) uses the stereo hits in the CPS and FPS detectors (independently) together with the axial hits acquired from the L1 trigger. The L2PS calculates η and ϕ of the PS clusters and can match the clusters to the calorimeter clusters or tracks.
- The L2 muon trigger (L2Muon) uses the L1Muon output as well as the information from the muon detectors to improve the quality of the muon candidate using timing information. Muon stubs (track segments) from all three layers of the muon system are combined and used to calculate the quality of the muon candidate and its p_T .

The individual L2 triggers send the information about the objects, that were identified, with their properties to the L2Global processor. It also accepts information from the sub-

detectors, and makes the trigger decision based on the comparison of global physics objects, found with the algorithms, with the signatures of the real objects expected in the detector.

3.2.10.3 Level 3 trigger

The Level 3 trigger accepts the output of the L2. The input rate is roughly 1 kHz, and is reduced after the L3 decision to 100–150 Hz. The L3 uses a fully programmable software for a fast reconstruction of the events. This software is similar to the one used in the full offline reconstruction, but is optimized to run fast. The L3 trigger receives the L2 output and also uses full detector information from all the subsystems. At this stage, auxiliary variables, such as angles and separation between objects, invariant mass, *etc.*, can be calculated to aid the trigger decision. Just as in case of L1 and L2, at L3 filtering can be performed separately for different objects by means of specialized software tools:

- The L3 tracking tool starts a track finding algorithm from hits in the outer CFT layers. The algorithm calculates the link curvature in the outer two layers, and continues the link to the adjacent layers as long as the curvatures in all of them are consistent with each other. Then the longest path is kept as a track candidate (in case that the candidate track p_T exceeds the threshold set by a specific L3 trigger term). The χ^2 of the fit is calculated. The algorithm then continues to build a track by adding the links using the SMT layers. The extended track candidate is kept if its χ^2 is smaller than that, obtained just from the CFT.
- The L3 jet tool selects jets using the Simple Cone Algorithm based on the transverse energy. The high-precision calorimeter readout and the precise position of the primary vertex are crucial for the selection of jets. Additional suppression of hot calorimeter cells improves the L3 jet triggers turn-ons.
- The L3 electron tool identifies electrons as cones with $\Delta R = \sqrt{\Delta\phi^2 + \Delta\eta^2} = 0.25$. Additional requirements on the shower shape of the cluster in the calorimeter, E_T ,

\cancel{E}_T , and the fraction of energy deposited in the EM section of the calorimeter (> 0.9) aid in the selection.

- The L3 muon tool uses the L2 output and improves the momentum resolution by means of applying additional constraints on the muon candidates, such as matching the hits in the muon system to the central tracks, applying vertex constraints, isolation, timing cuts, *etc.*
- The L3 \cancel{E}_T tool calculates the \cancel{E}_T using the energy deposits in calorimeter cells with the initial assumption of the (0, 0, 0) position of the primary vertex (PV). In cases when the primary vertex tool returns the PV position different from (0, 0, 0), the \cancel{E}_T can be quickly corrected for that. The L3 \cancel{E}_T filter can be used either standalone, or added to any other L3 filter for additional rejection.

Typically, a set of requirements on L1, L2, and L3 trigger terms combined with logic “AND” forms a complete trigger. Triggers can be combined into groups with the same requirements on L1 (or L1 and L2). A typical example of a single EM trigger is “E1_SHT27”. Its breakdown at all three trigger levels is shown below.

- L1: CSWEM(1,19.,3.2) – a term requires at least one EM object with $E_T > 19$ GeV and $|\eta| < 3.2$;
- L2: L2CALEM(1,19,X,0.4) OR L2CALEM(1,25,X,X) – the trigger term selects events with one EM object with $E_T > 19$ GeV and EM likelihood > 0.4 “OR” events with one EM object with $E_T > 25$ GeV and no isolation or likelihood cuts.
- L3: Ele(ELE_NLV_SHT,1,27.,0.,3.6,-99.,99.,-1.) – this trigger bit is set to true if an electron is found satisfying tight shower shape requirements with $E_T > 27$ GeV.

3.2.11 Data acquisition system

The $D\bar{O}$ data acquisition system (L3DAQ) schematic view is shown in Fig. 3.21. The L3DAQ system transports data from the subdetectors to the L3 farm nodes, and controls the flow

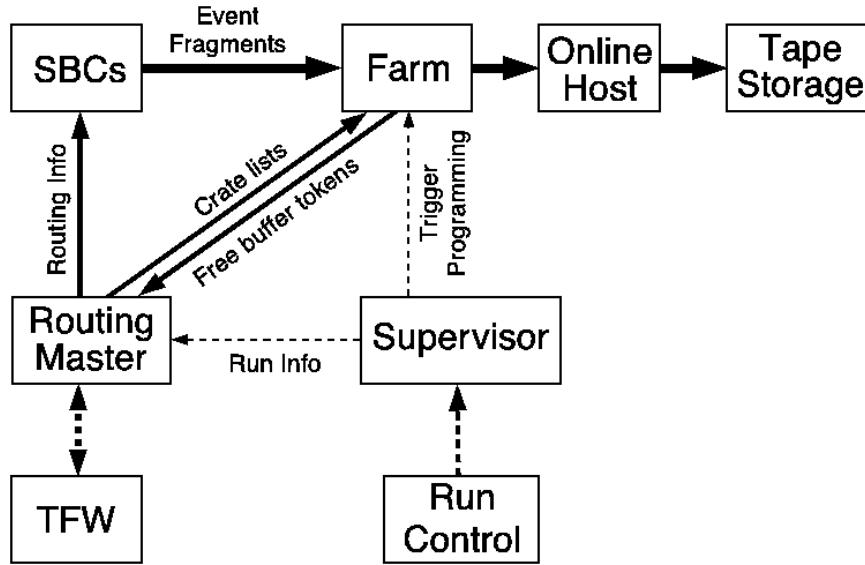


Figure 3.21: *Schematic view of the $D\bar{0}$ detector data acquisition system.*

of information from the L3 trigger to the datalogger and tape storage. A COOR program (running on the online host) handles the data acquisition, as well as triggering and overall coordination.

All nodes in the L3DAQ system (as well as the VME readout crates) are based on the SBC computers. The data acquisition process is a multi-stage process, that starts from the VME readout crates. A process, known as a routing master (RM), sends the information from the VME crate to one (or more) of the L3 farms. Another process, an event builder (EVB), combines together the event fragments and sends the complete event to the L3 trigger filters. Both processes are controlled by the COOR program, which also informs the L1, L2 and L3 filters of the availability of the next event. After the successive decision of the chain of the trigger filters, the COOR sends a raw event to the buffer. The events from the buffer are transmitted to the storage facility and are written to tape.

Chapter 4

Data Analysis Techniques

The analog information from various subdetectors of the DØ detector (see Section 3.2) is digitized and stored on tapes. However, data stored in this format are not convenient for analyzers. These data have to be processed with special reconstruction software called DØRECO (DØ Offline Reconstruction Software). This software reconstructs physics objects such as tracks, electrons, photons, jets, muons, vertices, and missing transverse energy, and provides analyzers with their properties.

4.1 Track Reconstruction

Tracks, which are basically trajectories of the charged particles in 3-D space, are reconstructed from the hits in the central tracking system. Two algorithms, the Alternative Algorithm [36] and the Histogramming Track Finder [37], are used in parallel to reconstruct the tracks. The final tracks are obtained from the combination of both algorithms (with duplicate tracks removed).

4.1.1 Alternative Algorithm

The Alternative Algorithm (AA) starts the tracks finding from the innermost layers of the SMT. Three hits in the $x - y$ plane in either barrels or F-disks are used for an initial track hypothesis. The next hit is selected in any successive layer if $\Delta\phi$, measured with respect to the straight line through the beam spot and the first hit, is less than 0.08. The algorithm

then looks for the third hit in successive layers of the SMT that satisfies the following criteria:

- The three hits must belong to the circle of radius greater than 30 cm.
- The χ^2 of the fit must be less than 16.
- The distance of the closest approach of the initial track has to be smaller than 2.5 cm.

The initial track is then extrapolated to the hits in the outer layers of the SMT and CFT. These hits are selected from a window of a definite size (this size is determined by the expectation of the track hypothesis), and are added to the track if the χ^2 of an extended track is still below 16. If more than one hit is found in this window, each of the hits is added to the track separately, thus making multiple track hypotheses. The algorithm skips the layer if there are no hits in this layer within the window. The algorithm continues until all hypotheses are exhausted. The track hypotheses from the list are then sorted using the following requirements:

- There must be at least four hits in the central tracker, with hits both in the axial and stereo layers (*i.e.* track hypothesis is discarded if a track is just two-dimensional).
- No more than three inside misses (in between any two hits of a track hypothesis), no more than six total forward and backward misses (missed hits in the track extrapolation path), no more than two misses in the SMT are allowed. In addition, a maximum of four inside misses and a forward miss, or three inside missed and a backward miss is allowed.
- $N_{hits}/5 \geq N_{miss}$.

If the above requirements are fulfilled, the track is added to the pool. Within this pool, tracks are ordered by the total number of hits, the number of misses and the χ^2 of the fit. In cases, where two tracks possess the same number of hits, the one with the lower number

of misses is given the priority, and so on. Also, within the pool of track candidates there might be three-dimensional tracks that share the axial hits. This is allowed, if for each track $N_{shared} \leq \frac{2}{3}N_{tot}$ and $N_{shared} \leq \frac{1}{5}N_{tot}$ OR $N_{tot} - N_{shared} \geq 3$, where N_{shared} (N_{tot}) is the shared (total) number of axial hits. The preliminary vertex then can be estimated, which is used in cases when there are too few or zero hits in the SMT, and the algorithm has to be performed for the second time to search for hits in the CFT. This allows for a smaller combinatorial background due to a larger number of hits in the CFT. The two runs are then combined with duplicate tracks removed, and the final list of tracks is declared an AA-track list.

4.1.2 Histogramming Track Finder

A charged particle, moving in a constant magnetic field perpendicular to the field lines, travels in a circular orbit with a curvature $\rho = qB/p_T$. Here, B is the magnetic field, and q and p_T are the charge and the transverse momentum of the particle. Two other variables, that describe this circle are the distance of the closest approach (DCA) of the particle with respect to the beam line in the $x - y$ plane, and the azimuthal angle ϕ measured at the DCA point. The three parameters, ρ , ϕ , and DCA, define a unique circle in the $x - y$ plane. The Histogramming Track Finder (HTF) method is based on the fact that a collection of circles intersecting a chosen hit in the $x - y$ plane can be mapped into a straight line in the $\rho - \phi$ space. This is done using the Hough transformation method. A two-dimensional histogram ($\rho - \phi$) is filled for each hit. All hits that belong to the same track correspond to the same point in the $\rho - \phi$ space, a clear peak will be formed for a good track. The Kalman filter is then employed to remove noisy or fake tracks.

4.2 Electromagnetic Object Reconstruction

Since photons are the most important particles involved in our studies, we describe the electromagnetic (EM) object reconstruction in greater details compared to other objects. When

a high-energy EM object (electron, positron, or photon) passes through matter, it loses its energy via production of other particles. Photons mostly lose energy by e^+e^- pair production, and electrons (positrons) – by bremsstrahlung. These daughter particles interact with matter in the same way. The EM shower develops in the transverse and longitudinal directions while secondary particles are energetic enough to produce new particles. Radiation length, X_0 , is the mean distance that an electron travels in matter before emitting a photon. The longitudinal development of the shower scales as the X_0 , with the maximum of the shower around $6 X_0$. Roughly 98% of the total energy of the shower is contained in 20 – $22 X_0$. The transverse development of the EM shower scales as the Molière radius, R_M . The width of the shower can be estimated as $3.5 R_M$. Showers initiated by electrons and photons share the same basic properties. However, due to the fact that the mean distance that a photon travels to produce an e^+e^- pair is $\frac{9}{7} X_0$, showers initiated by photons typically start deeper in material compared to showers produced by electrons.

A Simple Cone Algorithm [38] is used to construct calorimeter clusters. The algorithm accepts a list of all EM towers in the calorimeter. Towers with $E_T > 0.5$ GeV are used as seeds, and a cone of $\Delta R = 0.4$ is drawn around each seed. The algorithm then loops over all towers in the cone. Each time another tower is found in this cone, it is added to the cluster, the position of the cluster in the $\eta - \phi$ plane is recalculated, and a cone of radius 0.4 is drawn around this new position of the cluster. The algorithm iterates until all possible towers are checked. If the total energy of the cluster of $\Delta R = 0.4$ exceeds 1.5 GeV, and at least 90% of the cluster’s energy is contained in the EM section of the calorimeter, the cluster is accepted and stored for further checks.

At the next stage of the algorithm, the calorimeter isolation variable is calculated for each cluster. The graphical visualization of this variable is shown in Fig. 4.1. The tower with the highest energy in the cluster is selected, and an array of 81 towers (9×9) centered at this tower is created. A circle of radius $R = 0.4$ is drawn, and the sum of energies contained in the EM and HAD sections of the towers within this circle is calculated ($E_{\text{tot}}(0.4)$). Then

the sum of energies (EM only) in the cone of $\Delta R = 0.2$, $E_{EM}(0.2)$, is calculated. The calorimeter isolation is then calculated as:

$$\mathcal{I} = \frac{E_{\text{tot}}(0.4) - E_{EM}(0.2)}{E_{EM}(0.2)} \quad (4.1)$$

If $\mathcal{I} < 0.2$, the cluster is considered as isolated and is stored, otherwise it is rejected. This allows one to suppress possible backgrounds from EM-like jets (jets with most of their energy carried away by photons from π^0 decays and in most cases accompanied by charged pions).

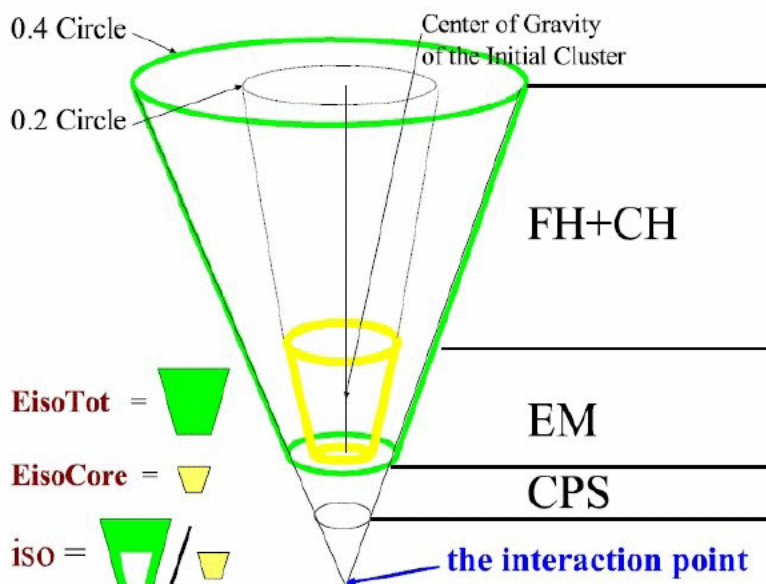


Figure 4.1: Schematic view of the calorimeter isolation.

Once the full list of accepted EM clusters is created, variables, that are used in the analyses to improve the quality of the EM objects, differentiate between photons and electrons, and suppress the backgrounds, are constructed. The list of the variables used in this dissertation is given below.

- The width of the EM cluster at the third layer of the EM calorimeter in $r - \phi$, $sigphi$ or σ_ϕ , and the width of the cluster in z , $sigz$ or σ_z , are also used in the analysis as a part of the standard electron and photon identification criteria. Usually, for the

photons in the central calorimeter only *sigphi* is used with an upper threshold of 14–18 cm², while for the photons and electrons reconstructed in the endcaps, the following parameterizations are used:

$$sigphi < 7.3 \cdot \eta^2 - 35.9 \cdot |\eta| + 45.7; \quad sigz < 7.5 \cdot \eta^2 - 36.0 \cdot |\eta| + 44.8. \quad (4.2)$$

- The HMatrix variables [39], *HMx7* and *HMx8*, are constructed out of seven or eight variables from the MC simulation of electrons. They are used to discriminate between the electromagnetic and hadronic showers by analyzing their shapes. The variables used to construct the HMatrix are: the energy fractions in all four layers of the EM section of the calorimeter, the total energy of the shower, the position of the primary vertex, the shower width in $r - \phi$ (and in z for *HMx8*) at the third EM layer. The covariance matrix is constructed as

$$M_{ij} = \frac{1}{N} \sum_{n=1}^N (x_i^n - \langle x_i \rangle)(x_j^n - \langle x_j \rangle), \quad (4.3)$$

where the summation is performed over the MC electrons, and x_i ($\langle x_i \rangle$) is the value (expectation value) of variable i . Then, the χ_{HMx}^2 variable is defined as

$$\chi_{HMx}^2 = \sum_{ij}^{7 \text{ or } 8} (x_i^d - \langle x_i \rangle) H_{ij} (x_j^d - \langle x_j \rangle), \quad (4.4)$$

where x_i^d ($\langle x_i \rangle$) is the value (expectation value) of variable i in data (MC), and H is the inverse covariance matrix M . Typically, HMatrix variables for real EM showers are smaller than those for showers from EM-like jets, which allows one to distinguish between them.

- Matching of the calorimeter cluster to the central track can be done in two ways: two different χ^2 probabilities are used. The so-called *spatial track match* χ^2 probability is defined as

$$\chi^2 = \left(\frac{\Delta\phi}{\sigma(\phi)} \right)^2 + \left(\frac{\Delta z}{\sigma(z)} \right)^2, \quad (4.5)$$

where $\Delta\phi$ and Δz are the separations between the position of an EM cluster at the third layer of the EM calorimeter and the central track, and $\sigma(\phi)$ and $\sigma(z)$ are the resolutions of these quantities. From Eq. 4.5 it is obvious that the spatial track match χ^2 probability depends only on the relative position of the track and the EM cluster. An extra term of the form $\left(\frac{E_T/p_T-1}{\sigma(E_T/p_T)}\right)^2$ can be added to the χ^2 formula, thus forming another track match χ^2 probability. This variable results in a lower misidentification rate, but also lower efficiency, compared to the spatial one. Typical values of the spatial track match χ^2 probability for electrons exceed 0.001–0.01, while that for photons is either not used or must not exceed 0.001.

- The track isolation variable, *IsoHC4*, is applicable to photons and allows one to significantly suppress the backgrounds from misidentified jets, as they are likely to have a rather high tracker activity. It is defined as the sum of p_T of all reconstructed tracks around a photon candidate in an annulus with openings $0.05 < \Delta R < 0.4$, if these tracks are within 2 cm from the primary vertex or the pointed vertex of the photon in the z direction. The inner opening of 0.05 allows photons to convert in the tracker. The typical value of the track isolation for the photons is less than 1.5–2 GeV/ c .
- Hits-on-the-road variables [40] are also used in this dissertation, and are defined as the probability of an EM object to have a track based on the density of hits in the central tracker. Another variable, *emhits_e_f_discriminant*, can be obtained using the density of hits information, and is used as a powerful tool to discriminate between the real electrons and fakes, that tend to have *emhits_e_f_discriminant* close to zero. Most of the time, this variable is “OR’ed” with the spatial track match χ^2 probability, e.g. (*emhits_e_f_discriminant* > 0.5 || $\chi_{spatial}^2 > 0.001$). It is worth mentioning, that this combination has to be inverted for the photons.
- Matching the calorimeter cluster with the preshower cluster is of a great importance

for some of the analyses with photons (see Section 5.2). The matching algorithm looks for preshower clusters in the $\Delta\eta \times \Delta\phi = 0.1 \times 0.1$ window around the EM cluster in the calorimeter, and matches the calorimeter cluster to the most energetic preshower cluster. In case of the positive match, a flag is raised, and the position and the energy of an EM object is recalculated to adjust for the preshower cluster contribution. Only CPS match is used in the analyses described in this dissertation.

4.3 Jet Reconstruction

At hadron colliders, collisions of energetic hadrons are, in fact, collisions of partons (quarks and gluons) that form these hadrons. Partons, produced in these collisions, fragment into hadronic jets - bunches of hadrons, that shower in the calorimeter. As opposed to the EM showers with transverse dimensions that depend on the properties on the material, showers from jets can vary greatly depending on the constituent particles of these jets. However, even in this case, jets are identified using a cone algorithm. This algorithm must be flexible enough to identify all kinds of jets, and must reconstruct the properties of the parton that initiated the jet. The Run II Cone Algorithm [41] involves three steps: clustering, midpoint addition and splitting/merging.

The clustering process starts with the reconstruction of towers from the calorimeter cells. Cells with excessive noise are removed [42], and only cells with the energy greater than 2.5 times the width of the signal of the electronics noise (so-called *pedestal*) are considered. The four-momentum of a tower is the sum of the four-momenta of all cells in this tower. The list of towers is passed to the Simple Cone Algorithm [38], that constructs jet preclusters. From the list of towers, the algorithm builds a p_T -ordered (decreasing) list down to the threshold of $p_T > 500$ MeV/ c . The leading- p_T item is chosen as the precluster seed (P). The algorithm then calculates the separation of the remaining items from the list (J) from the precluster seed: $\Delta R(P, J)$. If $\Delta R(P, J) < 0.3$ and the momentum of the item $p_T^J > 1$ MeV/ c , the item is added to the P . The process is iterative, and results in a number of preclusters ordered

by their decreasing p_T^P .

These preclusters are then used to build the so-called *proto-jets* and *proto-jet candidates* (PC). The algorithm receives the list of preclusters and the list of calorimeter cells from the previous stage. It is an iterative algorithm, that chooses the seed and adds items to it in a specified cone in the rapidity–azimuthal angle space. The opening of the cone depends on the type of the jet and is $\Delta R = 0.5$ ($\Delta R = 0.7$) for a JCCB (JCCA) jet. The precluster is seeded as a PC if its separation from the closest neighboring precluster exceeds half of the cone size. Otherwise, the algorithm tests the next precluster from the list. When the seed is chosen, four-momenta of all the items in a cone around the PC are added to form a new proto-jet candidate (PC'). The process iterates until $p_T^{PC'} < 3 \text{ GeV}/c$, or $\Delta R(PC, PC') < 0.001$, or the iteration number is 50. This is done for all preclusters from the list.

To suppress the sensitivity of the method to soft radiation, a midpoint algorithm is applied. A midpoint between two proto-jets separated from each other by at least a cone size, but not more than two cone sizes. The midpoint is then used as a seed to form new proto-jets. The original list of proto-jets from the clustering stage together with these new proto-jets are passed to the third step of the Run II Cone Algorithm – merging and splitting.

Quite often the items (*e.g.* calorimeter cells, towers, *etc.*) are shared between two proto-jets, thus causing double counting. To take this into account, the sum of the four-momenta of the shared items with the highest- p_T proto-jet is calculated. If this sum exceeds 50% of the PJ energy, the two proto-jets are merged. Otherwise, the proto-jets are split, and the shared items are assigned to the closest proto-jet in R . This final process is also iterative, and continues until all possible combinations are checked.

4.4 Muon Reconsruction

Muon candidates are reconstructed using hits in the wire chambers and scintillation counters of the local muon system, as well as hits in the central tracking system. Reconstruction

begins with a construction of the so-called *local muon track segments* in the wire chambers starting with just two hits. This is done separately in the forward and central muon systems, and for one octant at a time. The Linked List Algorithm [43] transforms wires in the muon chambers into a special coordinate system with wires in the z direction. If the two hits do not belong to the same wire and are not more than 20 cm apart in the y direction, then the local segment is built. This local segment is then matched to other segments if possible. The resulting array of segments is used to construct local tracks in the wire chambers. The track candidate with the best fit of segments is then matched to the hits in the scintillation counters, and re-fit is performed. The described procedure is performed in all three layers (A-, B- and C-) of the muon system. Matching the track stubs between the layers improves the quality of the track. If a track match between the innermost A-layer and one of the outer layers (after the toroid) is satisfied, a local muon p_T measurement is performed, since the magnetic field in the toroid bends the trajectories of the muon candidates.

Matching the local muon candidate to the track reconstructed in the central tracking system allows one to improve the p_T measurement of a muon candidate due to a larger number of hits in the central tracker and stronger magnetic field. Information on the number of segments, number of hits in the wire chambers and scintillation counters, and a match to the central track is then used to group the muon candidates by their quality and type. The type is qualified by the number of segments, $nseg$, and the quality is a combination of $nseg$ and the number of hits in the muon system. This information is summarized in Tables 4.1, 4.2 [44, 45].

Table 4.1: *Muon types.*

<i>nseg</i>	Central track match and muon system layers used
3	Central track + local muon track in A-, B-, and C-layer
2	Central track + local muon in B- and C-layers
1	Central track + local muon in A-layer
0	Central track + local muon hits
-1	Local muon in A-layer; no central track match
-2	Local muon in A- and B-layer; no central track match
-3	Local muon track in A-, B-, and C-layer; no central track match

Table 4.2: Muon quality. Here, N_A^w (N_{BC}^w) is the number of wire hits in the A-layer (BC-layers), N_A^{sc} (N_{BC}^{sc}) is the number of scintillator hits in the A-layer (BC-layers), and χ_{loc}^2 is the criterion of the local fit convergence.

Muon quality	nseg	Number of hits
Tight	$ nseg = 3$	$N_A^w \geq 2, N_A^{sc} \geq 1, N_{BC}^w \geq 3, N_{BC}^{sc} \geq 1, \chi_{loc}^2 > 0$
Medium	$ nseg = 3$	$N_A^w \geq 2, N_A^{sc} \geq 1, N_{BC}^w \geq 2, N_{BC}^{sc} \geq 1$
Medium	$nseg = 2$	$N_{BC}^w \geq 2, N_{BC}^{sc} \geq 1$, located in octants 5 and 6 with $ \eta < 1.6$
Medium	$nseg = 1$	$N_A^w \geq 2, N_A^{sc} \geq 1$, located in octants 5 and 6 with $ \eta < 1.6$
Loose	$ nseg = 3$	$N_A^w \geq 2, N_A^{sc} \geq 1, N_{BC}^w \geq 2, N_{BC}^{sc} \geq 1$ (allows 1 test to fail)
Loose	$nseg = 2$	$N_{BC}^w \geq 2, N_{BC}^{sc} \geq 1$
Loose	$nseg = 1$	$N_A^w \geq 2, N_A^{sc} \geq 1$

Cosmic or beam halo muons are identified in the detector with a help of two additional variables, $isCosmic$ and $isCosmicT$. Both variables are based on the timing of the scintillator hits. If the scintillator timing disagrees with the exact time of the $p\bar{p}$ collision with more than 10 ns, then $isCosmic = 1$. If, in addition to that, a muon candidate central track $DCA > 0.16$ cm, then the $isCosmicT$ flag is raised.

4.5 Vertex Reconstruction

The position of the proton-antiproton collision is described by the 3-D coordinate, referred to as primary vertex (PV). It is absolutely important to determine the PV with high accuracy, as the PV is used in the calculation of the transverse energy and the \cancel{E}_T . Also, all objects in the detector are reconstructed with respect to the PV. A three-step algorithm is used to reconstruct the PV: track selection, vertex fitting, and vertex selection [46, 47].

In the first step, tracks with $p_T > 0.5$ GeV/ c are selected if they have at least two hits in the SMT detector. The tracks that are less than 2 cm apart from each other along the z axis are then clustered together. More than one such cluster is allowed in one event, indicating different interactions.

In the second step, all tracks within one cluster are fitted into a common vertex using a Kalman Filter fitting algorithm, and a χ^2 for each fit is calculated. The tracks with the highest χ^2 contribution are removed. Then, for each of the remaining tracks the DCA significance, defined as DCA/σ_{DCA} , is calculated. Here, DCA is the distance of the closest approach of the track, and σ_{DCA} is its uncertainty. Tracks with DCA significance above five are rejected. After this preselection, the tracks are fitted into a common vertex using the Adaptive Vertex Fitting (AVF) algorithm [48]. The purpose of the method is to re-weigh the track errors taking into account the χ^2 contribution of this track to the vertex.

After all vertices in the event have been found, they are ordered in the probability of each vertex of belonging to a minimum bias (MB) events (which are simply additional interactions in a certain beam crossing). This probability is the product of the probabilities

for each track to be originated from the MB interaction. The vertex with the lowest such probability is selected as the primary vertex in the event.

4.6 Missing Transverse Energy

As the proton-antiproton collisions in the DØ detector occur at a very small angle to the beam line, the transverse energy (momentum) in an event should be close to zero. This means that the vector sum of the transverse momenta of all the particles after the collision must be zero. In practice, this does not happen very often, as the resolution of the detector components is finite. Also, non-interacting particles (*e.g.* neutrinos) can carry away a significant amount of energy without being reconstructed. This makes the vector sum of the transverse momenta in an event rather large. In such cases, by definition, the imbalance of the transverse energy is assigned as the missing transverse energy, \cancel{E}_T [49].

The \cancel{E}_T reconstruction starts with the vector sum of the energy depositions in each calorimeter cell (excluding the coarse hadronic section) in the x and y directions independently (Eq. 4.6). Then these sums with the negative sign are called the x and y components of the missing transverse energy (Eq. 4.7). Finally, the \cancel{E}_T is constructed as shown in Eq. 4.8. Calorimeter towers can also be used for this calculation instead of cells.

$$E_{Tx} = \sum_i^{N_{cells}} E_i \times \cos\theta_i, E_{Ty} = \sum_i^{N_{cells}} E_i \times \sin\theta_i \quad (4.6)$$

$$\cancel{E}_{Tx} = -E_{Tx}, \cancel{E}_{Ty} = -E_{Ty} \quad (4.7)$$

$$\cancel{E}_T = \sqrt{\cancel{E}_{Tx}^2 + \cancel{E}_{Ty}^2} \quad (4.8)$$

The \cancel{E}_T is further corrected for the muons that do not shower in the calorimeter. If a muon candidate is matched to a central track, the p_T of this track is subtracted from the \cancel{E}_T . In addition, the \cancel{E}_T is corrected for the jets and corrections to their energy, and EM objects energy corrections.

Chapter 5

Measurement of the $Z\gamma$ Cross Section

The cross sections of the gauge bosons production span a wide range – from nanobarns to femtobarns (see Fig. 5.1). The largest by far is the single W boson production cross section, followed by a single Z boson production. Diboson production cross sections are a few orders of magnitude lower, which makes the diboson processes rather rare and challenging to detect.

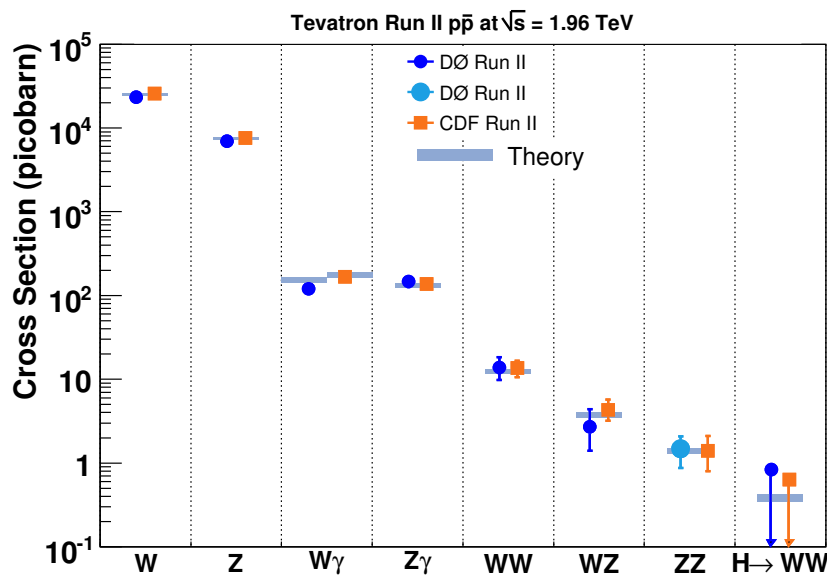


Figure 5.1: Gauge bosons cross sections.

A Z boson is not a stable particle and has several decay modes: hadronic, leptonic (either

charged or neutral), *etc.* Hence, there are several $Z\gamma$ final state signatures. Each mode has its own advantages and disadvantages. Below we list the most interesting of them, ordered by the branching fraction (\mathcal{B}), with the key features of each mode.

- $Z + \gamma \rightarrow jets + \gamma$
 - very large $\mathcal{B} \approx 70\%$,
 - very large contamination from QCD background.
- $Z + \gamma \rightarrow \nu\bar{\nu} + \gamma$
 - large $\mathcal{B} \approx 20\%$,
 - Z boson is not reconstructed.
- $Z + \gamma \rightarrow \ell\ell + \gamma$ ($\ell = e, \mu, \text{ or } \tau$)
 - $\mathcal{B} \approx 10\%$ (for all 3 lepton families),
 - very clean signal,
 - can be used to calibrate the detector and cross check the luminosity measurements.

In the following we describe a measurement of the $Z\gamma \rightarrow ee(\mu\mu)\gamma$ (see Section 5.1) and $Z\gamma \rightarrow \nu\bar{\nu}\gamma$ (see Section 5.2) cross section, and restrictions on the strength of the couplings between a Z boson and a photon (see Chapter 6). Since we study only the real parts of the couplings in this analysis, we will omit the notation Re in the text and plots when referring to the couplings.

5.1 $Z\gamma \rightarrow \ell\ell\gamma$ Cross Section

5.1.1 Data samples

The cross section measurement in the charged lepton channel (charged lepton is either an electron or a muon) is done on the full sample of Run IIa data collected with the DØ detector

between the 21st of October 2002 and the 22nd of February 2006 (runs 166503 – 215670), covering v8 – v14 trigger lists. The DØ Run II data taking period has started in April 2002 and is still going. During the long shutdown in 2006 (February – June), an upgrade of the DØ detector has been performed. The main reason for this upgrade was to install a Layer 0 subdetector (see Section 3.2.2) and prepare the DØ detector for higher instantaneous luminosities, expected from the Tevatron and the Accelerator Division. The data taking period prior to this shutdown is known as Run IIa, while the one after the 2006 shutdown is known as Run IIb. Run IIb data taking period has also been divided into two subperiods – pre-2007-shutdown and postshutdown. No major changes to the detector have been made during the 2007 (August – October) shutdown, so we will collectively refer to any data taken after 2006 shutdown as Run IIb data.

We use Common Samples Group [50] 2EMhighpt and 2MUhighpt CAF [51] trees reconstructed or fixed with p17.09.01, p17.09.03, and p17.09.06 DØ reconstruction software versions:

- CSG_CAF_2EMhighpt_PASS3_p17.09.03,
CSG_CAF_2EMhighpt_PASS2_p17.09.01,
CSG_CAF_2MUhighpt_PASS3_p17.09.03, and
CSG_CAF_2MUhighpt_PASS2_p17.09.01 with cable-swap data removed by cutting on run number;
- CSG_CAF_2EMhighpt_PASS3_p17.09.06 and
CSG_CAF_2MUhighpt_PASS3_p17.09.06 with cable-swap data that has been re-reconstructed using d0reco p17.09.06.

Events in the data samples are required to pass the standard DØ data quality (DQ) checks in order to avoid double counting and remove the events affected by the subdetectors problems. In details, runs in the data sample are required to be declared as GOOD or REASONABLE by the CFT group and not to be declared as BAD by the CAL group. For

Table 5.1: *Summary of Run IIa triggers used in the electron channel.*

Trigger version	Run range	Trigger
v8 – v11	166503 – 178721	EM_HI_SH EM_MX_SH EM_HI_2EM5_SH EM_MX EM_HI
v12	177311 – 194566	E1_SH30 E1_SHT20 E2_SHT20 E3_SHT20
v13	194567 – 208122	E1_SH30 E1_SHT22 E2_SHT22 E3_SHT22
v14	207217 – 215670	E1_ISH30 E1_ISHT22 E1_SH35 E1_SHT25 E3_ISH30 E3_ISHT22 E3_SH35 E3_SHT25

the muon final state we also require the runs not to be marked as BAD by the SMT group, and exclude BAD or SPECIAL MUON runs. We also exclude luminosity blocks which were troubled by transient problems in calorimeter and identified by JET/MET groups.

After the DQ requirements, events in the data samples have to fulfill the trigger requirements. For the electron channel, the event must satisfy an "OR" of the unrescaled single high- E_T EM triggers. These triggers are combined into 7 trigger lists (v8 – v14). The data taking period is divided into 4 epochs during which different trigger lists are applied. These triggers are summarized in Table 5.1. The efficiency of this collection of triggers is almost 100% for a high- E_T EM object (see Section 5.1.5.2).

In the muon channel, we use dimuon and single-muon triggers for the event selection. Both the muon trigger definitions and prescale factors were changing over the period of time

Table 5.2: *Summary of Run IIa triggers used in the muon channel.*

Trigger version	Run range	Trigger
v8 – v10	165662 – 173481	2MU_A_L2M0 2MU_A_L2M0_TRK5 2MU_A_L2M0_TRK10 2MU_A_L2M0_L3L6 2MU_A_L2M0_L3L15 2MU_A_L2ETAPHI
v11	173482 – 178721	as v8 – v10 or MUW_W_L2M3_TRK10
v12	177311 – 194566	as v8 – v10
v13a	194567 – 196584	DMU1_LM6
v13b – v13e	201485 – 208144	MUH1_LM15
v14	207217 – 215670	DMU1_2LM6

when the data set was collected. Therefore, to calculate trigger efficiencies we divide the data sample into several data sets. The first data set comprises of data taken with an “OR” of the unrescaled dimuon triggers: 2MU_A_L2M0, 2MU_A_L2M0_TRK5, 2MU_A_L2M0_TRK10, 2MU_A_L2M0_L3L6, 2MU_A_L2M0_L3L15, or 2MU_A_L2ETAPHI. These data correspond to runs 165662–173481. The second data set is taken after run 173481, when we require the event to trigger either one of the unrescaled dimuon triggers described above, or the unrescaled single-muon trigger MUW_W_L2M3_TRK10. The third data set corresponds to runs 173481–181100 when a single-muon trigger was rescaled, so we require the event to fire one of the unrescaled dimuon triggers. The data collected with the trigger list version 13a (runs 194567 through 196584) are required to fire dimuon trigger DMU1_LM6 when it is unrescaled, and the data collected with trigger list versions 13b–13e (runs 201485 through 208144) are required to fire the unrescaled single-muon trigger MUH1_LM15. The data collected with trigger list version 14 are required to satisfy dimuon DMU1_2LM6 trigger requirements when it ran unrescaled. The muon triggers are summarized in Table 5.2. The trigger efficiency of the muon data selection is calculated separately for these data sets using standard CAF and MUON identification tools as described in [52] (see Section 5.1.6.2).

Table 5.3: *Summary of integrated luminosity in the electron channel.*

Trigger version	Dates	Run range	$\int \mathcal{L}dt, \text{pb}^{-1}$
v8 – v11	11/21/02 – 07/07/03	166503 – 178721	127 ± 8
v12	05/26/03 – 06/28/04	177311 – 194566	240 ± 14
v13	06/28/04 – 07/13/05	194567 – 208122	392 ± 24
v14	07/05/05 – 02/22/06	207217 – 215670	350 ± 21
Total	11/21/02 – 02/22/06	166503 – 215670	1109 ± 67

Table 5.4: *Summary of integrated luminosity in the muon channel.*

Trigger version	Dates	Run range	$\int \mathcal{L}dt, \text{pb}^{-1}$
v8 – v11	11/21/02 – 07/07/03	166503 – 178721	105 ± 6
v12	05/26/03 – 06/28/04	177311 – 194566	225 ± 14
v13	06/28/04 – 07/13/05	194567 – 208122	364 ± 22
v14	07/05/05 – 02/22/06	207217 – 215670	315 ± 19
Total	11/21/02 – 02/22/06	166503 – 215670	1009 ± 61

The integrated luminosity for the electron and muon samples with the above data quality applied is calculated using the standard `DØ getLuminosity` method in `lm_tools` package with the `newconstant` option following the procedure described in the DØ Note 5243 [53, 54], and is summarized in Tables 5.3 and 5.4. A 6.1% uncertainty is assigned to the obtained luminosity values.

We estimate the total integrated luminosity of 2EMhighpt sample, after the applied data quality and trigger selection, to be $1109 \pm 67 \text{ pb}^{-1}$, while that for the 2MUhighpt sample to be $1009 \pm 61 \text{ pb}^{-1}$.

5.1.2 Monte Carlo samples

In order to have an understanding of the final state we are investigating, we need to have a Monte Carlo generator suitable for the $Z\gamma$ production. There are a few options: PYTHIA [55], MCFM [56] and Baur generator [12]. Unfortunately, PYTHIA does not describe the anomalous $Z\gamma$ production, and MCFM as of v3.0 is not complete for the $Z\gamma$ process. To the contrary, the Baur MC generator was specifically designed to model both SM and anomalous $Z\gamma$

processes.

In our analysis, we use the leading order (LO) Baur event generator to generate the $Z\gamma \rightarrow \ell\ell\gamma$ processes using CTEQ6L1 (LO with LO α_s) libraries [57, 58]. In order to avoid potentially dangerous boundary effects, events are generated with looser kinematic requirements than those applied in data. We require the photon transverse energy $E_T > 3$ GeV and the separation from both of the leptons to be $\Delta R = \sqrt{(\Delta\phi)^2 + (\Delta\eta)^2} > 0.4$. The generator allows to simulate initial state radiation (ISR), final state radiation (FSR), and Drell-Yan (DY) (see Section 2.2.2) processes with or without anomalous couplings.

5.1.2.1 QCD corrections

In addition to the cross section measurement we perform the search for the anomalous $Z\gamma$ production, which will be described in Chapter 6. As the photon E_T spectrum is one of the most sensitive distributions for the search for the new physics (see Section 2.2.2), it is important to simulate the shape of the photon E_T spectrum properly. As described in Section 2.2.3, NLO QCD corrections due to the soft gluon radiation and virtual corrections cannot be neglected at the Tevatron center-of-mass energies. There are several ways to incorporate the QCD corrections in this analysis. The first method is based on the boost of the Z boson and the photon four-vectors using the momenta from the PYTHIA simulation of the Z boson and photon production. The second method assumes the correction of the LO photon E_T spectrum with the so-called K -factor, or the ratio of the photon E_T spectra from the NLO and LO $Z\gamma$ processes. The E_T -dependent K -factor is derived from the ISR NLO $Z\gamma$ Baur Monte Carlo generator [13], and is measured by comparing the LO (with LO PDFs) and NLO (with NLO PDFs) photon E_T distribution [59] generated for the $Z\gamma$ process with no anomalous couplings [60]. This K -factor corrects both the overall normalization of the photon E_T spectrum and its shape. The SM K -factor is shown in Fig. 5.2. The average NLO correction to the LO $Z\gamma$ cross section is found to be $\approx 35\%$, as expected [13]. The variation of the NLO QCD corrections for the anomalous $Z\gamma$ production from the SM one was found to be negligible for the set of requirements and the form-factor scale used in

this analysis. It was also found that the two methods of the QCD corrections application result in the same scale factors and the same photon E_T shape correction, hence we will not differentiate between the methods and will collectively refer to their output as NLO QCD corrections. If not stated otherwise, we assume that we operate with the NLO MC samples throughout this dissertation.

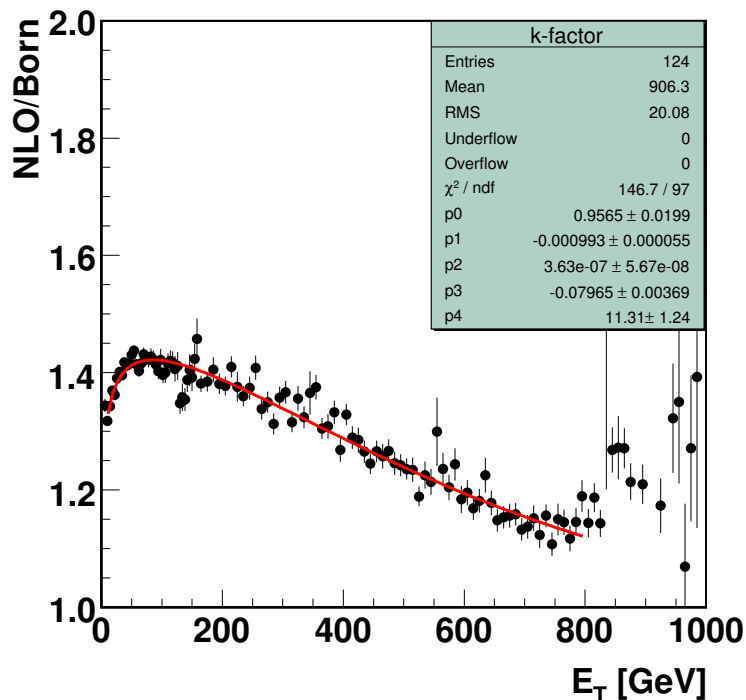


Figure 5.2: K -factor as a function of photon E_T obtained from NLO $Z\gamma$ Baur generator for the standard model $Z\gamma \rightarrow \ell\ell\gamma$ process.

5.1.2.2 The DØ detector simulation

The generator output is organized as a look-up table of four-vectors of the particles (two leptons, a Z boson, and a photon). Also, the values of the cross sections of the $Z\gamma$ processes are stored.

Once the MC samples are generated, one needs to run these samples through the DØ detector simulation. This is essential, since the detector is not perfect, its efficiency is not

100%, and its response to different particles needs to be taken into account. This process is known as *smearing*. There are several tools at DØ that can be used for that. One of them is the full GEANT [61] simulation of the DØ detector. Due to a very detailed modeling of the detector, it is time consuming. Since we generate literally thousands of MC samples, it would take a long time to run them through the full detector simulation. Another option is to use a fast simulation program of the DØ detector, the Parameterized Monte Carlo Simulation (PMCS) [62]. This package has been trained on real data, and allows one to have a realistic estimate of the smearing of the particle energy, momentum, angles, *etc.* The software is divided into the smearing and utility packages. The former do the actual smearing, individually for each type of particles (EM objects, jets, muons, missing transverse energy, *etc.*), and the latter are responsible for the communication between the packages, unpacking the generator output, and producing its own output. The four-vectors of the final state particles from the generator are used as an input to the PMCS to model the DØ detector response and to measure the total efficiency and acceptance of the event selection.

5.1.2.3 PDF uncertainty

The obtained K -factor is used to estimate the value of the NLO $Z\gamma$ cross section (that also includes FSR and DY processes). For the kinematic requirements on the $Z\gamma$ system ($M_{\ell\ell} > 30 \text{ GeV}/c^2$, photon $E_T > 7 \text{ GeV}$, and $\Delta R > 0.7$) the LO cross section is estimated to be 3.53 pb, and the NLO cross section is 4.74 pb. We generate MC samples with more than 100,000 events per sample, so the statistical uncertainty on the theoretical cross section is insignificant. The main systematic uncertainty on the cross section comes from the choice of the parton distribution functions (PDF) set and library (see Section 5.1.2). The PDF uncertainty on the cross section is calculated using the standard procedure documented in Ref. [57]. We generate 40 samples of NLO $Z\gamma$ Monte Carlo simulation with different CTEQ6M [57, 58] sets to calculate the uncertainty as

$$\Delta\sigma = \frac{1}{2} \left(\sum_{i=1}^{N_p=20} [\sigma_i^+ - \sigma_i^-]^2 \right)^{1/2}, \quad (5.1)$$

where σ_i^+ and σ_i^- are the predictions of the NLO $Z\gamma$ cross section based on $i^+ - th$ and $i^- - th$ PDF set. The systematic uncertainty due to the choice of PDF for the set of cuts described above is calculated to be 4.7%. Thus, the standard model prediction of the NLO $Z\gamma \rightarrow \ell\ell\gamma$ cross section with $M_{\ell\ell} > 30 \text{ GeV}/c^2$, photon $E_T > 7 \text{ GeV}$, and $\Delta R > 0.7$ is estimated to be $4.74 \pm 0.22 \text{ pb}$.

5.1.3 Data selection

The $Z\gamma \rightarrow \ell\ell\gamma$ events contain two high-energetic leptons, that are consistent with the Z boson decay, and a photon in the final state. In the following Sections 5.1.3.1, 5.1.3.2, and 5.1.3.3 we describe the chosen selection criteria.

5.1.3.1 $Z \rightarrow ee$ selection

To select $Z \rightarrow ee$ decay candidates we require an event to have a pair of EM clusters reconstructed with a Simple Cone Algorithm (see Section 4.2) with a transverse energy $E_T > 15 \text{ GeV}$. To be less sensitive to the single-EM trigger turn-ons, we require at least one of the clusters to have $E_T > 25 \text{ GeV}$. At least one cluster must be in the central calorimeter (CC), defined by the detector pseudorapidity of $|\eta| < 1.1$. The other cluster can be either in the CC region or in the end-cap calorimeter (EC) with $1.5 < |\eta| < 2.5$.

The clusters must pass the following standard EM identification criteria [63, 64] (for the definition and a more detailed description of the variables please see Section 4.2):

- At least 90% of the total energy has to be deposited in the EM section of the calorimeter.
- The calorimeter isolation, $\mathcal{I} = \frac{E_{\text{tot}}(0.4) - E_{\text{EM}}(0.2)}{E_{\text{EM}}(0.2)}$ must be below 0.2, where $E_{\text{tot}}(0.4)$ is the total energy deposited in the calorimeter in a cone of radius $\Delta R = 0.4$, $E_{\text{EM}}(0.2)$ is the EM energy in a cone of radius 0.2.
- The cluster must have good shower shape agreement, *i.e.* the χ_{HMx}^2 variable constructed from 7-variable (8-variable) H-matrix must be less than 12 (20) for the CC

(EC) electron candidates. We will denote these χ^2 variables as $HMx7$ and $HMx8$, respectively.

- The probability of a spatial track match must be above 0.01 in both CC and EC regions.

In addition, we require the invariant mass of two electron candidates, M_{ee} , (Fig. 5.3) to be greater than $30 \text{ GeV}/c^2$. Due to different acceptances and efficiencies in the CC and EC regions, we divide the analysis in the electron channel into two parts: the data with both electrons identified in the central region (CC-CC), and the data with one electron in the central region, and the other in the endcap (CC-EC). The selection criteria yield 65,957 $Z \rightarrow ee$ candidate events (38,323 CC-CC and 27,634 CC-EC events).

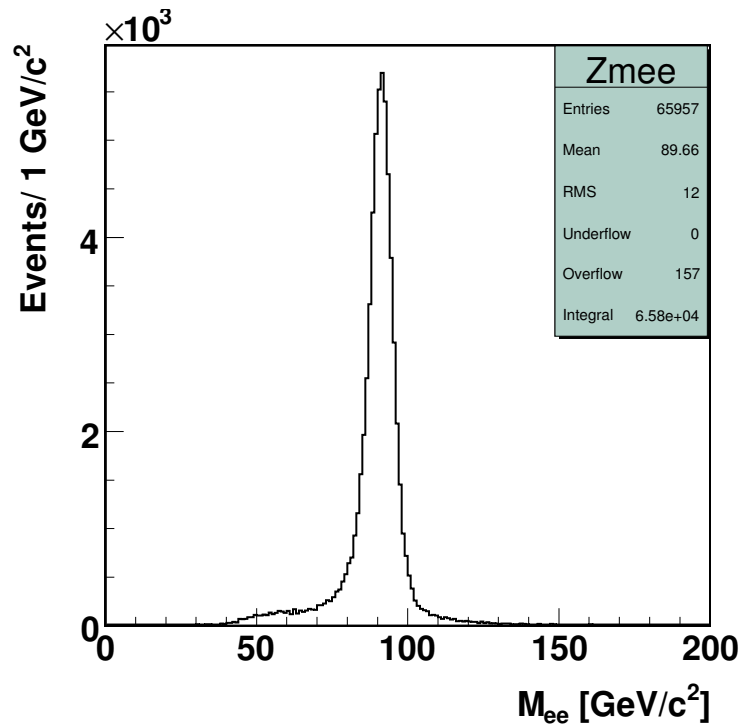


Figure 5.3: *Invariant mass of two selected electrons (CC-CC and CC-EC topologies combined).*

5.1.3.2 $Z \rightarrow \mu\mu$ selection

To select $Z \rightarrow \mu\mu$ decay candidates we require an event to have a pair of muon candidates with $p_T > 15$ GeV/ c . To be less sensitive to the muon trigger turn-ons, we require at least one of the muon candidates to have $p_T > 20$ GeV/ c . A muon is identified as a central track reconstructed with the CFT (and SMT) detectors and matched to a muon object reconstructed in the muon chambers of at least loose quality [44, 45] (see Section 4.4). The transverse momentum of a muon candidate is calculated from the combined fit of hits in the CFT (and SMT) and the muon detectors.

The muon candidates must be in the geometrical acceptance of the muon chambers. This requirement excludes muons that are close to the beam line (both of the x and y coordinates of a track at the muon chamber A-layer is below 110 cm), and it excludes muons in the bottom gap defined by $4.15 \text{ rad} < \phi < 5.15 \text{ rad}$ and A-layer detector pseudorapidity $|\eta| < 1.25$. The invariant mass of muon candidates, $M_{\mu\mu}$, that is obtained by using the central track information only, must be above 30 GeV/ c^2 .

To reduce background from $b\bar{b}$ processes, we apply calorimeter and track isolation requirements [65] to the muon candidates:

- The sum of p_T of all tracks reconstructed in the cone centered on the muon trajectory with an opening angle $\Delta R = 0.5$ must be below 3.5 GeV/ c .
- The sum of transverse energies E_T of the calorimeter cells identified between the cones with $\Delta R = 0.1$ and $\Delta R = 0.4$ centered on the muon's trajectory must be below 2.5 GeV.

We require at least two out of four isolation requirements on two muon candidates to be satisfied.

To reduce the contamination from cosmic ray muons, we require two muon candidates not to be exactly back-to-back, *i.e.* the angle between the muon candidates $\Delta\alpha_{\mu\mu}$ must

exceed 0.05 rad:

$$\Delta\alpha_{\mu\mu} = |\Delta\phi_{\mu\mu} + \Delta\theta_{\mu\mu} - 2\pi| > 0.05, \quad (5.2)$$

where $\Delta\phi_{\mu\mu}$ and $\Delta\theta_{\mu\mu}$ are the separations in polar and azimuthal angles of muon candidates. We also require muons to originate close to the beam spot, as cosmic muons are less likely to be produced near the interaction point. The distance of the closest approach, DCA [66], is a variable defined as the shortest distance between the beam line and the direction of an object in the $r - \phi$ plane. We require the DCA of the muon candidates to be below 0.2 cm, when the track has been reconstructed from the CFT hits. If a track has been reconstructed with both CFT and SMT, we tighten the requirement on DCA to 0.02 cm. In addition we require two muon candidates to originate within 2 cm from each other in the z direction.

After the selection criteria are applied, we observe 73,184 $Z \rightarrow \mu\mu$ candidate events. The invariant mass distribution of two muon candidates, $M_{\mu\mu}$, is shown in Fig. 5.4.

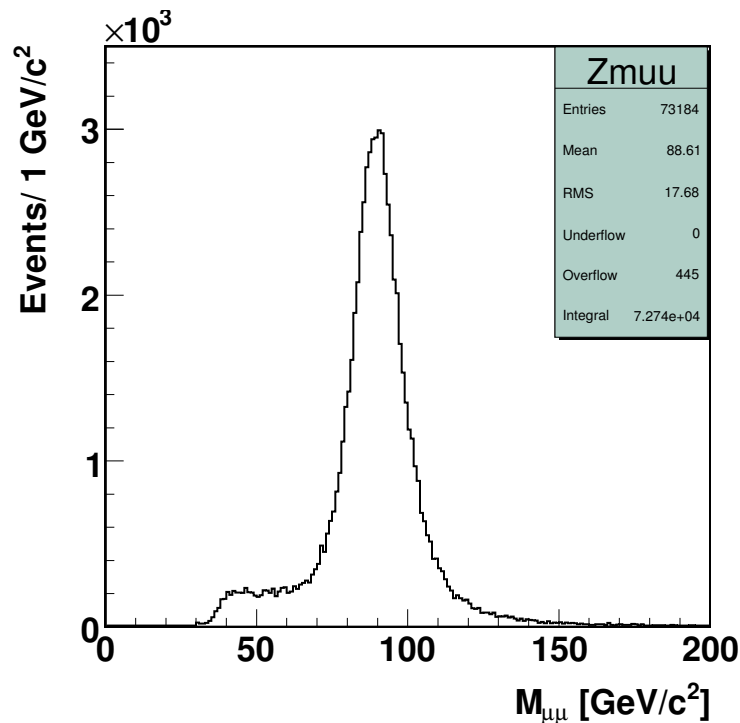


Figure 5.4: Invariant mass of the dimuon system.

5.1.3.3 Photon identification

Events that pass $Z \rightarrow \ell\ell$ selection criteria are further required to have a photon candidate with transverse energy $E_T > 7$ GeV and the separation from both leptons $\Delta R_{\ell\gamma} > 0.7$. The photon candidate must be reconstructed with a Simple Cone Algorithm (see Section 4.2) in the central calorimeter and inside ϕ -fiducial volume, and is required to pass the photon identification criteria described in the photon certification note [67]. The photon identification selection criteria are chosen in such a way that the efficiency of the photon selection criteria agrees well between electrons in data and MC, and also between photons and electrons in MC, while providing an effective rejection of photon-like jets. We use the standard *photon_id_tools* to produce plots and obtain efficiencies for the selected set of variables.

The following requirements are used to identify photon candidates:

- EM cluster reconstructed with Simple Cone Algorithm.
- The fraction of energy deposited in the EM layers, *emfrac*, must be above 0.9;
- The calorimeter isolation, *iso*, must be below 0.15.
- The square of the calorimeter's cluster width in the $r - \phi$ plane at the third floor of the EM calorimeter, *sigphi*, is below 14 cm^2 .
- The sum of transverse momenta of all track reconstructed in an annulus centered in a photon candidate's trajectory with opening $0.05 < \Delta R < 0.4$, *IsoHC4*, must be below $1.5 \text{ GeV}/c$. This requirement will be referred to as *track isolation*.
- The photon candidate must be inside the standard ϕ -fiducial volume defined as follows [68, 69]:

$$fm = fmod(16.0 \phi_\gamma/\pi, 1) \tag{5.3}$$

$$0.1 < fm < 0.9 \tag{5.4}$$

These criteria are almost identical to the ones prescribed by the Photon-ID group (known as the *core* cuts) [67]. We use looser cuts on the fraction of the energy deposited in the EM section of the calorimeter and the calorimeter isolation (these two variables are very correlated) to have a larger final sample, but hence we are more sensitive to the backgrounds. To suppress the misidentified jets background we cut harder on the track isolation. An extra requirement for the photon candidates to be in ϕ -fiducial volume of the calorimeter insures a well-understood energy scale, which is a crucial element for searching for anomalous trilinear gauge couplings. A comparison of the MC simulation of the energy scale for photons in fiducial volume and those in the intercryostat gaps is shown in Fig. 5.5. It is clear, that the EM objects reconstructed in the ϕ cracks of the calorimeter have their energy undermeasured (Fig. 5.5(b)). Also, the largest difference in photon identification efficiency between data and MC simulation is observed in the volume close to the calorimeter boundaries (Fig. 5.6). The requirement for a photon candidate to be reconstructed in a fiducial volume of the detector decreases this discrepancy.

5.1.3.4 Selected data

After applying all the event selection criteria described in Sections 5.1.3.1–5.1.3.3, we observe 453 (308 CC-CC and 145 CC-EC) $Z\gamma \rightarrow ee\gamma$ and 515 $Z\gamma \rightarrow \mu\mu\gamma$ candidate events. The dilepton mass versus dilepton plus photon invariant mass scatter plot is presented in Fig. 5.7.

The structure of this distribution reflects the SM processes through which the Z boson and a photon final state can be produced. Following from the kinematics, the ISR events (Fig. 2.2(a), (b)) have two leptons from an on-shell Z boson decay with $M_{\ell\ell} \approx M_Z$ and a photon, emitted by one of the interacting partons, resulting in $M_{\ell\ell\gamma} > M_Z$. Hence, the ISR events populate the vertical band on the plot. The on-shell Z boson FSR events (Fig. 2.2(c), (d)) cluster along the horizontal band at $M_{\ell\ell\gamma} \approx M_Z$ and have $M_{\ell\ell} < M_Z$. Drell-Yan events populate the diagonal band with $M_{\ell\ell} \approx M_{\ell\ell\gamma}$.

The most typical $Z\gamma \rightarrow ee\gamma$ and $Z\gamma \rightarrow \mu\mu\gamma$ events are shown in Fig. 5.8 and Fig. 5.9,

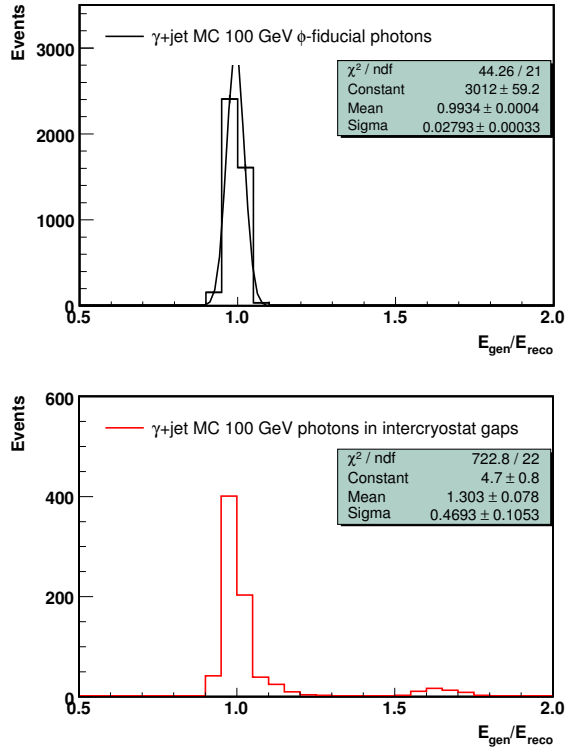


Figure 5.5: *The ratio of the MC truth energy to the reconstructed one for 100 GeV photons in ϕ -fiducial volume and those reconstructed in the intercrystal gaps. Significant loss of energy for the latter photons can hide potential signal of the anomalous $Z\gamma$ production; therefore, we require photons to be in ϕ -fiducial region only.*

respectively.

5.1.4 Photon identification efficiency

A photon, as seen in the DØ detector, is very much alike an electron modulo an absence of a track in the central tracking system. Therefore, it looks like it is natural to measure the efficiency of the photon identification criteria the way we measure the electron identification efficiency (see Section 5.1.5) using the tag-and-probe method [70, 71]. However, this method requires two objects of the same kind: two leptons, two photons, *etc.* Unfortunately, since we do not have a discovered source of the high- E_T diphoton resonance, such as $H \rightarrow \gamma\gamma$, this method is of a little use for the photons. Hence, when measuring the photon identification

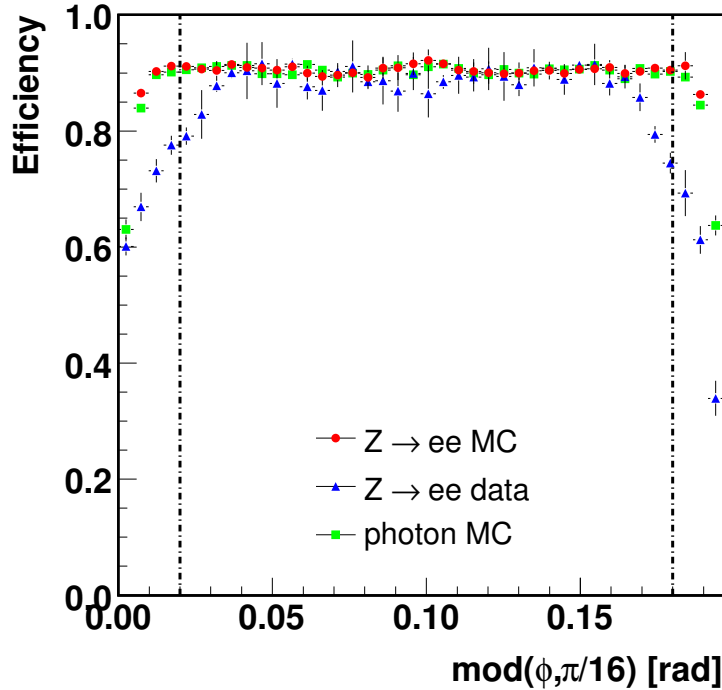


Figure 5.6: Overall efficiency of the photon selection criteria as a function of $\text{mod}(\phi, \pi/16)$. Black dash-and-dotted lines show the standard fiducial boundaries.

efficiency, we need to follow these guidelines:

- We must heavily rely on MC simulation and trust it.
- We must assume that the MC describes photons, electrons and the difference between the data and MC simulation correctly.
- We then treat electrons as photons, and choose and tune the selection criteria using the tag-and-probe method for the $Z \rightarrow ee$ decay in data and MC.
- The next step is to measure the efficiency of the selected cuts for the photons using the γ +jets MC.
- And, finally, we need to correct this efficiency for the data/MC difference.

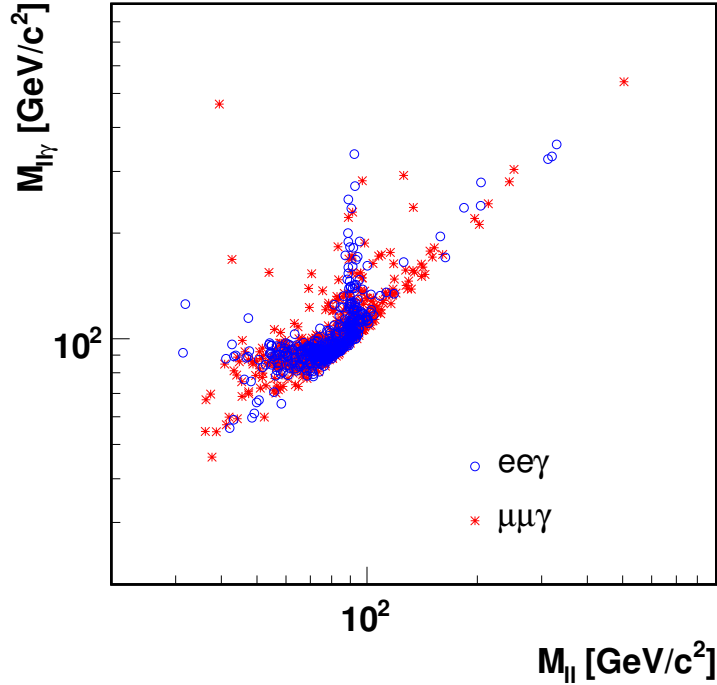


Figure 5.7: *Invariant mass of the dilepton system vs. invariant mass of dilepton and a photon system.*

Since we do not explicitly require photons in the $Z\gamma \rightarrow \ell\ell\gamma$ analysis to have no track match between the calorimeter cluster and hits in the tracking system (a cut, orthogonal for photons and electrons), we can readily measure the efficiency of photon cuts described in Section 5.1.3.3 using the methods incorporated in the *photon_id_tools* [67].

The overall efficiency of the photon identification criteria in the central calorimeter obtained from γ +jet MC samples is shown as a function of the photon transverse energy in Fig. 5.10(a) and is fitted to the following functional form:

$$\epsilon_{\gamma}(CC) = 0.972 - \frac{0.168}{\sqrt{E_T}} - \frac{0.267}{E_T}, \quad (5.5)$$

where E_T is expressed in units of GeV.

Efficiencies of the same set of cuts measured in $Z \rightarrow ee$ data and MC are shown in Fig. 5.10(b). The measurement is performed using a tag-and-probe method in accordance with the prescription given in Ref. [72]. In this method a tag electron is required to be an

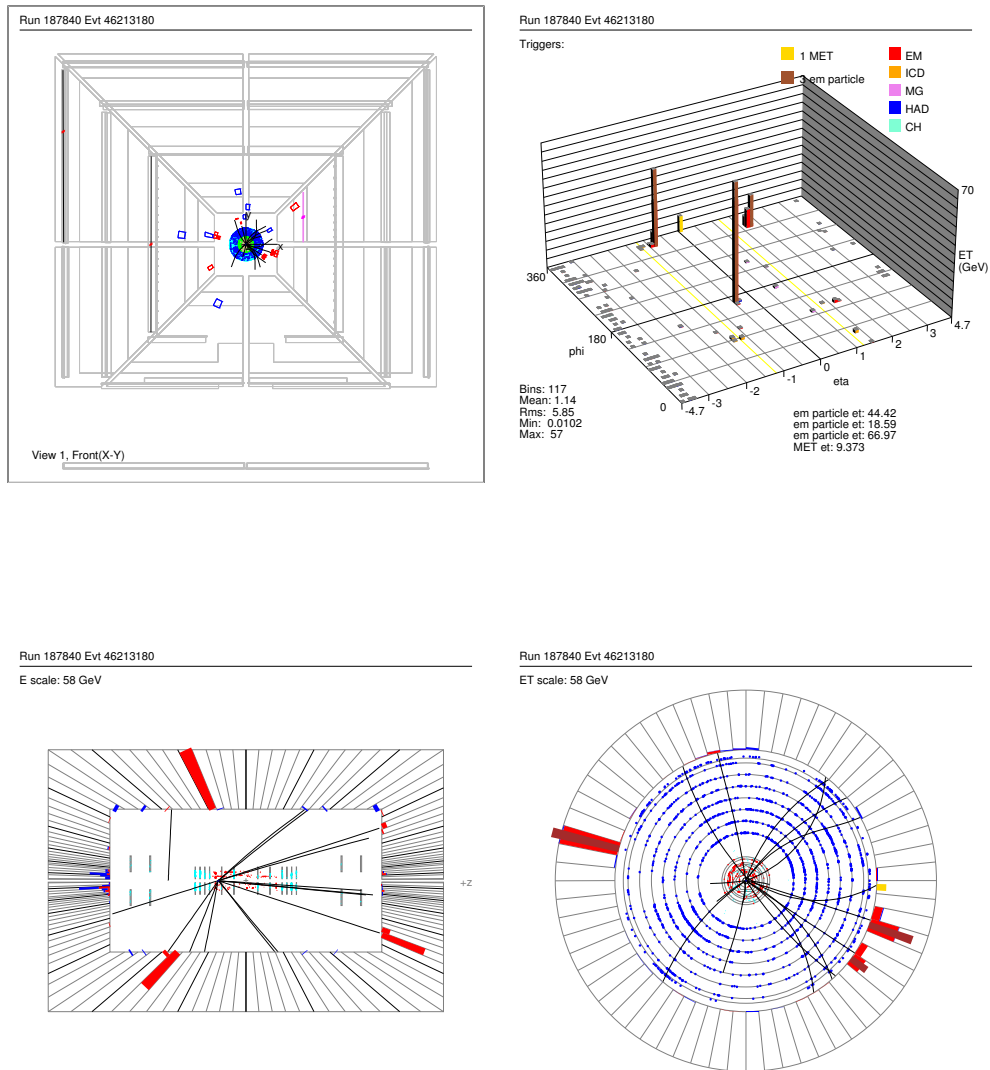


Figure 5.8: Event display of a $Z\gamma \rightarrow ee\gamma$ event. Upper row: (left) as seen from the front in the $x - y$ plane, muon spectrometer layers are shown; (right) calorimeter lego plot. Lower row: (left) side view ($z - y$ plane); (right) $r - \phi$ view with hits in the tracker, reconstructed tracks, and three EM showers in the calorimeter (red).

EM object of a good quality (to suppress the backgrounds), passing all the selection criteria and trigger requirements. A probe electron is an EM object satisfying all the selection

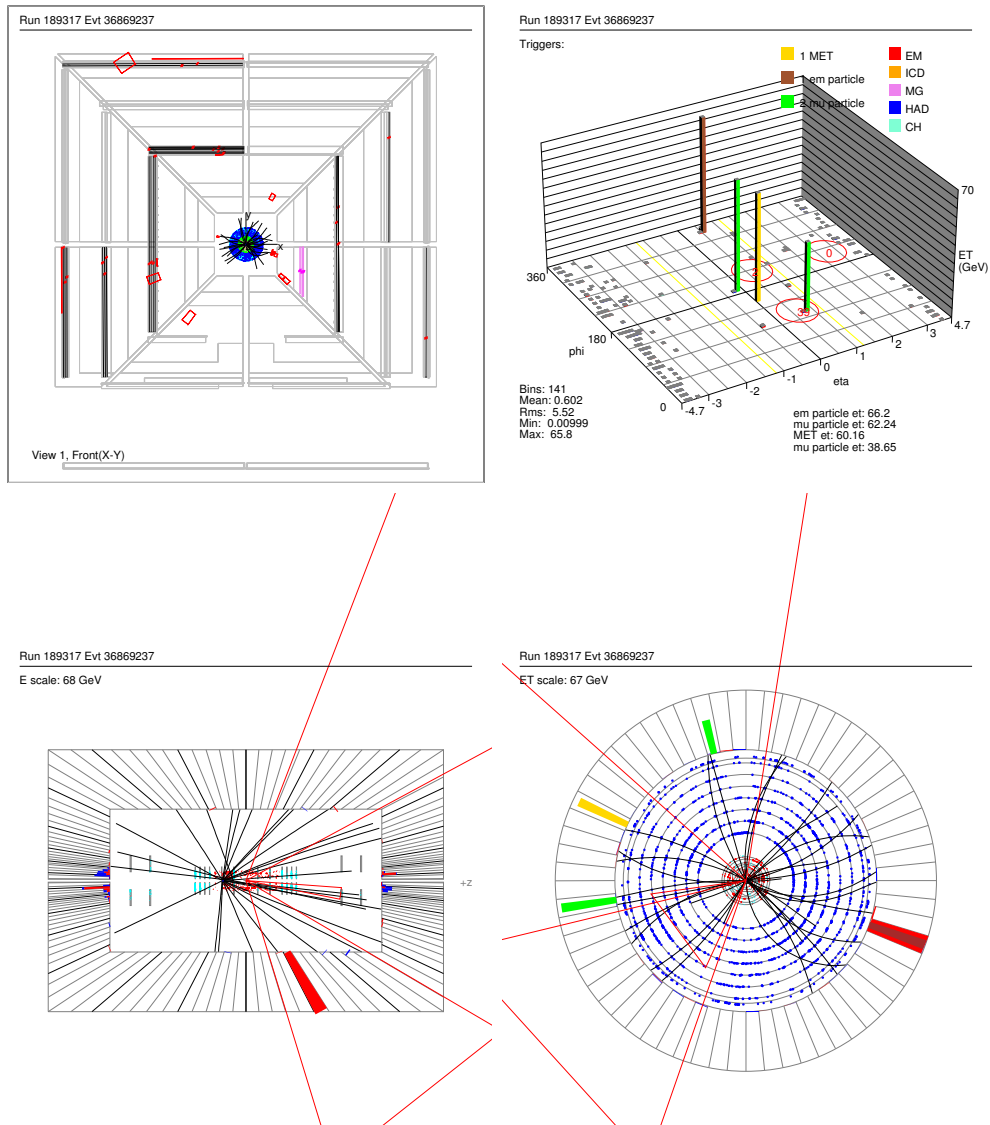


Figure 5.9: Event display of a $Z\gamma \rightarrow \mu\mu\gamma$ event. Upper row: (left) as seen from the front in the $x - y$ plane, muon spectrometer layers are shown; (right) calorimeter lego plot. Lower row: (left) side view ($z - y$ plane); (right) $r - \phi$ view with hits in the tracker, reconstructed tracks one EM shower in the calorimeter (red), and reconstructed muon candidates (green).

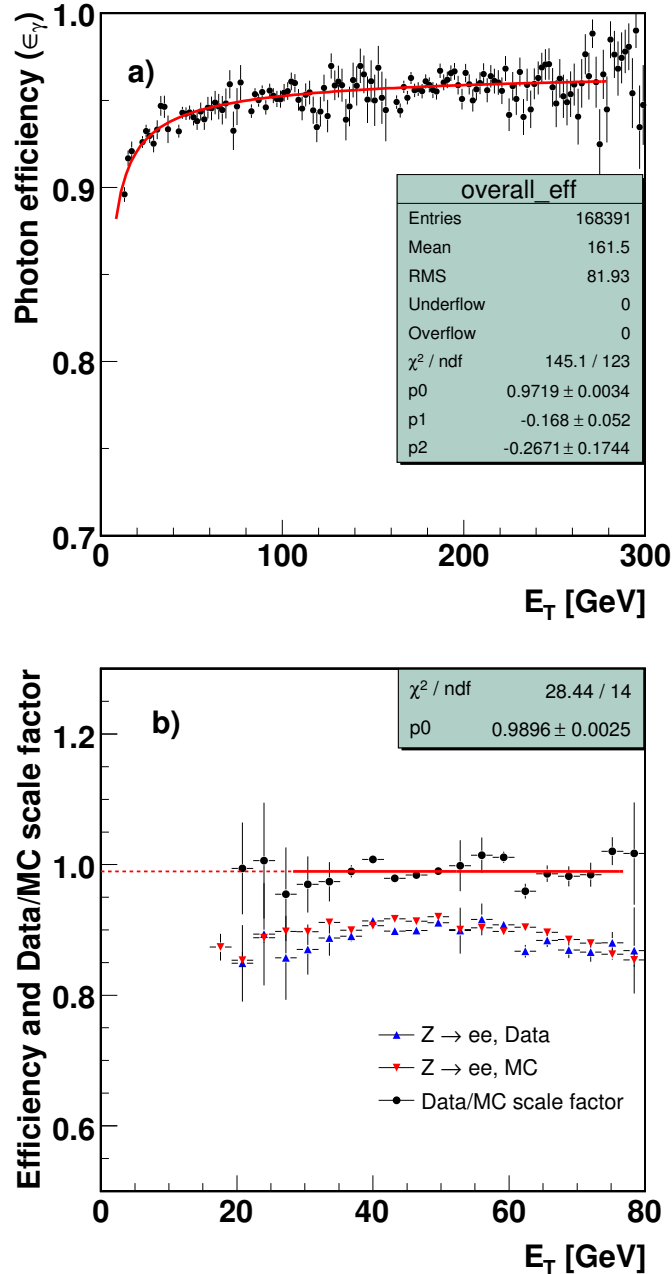


Figure 5.10: (a) Efficiency, ϵ_γ , of the photon reconstruction vs. photon transverse energy in CC. (b) Efficiencies in $Z \rightarrow ee$ data and Monte Carlo, and their ratio fitted to a zero degree polynomial (red horizontal line).

criteria except for the trigger requirement and the set of requirements under study. To reduce possible backgrounds, a tag is required to be reconstructed in the central calorimeter,

where the tracking efficiency is high. Events with 2 tag electrons are counted twice. The background (while already being rather low) is subtracted from under the invariant mass peak. The remaining distributions are then fitted to a combination of an error function (*TMath* :: *Erf*) and a Voigt function (*TMath* :: *Voigt*) with a number of parameters. These parameters are either set free or fixed at different stages of the fitting. The ratio of the efficiencies in data and MC (so-called *data/MC scale*) is also shown in Fig. 5.10(b). We correct the photon efficiency estimated from MC for this ratio. The average value of the data/MC ratio for the set of requirements described in Section 5.1.3.3 is 0.990 ± 0.003 .

5.1.5 Electron identification efficiency and $Z\gamma \rightarrow ee\gamma$ acceptance and efficiencies

The $Z\gamma \rightarrow ee\gamma$ reconstruction efficiency can be calculated as a product of the following terms: fiducial and kinematic acceptance, trigger efficiency, electron identification efficiency, and photon reconstruction efficiency. The electron identification efficiency can be, in turn, calculated as a product of the following terms: preselection efficiency, H-matrix efficiency, and spatial track match efficiency. Electron identification efficiencies are measured using the tag-and-probe method [72], [71]. Common Samples Group [50] p17 1EMloose data set is used to measure the preselection efficiency, and 2EMhighpt data set is used to determine H-matrix and spatial track match efficiencies.

5.1.5.1 Kinematic and geometrical acceptance

The acceptance for $Z\gamma \rightarrow ee\gamma$ process is calculated using the MC described in Section 5.1.2. We count the number of events that are generated (N_{gen}) with photon $E_T > 7$ GeV, dilepton mass $M_{\ell\ell} > 30$ GeV/ c^2 , and separation between a photon and any lepton from the Z decay $\Delta R_{\ell\gamma} > 0.7$. We also count the number of events which are reconstructed within the fiducial requirements (N_{selected}). These fiducial requirements (see Sections 5.1.3.1, 5.1.3.3) are that there must be one photon candidate, separated from module boundaries in ϕ , with $E_T > 7$ GeV; two electrons (one of them must be in the CC region) with reconstructed

$E_T > 15$ GeV (at least one of them must have $E_T > 25$ GeV), separated from the photon by $\Delta R > 0.7$, and the reconstructed invariant mass of the pair of electrons $M_{ee} > 30$ GeV/ c^2 .

The acceptance A is then calculated as:

$$A = \frac{N_{\text{selected}}}{N_{\text{gen}}}, \quad (5.6)$$

and is found to be 0.085 ± 0.001 for the CC-CC topology, and 0.058 ± 0.001 for the CC-EC topology. The uncertainty in the acceptance is statistical. The major source of systematic uncertainty ($\sim 5\%$) in the acceptance is due to the uncertainty on the parton distribution functions (PDF), described in Section 5.1.2.3. Therefore, the acceptance in the CC-CC topology is

$$A_{\text{CC-CC}} = 0.085 \pm 0.001(\text{stat.}) \pm 0.004(\text{syst.}) \quad (5.7)$$

$$A_{\text{CC-EC}} = 0.058 \pm 0.001(\text{stat.}) \pm 0.003(\text{syst.}) \quad (5.8)$$

5.1.5.2 Single-electron trigger efficiency

The trigger efficiency for the $Z\gamma \rightarrow ee\gamma$ final state is the same as for the $Z \rightarrow ee$ decay. Single-electron trigger efficiencies measurement for the trigger versions v8–v11, v12, v13 and v14 is described in Ref. [73, 74]. The paper also describes the behavior of “OR’ed” calorimeter only single-electron triggers. The efficiencies are available as text files, and the “OR’ed” trigger parameterizations can be found elsewhere [75]. Using these parameterizations with the signal PMCS Monte Carlo, we estimate the average trigger efficiency for each of the different trigger versions. The results of the studies are presented in Table 5.5. To estimate the trigger efficiency averaged over all trigger versions, we weigh each trigger version average efficiency by the ratio of relative integrated luminosity corresponding to the specified trigger version, and then use the following formula:

$$\epsilon_{\text{trig}} = \frac{\sum \epsilon_{\text{trig.ver.}} \cdot w_{\text{trig.ver.}}}{\sum w_{\text{trig.ver.}}} \quad (5.9)$$

We estimate the average single-electron trigger efficiency for the $Z\gamma$ process to be 0.99 ± 0.01 .

Table 5.5: Summary of the “OR’ed” calorimeter-only single-electron trigger efficiencies.

Trigger version	Efficiency, $\epsilon_{trig.ver.}$	Trigger list weight, $w_{trig.ver.}$	$\epsilon_{trig.ver.} \cdot w_{trig.ver.}$
v8–v11	0.975	0.124	0.121
v12	0.996	0.241	0.240
v13	0.984	0.389	0.383
v14	0.987	0.246	0.243
Total		1.0	0.987

5.1.5.3 Electron preselection efficiency

Preselection efficiency is defined as the percentage of EM objects, reconstructed with a Simple Cone Algorithm, that pass the following criteria:

- Fraction of energy deposited in the electromagnetic calorimeter must be above 0.9.
- Calorimeter isolation must be below 0.15.

The preselection efficiency results for the CC and EC electrons as functions of the electron transverse energy, detector η , detector ϕ and $phimod$ are presented in Fig. 5.11. It turns out, that while being rather flat in E_T for $E_T > 25$ GeV, the preselection efficiency drops in the low- E_T region (see Fig. 5.12). Further on we use the detector η preselection efficiency distributions for two E_T ranges as look-up tables in the PMCS.

5.1.5.4 Electron H-matrix efficiency

In order to estimate the efficiency of the χ_{HMx}^2 variable constructed from the H-matrix quantity, we select di-electron events that satisfy the following requirements:

- $E_T > 15$ GeV.
- Reconstructed either in CC or EC region.
- EM fraction above 0.90.
- Calorimeter isolation is below 0.15.

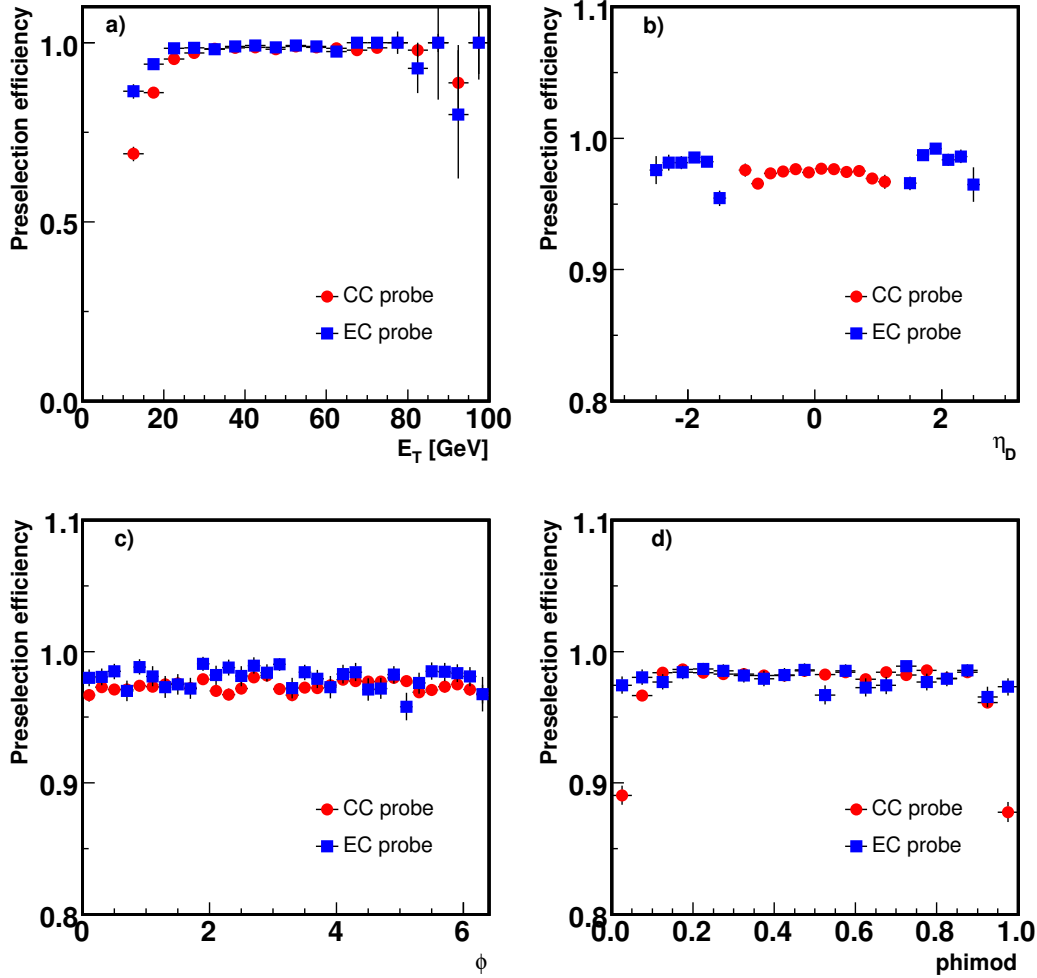


Figure 5.11: *Electron preselection efficiency dependencies as a function of (a) E_T , (b) η_{Det} , (c) ϕ and (d) $phimod$. Red dots and blue squares correspond to the CC and EC region probes, respectively.*

“Tight” electrons are required to have the probability of the spatial track match above 0.01, and the tag electron is also required to satisfy the shower shape agreement ($HMx7 < 12$ and $HMx8 < 20$ in the CC and EC regions, respectively) and the trigger requirements.

The formula for the efficiency of the H-Matrix requirement is:

$$\epsilon_{HMx} = \frac{2n(tt) + n(tp)}{2n(tt) + n(tp) + n(tf)}, \quad (5.10)$$

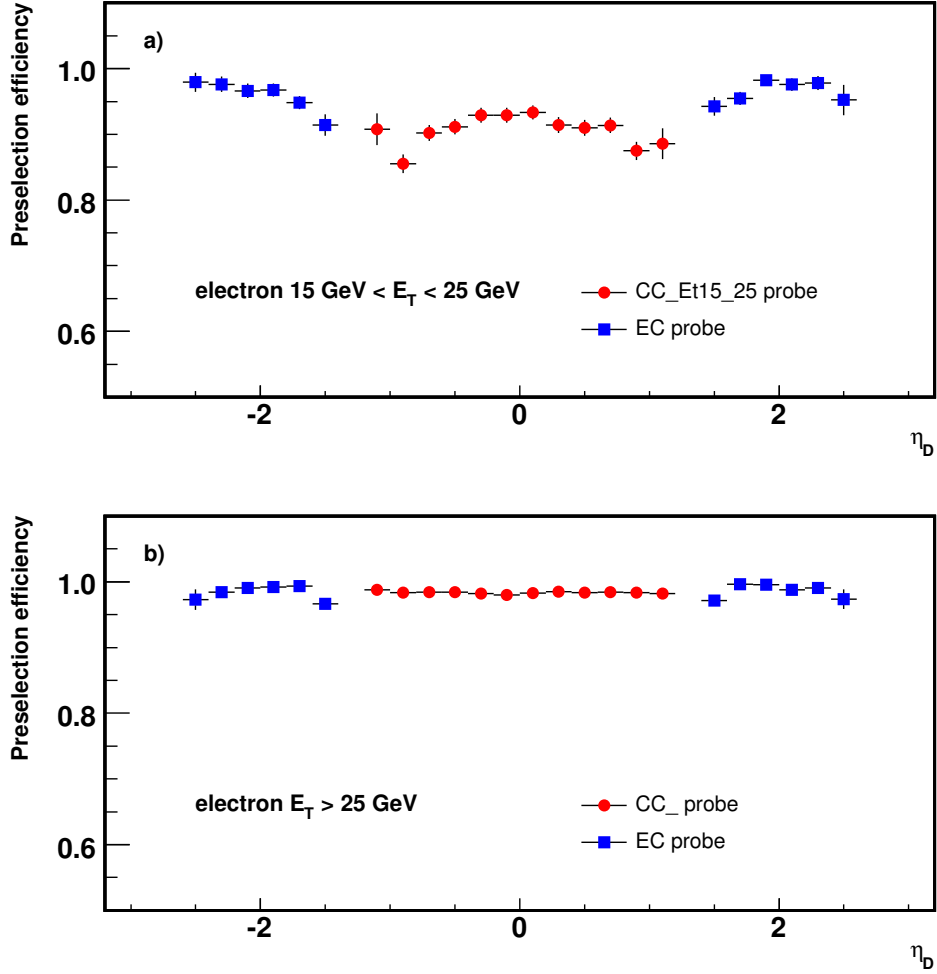


Figure 5.12: Preselection efficiency η_D dependencies for probe electrons transverse energy ranges (a) $15 \text{ GeV} < E_T < 25 \text{ GeV}$ and (b) $E_T > 25 \text{ GeV}$. Red dots and blue squares correspond to the CC and EC region probes, respectively.

where $n(tt)$ is the number of events with two tight electrons, $n(tp)$ is the number of events with one tight electron and the other electron satisfying H-Matrix requirements but failing tight criteria, $n(tf)$ is the number of events with one tight electron and the other electron failing H-Matrix requirements. The number of events is calculated by fitting the di-electron invariant mass by the Breit-Wigner distribution and the QCD background shape adopted from the *em_cert* package [70, 72]. H-matrix efficiency distributions as functions of electron

E_T , detector η , ϕ , and $phimod$ are shown in Fig. 5.13. Further on we use the detector η H-matrix efficiency distributions for four different electron E_T ranges as look-up tables in the PMCS, as shown in Fig. 5.14.

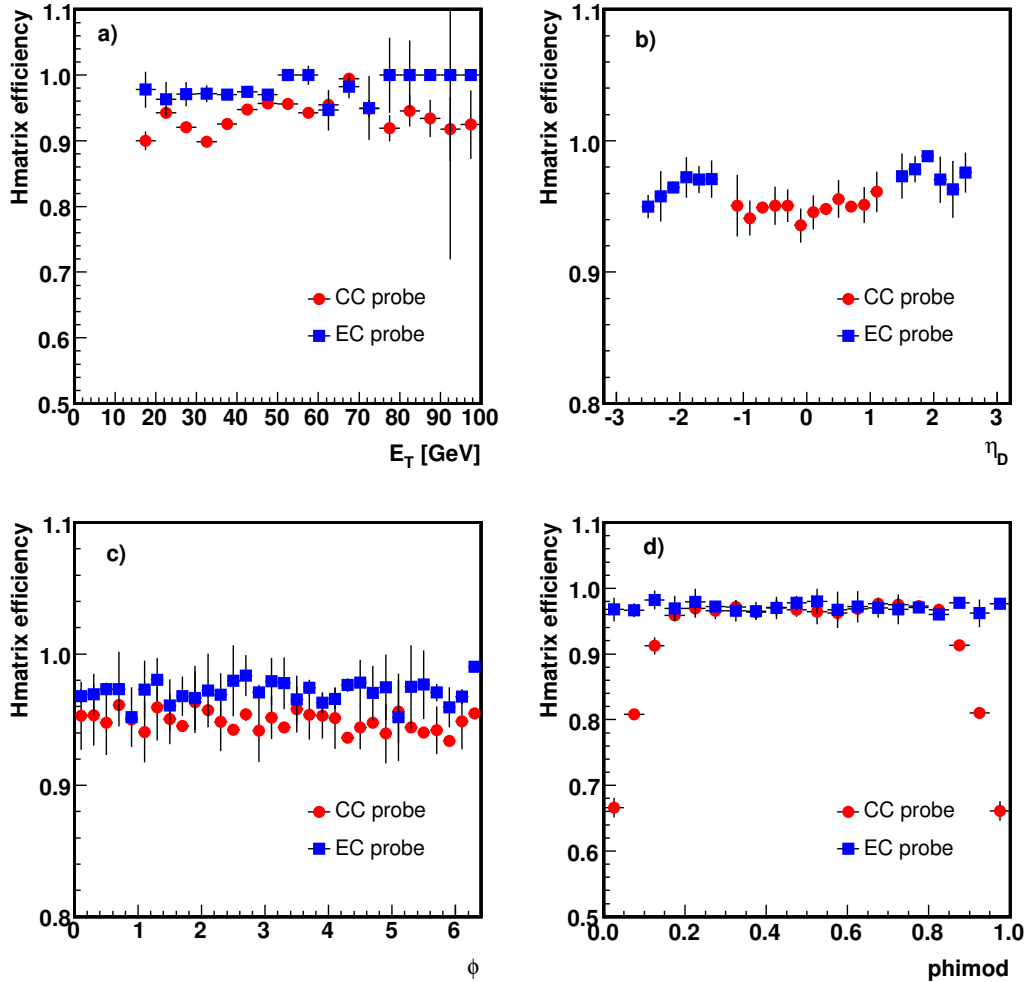


Figure 5.13: *H-matrix efficiency dependencies as functions of (a) E_T , (b) η_{Det} , (c) ϕ and (d) $phimod$. Red dots and blue squares correspond to CC and EC region probes, respectively.*

5.1.5.5 Spatial track match efficiency

To estimate the efficiency of track match requirements, we select events with two electron candidates that pass the following requirements:

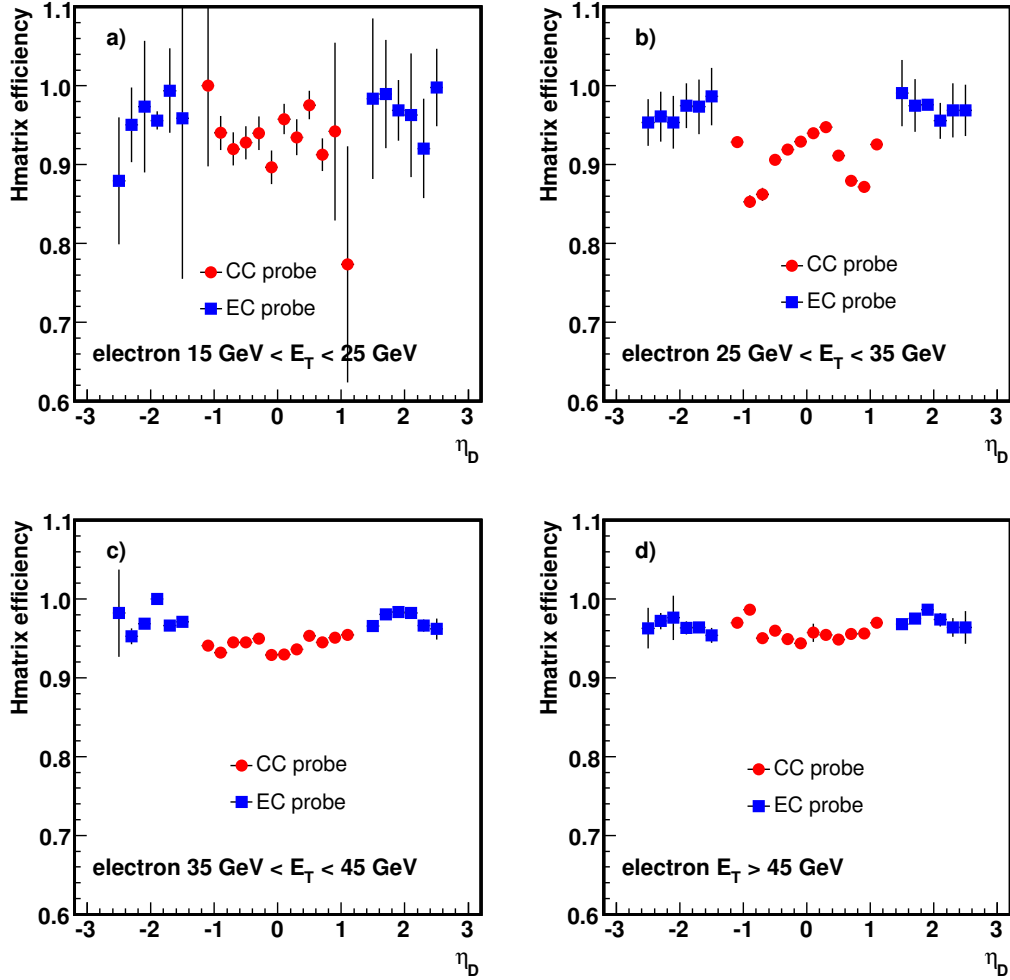


Figure 5.14: *H*-matrix efficiency η_D dependencies for four probe electrons transverse energy ranges (a) $15 \text{ GeV} < E_T < 25 \text{ GeV}$, (b) $25 \text{ GeV} < E_T < 35 \text{ GeV}$, (c) $35 \text{ GeV} < E_T < 45 \text{ GeV}$, and (d) $E_T > 45 \text{ GeV}$. Red dots and blue squares correspond to CC and EC region probes, respectively.

- EM fraction above 0.9.
- Calorimeter isolation below 0.15.
- $E_T > 15 \text{ GeV}$.
- Good shower shape agreement ($\text{HMx7} < 12$ and $\text{HMx8} < 20$ in the CC or EC regions, respectively).

Then we obtain the number of Z candidate events with both electrons spatially matched to tracks with probability above 0.01, N_2 , and that with only one electron spatially matched to a track, N_1 . The efficiency of track matching is calculated using the following formula

$$\epsilon_{\text{TRK}} = \frac{2N_2}{2N_2 + N_1}. \quad (5.11)$$

We estimate the number of Z candidates by fitting the invariant mass distribution to a Breit-Wigner and a data QCD distribution. Track match efficiency dependences as functions of electron E_T , detector η , ϕ , and $phimod$ are shown in Fig. 5.15. Track match efficiency depends greatly on the z vertex position, hence further on we use the detector η spatial track match efficiency distributions for six different z vertex ranges as look-up tables in the PMCS, as shown in Fig. 5.16.

5.1.5.6 Summary of the $Z\gamma \rightarrow ee\gamma$ efficiency studies

We combine the individual electron and photon efficiencies determined as functions of detector η , EM object E_T , and z vertex (see Sections 5.1.4 and 5.1.5.1–5.1.5.5) in the following way, as stated in Section 5.1.5:

$$\begin{aligned} \epsilon_{Z\gamma \rightarrow ee\gamma} = A \times \epsilon_{Trig} \times \epsilon_\gamma \times \epsilon_{EM} = & \quad (5.12) \\ & A \times \epsilon_{Trig} \times \epsilon_\gamma \times \\ & \epsilon_{presel}(E_{T1}, \eta_{D1}) \times \epsilon_{presel}(E_{T2}, \eta_{D2}) \\ & \times \epsilon_{HMx}(E_{T1}, \eta_{D1}) \times \epsilon_{HMx}(E_{T2}, \eta_{D2}) \\ & \times \epsilon_{Trk}(z_v, \eta_{D1}) \times \epsilon_{Trk}(z_v, \eta_{D2}). \end{aligned}$$

In this equation, lower indices 1 (2) in round brackets denote the efficiency of the leading (trailing) electron as a function of the corresponding variable (*e.g.* E_{T1} , *etc.*), A is the acceptance, ϵ_{Trig} is the averaged trigger efficiency, and ϵ_γ is the photon efficiency. The resulting efficiency is used as a look-up table in the PMCS. Table 5.6 summarizes results of the acceptance and efficiency studies in the electron channel.

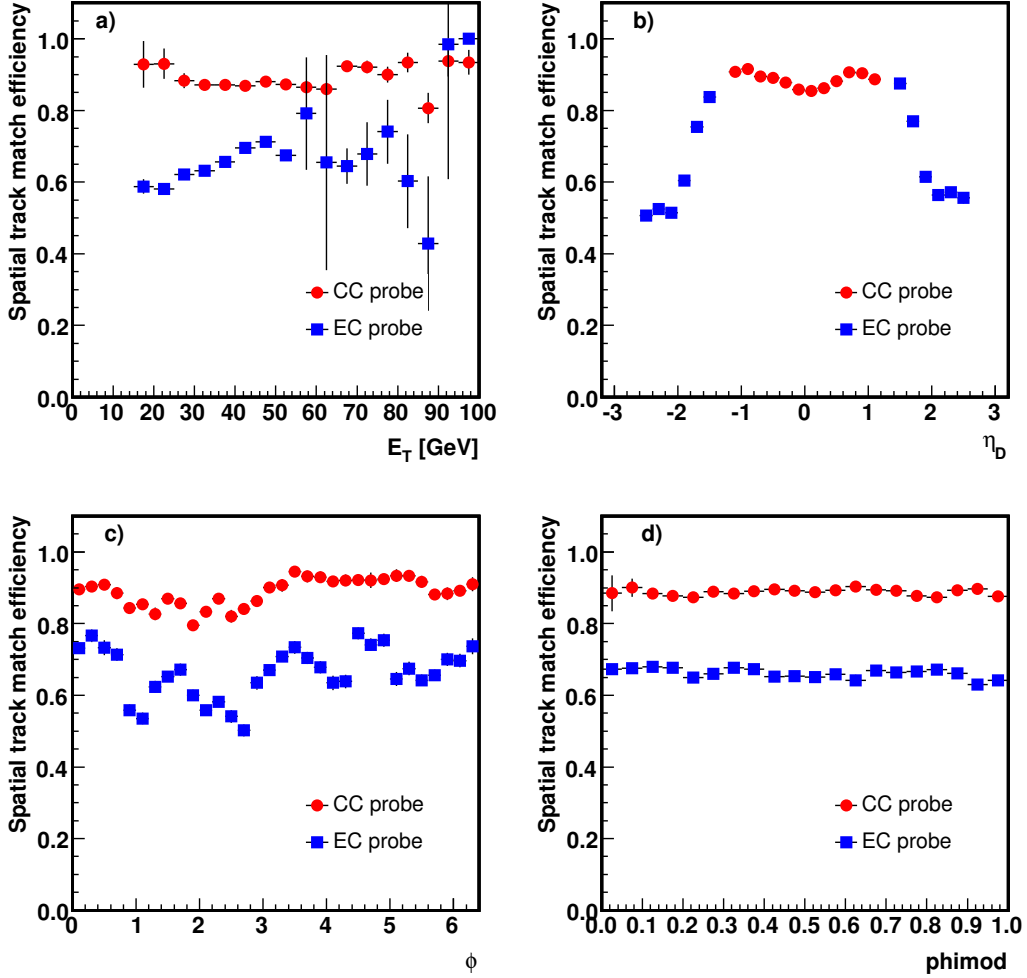


Figure 5.15: *Spatial track matching efficiency dependences as functions of (a) E_T , (b) η_{Det} , (c) ϕ and (d) phimod . Red dots and blue squares correspond to CC and EC region probes, respectively.*

We estimate the overall efficiency $\epsilon_{Z\gamma \rightarrow ee\gamma}$ of the event selection criteria to reconstruct $Z\gamma \rightarrow ee\gamma$ process with di-electron invariant mass above $30 \text{ GeV}/c^2$ and a photon with $E_T > 7 \text{ GeV}$, separated from both of electrons with $\Delta R > 0.7$ to be 0.049 ± 0.003 for the CC-CC topology, and 0.026 ± 0.002 for the CC-EC topology.

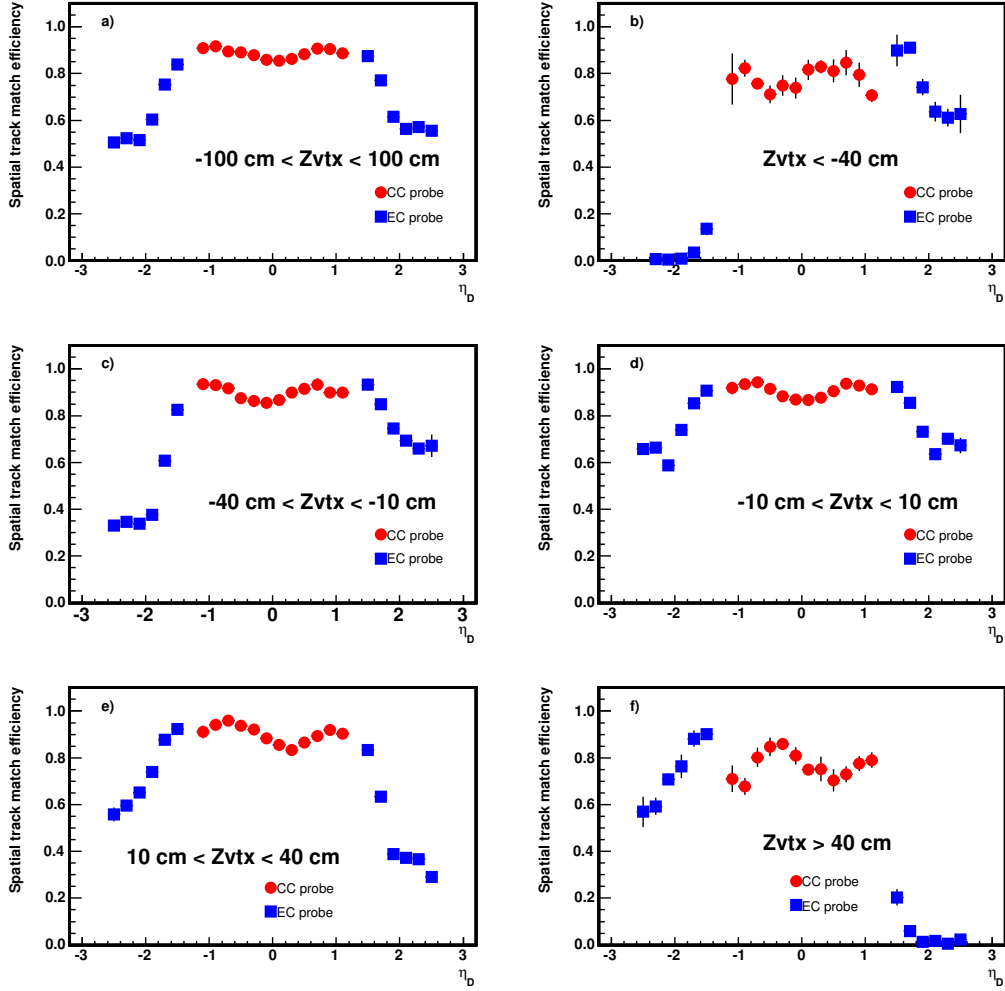


Figure 5.16: Spatial track matching efficiency η_D dependences for six z vertex ranges (a) $-100 \text{ cm} < z_v < 100 \text{ cm}$, (b) $z_v < -40 \text{ cm}$, (c) $-40 \text{ cm} < z_v < -10 \text{ cm}$, (d) $-10 \text{ cm} < z_v < 10 \text{ cm}$, (e) $10 \text{ cm} < z_v < 40 \text{ cm}$, (f) $z_v > 40 \text{ cm}$. Red dots and blue squares correspond to CC and EC region probes, respectively.

5.1.6 Muon identification efficiency and $Z\gamma \rightarrow \mu\mu\gamma$ acceptance and efficiencies

$Z\gamma \rightarrow \mu\mu\gamma$ reconstruction efficiency can be calculated as a product of the following independent terms: geometrical and kinematic acceptance, and muon identification efficiency $\epsilon_{Z\gamma}^{MC}$; trigger efficiency ϵ_{trig} ; muon isolation ϵ_{iso} ; and photon reconstruction efficiency ϵ_γ .

Table 5.6: *Summary of efficiencies for the electron channel.*

Requirement	CC-CC topology	CC-EC topology	Combined
Acceptance	0.0847 ± 0.0040	0.0582 ± 0.0027	0.1429 ± 0.0067
Trigger	0.99 ± 0.01	0.99 ± 0.01	0.99 ± 0.01
Electron pair efficiency	0.646 ± 0.022	0.508 ± 0.024	0.590 ± 0.024
Photon efficiency	0.897 ± 0.020	0.894 ± 0.021	0.896 ± 0.020
Total	0.0486 ± 0.0031	0.0262 ± 0.0019	0.0748 ± 0.0050

5.1.6.1 Kinematic and geometrical acceptance

We estimate the efficiency of acceptance and kinematics $\epsilon_{Z\gamma}^{MC}$ and the photon identification efficiency ϵ_γ using the PMCS described in Section 5.1.2. We count the number of events that are generated (N_{gen}) with photon $E_T > 7$ GeV, dimuon mass $M_{\mu\mu} > 30$ GeV/ c^2 , and a separation between a photon and muons from the Z decay $\Delta R_{\mu\gamma} > 0.7$. We also count the number of events which are reconstructed within the fiducial requirements (N_{selected}). These fiducial requirements are that there must be one photon candidate, separated from module boundaries in ϕ , with $E_T > 7$ GeV, two muons that are in the geometrical acceptance of the muon chambers, leading muon reconstructed p_T must be greater than 20 GeV/ c , trailing muon reconstructed p_T must be greater than 15 GeV/ c , and separation from the photon must be $\Delta R > 0.7$, and the reconstructed invariant mass of dimuon pair $M_{\mu\mu} > 30$ GeV/ c^2 . In addition, we require muons to be of loose quality, and to be matched to central tracks. The efficiency of the two latter requirements is measured from the PMCS to be $\epsilon_{\mu ID} = 0.788 \pm 0.016$, and the efficiency of the muon isolation and cosmic cut is measured in the $Z \rightarrow \mu\mu$ study to be $\epsilon_{iso} = 0.987 \pm 0.006$.

The acceptance and kinematics efficiencies and the photon identification efficiency are estimated to be

$$\epsilon_{Z\gamma}^{MC} = 0.143 \pm 0.007, \quad (5.13)$$

$$\epsilon_\gamma = 0.896 \pm 0.020. \quad (5.14)$$

Table 5.7: *Summary of muon trigger efficiencies.*

Trigger version	Run range	Trigger combination	Efficiency	Sample weight
v8 – v12	166503 – 194566	see Ref. [76]	0.853 ± 0.006	0.327
v13a	194567 – 196584	DMU1_LM6	0.627 ± 0.001	0.052
v13b	201485 – 201936	MUH1_LM15	–	0.003
v13c	202152 – 204805	MUH1_LM15	0.634 ± 0.004	0.119
v13d	204807 – 206161	MUH1_LM15	0.684 ± 0.005	0.080
v13e	206162 – 208144	MUH1_LM15	0.679 ± 0.005	0.106
v14a	207217 – 211213	DMU1_2LM6	0.522 ± 0.005	0.159
v14b	211214 – 212107	DMU1_2LM6	0.515 ± 0.008	0.068
v14c	211804 – 215670	DMU1_2LM6	0.542 ± 0.008	0.086

5.1.6.2 Muon trigger efficiency

The muon trigger efficiency for v8–v12 trigger lists has been studied in details elsewhere [76]. As the muon triggers combination used in this analysis for the v8–v12 trigger lists is identical to the one used in Ref. [76], we adopt the quoted value of the muon trigger efficiency for that data taking period of 85%. Due to the changes in the luminosity monitor electronics, DØ detector shutdowns and DØ solenoid current change, v13 and v14 trigger lists are divided into eight major data taking periods [52]. Using standard CAF and MU ID tools we calculate trigger efficiencies for each period separately [52, 77]. The muon trigger efficiencies with the corresponding data sample weights are summarized in Table 5.7. We estimate the average muon trigger efficiency for the whole data taking period by weighting the efficiency value for each trigger version by the ratio of relative integrated luminosity corresponding to the specified trigger version (see Section 5.1.5.2). The resulting trigger efficiency is:

$$\epsilon_{trig} = 0.68 \pm 0.01. \quad (5.15)$$

5.1.6.3 Summary of the $Z\gamma \rightarrow \mu\mu\gamma$ efficiency studies

We estimate the total efficiency $\epsilon_{Z\gamma \rightarrow \mu\mu\gamma}$ of the event selection criteria to reconstruct the $Z\gamma \rightarrow \mu\mu\gamma$ final state with the photon $E_T > 7$ GeV, dimuon mass $M_{\mu\mu} > 30$ GeV/ c^2 , and

a separation between a photon and muons from the Z decay $\Delta R_{\mu\gamma} > 0.7$ to be

$$\epsilon_{Z\gamma\rightarrow\mu\mu\gamma} = \epsilon_{Z\gamma}^{MC} \times \epsilon_{trig} \times \epsilon_{\mu ID} \times \epsilon_{iso} \times \epsilon_{\gamma} = 0.086 \pm 0.005. \quad (5.16)$$

5.1.7 Backgrounds

The main background to the $Z\gamma$ process is the Z +jet production, where a jet is misidentified as a photon. We will refer to a jet with most of its energy carried by photons, and misidentified as an electron or a photon candidate, as an EM-like jet. The background determination is a two-step process.

First, we calculate the E_T -dependent rate at which an EM-like jet is misreconstructed as a photon, f (or *fake rate*). This is done on a data sample of events, where a jet triggers the event (*i.e.* one of the following jet triggers is fired: JT_15TT, JT_25TT_NG, JT_45TT, JT_65TT, JT_95TT, JT_125TT) and a high quality jet is reconstructed and matched to the jet trigger object. Further, this sample is narrowed down by a requirement of a presence of EM objects reconstructed with a Simple Cone Algorithm in the central calorimeter with $E_T > 10$ GeV and separated from the jet that triggers the event. More details on the event selection can be found in Ref. [67]. By construction, most of these EM objects are, in fact, jets that mimic an EM object. Then, the E_T -dependent fake rate is defined as a transverse energy distribution of all photon candidates in these events that satisfied the photon identification criteria normalized by the transverse energy of all EM candidates in the sample. This ratio is plotted in Fig. 5.17(a). The misidentification rate rapidly decreases from about 20% for the photon $E_T = 10$ GeV to $\approx 4\%$ at 80 GeV, then it raises again to 15% at $E_T = 220$ GeV.

However, by construction direct, or *prompt*, photons will contaminate this jet-enriched data sample. The direct photon contribution is most pronounced in the high- E_T region, and has to be eliminated from the fake rate determination. To estimate this contribution, the outputs of the photon Artificial Neural Network (γ -ANN), obtained from γ +jet and dijet MC samples, are fitted to the data in each E_T bin. Each of the former two distributions is

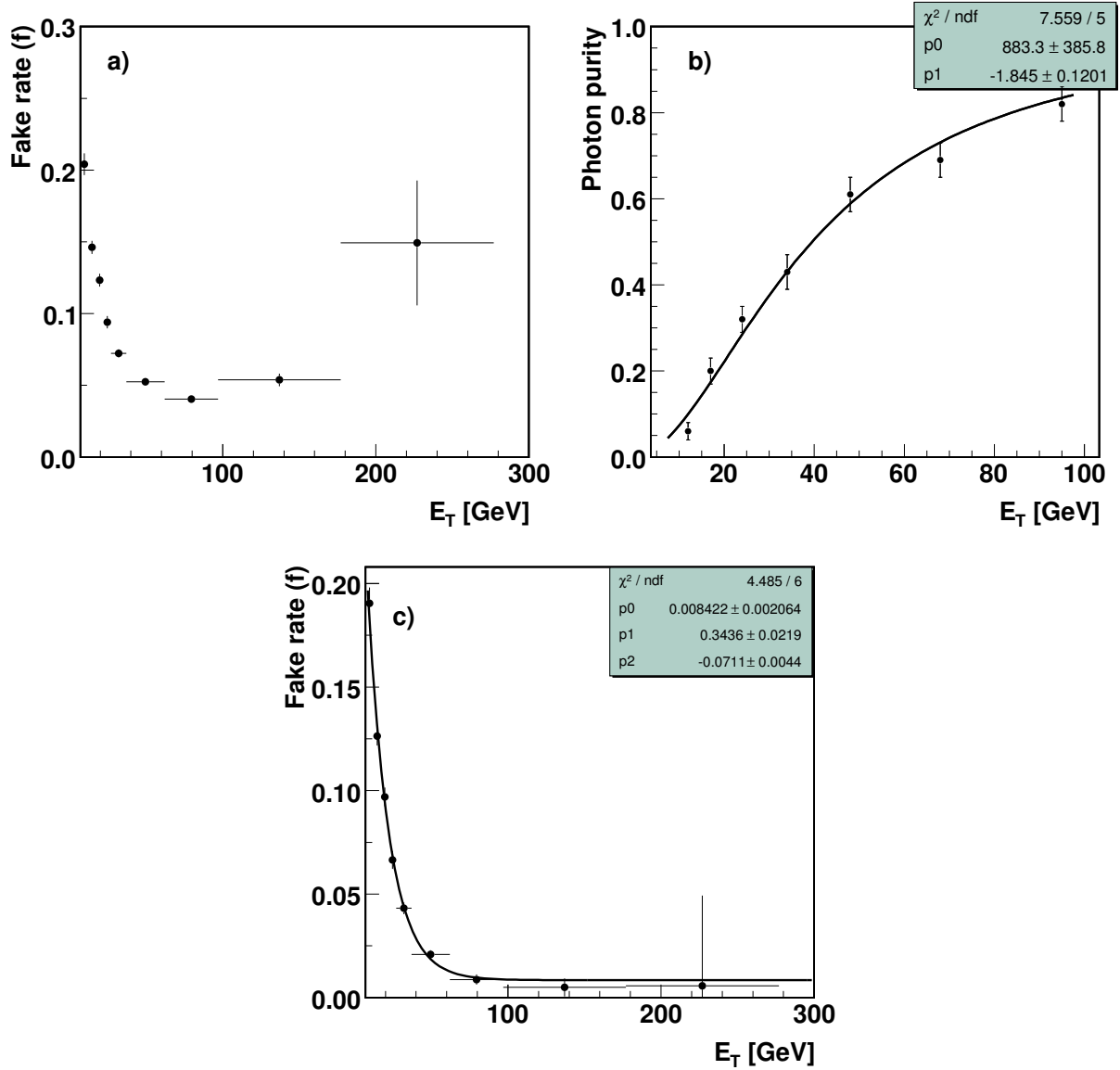


Figure 5.17: (a) Rate for an EM-like jet to satisfy photon identification criteria. No subtraction from the direct photon contribution is made. (b) Photon purity in CC region. (c) Rate, f , for an EM-like jet to satisfy photon selection criteria. Contribution from direct photons is subtracted.

weighted the way so that the shape of their sum reproduces the γ -ANN output shape from the data with the largest likelihood. Then the direct photons contribution (also known as *purity*) is defined as the ratio of events from the γ +jet sample over the sum of events from γ +jet and dijet MC sample. For the set of cuts described in Section 5.1.3.3, the photon

purity is shown in Fig. 5.17(b) [78, 79]. The purity is roughly 10% at low E_T , and is rapidly growing to 50% (85%) at 40 GeV (100 GeV). Numerically the contribution from the direct photons, $P_{direct\gamma}$, is given in Eq. 5.17.

$$P_{direct\gamma} = \frac{1}{1 + 883 \cdot (E_T)^{-1.85}}. \quad (5.17)$$

The resultant rate at which an EM-like jet passes the photon identification criteria is shown in Fig. 5.17(c) and is described by the following functional form:

$$f = 0.008 + 0.344 \cdot e^{-0.071 \cdot E_T}. \quad (5.18)$$

The corrected misidentification rate drops from about 20% at 10 GeV to less than 1% at $E_T > 80$ GeV.

To estimate the Z +jet background, we use the matrix method of background determination [80]. We construct two data samples:

- In the first sample an event consists of a Z boson and a photon candidate that is reconstructed with a Simple Cone Algorithm, and identified in the geometrical acceptance defined for the photon candidates. This sample is referred to as the Z +EM sample. We will refer to the number of photon candidates distribution in each E_T bin as $dN/dE_T[Z + EM]$.
- The second sample is the sample of a Z boson candidates and photon candidates that pass all the photon selection criteria described in Section 5.1.3.3. This sample is also known as the *final $Z\gamma$ sample*. We will refer to the number of photon candidates distribution in each E_T bin in the final sample as $dN/dE_T[\text{final}]$.

The former distribution consists of real photons, $dN/dE_T[Z + \gamma]$, and EM-like jets, $dN/dE_T[Z + \text{jet}]$:

$$dN/dE_T[Z + EM] = dN/dE_T[Z + \gamma] + dN/dE_T[Z + \text{jet}] \quad (5.19)$$

When selection criteria are applied, the $dN/dE_T[\text{final}]$ distribution is formed by folding the E_T -dependent efficiency, ϵ_γ , and $dN/dE_T[Z + \gamma]$, and the fake rate, f , from Eq. 5.18 and $dN/dE_T[Z + \text{jet}]$ as follows:

$$dN/dE_T[\text{final}] = \epsilon_\gamma dN/dE_T[Z + \gamma] + f dN/dE_T[Z + \text{jet}] \quad (5.20)$$

The estimated background to the contribution is then $N_{QCD} = f dN/dE_T[Z + \text{jet}]$ and can be calculated from the previous equations in the following way: first, fold the left and right sides of Eq. 5.19 by ϵ_γ

$$\epsilon_\gamma dN/dE_T[Z + \text{EM}] = \epsilon_\gamma dN/dE_T[Z + \gamma] + \epsilon_\gamma dN/dE_T[Z + \text{jet}] \quad (5.21)$$

Then, subtract Eq. 5.20 from it

$$\epsilon_\gamma dN/dE_T[Z + \text{EM}] - dN/dE_T[\text{final}] = \epsilon_\gamma dN/dE_T[Z + \text{jet}] - f dN/dE_T[Z + \text{jet}] \quad (5.22)$$

Thus,

$$dN/dE_T[Z + \text{jet}] = \frac{\epsilon_\gamma dN/dE_T[Z + \text{EM}] - dN/dE_T[\text{final}]}{\epsilon_\gamma - f}, \quad (5.23)$$

and

$$N_{QCD} = f dN/dE_T[Z + \text{jet}] = f \frac{\epsilon_\gamma dN/dE_T[Z + \text{EM}] - dN/dE_T[\text{final}]}{\epsilon_\gamma - f}. \quad (5.24)$$

We obtain $29.5 \pm 4.8(\text{stat.}) \pm 3.1(\text{syst.})$ background events for the CC-CC topology and $25.7 \pm 3.8(\text{stat.}) \pm 2.5(\text{syst.})$ for the CC-EC topology in the electron channel ($55.2 \pm 6.1(\text{stat.}) \pm 5.6(\text{syst.})$ combined CC-CC and CC-EC), and $61.3 \pm 6.5(\text{stat.}) \pm 6.2(\text{syst.})$ in the muon channel. The systematic uncertainty on the $Z+\text{jet}$ background mostly comes from the uncertainty on the photon efficiency and the rate at which an EM-like jet is misreconstructed as a photon.

Table 5.8: Summary of the components for the $Z\gamma \rightarrow ee\gamma$ cross section calculation.

Parameter	CC-CC topology	CC-EC topology	CC-CC and CC-EC
N_{cand}	308 ± 17.6	145 ± 12.0	453 ± 21.3
N_{bkg}	29.5 ± 5.7	25.7 ± 4.6	55.2 ± 8.3
$\epsilon_{Z\gamma \rightarrow ee\gamma}$	0.0486 ± 0.0031	0.0262 ± 0.0019	0.0748 ± 0.0050
$\int \mathcal{L}dt, \text{ pb}^{-1}$	1109 ± 67	1109 ± 67	1109 ± 67

Table 5.9: Summary of the components for the $Z\gamma \rightarrow \mu\mu\gamma$ cross section calculation.

Parameter	Value
N_{cand}	515 ± 22.7
N_{bkg}	61.3 ± 9.0
$\epsilon_{Z\gamma \rightarrow \mu\mu\gamma}$	0.0858 ± 0.0047
$\int \mathcal{L}dt, \text{ pb}^{-1}$	1009 ± 61

5.1.8 Cross section calculation

The cross section for the $Z\gamma$ production times the branching fraction for the $Z \rightarrow \ell\ell$ is evaluated to the following formula

$$\sigma \cdot \text{Br}(Z \rightarrow \ell\ell) (M_{\ell\ell} > 30 \text{ GeV}/c^2, E_T(\gamma) > 7 \text{ GeV}, \Delta R(\ell\gamma) > 0.7) = \frac{N_{\text{cand}} - N_{\text{bkg}}}{\epsilon_{Z\gamma \rightarrow \ell\ell\gamma} \cdot \int \mathcal{L}dt}, \quad (5.25)$$

where N_{cand} and N_{bkg} are the number of candidate events and estimated number of background events, $\epsilon_{Z\gamma \rightarrow \ell\ell\gamma}$ is the total efficiency of the selection criteria, and $\int \mathcal{L}dt$ is the data sample integrated luminosity.

In Table 5.8 we summarize the values of the parameters of Eq. 5.25 for the electron mode cross section calculation. Similarly, we provide the values of the same parameters in the muon mode in Table 5.9.

Plugging the numbers from Tables 5.8, 5.9 into Eq. 5.25, we calculate the cross section of the $Z\gamma \rightarrow ee\gamma$ process in the CC-CC mode in the electron channel to be:

$$\sigma \cdot \text{Br}(Z \rightarrow ee)_{\text{CC-CC}} = 5.17 \pm 0.34(\text{stat.}) \pm 0.38(\text{syst.}) \pm 0.31(\text{lumi.}) \text{ pb}. \quad (5.26)$$

The same for the CC-EC topology is:

$$\sigma \cdot \text{Br}(Z \rightarrow ee)_{CC-EC} = 4.11 \pm 0.43(\text{stat.}) \pm 0.33(\text{syst.}) \pm 0.25(\text{lumi.}) \text{ pb.} \quad (5.27)$$

The same for the $Z\gamma \rightarrow \mu\mu\gamma$ process is:

$$\sigma \cdot \text{Br}(Z \rightarrow \mu\mu) = 5.24 \pm 0.27(\text{stat.}) \pm 0.30(\text{syst.}) \pm 0.31(\text{lumi.}) \text{ pb.} \quad (5.28)$$

The measurements in the electron and muon channel are combined using Best Linear Unbiased Estimate (BLUE) [81] technique. The method combines three measurements taking into account correlations in the systematic uncertainties. We treat photon identification and background uncertainties as fully correlated between the electron and muon channels. The systematic uncertainty in central electron identification is treated to be 100% correlated between the CC-CC and CC-EC topologies. Other uncertainties are treated as fully uncorrelated. We summarize all the uncertainties in Table 5.10.

The error matrix associated with these three measurements is:

$$V = \begin{pmatrix} 0.2556 & 0.0429 & 0.0176 \\ 0.0429 & 0.3002 & 0.0175 \\ 0.0176 & 0.0175 & 0.1618 \end{pmatrix} \quad (5.29)$$

The result of the minimization of the χ^2 with one free parameter, the value of the cross section of $Z\gamma \rightarrow \ell\ell\gamma$, is:

$$\sigma \cdot \text{Br}(Z \rightarrow \ell\ell)(\text{data}) = 4.96 \pm 0.30(\text{stat.} + \text{syst.}) \pm 0.30(\text{lumi.}) \text{ pb.} \quad (5.30)$$

The LO Baur generator [12] with the photon E_T corrected for the NLO/LO K -factor is used to estimate the value of the NLO $Z\gamma$ cross section. For the photon $E_T > 7$ GeV, dilepton mass above 30 GeV/ c^2 and separation of the photon from leptons $\Delta R > 0.7$ the NLO $Z\gamma$ cross section is calculated to be:

$$\sigma \cdot \text{Br}(Z \rightarrow \ell\ell)(\text{theory}) = 4.74 \pm 0.22 \text{ pb.} \quad (5.31)$$

The uncertainty on the SM cross section includes the uncertainty due to the choice of the PDF set and group (see Section 5.1.2.3). As seen from Eq. 5.30 and Eq. 5.31, the measured combined cross section times branching fraction agrees well within uncertainties with the SM prediction.

Table 5.10: Summary of the uncertainties of the $Z\gamma \rightarrow \ell\ell\gamma$ cross section for the electron CC-CC, electron CC-EC, and muon channels.

Quantity	CC-CC, pb	CC-EC, pb	correlation	muon channel, pb	correlation
$\epsilon_{CC \text{ electron}}$	0.1761	0.1400	100%	–	–
$\epsilon_{EC/CC \text{ electron}}$	0.1761	0.1942	0	–	–
ϵ_γ	0.1153	0.0965	100%	0.1170	100%
Acceptance	0.2442	0.1907	0	0.2570	–
Trigger efficiency	0.0522	0.0415	100%	0.0385	0
Background (stat)	0.0891	0.1309	0	0.0751	0
Background (syst)	0.0575	0.0861	100%	0.0716	100%
Number of events	0.3267	0.4134	0	0.2622	0
Total systematic uncertainty	0.3754	0.3348		0.2956	
Total statistical uncertainty	0.3387	0.4336		0.2727	
Total uncertainty	0.5056	0.5479		0.4022	

5.1.9 Observed distributions

The photon candidate E_T spectra, dilepton invariant mass and dilepton plus photon invariant mass distributions in data with overlaid QCD background and MC prediction are shown in Fig. 5.18 for the electron and muon channels separately, and in Fig. 5.19 for the electron and muon channel combined. None of the kinematic distributions show a significant deviation of the observed data from the SM predictions. Having found no indication for anomalous $Z\gamma$ production, we can set limits on the size of the trilinear couplings between a Z boson and a photon (see Chapter 6).

5.2 $Z\gamma \rightarrow \nu\bar{\nu}\gamma$ Cross Section

5.2.1 Data samples

The cross section measurement of the $Z\gamma \rightarrow \nu\bar{\nu}\gamma$ process is done on the Run II data [50] collected with the DØ detector [35] between the 21st of October 2002 and the 12th of September 2008 (runs 166503–245473), covering v8–v16 trigger lists. This data set is divided into two separate data sets: Run IIa and Run IIb (see Section 5.1.1).

We use the following data samples:

Run IIa:

- CSG_CAF_EMinclusive_PASS3_p17.09.03,
- CSG_CAF_EMinclusive_PASS3_p17.09.06, and
- CSG_CAF_EMinclusive_PASS3_p17.09.06b.

Run IIb:

- CSG_CAF_EMinclusive_PASS2_p21.10.00,
- CSG_CAF_EMinclusive_PASS4_p21.10.00_p20.12.00,
- CSG_CAF_EMinclusive_PASS4_p21.10.00_p20.12.01,

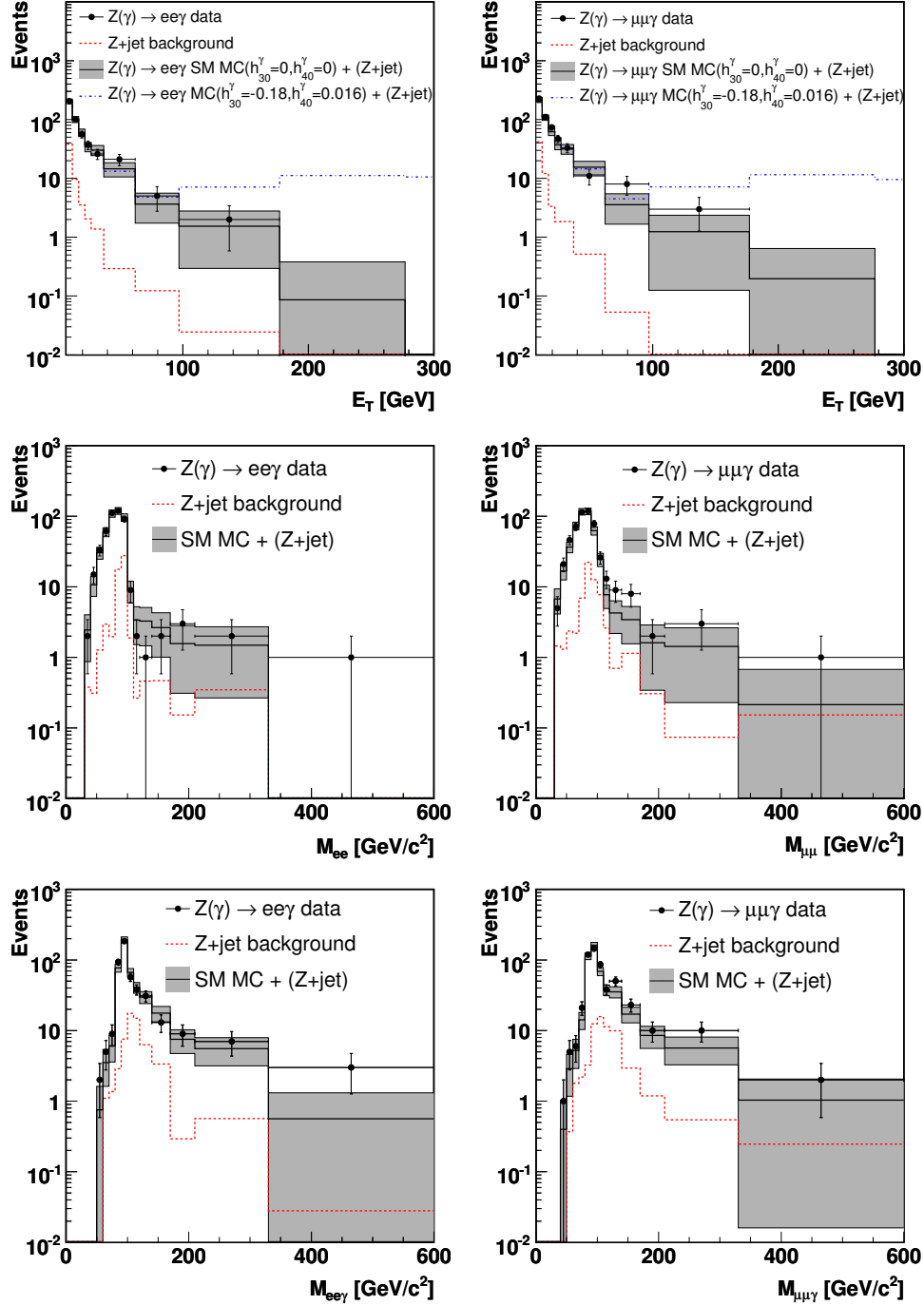


Figure 5.18: First row: photon E_T spectrum in data, Monte Carlo (two points in the grid of anomalous coupling points) and QCD background in the electron (left) and muon (right) channels. Second row: di-electron (left) and dimuon (right) mass distributions in data, MC and QCD background. Third row: di-electron and photon (left), and dimuon and photon (right) mass distributions in data, MC and QCD background. All MC distributions are normalized to the integrated luminosity.

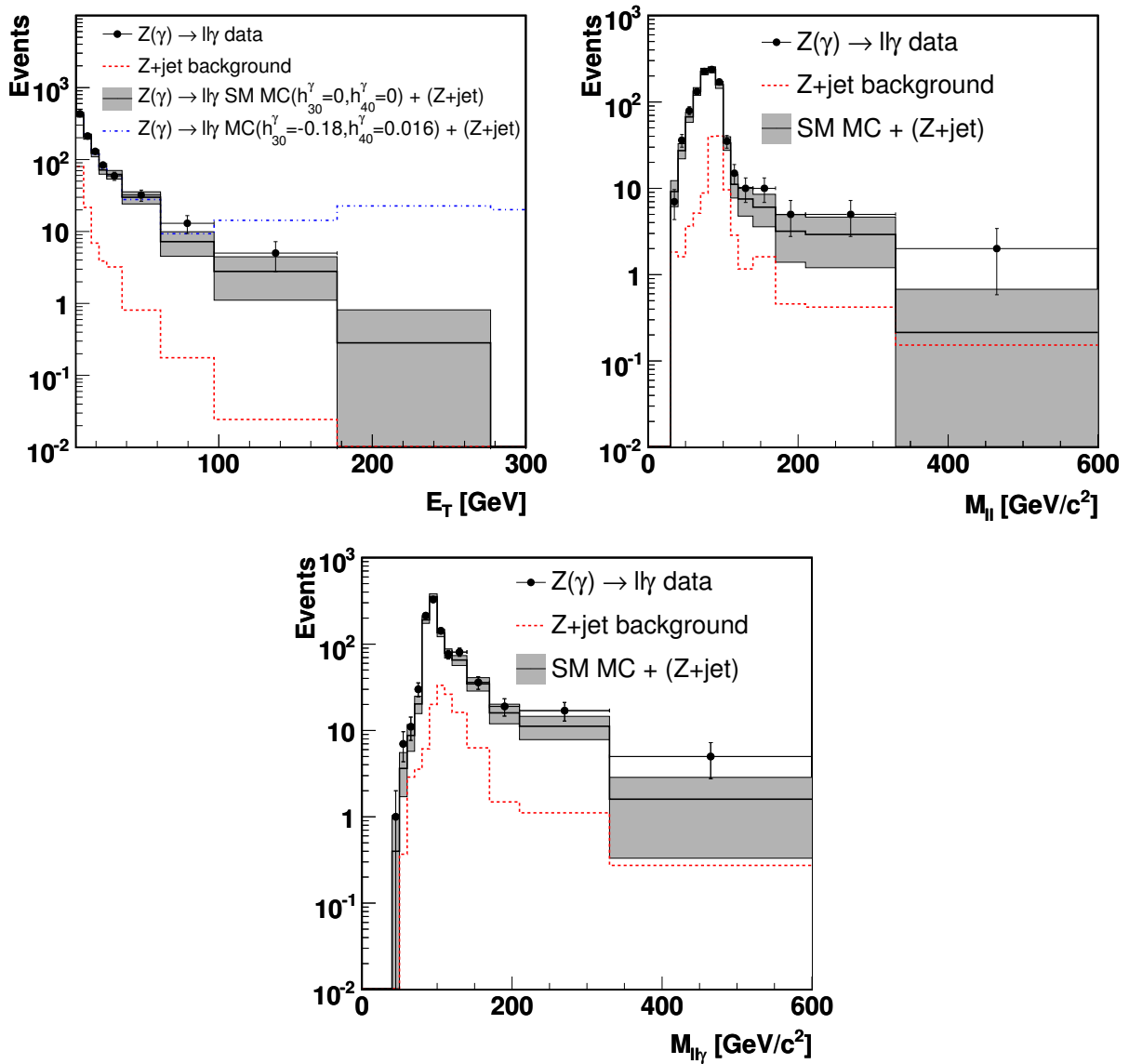


Figure 5.19: First row: photon E_T spectrum (left) and dilepton invariant mass distribution (right) in data, Monte Carlo and QCD background for the electron and muon channels combined. Second row: dilepton and photon mass distribution in data, Monte Carlo and QCD background for the electron and muon channels combined. All MC distributions are normalized to the integrated luminosity.

Table 5.11: *Summary of Run IIa triggers used in the neutrino channel.*

Trigger version	Run range	Trigger
v8 – v11	166503 – 178721	EM_HI_SH EM_MX_SH EM_HI_2EM5_SH EM_HI
v12	177311 – 194566	E1_SH30 E1_SHT20 E2_SHT20 E3_SHT20
v13	194567 – 208122	E1_SH30 E1_SHT22 E2_SHT22 E3_SHT22
v14	207217 – 215670	E1_ISH30 E1_ISHT22 E1_SH35 E1_SHT25 E3_ISH30 E3_ISHT22 E3_SH35 E3_SHT25

- CSG_CAF_EMinclusive_PASS4_p21.10.00_p20.12.02, and
- CSG_CAF_EMinclusive_PASS4_p21.10.00_p20.12.04.

An “OR” of single-EM high- E_T triggers is used for the event selection, and is summarized in Tables 5.11, 5.12.

As some of the triggers can be prescaled, depending on the trigger list and instantaneous luminosity, we make sure that we calculate the integrated luminosity for unprescaled triggers only. They are (ordered by the trigger list): EM_MX, E1_SH30, E1_SH35, E1_SHT25, and E1_SHT27. After the trigger requirements, and after applying all the standard $D\bar{O}$ data quality requirements and rejecting duplicate events and bad luminosity blocks, the integrated luminosity is 1045 ± 63 (2594 ± 158) pb^{-1} for the Run IIa (Run IIb) sample (see Table 5.13). The standard $D\bar{O}$ *lm_tools* package is used to determine the luminosity.

Table 5.12: *Summary of Run IIb triggers used in the neutrino channel.*

Trigger version	Run range	Trigger
v15 – v15.5	222865 – 230124	E1_SHT25 E1_SH35 E1_L70 E2_SHT25 E2_SH35 E2_L70 E1_ISHT22 E1_ISH30 E2_ISHT22 E2_ISH30
v15.5 – v16	230126 – 240743	E1_LH2SH27 E1_LH2L70 E1_SHT50 E1_SH60 E1_L80 E2_LH2SH27 E2_LH2L70 E2_SHT50 E2_SH60 E2_L80 E1_LH2ISH24 E2_LH2ISH24
v16	240390 – 245473	E1_SHT27 E1_LH3SH27 E1_SHT27_NOLUM E1_LH3ISH25 E2_LH3ISH25

Table 5.13: *Integrated luminosity of the data sets.*

	Delivered	Recorded	Good
Run IIa, pb ⁻¹	1310 ± 80	1200 ± 73	1045 ± 63
Run IIb, pb ⁻¹	3030 ± 185	2830 ± 173	2594 ± 158
Total, fb ⁻¹	4.34 ± 0.27	4.03 ± 0.25	3.64 ± 0.22

5.2.2 Monte Carlo samples, QCD corrections and PDF uncertainty

As in case of the $Z\gamma \rightarrow \ell\ell\gamma$ production (see Section 5.1.2), we use the LO Baur event generator [12] to generate SM and anomalous $Z\gamma \rightarrow \nu\bar{\nu}\gamma$ samples using CTEQ6L1 libraries [57, 58].

The LO photon E_T distribution is further corrected for the QCD NLO effects with the E_T -dependent K -factor (see Section 5.1.2.1). The shape and the absolute value of the K -factor strongly depend on the jet veto that we apply in the $Z\gamma \rightarrow \nu\bar{\nu}\gamma$ analysis: by rejecting events with high- p_T jets we reduce the NLO effects. As we veto events where jets with p_T above 15 GeV/ c are found, we studied how the jet energy scale (JES) affects the K -factor determination. As for the 15 GeV/ c jets the JES and resolution is 5% or roughly 1 GeV/ c [82, 83], we estimated the K -factor for the cases of 14, 15, and 16 GeV/ c jet veto. The resulting K -factor photon E_T dependence is shown in Fig. 5.20 for all cases. The uncertainty due to the K -factor fit equals 4.7% for the SM MC, and 6% for the AC MC samples for the 15 GeV/ c jet veto case. We also overlay the three K -factor fits in one plot in Fig. 5.21 to estimate the uncertainty on the K -factor due to the uncertainty on the determination of the jet transverse momenta. This uncertainty is calculated to be roughly 3%, which results in the overall uncertainty on the K -factor to be 5.5% (propagated to the uncertainty on the number of the predicted events). The PMCS (see Section 5.1.2.2) is further used to model the DØ detector response.

We use the NLO Baur generator and CTEQ6M [57, 58] 40 PDF sets to determine the uncertainty on the acceptance due to the PDF variation. Using the cross section values for all 40 samples, we calculate this uncertainty in accordance with Eq. 5.1. The systematic uncertainty due to the choice of PDF is calculated to be 5% for CTEQ6M libraries. The same for the CTEQ6.1 libraries is estimated to be 4%. The mean values of the cross sections (for the 0-th set) agree well between CTEQ6M and CTEQ6.1. We also modeled the process under study with the MCFM v5.3 event generator [56] using various CTEQ6 libraries: CTEQ6M [58], CTEQ6.1 [58], CTEQ6.5 [84], and CTEQ6.6 [85], and the deviation of the

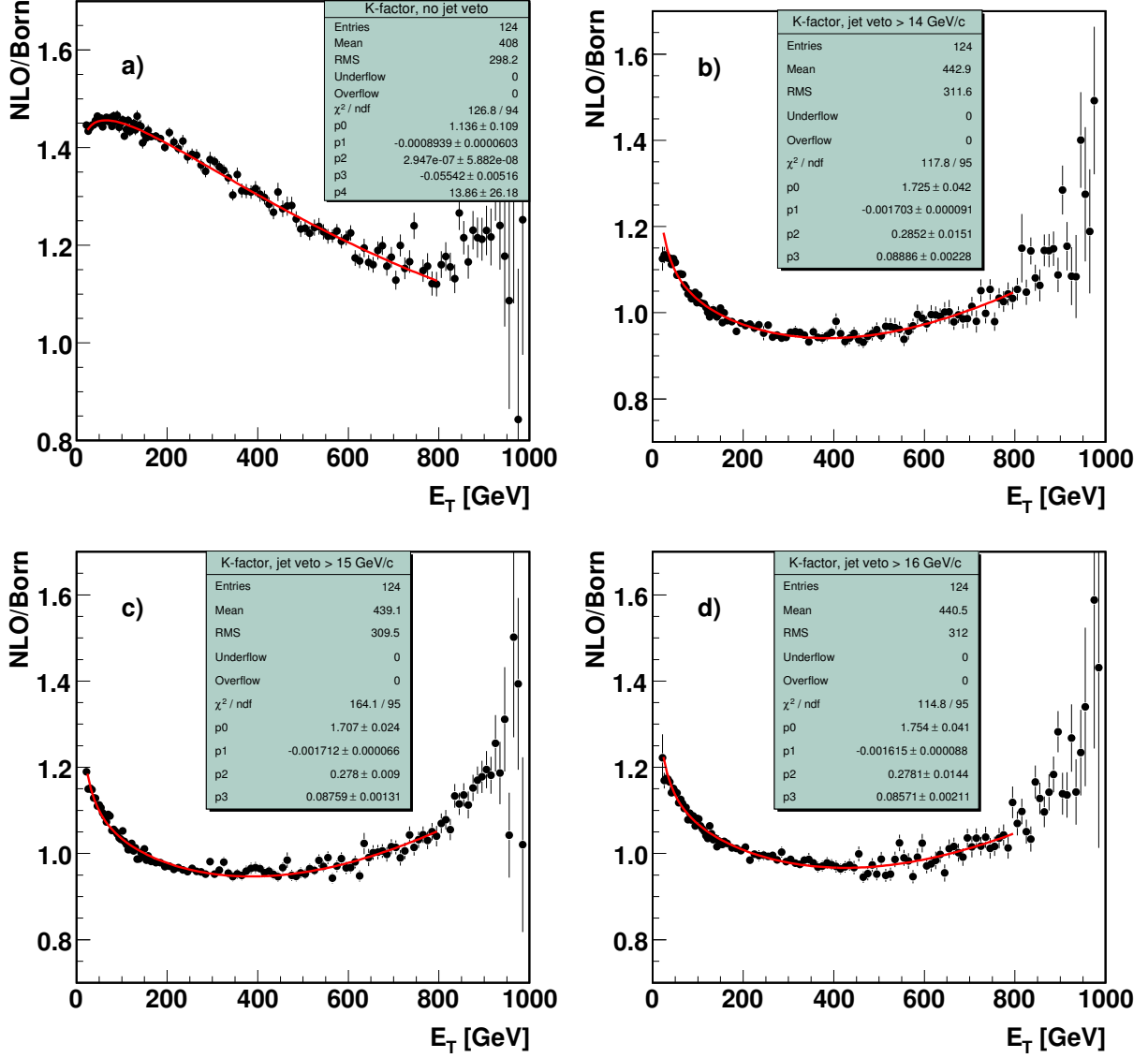


Figure 5.20: *K-factor as a function of photon E_T obtained from the NLO $Z\gamma$ Baur generator: (a) no jet veto is applied, (b) jets with $p_T > 14$ GeV/c are vetoed, (c) jets with $p_T > 15$ GeV/c are vetoed (the cut, used in this current analysis), and (d) jets with $p_T > 16$ GeV/c are vetoed.*

cross section for all four did not exceed 5%. The systematic uncertainty due to the PDF set choice for CTEQ6.1 libraries using the MCFM generator is calculated to be +8.7%/-5.5%. Based on these studies, we assign a 7% uncertainty due to the choice of the PDF libraries

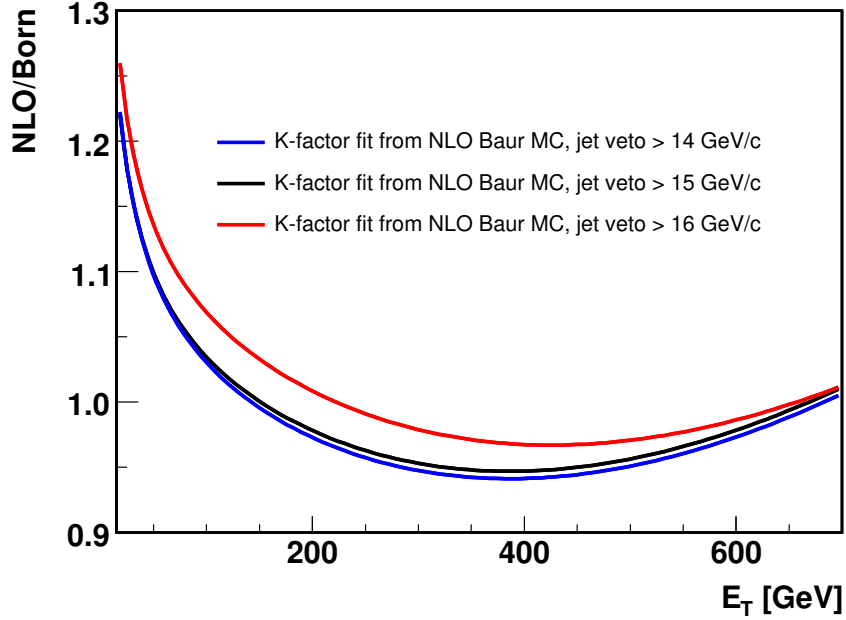


Figure 5.21: *K-factor as a function of photon E_T for various cuts on the jet transverse momentum.*

and sets in this current analysis.

5.2.3 Event selection

The $Z\gamma \rightarrow \nu\bar{\nu}\gamma$ candidate events are required to have one high- E_T photon and a significant amount of missing transverse energy, \cancel{E}_T . The event selection includes not only a photon reconstruction criteria, but also an application of a number of kinematic cuts to suppress the backgrounds to the process under study.

5.2.3.1 Photon identification

The photon candidate must be reconstructed in the central calorimeter and inside the ϕ -fiducial volume (see Section 5.1.3.3), and is required to pass the *core* photon identification criteria described in the photon certification notes [64, 67]. The photon transverse energy is required to be above 90 GeV. This threshold has been optimized (see Ref. [86, 87]).

The following requirements are used to identify photon candidates. Due to the difference

in the photon identification in Run IIa and Run IIb parts of the analysis, we quote cuts for both of them, with the Run IIb (so-called *p20*) criteria embedded in brackets.

Core (core2) cuts:

- EM cluster reconstructed with the Simple Cone Algorithm.
- The fraction of energy deposited in the EM layers: $emfrac > 0.97$ (0.95).
- The calorimeter isolation: $iso < 0.07$ ($newiso < 0.07$). The *newiso* variable is a modified calorimeter isolation variable, defined as: $\mathcal{I} = \frac{E_{tot}(0.4) - E_{EM}(0.2) - \alpha \mathcal{L}}{E_{EM}(0.2)}$. Here, \mathcal{L} is the instantaneous luminosity and $\alpha = 0.0033 \cdot 10^{-32}$ GeV cm² s. This modification has been made in Run IIb in order to improve the isolation variable at higher instantaneous luminosities.
- The square of the calorimeter's cluster $r - \phi$ width in the third layer of the EM calorimeter: $sigphi < 14$ cm² (16 cm²).
- The sum of transverse momenta of all tracks reconstructed in the annulus centered in a photon candidate's trajectory with an opening $0.05 < \Delta R < 0.4$: $IsoHC4 < 2$ GeV/ c (2 GeV/ c).

This set of cuts does not eliminate the possibility for electrons to be misreconstructed as photons. In order to suppress this background, we require a photon to have neither an associated track in the central tracker nor a significant density of hits in the SMT and CFT consistent with a track: $!(prbtrk > 0.001 \ || \ emhits_e_f_discriminant > 0.5)$ (the so-called *anti-track match*; for more details, see Ref. [40]). In addition, we require a photon candidate to be matched to a CPS cluster.

To estimate the efficiency of the photon reconstruction criteria, we use the *photon_id_tools*, as described in Section 5.1.4. The efficiency curves (obtained from the γ +jet MC samples) and data/MC scale factors (obtained from $Z \rightarrow ee$ data and MC samples), for the above

core cuts and two additional cuts are shown in Figs. 5.22–5.24. These E_T -dependent distributions are used in the acceptance calculation routine to estimate the total efficiency of the event selection criteria. The photon anti-track match efficiency measurement for the Run IIa part of the analysis is estimated from data to be 0.91 ± 0.03 , and is described in details elsewhere [88]. Since this efficiency is measured from data, there is no need to correct this value for the data/MC scale factor. The same efficiency for the Run IIb photons is estimated from the γ +jet MC to be 0.796 ± 0.022 . Due to the fact that the anti-track match requirements for photons and electrons are orthogonal, we cannot use the standard tools and $Z \rightarrow ee$ samples to estimate the anti-track match scale factor (SF_{atrk}). We first determine the anti-track match efficiency in data and MC using the $Z + \gamma$ events in data and $\gamma + jet$ MC. This efficiency is the ratio of number of events containing a Z boson (or a jet) and a photon after and before we apply the anti-track match criteria. We estimate the anti-track match efficiency to be 0.798 ± 0.035 in Run IIb data and 0.7911 ± 0.0005 in Run IIb MC, which results in the SF_{atrk} of 1 ± 0.044 . Additional information on the anti-track match efficiency can be found in Ref. [89].

5.2.3.2 EM pointing algorithm

As described in Section 3.2.6, the DØ EM calorimeter is finely segmented in both longitudinal and transverse directions. The purpose of the pointing algorithm is to calculate the origin and the direction of particles that shower in the calorimeter [90]. At each layer, each cell, that is affected by an EM shower, is given a relative weight that depends on the energy deposited in this particular cell. These weights and the coordinates of individual cells are used to calculate the energy weighted centroid $\langle x \rangle$, $\langle y \rangle$ and $\langle z \rangle$ position of the EM shower at each of the four layers of the calorimeter. The coordinates are further corrected using the correction map (obtained from studies of the trajectories of the EM particles using photon MC or $Z \rightarrow ee$ data).

The corrected 3-D coordinates of the shower at four calorimeter layers and CPS are fitted to a straight line independently in the $z - y$ and $r - \phi$ planes. Extrapolating the fit

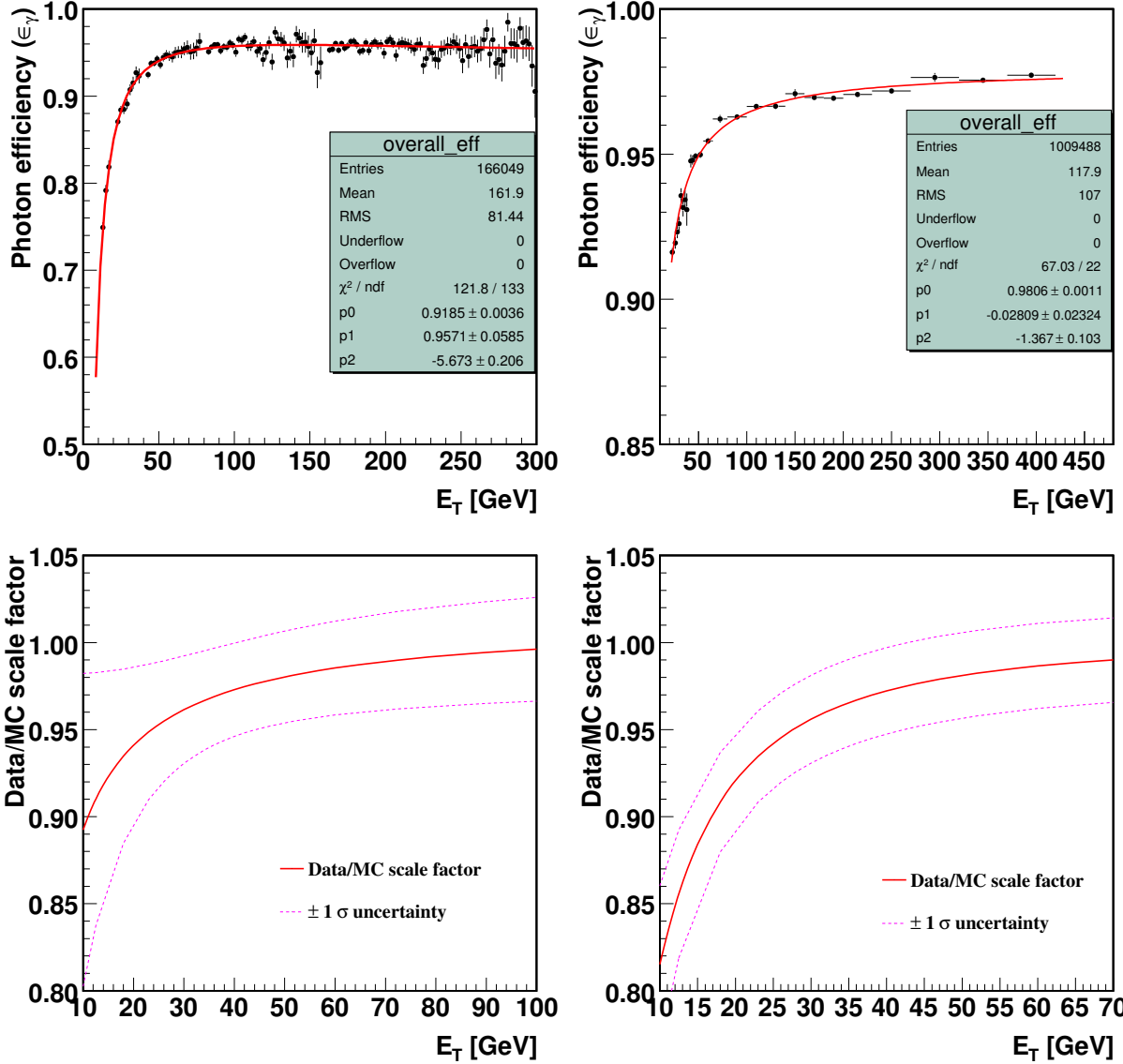


Figure 5.22: Photon core efficiency (from γ +jet MC) and scale factors for Run IIa (left) and Run IIb (right) samples. The uncertainty on the scale factors comes from the systematic uncertainties on the efficiency fits for electrons in data and MC. We also apply 1% (1.5%) additional uncertainty to the electron fits in data (MC) due to the background subtraction procedure. For more information, please see DØ Notes 4976 and 5761.

in the $z - y$ plane until it hits the beam line gives us an estimated z -position (the so-called *pointed vertex*) of the EM particle origin. And calculating the minimal distance between the fit and the beam line in the $r - \phi$ plane allows one to extract the DCA of the EM

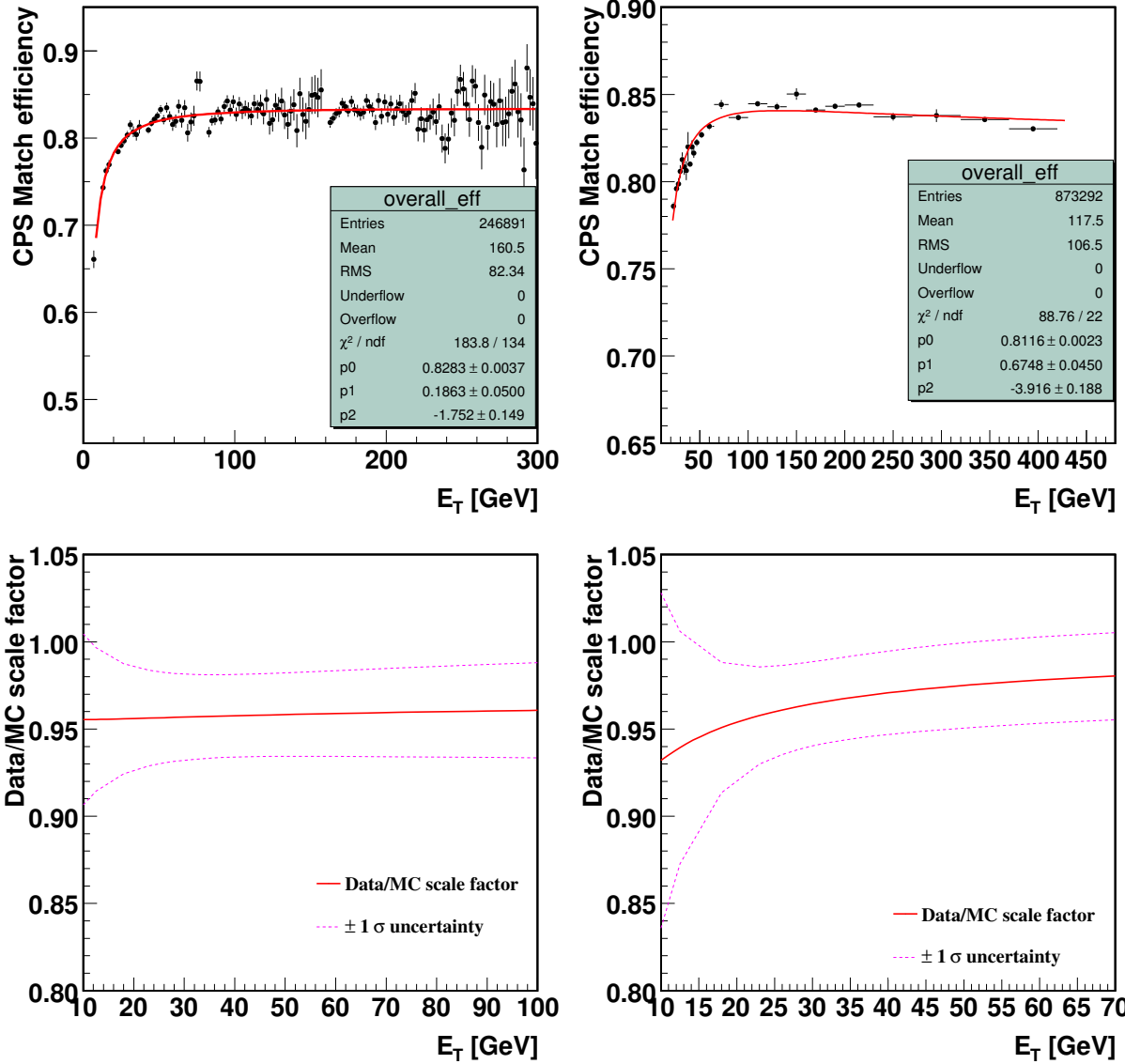


Figure 5.23: *CPS match efficiency (from γ +jet MC) and scale factors for Run IIa (left) and Run IIb (right) samples. The uncertainty on the scale factors comes from the systematic uncertainties on the efficiency fits for electrons in data and MC. We also apply 1% (1.5%) additional uncertainty to the electron fits in data (MC) due to the background subtraction procedure. For more information, please see DØ Notes 4976 and 5761.*

particle. Typical resolution of the pointing algorithm is on the order of 2–3 cm.

The EM pointing algorithm is used in this portion of the dissertation as a powerful tool that allows us to select the signal sample, estimate the backgrounds to the photons, and

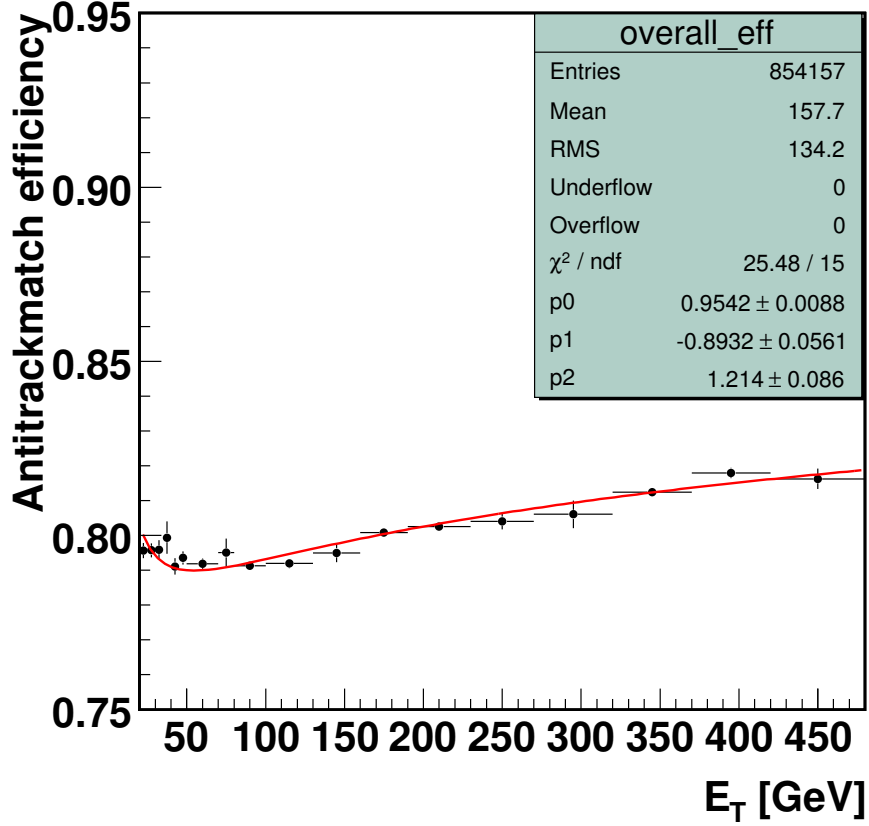


Figure 5.24: Anti-track match efficiency for Run IIb sample (from γ +jet MC).

significantly suppress the non-collision backgrounds (see Section 5.2.5).

5.2.3.3 Kinematic cuts

A cut on the missing transverse energy, $\cancel{E}_T > 70$ GeV, is applied to remove the multijet QCD background. It has been shown in Refs. [86, 91] that with the photon E_T cut released to 50 GeV, the multijet background can be approximated as:

$$N_{QCD \text{ multijet}} = \exp(7.88 - 0.12 \cdot \cancel{E}_T). \quad (5.32)$$

The cut $\cancel{E}_T > 70$ GeV, together with the requirement that there must be no jets in the event with $p_T > 15$ GeV/ c (which will be referred to as *jet veto*), ensures us that the QCD background is under control, and can be neglected. Also, the jet veto allows us to avoid

unphysically large \cancel{E}_T due to the mismeasured jets transverse momenta.

The signature of the $Z\gamma \rightarrow \nu\bar{\nu}\gamma$ process in the detector – a single photon and significant \cancel{E}_T – can be easily mimicked by various background processes (non-collision processes, electroweak backgrounds, *etc.*). In order to further reduce the backgrounds, we apply a set of requirements described below. A detailed description of the kinematic cuts can be found in Refs. [86, 87].

- We reject events that contain muon candidates of loose quality reconstructed in the muon system of the DØ detector.
- We reject events with identified cosmic muons. In addition, we impose a muon-stub veto [92]. The purpose of this cut is to remove photons produced by the cosmic muons that undergo bremsstrahlung in the detector. The hits in the A-layer of the muon system in such events are aligned with the calorimeter cluster. The algorithm extrapolates hits in the A-layer to the position of the EM cluster in the calorimeter, and calculates $|\cos(\theta)|$ between these vectors [93]. We discard an event if $|\cos(\theta)| > 0.9$ ($|\cos(\theta)| > 0.95$) in Run IIa (Run IIb) data.
- Events with any isolated tracks with $p_T > 6.5$ GeV/ c (8 GeV/ c) in Run IIa (Run IIb) data are rejected. This requirement suppresses events with charged leptons that are not reconstructed anywhere else except the central tracker. A track is called isolated if the ratio between the scalar sum of the p_T of all the tracks (that are within 2 cm from the interaction point) in the annulus $0.1 < \Delta R < 0.4$ around the track and the p_T of the track itself is less than 0.3 (0.9) in Run IIa (Run IIb) data. If a track is within $\Delta R < 0.3$ from the photon candidate, the veto is not applied.
- We require at least one primary vertex in the event to be within 10 cm from the photon vertex estimated by the pointing algorithm (see Section 5.2.3.2) in the z direction ($\Delta Z_{min} < 10$ cm cut). If there are more than one primary vertex in the event, we loop over all vertices and pick the one that is closest to the pointed photon vertex.

- We require the minimum energy fraction deposited by the photon candidate in the third layer of the EM calorimeter to exceed 10%. This requirement is based on the geometry of the detector, since the EM showers from the EM objects that originate from the interaction point have a maximum in the third layer (see Section 3.2.6). Non-collision EM objects are more likely to deposit most of their energy in the first EM layer.
- We require the $HMx7$ variable associated with the photon candidate not to exceed 30 (35) in Run IIa (Run IIb) data.
- The distance of the closest approach (DCA) of the photon candidate is required to be less than 4 cm. As seen from Fig. 5.26, most of the signal-like candidates have $DCA < 4$ cm, while non-collision photon candidates are less likely to be produced near the beam line.
- We reject events with additional EM objects identified in the calorimeter that have $E_T > 15$ GeV in Run IIb data set.

As we impose the jet veto, the \cancel{E}_T must be balanced with the photon E_T . Thus, the $\cancel{E}_T > 70$ GeV requirement is fully efficient for photon $E_T > 90$ GeV cut in both Run IIa and Run IIb. The efficiency of the kinematic requirements is estimated using isolated electron candidates from the $W \rightarrow e\nu$ data sample. We estimate the efficiency variation due to selection criteria to be $\approx 3\%$. Therefore, we assign a systematic uncertainty due to estimation of the kinematic efficiency from $W \rightarrow e\nu$ sample to be 3%. The kinematic cuts efficiencies are summarized in Table 5.14.

Table 5.14: Summary of efficiencies of the kinematic cuts.

Requirement	Run IIa	Run IIb
μ veto	0.934 ± 0.003	0.918 ± 0.003
Cosmics+ μ -stub	0.909 ± 0.004	0.839 ± 0.004
Isolated high p_T tracks	0.865 ± 0.004	0.828 ± 0.004
ΔZ_{min}	0.942 ± 0.003	0.928 ± 0.003
EM3 fraction	1 ± 0.001	0.992 ± 0.001
$HMx7$	0.994 ± 0.001	0.995 ± 0.001
DCA	0.968 ± 0.003	0.966 ± 0.002
High E_T EM	–	0.935 ± 0.003
$\#_T$	1 ± 0.001	1 ± 0.001
Total	$0.666 \pm 0.005(\text{stat.}) \pm 0.03(\text{syst.})$	$0.528 \pm 0.005(\text{stat.}) \pm 0.03(\text{syst.})$

Table 5.15: *Summary of efficiencies for the neutrino channel.*

Requirement	Run IIa	Run IIb
Acceptance	0.638 ± 0.045	0.638 ± 0.045
Trigger	0.99 ± 0.01	0.99 ± 0.01
Photon preselection efficiency	0.99 ± 0.005	0.99 ± 0.005
Photon core efficiency	0.958 ± 0.007	0.966 ± 0.003
Photon core scale factor	0.999 ± 0.025	0.997 ± 0.025
CPS match efficiency	0.831 ± 0.005	0.840 ± 0.011
CPS match scale factor	0.961 ± 0.025	1.013 ± 0.025
Antitrack match efficiency	0.91 ± 0.03	0.796 ± 0.022
Antitrack match scale factor	—	1 ± 0.044
Kinematic cuts efficiency	0.666 ± 0.030	0.528 ± 0.030
Total photon efficiency	0.688 ± 0.034	0.646 ± 0.041
Total efficiency, $\epsilon_{Z\gamma \rightarrow \nu\bar{\nu}\gamma}$	0.290 ± 0.028	0.216 ± 0.024

Events that pass the requirements described in Sections 5.2.3.1, 5.2.3.3 form the so-called *final photon sample* (we will use this definition in Section 5.2.5). After applying all the selection criteria we observe 27 (24) candidate events in Run IIa (Run IIb) data.

The most typical $Z\gamma \rightarrow \nu\bar{\nu}\gamma$ event is shown in Fig. 5.25.

5.2.4 Summary of the $Z\gamma \rightarrow \nu\bar{\nu}\gamma$ efficiency studies

The total $Z\gamma \rightarrow \nu\bar{\nu}\gamma$ reconstruction efficiency is a product of the following terms: fiducial and kinematic acceptance, trigger efficiency, photon reconstruction efficiency and kinematic cuts efficiency. The efficiency of each term, averaged over the whole E_T range, is estimated using the PMCS output described in Section 5.1.2.2, separately for Run IIa and Run IIb samples due to different selection criteria.

Using the E_T -dependent efficiency distributions described in Section 5.2.3.1, the efficiency values of the kinematic cuts (see Section 5.2.3.3) and the trigger efficiency as input parameters to the signal PMCS MC, we estimate the total efficiency of the event selection criteria. Table 5.15 summarizes the results of acceptance and efficiency studies. The total uncertainty on the acceptance includes the PDF uncertainty ($\approx 7\%$).

Using the total efficiency numbers from Table 5.15, we estimate the SM prediction of the

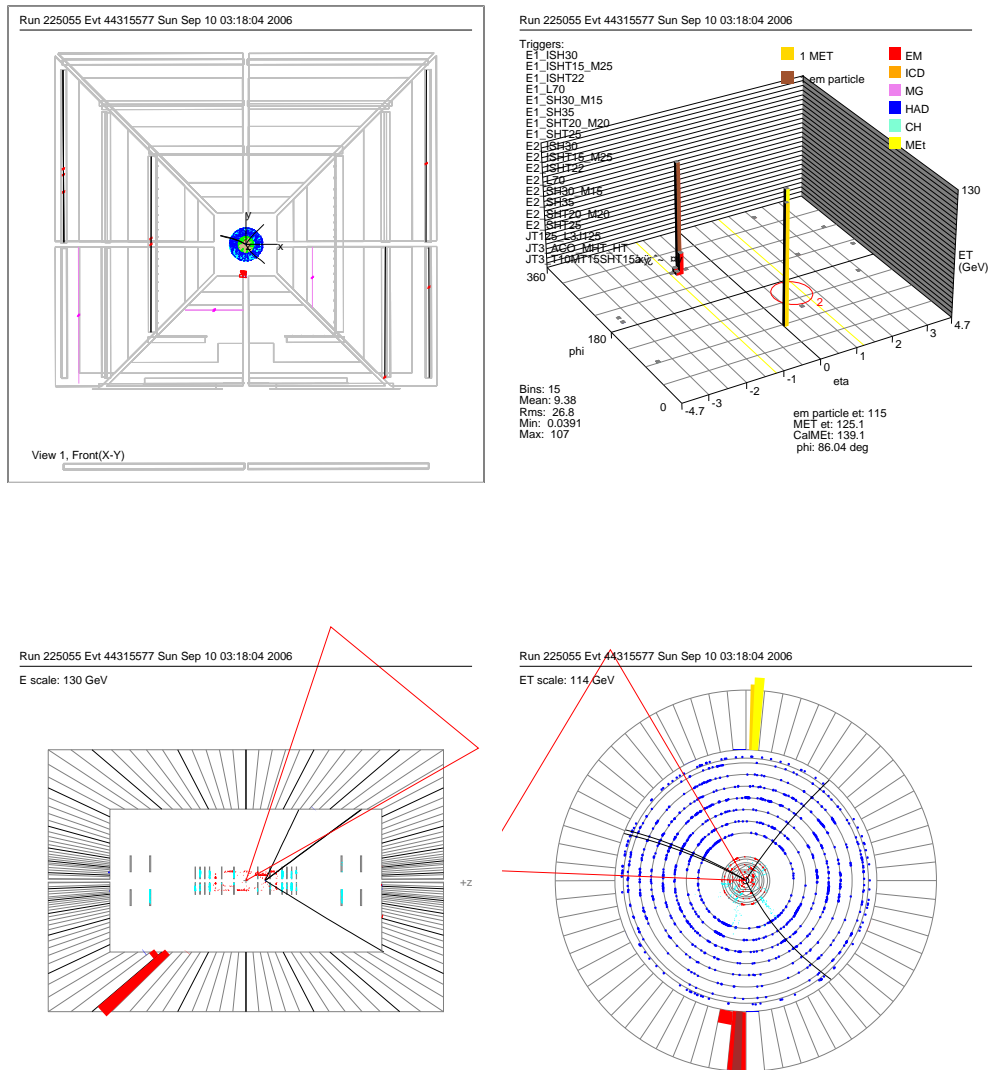


Figure 5.25: Event display of a $Z\gamma \rightarrow \nu\bar{\nu}\gamma$ event. Upper row: (left) as seen from the front in the $x-y$ plane, muon spectrometer layers are shown; (right) calorimeter lego plot. Lower row: (left) side view ($z-y$ plane), very little activity in the tracker and calorimeter is seen; (right) $r-\phi$ view with hits in the tracker, four reconstructed tracks, one EM shower in the calorimeter, and \cancel{E}_T balancing this energy deposit.

number of signal events to be 11.8 ± 1.5 and 21.9 ± 3.0 for Run IIa and Run IIb, respectively. The PDF uncertainty and the uncertainty due to the K -factor estimation are taken into account.

5.2.5 Backgrounds

The backgrounds to the $Z\gamma \rightarrow \nu\bar{\nu}\gamma$ process are processes, that produce large \cancel{E}_T accompanied by a real photon or an object misidentified as a photon. These processes are:

- $W/Z + \text{jet}$ – a jet is misidentified as a photon.
- Non-collision – muons from beam halo or cosmic rays produce photons through bremsstrahlung.
- $W \rightarrow e\nu$ – an electron is misidentified as a photon.
- $W + \gamma$ – a lepton is not reconstructed.

The first two backgrounds are estimated from data using the EM pointing (see Section 5.2.3.2) DCA distributions (the so-called *DCA templates method*). Three DCA templates are constructed: signal-like (e/γ), non-collision, and misidentified jets template. As the definition of the DCA is the shortest distance from the beam line to the direction of an object in the $r - \phi$ plane, it is natural to expect the DCA distribution of real photons produced in the collision to be rather narrow, while that of the misidentified jets is expected to be wider due to a wider shower in the calorimeter. Finally, photons from non-collision events are even less likely to be produced near the beam line, which results in a very wide DCA distribution. All three templates are obtained strictly from data samples. The e/γ DCA template is obtained from a sample of isolated electrons. The misidentified jets template is obtained from a fake photon sample that passes all the criteria described in Section 5.2.3, modulo inverted track isolation requirement. The non-collision template is obtained from a sample of photons found in events with no primary vertex, or with less than three tracks per event, or with identified cosmic muons. All three DCA templates are shown in Fig. 5.26

as inserts. It is worth mentioning that the shapes of the templates are identical in Run IIa and Run IIb data.

The first step is to estimate the number of the misidentified jets background. This is done using an EM + jet data sample, where an EM object passes all the photon identification criteria except the track isolation criteria. Number of events that fail the track isolation in that sample is denoted as N_1 . The DCA of the rest of the events in that sample is then fitted to a linear sum of the e/γ and misidentified jets DCA templates. N_2 is then the number of the misidentified jets that fulfill the track isolation requirement. Finally, the number of the misidentified jets background in the final photon sample (see Section 5.2.3.3) is the number of events in the fake photon sample times N_2/N_1 . Finally, the DCA distribution of the final photon sample is fitted to a linear sum of all three DCA templates (with the fixed misidentified jets contribution). Thus, we estimate the number of the non-collision background events. The result of the fit is presented in Fig. 5.26. After the fit is performed, the DCA < 4 cm cut is applied since most of the signal is concentrated in this region. An extra 0.5 events systematic uncertainty is applied due to the uncertainty in the shape of the e/γ templates.

The $W \rightarrow e\nu$ background is estimated from a sample of isolated electrons, where electrons pass the photon identification criteria (except for the anti-track match requirement), described in Section 5.2.3.1. The resulting number of events is then corrected for the track match inefficiency, and the efficiency of the kinematic cuts.

The $W + \gamma$ background is estimated from $W + \text{jets}$ ($W + \gamma$) PYTHIA MC for Run IIa (Run IIb). The requirements, described in Section 5.2.3, are applied to the MC samples to estimate the acceptance of the selection criteria. Then, the data to MC scale factors are applied to correct for the differences in efficiencies between data and MC. The final acceptance numbers are then multiplied by the process cross section values, obtained from the generator, and the luminosity of the corresponding data sample.

Table 5.16 summarizes the background sources to the $Z\gamma \rightarrow \nu\bar{\nu}\gamma$ process. As it has been stated before, the multijet QCD background is negligible for the set of cuts used in this analysis (see Section 5.2.3.3).

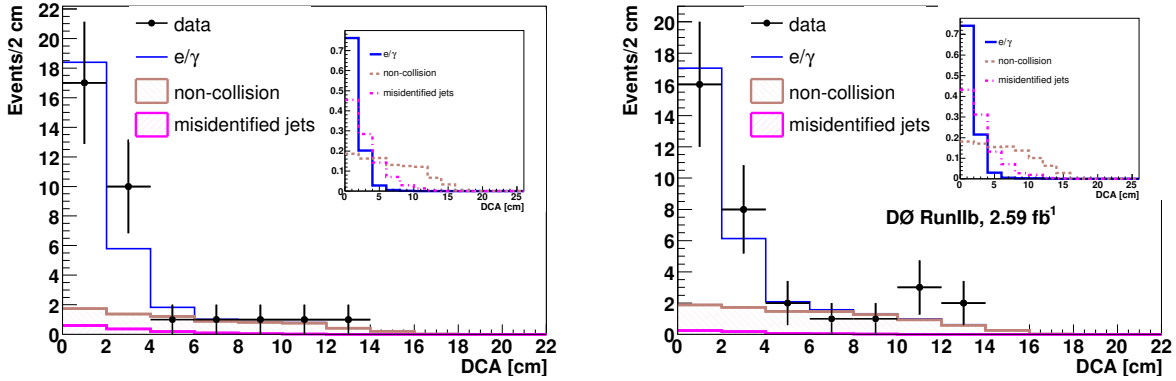


Figure 5.26: The e/γ , non-collision and misidentified jets DCA distributions (inserts). The fit of the linear sum of the three DCA templates to the DCA distribution in the final photon sample (main plots). Left - Run IIa, right - Run IIb.

Table 5.16: *Summary of backgrounds.*

Background	Run IIa	Run IIb
$W \rightarrow e\nu$	$3.466 \pm 0.194(\text{stat.}) \pm 0.236(\text{syst.})$	$6.197 \pm 0.233(\text{stat.}) \pm 0.423(\text{syst.})$
$W/Z + \text{jet}$	$0.964 \pm 0.186(\text{stat.}) \pm 0.901(\text{syst.})$	$0.409 \pm 0.183(\text{stat.}) \pm 0.100(\text{syst.})$
non-collision	$2.141 \pm 0.227(\text{stat.}) \pm 1.257(\text{syst.})$	$3.191 \pm 0.319(\text{stat.}) \pm 1.440(\text{syst.})$
$W + \gamma$	$0.331 \pm 0.029(\text{stat.}) \pm 0.072(\text{syst.})$	$0.571 \pm 0.062(\text{stat.}) \pm 0.103(\text{syst.})$
Total background	$6.902 \pm 0.353(\text{stat.}) \pm 1.644(\text{syst.})$	$10.368 \pm 0.440(\text{stat.}) \pm 1.588(\text{syst.})$

Table 5.17: Summary of the components for the $Z\gamma \rightarrow \nu\bar{\nu}\gamma$ production cross section calculation.

Parameter	Run IIa	Run IIb
N_{cand}	27 ± 5.2	24 ± 4.9
N_{bkg}	$6.902 \pm 0.353(\text{stat.}) \pm 1.644(\text{syst.})$	$10.368 \pm 0.440(\text{stat.}) \pm 1.588(\text{syst.})$
$\epsilon_{\nu\bar{\nu}\gamma}$	0.290 ± 0.028	0.216 ± 0.024
$\int \mathcal{L} dt, \text{ pb}^{-1}$	1045 ± 63	2594 ± 158

5.2.6 Cross section calculation

The cross section for $Z\gamma$ production times the branching fraction for the $Z \rightarrow \nu\bar{\nu}$ is calculated using Eq. 5.25 (see Section 5.1.8). We summarize the values of the parameters of this equation in Table 5.17 for both Run IIa and Run IIb data. The cross section for the process $Z\gamma \rightarrow \nu\bar{\nu}\gamma$ in the Run IIa data set is measured to be:

$$\sigma \cdot \mathcal{B}(Z \rightarrow \nu\bar{\nu}) = 0.067 \pm 0.017(\text{stat.}) \pm 0.009(\text{syst.}) \pm 0.004(\text{lumi.}) \text{ pb.} \quad (5.33)$$

The same for the Run IIb data set is:

$$\sigma \cdot \mathcal{B}(Z \rightarrow \nu\bar{\nu}) = 0.024 \pm 0.009(\text{stat.}) \pm 0.004(\text{syst.}) \pm 0.002(\text{lumi.}) \text{ pb.} \quad (5.34)$$

The two measurements are combined together using the BLUE technique (see Section 5.1.8). We treat the acceptance uncertainty (including the uncertainty due to the PDF choice), the trigger uncertainties, and the systematic uncertainty on the $W\gamma$ background (as it is estimated from Monte Carlo) as fully correlated between the two data sets, while all other uncertainties are treated as uncorrelated (see Table 5.18).

The error matrix associated with these measurements is given below:

$$V = \begin{pmatrix} 3.7 \cdot 10^{-5} & 8.5 \cdot 10^{-6} \\ 8.5 \cdot 10^{-6} & 9.3 \cdot 10^{-5} \end{pmatrix} \quad (5.35)$$

The combined cross section is measured to be:

$$\sigma \cdot \mathcal{B}(Z \rightarrow \nu\bar{\nu})(\text{data}) = 0.032 \pm 0.009(\text{stat.} + \text{syst.}) \pm 0.002(\text{lumi.}) \text{ pb.} \quad (5.36)$$

Table 5.18: Summary of the uncertainties of the $Z\gamma \rightarrow \nu\bar{\nu}\gamma$ cross section for the Run IIa and Run IIb data sets.

Quantity	Run IIa, pb	Run IIb, pb	correlation
ϵ_γ	0.0033	0.0016	0
Acceptance	0.0047	0.0017	100%
Trigger efficiency	0.0007	0.0003	100%
Kinematic cuts (stat)	0.0006	0.0002	0
Kinematic cuts (syst)	0.0030	0.0014	0
Background (stat)	0.0012	0.0008	0
Total background (syst)	0.0054	0.0028	0
(correlated background syst)	0.0002	0.0002	100%
Number of events	0.0172	0.0088	0
Total systematic uncertainty	0.0085	0.0039	
Total statistical uncertainty	0.0173	0.0088	
Total uncertainty	0.0192	0.0096	

The NLO theoretical prediction of the $Z\gamma \rightarrow \nu\bar{\nu}\gamma$ cross section for the photon $E_T > 90$ GeV is estimated to be:

$$\sigma \cdot \mathcal{B}(Z \rightarrow \nu\bar{\nu})(theory) = 0.039 \pm 0.004 \text{ pb.} \quad (5.37)$$

The uncertainty on the SM cross section includes 5.5% combined uncertainty due to the K -factor determination uncertainty and 7% PDF uncertainty. The measured combined cross section agrees well within errors with the SM prediction.

5.2.7 Observed distributions

The photon candidate E_T spectra in data with overlaid backgrounds and MC prediction are shown in Figs. 5.27, 5.28 for individual Run IIa and Run IIb, and combined data sets. A comparison between the observed z vertex, \cancel{E}_T , $phimod$, η and ϕ distributions in data with the same distributions obtained from MC samples is shown in Figs. 5.29, 5.30. The MC distributions are normalized to the number of events predicted by the SM for individual data sets. We observe no significant deviation of the data from the SM predictions, hence, we can set limits on the size of the couplings between a Z boson and a photon in the neutrino channel (see Chapter 6).

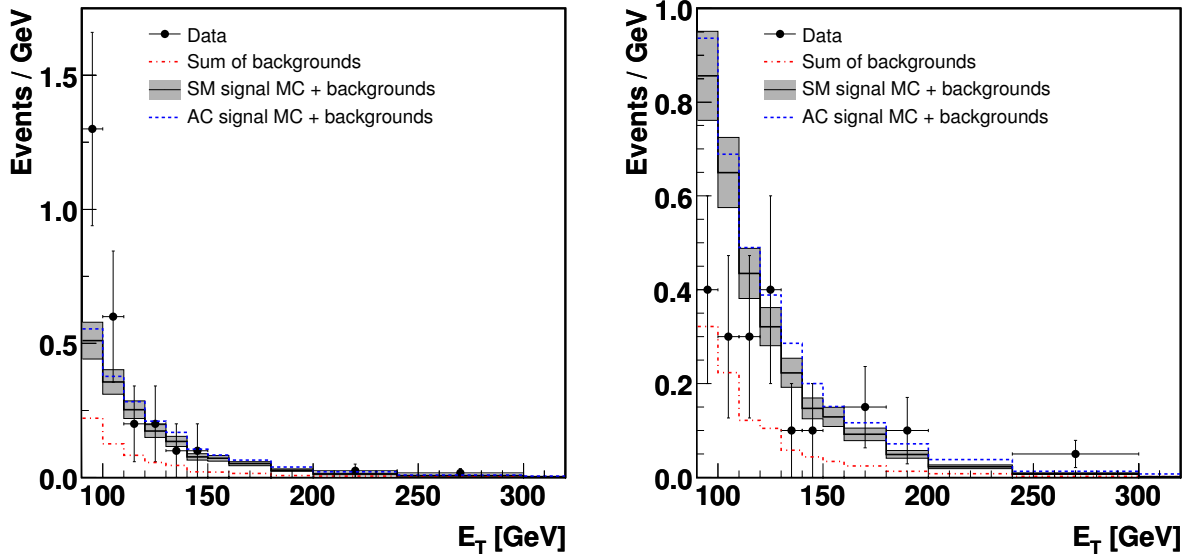


Figure 5.27: Photon E_T spectrum in Run IIa (left) and Run IIb (right) data, Monte Carlo (two points in the grid of anomalous coupling points) and sum of backgrounds. MC distributions are normalized to the integrated luminosity. The shaded band represents the 1 standard deviation (s.d.) systematic and statistical uncertainty on the Monte Carlo signal plus background. Last bin is the overflow bin.

5.2.8 Statistical significance of the measurements

To estimate the significance of the combined cross section measurement in the neutrino channel we run 10^8 pseudo-experiments of a background-only hypothesis, *i.e.* we calculate the probability of the estimated background fluctuating to the number of the observed events. This is done in four steps:

- We throw a random number using an estimated number of background events (N_{bkg}) with an estimated uncertainty (δN_{bkg}) using Gaussian statistics, and obtain $newN_{bkg}$ for Run IIa and Run IIb separately.
- Then for each value of $newN_{bkg}$, we obtain an observed number of events (N_{obs}) that came just from the background using Poisson statistics. The $newN_{bkg}$ and N_{obs} distributions are shown in Fig. 5.31.

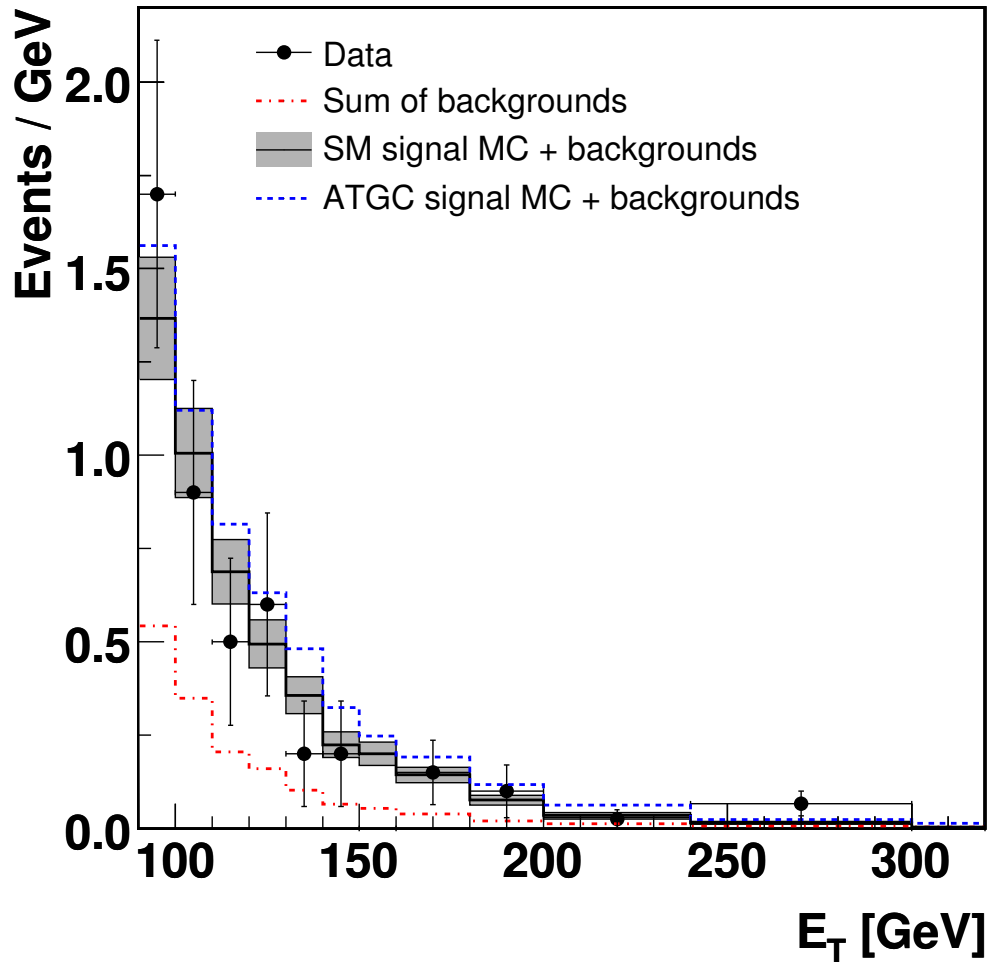


Figure 5.28: Photon E_T spectrum in combined Run IIa and Run IIb data, Monte Carlo (two points in the grid of anomalous coupling points) and sum of backgrounds. MC distributions are normalized to the integrated luminosity. The shaded band represents the 1 s.d. systematic and statistical uncertainty on the Monte Carlo signal plus background. Last bin is the overflow bin.

- Then for this new N_{obs} and estimated N_{bkg} for Run IIa and Run IIb, we use the BLUE technique to produce a cross section, measured in a background-only hypothesis. This cross section distribution is shown in Fig. 5.31 for all 100,000,000 pseudo-experiments.
- The last step is to count the number of pseudo-experiment outcomes with the cross section below the measured combined Run IIa and Run IIb cross section (represented

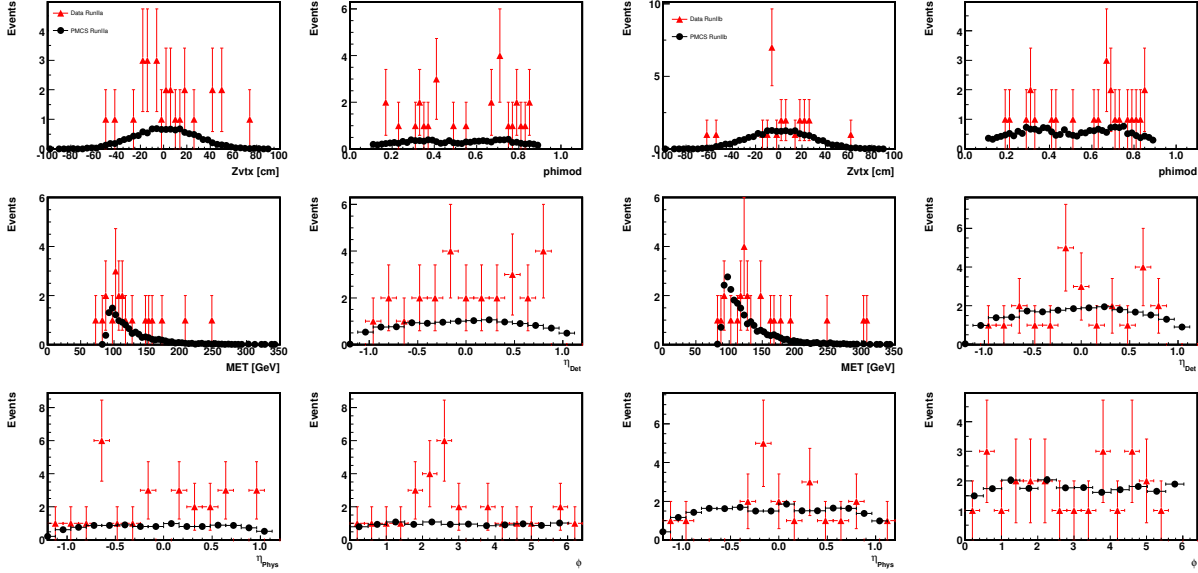


Figure 5.29: Photon z vertex, \cancel{E}_T , phimod , η and ϕ distributions in Run IIa and Run IIb data and PMCS output (without the background component overlaid).

by the vertical red line in Fig. 5.31).

The probability of the background to fluctuate into the number of events that we observe (expect from the SM) is calculated to be 3.1×10^{-7} (0.0). This corresponds to an observed (expected) significance of 5.12 standard deviations (s.d.) (8.38 s.d.), which allows us to claim the first observation of the $Z\gamma \rightarrow \nu\bar{\nu}\gamma$ production at the Tevatron.

Using the same procedure, we test the individual Run IIa and Run IIb cross section measurements for the consistency with the signal-plus-background hypothesis. The number of signal events is the number of the SM predicted events, quoted in Section 5.2.4. The $newN_{bkg}$, $newN_{sig}$ and N_{obs} distributions for Run IIa (Run IIb) are shown in Fig. 5.32 (Fig. 5.33). Since we overmeasure (undermeasure) the cross section in Run IIa (Run IIb) data compared to the SM prediction, we need to estimate the percentage of the pseudo-experiment outcomes with the cross section below (above) the ones, measured in data. We have 942,289 (146,776) out of one million entries in the histograms with the values below 0.067 pb (0.024 pb), respectively. Statistically this corresponds to 1.90 s.d. and 0.19 s.d.

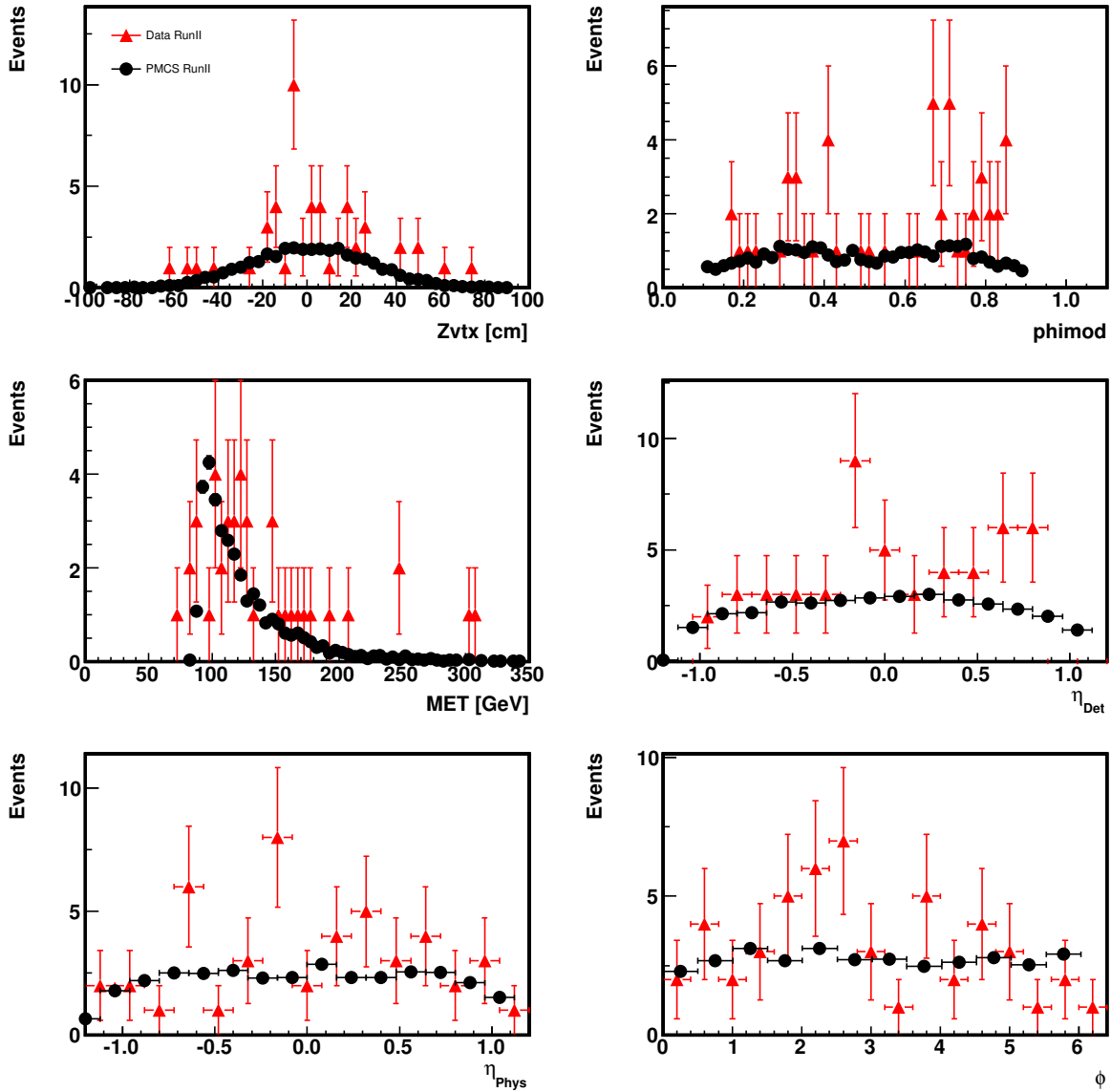


Figure 5.30: Photon z vertex, E_T , phimod , η and ϕ distributions in combined Run IIa and Run IIb data and PMCS output (without the background component overlaid).

for Run IIa and Run IIb. This proves that the observed events in the individual Run IIa and Run IIb data sets are consistent with the signal-plus-background hypothesis with less than 2 s.d. statistical significance.

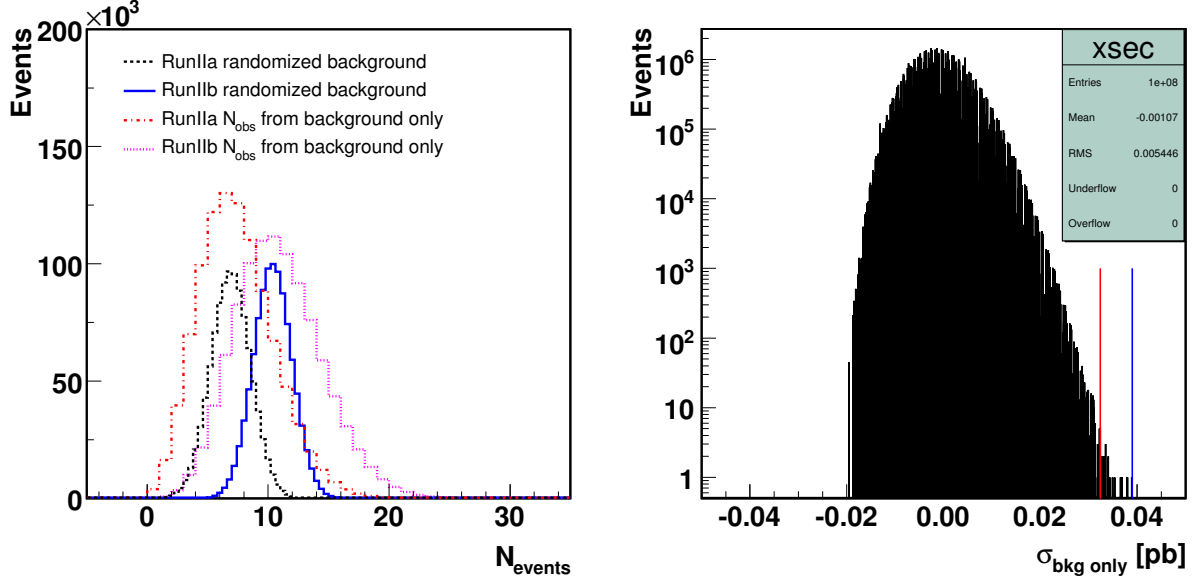


Figure 5.31: Distribution of number of background events, $newN_{bkg}$, and number of observed events, N_{obs} , (example, only 1M entries) for the background-only hypothesis (left) for all pseudo-experiments, and the combined cross section distribution for the background-only hypothesis (right). The red (blue) line represents the combined cross section measured in data (expected from theory).

5.3 Number of neutrino generations measurement

Measurement of the $Z\gamma$ cross section in the neutrino and electron plus muon channels allows one to estimate an important parameter of the SM, the number of neutrino generations (N_ν). The cross sections in these two channels are related according to the formula:

$$\frac{\Gamma_\nu}{\Gamma_\ell} = \frac{\sigma \cdot \mathcal{B}(Z \rightarrow \nu\bar{\nu})}{\sigma \cdot \mathcal{B}(Z \rightarrow \ell\bar{\ell})}, \quad (5.38)$$

where Γ_ν and $\Gamma_\ell = 83.984 \pm 0.086$ MeV [8] are the partial widths of the Z boson in the neutrino and electron plus muon decay channels, respectively. Then the number of neutrino generations is:

$$N_\nu = \frac{\Gamma_{invisible}}{\Gamma_\nu}, \quad (5.39)$$

where $\Gamma_{invisible} = 499.0 \pm 1.5$ MeV [8] is the partial width of the Z boson in the undetectable decay channel (sum of all neutrino families).

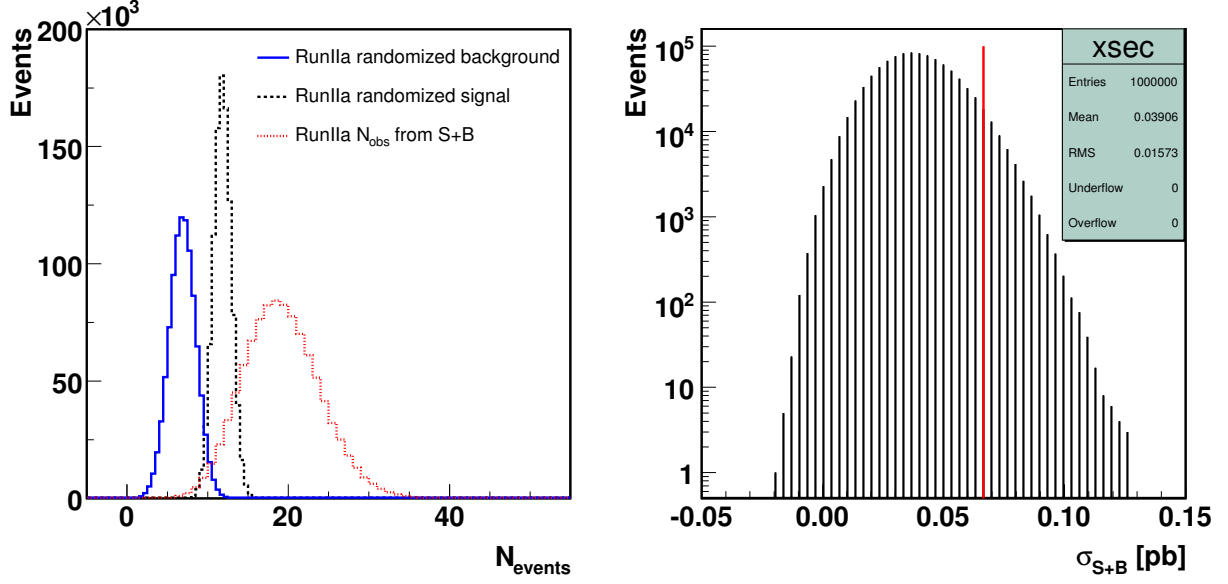


Figure 5.32: Distribution of number of Run IIa background events, $newN_{bkg}$, number of signal events, $newN_{sig}$, and number of observed events, N_{obs} , for the signal-plus-background hypothesis (left) for all pseudo-experiments, and the combined cross section distribution for the signal-plus-background hypothesis (right). The red line represents the Run IIa cross section measured in data.

The $\sigma \cdot \mathcal{B}(Z \rightarrow \nu\bar{\nu})$ is measured to be $0.032 \pm 0.009(\text{stat.} + \text{syst.}) \pm 0.002(\text{lumi.})$ pb (see Section 5.2.6) for the photon $E_T > 90$ GeV.

To measure the $\sigma \cdot \mathcal{B}(Z \rightarrow \ell\ell)$, we use the results of Sections 5.1.1–5.1.8 and simply tighten the photon E_T cut to 90 GeV. The number of the observed candidate events, the number of estimated background events in the electron plus muon channel, and the total efficiencies numbers are summarized in Table 5.19.

Using the BLUE method, we estimate the combined cross section in the electron and muon channels to be $0.016 \pm 0.007(\text{stat.} + \text{syst.}) \pm 0.001(\text{lumi.})$ pb. Further, we plug the measured cross section values in both neutrino and electron plus muon channels into Eq. 5.38–5.39. We calculate the partial width of the Z boson in the neutrino channel to be $\Gamma_\nu = 168.0 \pm 87.4$ MeV, and, hence, the number of neutrino generations to be $N_\nu = 3.0 \pm 1.6$. This measurement is in agreement with the LEP measurement of $N_\nu^{LEP} = 2.984 \pm 0.008$ [8].

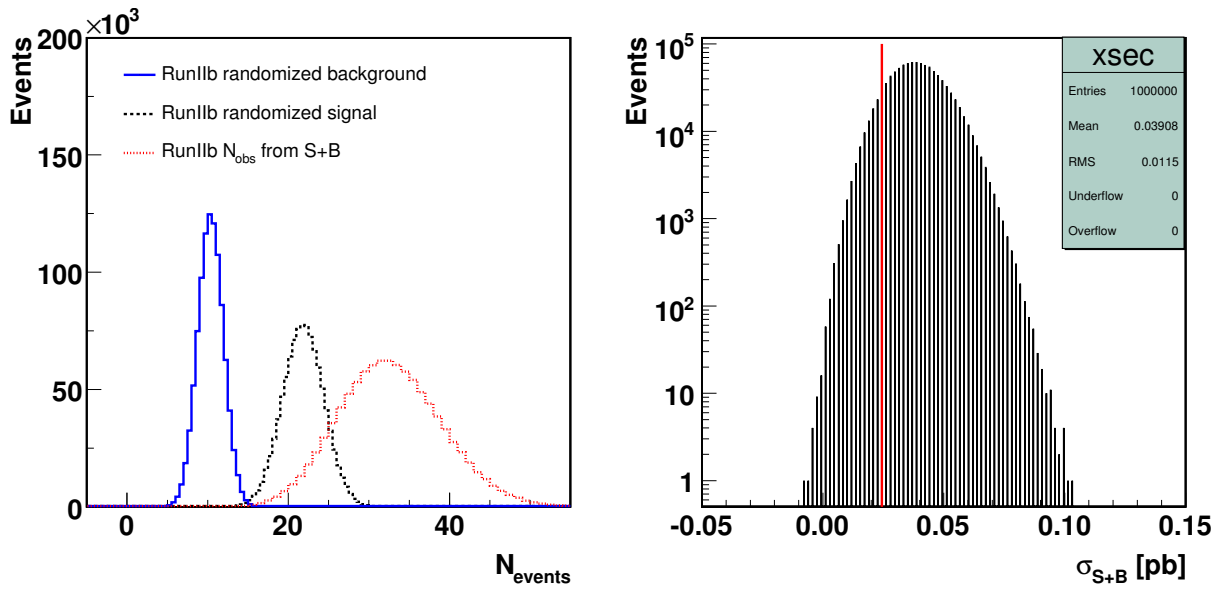


Figure 5.33: Distribution of number of Run IIb background events, $newN_{bkg}$, number of signal events, $newN_{sig}$, and number of observed events, N_{obs} , for the signal-plus-background hypothesis (left) for all 1M pseudo-experiments, and the combined cross section distribution for the signal-plus-background hypothesis (right). The red line represents the Run IIb cross section measured in data.

Table 5.19: Summary of the components to the calculation of the cross section for $Z\gamma \rightarrow \ell\ell\gamma$ decay for the photon $E_T > 90$ GeV.

Parameter	Electron channel, CC-CC topology	Electron channel, CC-EC topology	Muon channel
N^{cand}	3.0 ± 1.7	1.0 ± 1.0	3.0 ± 1.7
N^{bkg}	$0.045 \pm 0.031(\text{stat.}) \pm 0.010(\text{syst.})$	$0.018 \pm 0.018(\text{stat.}) \pm 0.004(\text{syst.})$	$0.040 \pm 0.030(\text{stat.}) \pm 0.010(\text{syst.})$
$\epsilon_{Z\gamma \rightarrow \ell\ell\gamma}$	0.144 ± 0.029	0.056 ± 0.018	0.198 ± 0.011
$\int \mathcal{L} dt$	$1109 \pm 67 \text{ pb}^{-1}$	$1109 \pm 67 \text{ pb}^{-1}$	$1009 \pm 62 \text{ pb}^{-1}$

Chapter 6

Setting Limits on Anomalous Trilinear Gauge Boson Couplings

Limits on anomalous $ZZ\gamma$ and $Z\gamma\gamma$ couplings are set by comparing the observed photon E_T spectrum from data with the E_T spectrum of the estimated background and the signal (see Sections 5.1.2, 5.2.2). We employ the binned likelihood method [94] with the likelihood calculated in each bin of the photon E_T distribution assuming Poisson statistics for the signal (both data and MC samples) and Gaussian uncertainties for the backgrounds, efficiencies, systematic uncertainties, and luminosity. We use the standard `DØ wzdiboson_llh` package with the `LLH` class to calculate the probabilities of the observations and the likelihood of the comparison.

The probability for observing N_i candidate events in bin i with an estimated signal of n_i and background b_i is calculated as:

$$P_i = \frac{(n_i + b_i)^{N_i}}{N_i!} e^{-(n_i + b_i)}. \quad (6.1)$$

The overall probability of observing a binned distribution is the product of all P_i :

$$P = \prod_{i=1}^{N_{bin}} P_i. \quad (6.2)$$

As both n_i and b_i have uncertainties, we treat them as Gaussian distributions with weights and integrate them:

$$P' = \int \mathcal{G}_{f_n} df_n \int \mathcal{G}_{f_b} df_b \prod_{i=1}^{N_{bin}} \frac{e^{-(f_n n_i + f_b b_i)} (f_n n_i + f_b b_i)^{N_i}}{N_i!}, \quad (6.3)$$

The negative log likelihood L is then used as a measure of the comparison between the observed data and predicted signal plus backgrounds:

$$L = -\log(P'). \quad (6.4)$$

6.1 Anomalous Couplings Limits in the Electron and Muon Mode

The photon E_T distributions in data, predicted signal and the backgrounds are shown in Figs. 5.18, 5.19. The MC distributions are normalized to the integrated luminosity. The effect of introducing anomalous couplings results in a raising photon E_T spectrum at high values of the photon momentum for the non-SM MC sample.

We generate 775 Baur MC samples with values of h_{30}^V from -0.3 to 0.3 ($V = Z, \gamma$ – see Section 2.2.2) with a step of 0.02, and h_{40}^V from -0.024 to 0.024 with a step of 0.002 for the form-factor scale $\Lambda = 1.2$ TeV. Following the procedure described above, for each pair of the anomalous couplings from the grid we calculate the negative log likelihood and then fit this distribution with a 6-parametric fitting function. The fitting function is of the form of Eq. 6.5, and is shown in Fig. 6.1.

$$fitf = p_0 + p_1 \cdot h_{30} + p_2 \cdot h_{40} + p_3 \cdot h_{30} \cdot h_{30} + p_4 \cdot h_{40} \cdot h_{40} + p_5 \cdot h_{30} \cdot h_{40}. \quad (6.5)$$

Using this smooth function, we calculate one-dimensional (two-dimensional) 95% C.L. axis limits (contour limits) by integrating the likelihood curve (likelihood surface). The following uncertainties are used as input variables into the *LLH* routine: 13% uncertainty on the background determination, $\approx 4.5\%$ on signal MC, and 6.1% on the luminosity determination. The resulting negative log likelihood distributions for all 775 MC samples (electron plus muon channels combined) are shown in Fig. 6.2.

The one-dimensional and two-dimensional limits on anomalous couplings in the electron and muon channels combined are shown in Fig. 6.3. The two-dimensional limits are represented by the solid ellipses, and the one-dimensional axis limits are represented by the ticks

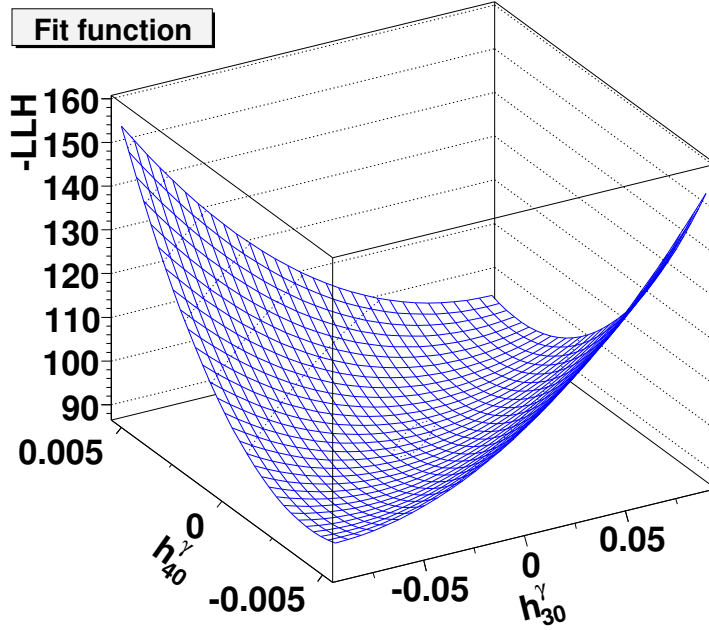


Figure 6.1: *Fitting function general behavior as a function of h_{30} and h_{40} .*

on the crosses. We set one coupling to its SM value (zero) and determine the limits on the second coupling as intersection points of the one-dimensional curve with the corresponding axis. These limits for $\Lambda = 1.2$ TeV are:

$$-0.085 < h_{30}^\gamma < 0.084, \quad -0.0053 < h_{40}^\gamma < 0.0054 \quad (h_i^Z = 0). \quad (6.6)$$

$$-0.083 < h_{30}^Z < 0.082, \quad -0.0053 < h_{40}^Z < 0.0054 \quad (h_i^\gamma = 0). \quad (6.7)$$

These one-dimensional limits on h_{30}^V (h_{40}^V) are roughly 2.5 (3.5) times tighter than those, set in Ref. [24].

6.2 Anomalous Couplings Limits in the Neutrino Mode

Following the prescription given in Section 6.1, we set limits on the anomalous trilinear gauge couplings in the neutrino channel. We generate 425 samples with values of h_{30}^V from

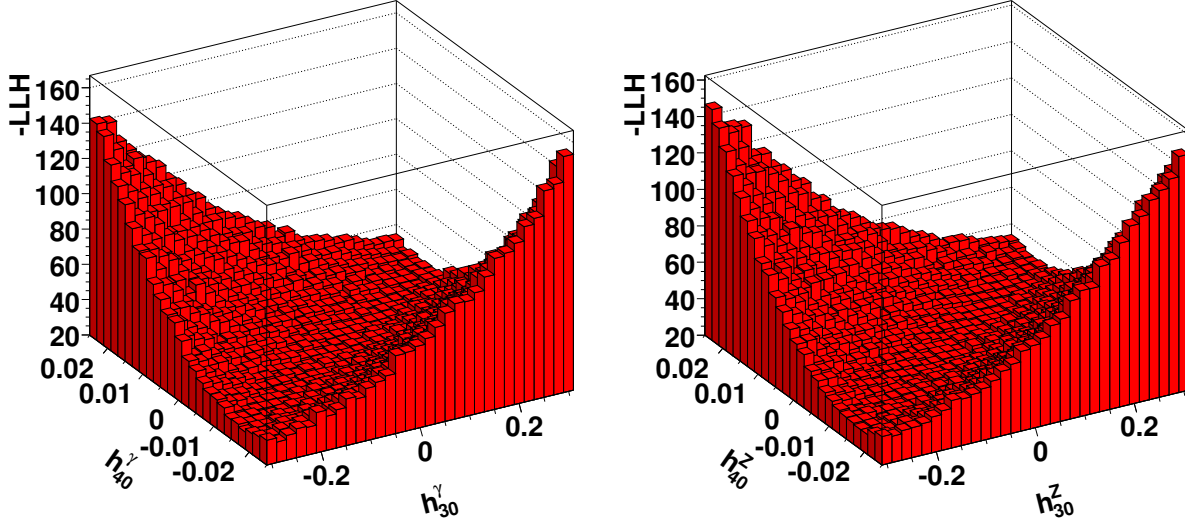


Figure 6.2: Negative value of log likelihood of all 775 fits of photon E_T spectrum from Monte Carlo $Z\gamma\gamma$ (left) and $ZZ\gamma$ (right) simulation and QCD background to the data for $\Lambda = 1.2$ TeV.

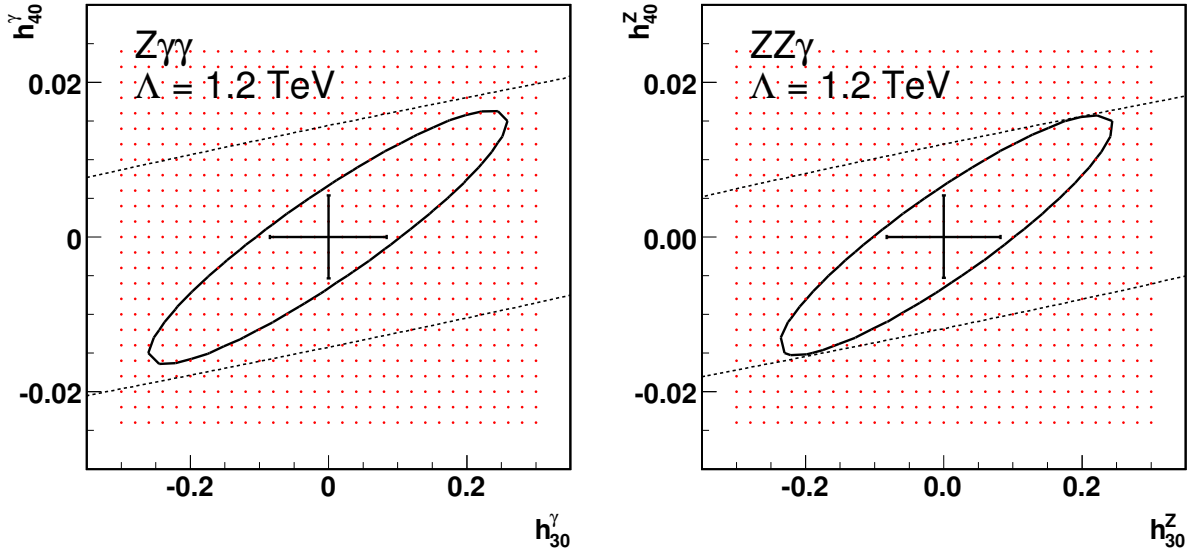


Figure 6.3: Two-dimensional contour (ellipse) and one-dimensional limits (ticks on the cross) of 95% C.L. on CP-conserving anomalous $Z\gamma\gamma$ (left) and $ZZ\gamma$ (right) couplings. Dashed straight lines indicate the unitarity limits for $\Lambda = 1.2$ GeV. Red dots represent the anomalous couplings grid.

-0.12 to 0.12 with a step of 0.01 ; and values of h_{40}^V from -0.008 to 0.008 with a step of 0.001 for the form-factor scale $\Lambda = 1.5$ TeV. The following uncertainties are used as input variables into the *LLH* routine: 24% (16%) uncertainty on the background determination, $\approx 12\%$ (13%) on signal MC, and 6.1% on the luminosity determination for Run IIa (Run IIb) data sets. The one-dimensional limits for $\Lambda = 1.5$ TeV in the neutrino channel are:

$$-0.036 < h_{30}^\gamma < 0.036, \quad -0.0019 < h_{40}^\gamma < 0.0019 \quad (h_i^Z = 0). \quad (6.8)$$

$$-0.035 < h_{30}^Z < 0.035, \quad -0.0019 < h_{40}^Z < 0.0019 \quad (h_i^\gamma = 0). \quad (6.9)$$

These (Eqs. 6.8, 6.9) are the tightest limits on the anomalous $Z\gamma\gamma$ and $ZZ\gamma$ couplings in the neutrino channel alone set at hadron colliders to date. These limits also improve the ones obtained in the charged leptonic mode due to three times larger branching ratio of the $Z \rightarrow \nu\bar{\nu}$ compared to $Z \rightarrow \ell\ell$, and more than three times more luminosity in the neutrino channel.

6.3 Combined Anomalous Couplings Limits

To further increase the sensitivity of the experiment to the anomalous $Z\gamma$ production, it is worth combining the limits obtained in the charged and neutral lepton channels. For this, we need to use the same form-factor scale in both modes. Hence, we generate the MC samples for $\Lambda = 1.5$ TeV for the charged leptons Z boson decay, and run the limit setting code over once again. The resulting one-dimensional limits in the combined electron plus muon channel for the form-factor scale $\Lambda = 1.5$ TeV are:

$$-0.075 < h_{30}^\gamma < 0.078, \quad -0.0036 < h_{40}^\gamma < 0.0036 \quad (h_i^Z = 0). \quad (6.10)$$

$$-0.075 < h_{30}^Z < 0.075, \quad -0.0036 < h_{40}^Z < 0.0037 \quad (h_i^\gamma = 0). \quad (6.11)$$

Adding the values of the negative log likelihood in the neutrino and electron plus muon channels, and fitting the resulting distribution with a 6-parametric function (Eq. 6.5), we obtain the following combined limits on the ATGC for $\Lambda = 1.5$ TeV:

$$-0.033 < h_{30}^\gamma < 0.033, \quad -0.0017 < h_{40}^\gamma < 0.0017 \quad (h_i^Z = 0). \quad (6.12)$$

$$-0.033 < h_{30}^Z < 0.033, \quad -0.0017 < h_{40}^Z < 0.0017 \quad (h_i^\gamma = 0). \quad (6.13)$$

These limits (Eqs. 6.12, 6.13) are roughly 3 times tighter than the previously published limits (see Section 6.1) [95], and the current h_{30}^V (h_{40}^V) limits are about 11 (29) times tighter than the most recent $D\bar{O}$ published results that included the neutrino channel [96]. These are the tightest limits in the world set at any hadron collider to date. The full summary of the limits on anomalous trilinear gauge couplings is presented in Table 6.1.

The negative values of logarithmic likelihood for all Monte Carlo samples generated with $\Lambda = 1.5$ TeV and the corresponding limits on anomalous coupling parameters for the combined neutrino and electron plus muon channel are shown in Figs. 6.4, 6.5. The two-dimensional limits are represented by the solid ellipses, and the one-dimensional axis limits are represented by the ticks on the crosses.

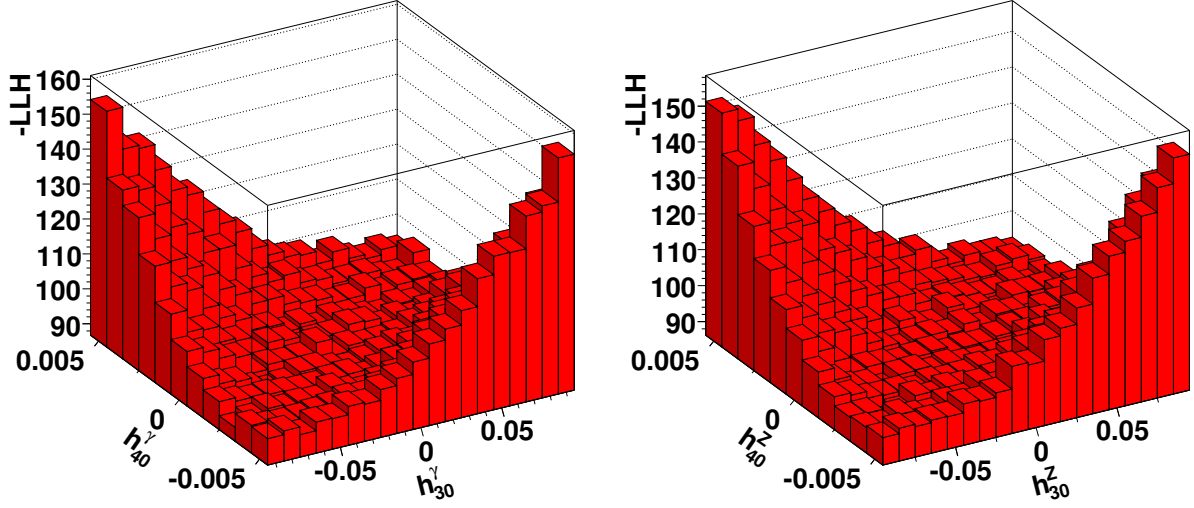


Figure 6.4: Negative value of log likelihood of fits of E_T spectrum from Monte Carlo $Z\gamma\gamma$ (left) and $ZZ\gamma$ (right) simulation and backgrounds to the data for $\Lambda = 1.5$ TeV in the combined neutrino and electron plus muon channel.

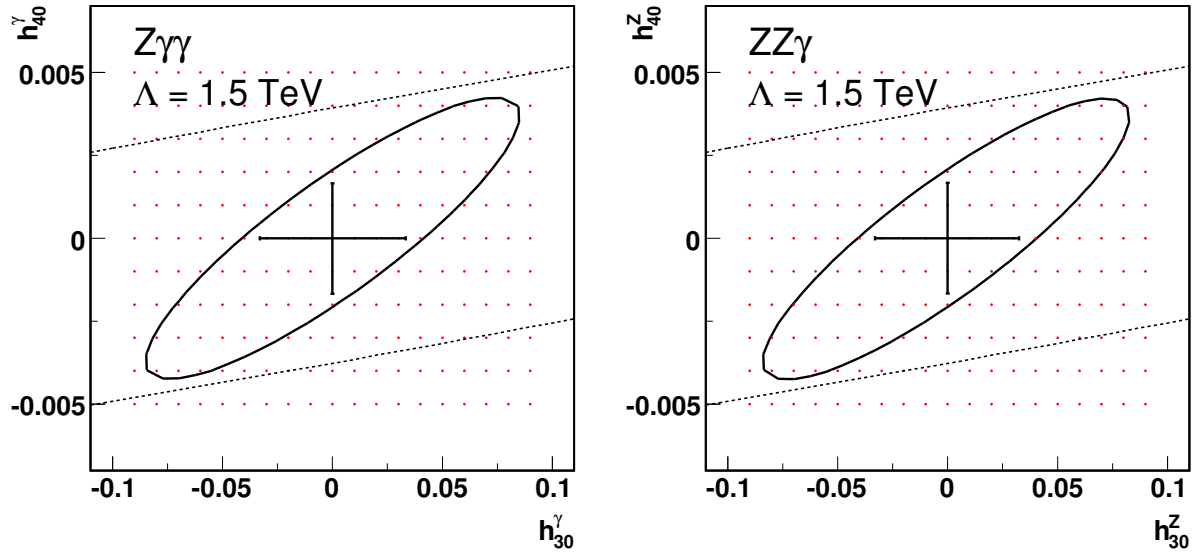


Figure 6.5: Two-dimensional contours (ellipses) and one-dimensional limits (ticks on the crosses) of 95% C.L. on CP-conserving anomalous $Z\gamma\gamma$ (left) and $ZZ\gamma$ (right) couplings in the combined neutrino and electron plus muon channel. Dashed straight lines indicate the unitarity limits for $\Lambda = 1.5$ TeV. Both two-dimensional contours are inside the unitarity boundaries. Red dots represent the anomalous couplings grid.

Table 6.1: Summary of the 95% C.L. one-dimensional anomalous couplings limits.

Channel and data set	Limits, $\Lambda = 1.2$ TeV	Limits, $\Lambda = 1.5$ TeV
$ee\gamma + \mu\mu\gamma$, 1 fb $^{-1}$	$ h_{30}^{\tilde{\gamma}} < 0.085$, $ h_{40}^{\tilde{\gamma}} < 0.0054$	$ h_{30}^{\tilde{\gamma}} < 0.079$, $ h_{40}^{\tilde{\gamma}} < 0.0036$
$ee\gamma + \mu\mu\gamma$, 1 fb $^{-1}$	$ h_{30}^{\tilde{Z}} < 0.083$, $ h_{40}^{\tilde{Z}} < 0.0054$	$ h_{30}^{\tilde{Z}} < 0.075$, $ h_{40}^{\tilde{Z}} < 0.0037$
$\nu\nu\gamma$, 3.6 fb $^{-1}$	$ h_{30}^{\tilde{\gamma}} < 0.042$, $ h_{40}^{\tilde{\gamma}} < 0.0029$	$ h_{30}^{\tilde{\gamma}} < 0.037$, $ h_{40}^{\tilde{\gamma}} < 0.0020$
$\nu\nu\gamma$, 3.6 fb $^{-1}$	$ h_{30}^{\tilde{Z}} < 0.041$, $ h_{40}^{\tilde{Z}} < 0.0029$	$ h_{30}^{\tilde{Z}} < 0.036$, $ h_{40}^{\tilde{Z}} < 0.0020$
$ee\gamma + \mu\mu\gamma + \nu\nu\gamma$ combined	$ h_{30}^{\tilde{\gamma}} < 0.038$, $ h_{40}^{\tilde{\gamma}} < 0.0025$	$ h_{30}^{\tilde{\gamma}} < 0.033$, $ h_{40}^{\tilde{\gamma}} < 0.0017$
$ee\gamma + \mu\mu\gamma + \nu\nu\gamma$ combined	$ h_{30}^{\tilde{Z}} < 0.037$, $ h_{40}^{\tilde{Z}} < 0.0025$	$ h_{30}^{\tilde{Z}} < 0.033$, $ h_{40}^{\tilde{Z}} < 0.0017$

Table 6.2: Comparison between the CP-conserving and CP-violating pair of couplings. The values of couplings are: $h_{30}^Z = h_{10}^Z = 0.02$, $h_{40}^Z = h_{20}^Z = -0.003$.

Parameter	CP-conserving	CP-violating
LO cross section, pb	0.0612	0.0602
NLO cross section, pb	0.0615	0.0604
Total efficiency	0.2109	0.2119

Table 6.3: Comparison between the CP-conserving and CP-violating pair of couplings. The values of couplings are: $h_{30}^Z = h_{10}^Z = 0.09$, $h_{40}^Z = h_{20}^Z = 0.005$.

Parameter	CP-conserving	CP-violating
LO cross section, pb	0.0498	0.0501
NLO cross section, pb	0.0505	0.0508
Total efficiency	0.2154	0.2154

6.4 Limits on CP-violating Couplings

As stated in Refs. [12, 13], couplings h_{30}^V and h_{40}^V are CP-conserving, and couplings h_{10}^V and h_{20}^V are CP-violating. The limits on h_{30}^V and h_{10}^V , as well as limits on h_{40}^V and h_{20}^V , are expected to be the same within the precision of the measurement. To verify this, we generate $Z\gamma \rightarrow \nu\bar{\nu}\gamma$ MC samples with non-zero values of CP-violating couplings and compare the predicted cross sections and main kinematic distributions with the corresponding CP-conserving samples. Tables 6.2, 6.3 summarize the comparison results for two pairs of couplings.

We compare the main kinematic distributions for the two sets of couplings in Figs. 6.6, 6.7. As seen from Tables 6.2, 6.3 and Figs. 6.6, 6.7, the disagreement between the CP-violating and corresponding CP-conserving MC samples is on the order of 1% or smaller. Hence, we estimate the limits on the CP-violating couplings to be the same as limits on the CP-conserving anomalous couplings within the precision of our measurement.

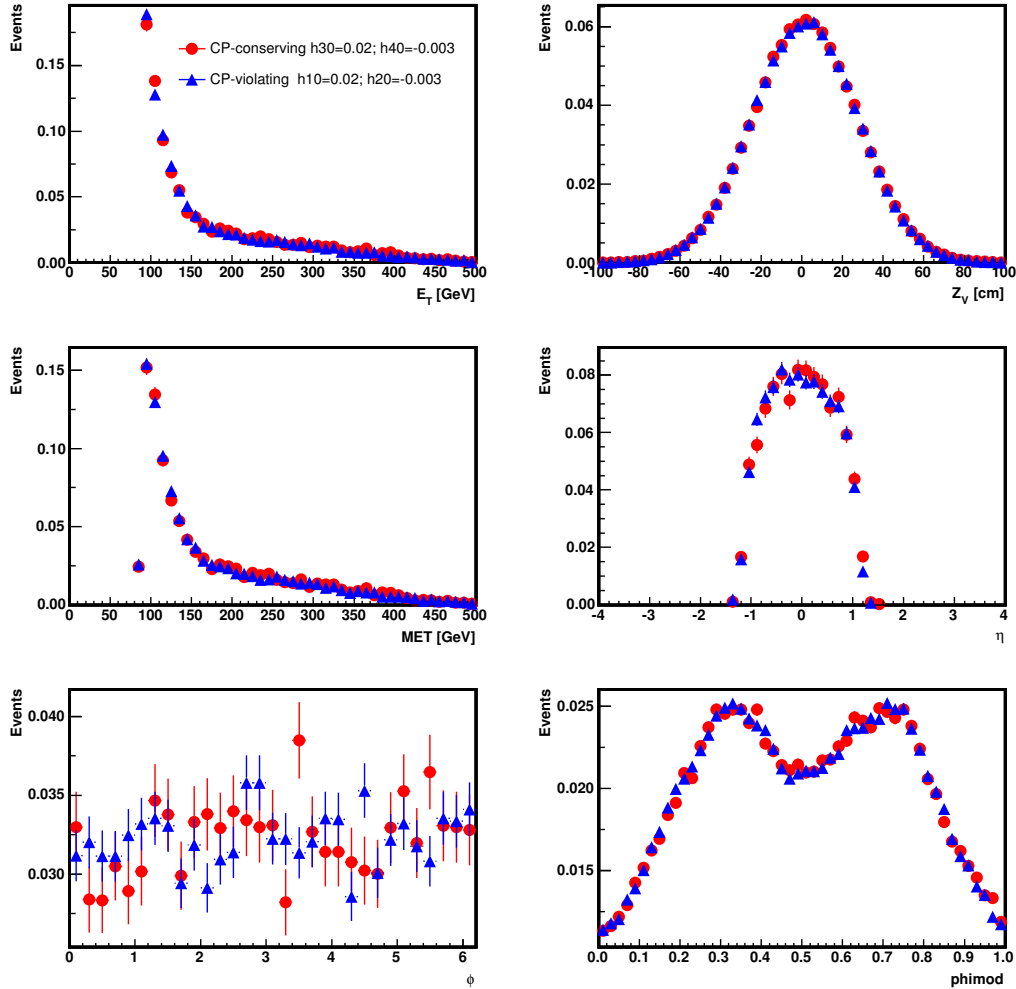


Figure 6.6: Kinematic distributions comparison between the CP-conserving and CP-violating pair of couplings. The values of couplings are: $h_{30}^Z = h_{10}^Z = 0.02$, $h_{40}^Z = h_{20}^Z = -0.003$.

6.5 Comparison between the Tevatron and LEP limits

In the past, studies of the $Z\gamma$ production have been performed by the CDF [18–20] and DØ [20–24] collaborations at the Tevatron collider, as well as at the CERN LEP electron-positron collider by the ALEPH [25], DELPHI [26, 32], L3 [27, 28], and OPAL [29] collaborations. The limits (Eqs. 6.12, 6.13) are superior to limits set by any collaboration at hadron colliders to date. In this Section, we compare limits described in Eqs. 6.12, 6.13 to the most

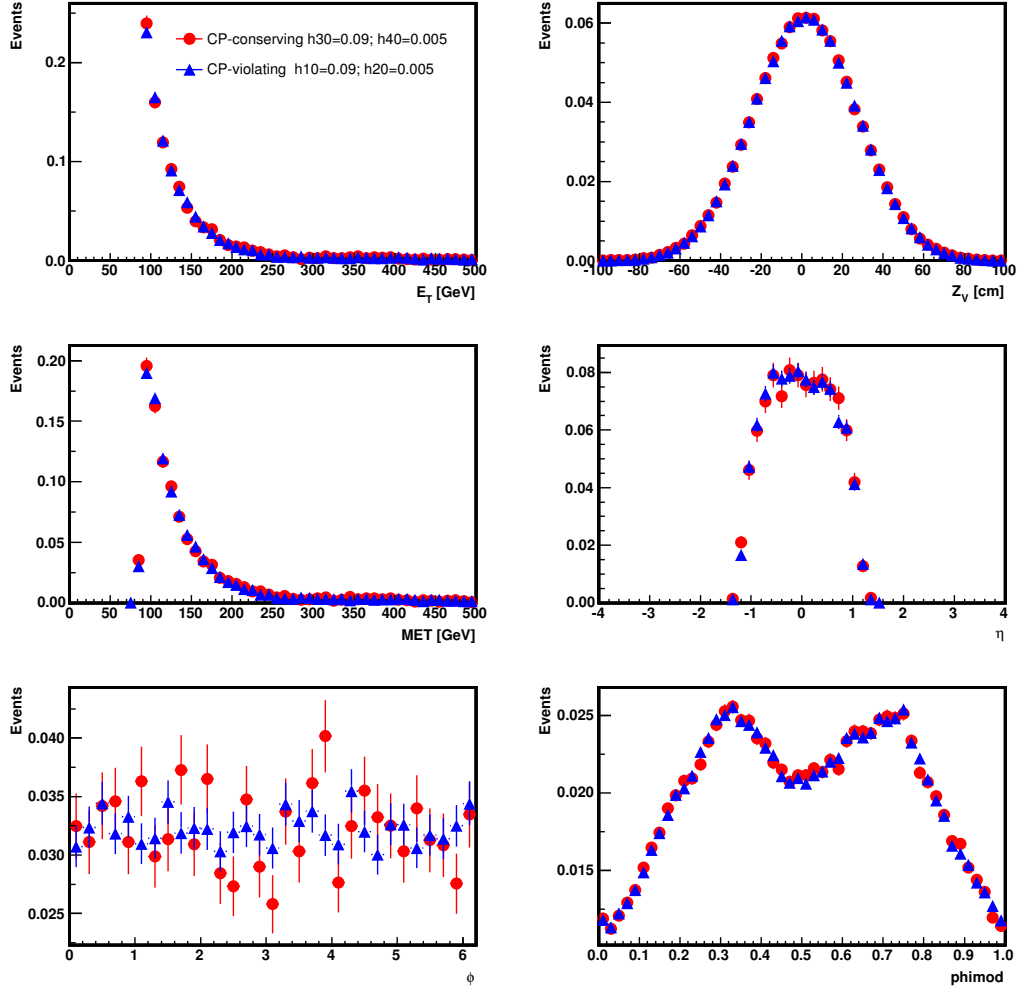


Figure 6.7: Kinematic distributions comparison between the CP-conserving and CP-violating pair of couplings. The values of couplings are: $h_{30}^Z = h_{10}^Z = 0.09$, $h_{40}^Z = h_{20}^Z = 0.005$.

recent combination of LEP results [30, 31]. The LEP combination of limits on ATGC is summarized and compared to the limits, described in this dissertation, in Table 6.4.

It is worth mentioning, that due to the specific of an electron-positron collider, the LEP collaborations set limits directly on $h_i^{Z,\gamma}$ (see Eq. 2.3), while due to the parton distribution functions analyzers at the Tevatron are able to set limits only on low-energy approximations of the couplings, $h_{i0}^{Z,\gamma}$. The conversion coefficient from LEP to Tevatron is $(1 + \hat{s}/\Lambda^2)^n > 1$ for our choice of n (see Section 2.2.2). From Table 6.4 it is clear, that three out of four

Table 6.4: *The 95% C.L. one-dimensional limits on the anomalous trilinear gauge couplings: combination of four LEP collaborations results, and current limits from the $D\bar{O}$ experiment at the Tevatron.*

LEP	Tevatron
$-0.049 < h_3^\gamma < -0.008$	$-0.033 < h_{30}^\gamma < 0.033$
$-0.002 < h_4^\gamma < 0.034$	$-0.0017 < h_{40}^\gamma < 0.0017$
$-0.20 < h_3^Z < 0.07$	$-0.033 < h_{30}^Z < 0.033$
$-0.05 < h_4^Z < 0.12$	$-0.0017 < h_{40}^Z < 0.0017$

Tevatron limits (h_{30}^Z , h_{40}^Z , and h_{40}^γ) are more restrictive than those (either converted or not) from LEP, and, hence, are the most stringent limits on ATGC in the world to date.

Chapter 7

Search For a Narrow Resonance Decaying into $Z\gamma$

Despite its tremendous success, the standard model (SM) in its current form may be a low energy approximation of a more fundamental theory. The SM does not describe gravity, and fundamental parameters such as masses and coupling constants are not derived from the theory. Many models exist to replace or extend the SM. A heavy partner of the Z boson, Z' , appears in grand unified theories, little Higgs models, models with extra spatial dimensions, and superstring theories. Scalar Higgs bosons, pseudo-scalar toponium, vector Z' bosons, and techniparticles could decay into the diboson final state $Z\gamma$ [97–102].

In this Chapter we describe a search for a narrow scalar or vector resonance decaying into $Z\gamma$ using approximately 1 fb^{-1} of data. This analysis considers leptonic decays of the Z boson into electron or muon pairs. A similar search had been carried out by the $D\bar{O}$ collaboration using a smaller data set corresponding to about 300 pb^{-1} [95, 103].

7.1 Particle Models

A scalar model and a vector model of particles that decay into $Z\gamma$ are used; both assume a resonance total width smaller than the resolution of the detector. We use the SM Higgs boson production model, as implemented in PYTHIA [55], for the scalar resonance decay into the $Z\gamma$ final state. To model the vector resonance decay, we use a generic color-singlet,

neutral, vector particle (V) implemented in MADEVENT [104]. The diagrams of the SM $Z\gamma$ processes are shown in Figs. 7.1(a), 7.1(b) (see also Figs. 2.2(a) and (b)), and the vector and scalar resonance diagrams are illustrated in Figs. 7.1(c), 7.1(d).

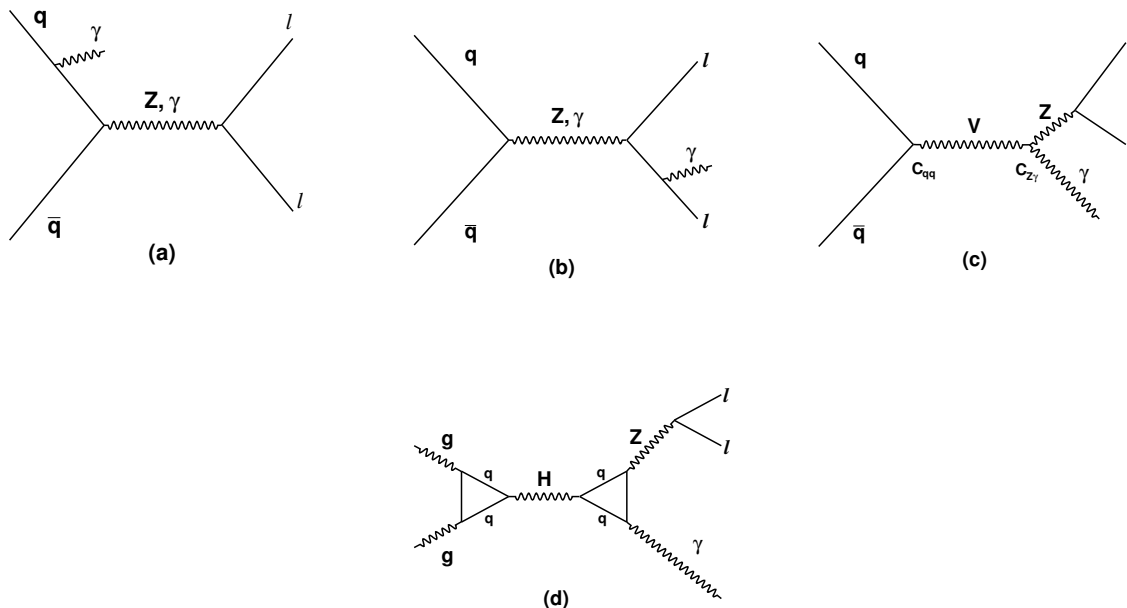


Figure 7.1: Feynman diagrams for the leading order processes which produce $Z\gamma$ candidates: (a) SM initial state radiation (ISR), (b) SM final state radiation (FSR), (c) $q\bar{q}$ pair annihilation into a V particle (obtained from MADGRAPH, adapted to produce a vector particle decaying into $Z\gamma$), and (d) Higgs production and decay (PYTHIA).

7.1.1 Scalar Particle

The SM Higgs boson's branching fraction to $Z\gamma$ is less than 0.003, which makes the first observation of the SM Higgs boson in the $Z\gamma$ channel rather improbable. However, for an understanding if an observed particle is the SM Higgs or some other particle, the $Z\gamma$ channel may be useful. Although in this analysis, the SM Higgs boson decay $Z\gamma$ is used to model the decay kinematics of scalar particles to $Z\gamma$, we treat the analysis as generic to any scalar particle. There are a number of models of the Higgs mechanism which are slightly different

from the SM version, such as fermiophobic Higgs model or fourth (or more) generation Higgs. These deviations can change the production cross section and/or branching fraction.

7.1.2 Vector Particle

In this analysis, we use a model which describes a generic color-singlet, charge-singlet, vector particle, named V , that decays to $Z\gamma$. As MADEVENT has only the SM Feynman rules implemented, the new couplings were added [105] as shown in Fig. 7.1(c). We assume that C_{qq} is the coupling between the V and initial state fermions $q\bar{q}$, with $q = u$ or d , and that $C_{Z\gamma}$ is the coupling between the V and $Z\gamma$. MADGRAPH produces Feynman diagrams and computes its squared amplitude. MADEVENT uses process-dependent information from MADGRAPH, integrates the squared amplitude over the phase space and produces weighted/unweighted events. A Z' is a good example of a V particle, but there is no model of fundamental Z' coupling to $Z\gamma$, since the Z' has no electric charge. However, if the Z' has a composite structure, as in technicolor models, then such a decay is possible.

7.2 Monte Carlo Samples

The MC samples used in this analysis are:

- PYTHIA [55] SM Higgs boson production in which the Higgs was forced to decay to $Z\gamma$, and the Z boson was forced to decay to leptons.
- MADEVENT [104] output samples in which an $SU(3)$ singlet, charge-singlet, spin-1 particle was forced to decay to $Z\gamma$, and the Z boson was forced to decay to leptons.

Twenty-six MC samples were generated with the resonance mass M_{Res} following the grid: $M_{Res} \in [120, 400] \text{ GeV}/c^2$ with a step of $20 \text{ GeV}/c^2$, and $M_{Res} \in [400, 900] \text{ GeV}/c^2$ with a step of $50 \text{ GeV}/c^2$. The vector resonance MC samples contain 300,000 events; the scalar resonance MC samples contain 300,000 events for $M_{Res} < 650 \text{ GeV}/c^2$, and then the sample size decreases from 60,000 to 1,000 for $M_{Res} = 650 \text{ GeV}/c^2$ to $M_{Res} = 900 \text{ GeV}/c^2$.

The PMCS [62] is used to model the DØ detector response and measure the acceptance of the event selection criteria.

7.3 Event Selection

The data sets and the event selection for this analysis are identical to those, used in the $Z\gamma \rightarrow \ell\ell\gamma$ cross section analysis (see Section 5.1). The analysis is done on approximately 1 fb^{-1} of data (see Section 5.1.1). Candidate events contain two leptons of the same flavor (electrons or muons) and a photon. The event selection criteria are described in details in Sections 5.1.3.1–5.1.3.3. These criteria are slightly optimized for this search, and the changes are described in Section 7.3.1.

7.3.1 Photon transverse energy and dilepton invariant mass cuts optimization

In the $Z\gamma \rightarrow \ell\ell\gamma$ cross section analysis, events were required to contain a photon with $E_T > 7 \text{ GeV}$ and two leptons with $M_{\ell\ell} > 30 \text{ GeV}/c^2$. In this search, we tighten the photon E_T and dilepton invariant mass ($M_{\ell\ell}$) requirements, and add a cut on lepton separation.

In order to improve the search for new particles, it is logical to isolate the phase space that makes the search more efficient. The photon E_T and $M_{\ell\ell}$ cuts are optimized with respect to $signal/\sqrt{signal + background}$, *i.e.* $S/\sqrt{S + B}$. The signal is based on MC samples of vector and scalar resonances (see Section 7.2). These samples are normalized to have a cross section times branching fraction of 0.5 pb (this approximately equals to the sensitivity of the search).

Two background sources, SM $Z\gamma$ obtained from Baur event generator [12, 13], and Z +jets background (measured from data), are considered (see Section 7.5). We varied the cut on the photon E_T from 7 GeV to 100 GeV, and the dilepton invariant mass cut from $30 \text{ GeV}/c^2$ to $100 \text{ GeV}/c^2$, and calculated the significance ($S/\sqrt{S + B}$). The results of the studies are shown in Table 7.1. The final conditions imposed are: photon $E_T > 20 \text{ GeV}$

Table 7.1: Optimization cuts on $M_{\ell\ell}$ and photon E_T for different particles/masses. $S/\sqrt{S+B}$ optimization does not include the cut on three-body ($M_{\ell\ell\gamma}$) mass, which is highly correlated with these cuts.

Mass (GeV/ c^2)	$M_{\ell\ell}$ cut (GeV/ c^2)	Photon E_T cut (GeV)	$S/\sqrt{S+B}$
Vector			
120	75	25	0.284
140	80	35	0.492
160	85	45	0.394
180	90	45	0.154
Scalar			
120	90	20	0.273
140	80	35	0.470
160	90	45	0.350
180	85	45	0.176

and dilepton mass $M_{\ell\ell} > 80 \text{ GeV}/c^2$.

7.3.2 Muon correction

In searches for a narrow mass resonance, a three-body ($M_{\ell\ell\gamma}$) mass resolution will directly affect the sensitivity. The $M_{\ell\ell\gamma}$ resolution is $> 8\%$ (4%–5%), in the muon (electron) channel, respectively. Given that we expect a known $M_{\ell\ell}$, and in order to make the muon channel three-body mass resolution approximately as good as that in the electron channel, we use the Lagrange multiplier technique to determine corrections to each muon which fix the dimuon mass to the nominal Z boson mass. If we neglect the muons' masses, a formulation for the dimuon mass can be written as:

$$M_{\mu\mu}^2 = 2 \cdot p_{T1} \cdot p_{T2} \cdot (\cosh(\Delta\eta) - \cos(\Delta\phi)), \quad (7.1)$$

where p_{T1} and p_{T2} are the transverse momenta of two muons, and $\Delta\eta$ and $\Delta\phi$ are the separations between the two muons in the pseudorapidity and the azimuthal angle. If we define the muons' curvatures as $k_{1,2} \equiv 1/p_{T1,2}$, then Eq. 7.1 transforms into:

$$k_1 \cdot k_2 - \frac{\cosh(\Delta\eta) - \cos(\Delta\phi)}{M_{\mu\mu}^2/2} = 0. \quad (7.2)$$

If we denote the best fit values for $k_{1,2}$ as $\bar{k}_{1,2}$, then $M_{\mu\mu}$ equals to M_Z , the Z mass measured at LEP. Thus we construct a χ^2 for minimization to be:

$$\chi^2 = \left(\frac{\bar{k}_1 - k_1}{\sigma_1} \right)^2 + \left(\frac{\bar{k}_2 - k_2}{\sigma_2} \right)^2 - 2 \cdot \lambda \cdot (\bar{k}_1 \cdot \bar{k}_2 - r^2), \quad (7.3)$$

where $\sigma_{1,2}$ corresponds to the resolution on the muon curvature $k_{1,2}$, λ is a lagrangian multiplier, and $r^2 \equiv \frac{\cosh(\Delta\eta) - \cos(\Delta\phi)}{M_Z^2/2}$.

The problem is linearized by setting $\bar{k}_{1,2} = k_{1,2} + \Delta k_{1,2}$ and assuming $\Delta k_{1,2} \ll k_{1,2}$. We neglect terms such as $\Delta k_1 \cdot \Delta k_2$, and obtain:

$$\chi^2 = \left(\frac{\bar{k}_1 - k_1}{\sigma_1} \right)^2 + \left(\frac{\bar{k}_2 - k_2}{\sigma_2} \right)^2 - 2 \cdot \lambda (k_1 \cdot k_2 + \Delta k_1 \cdot k_2 + k_1 \cdot \Delta k_2 - r^2). \quad (7.4)$$

We minimize the χ^2 function with respect to $k_{1,2}$ and λ and obtain:

$$\lambda = \frac{r^2 - k_1 \cdot k_2}{\sigma_1^2 \cdot k_1^2 + \sigma_2^2 \cdot k_2^2}, \quad (7.5)$$

$$\Delta k_{1,2} = \lambda \cdot k_{2,1} \cdot \sigma_{1,2}^2. \quad (7.6)$$

If the χ^2 after minimization, χ_{min}^2 , is less than seven, the constrained fit is used for the Z momentum and mass. In cases where the constraint χ_{min}^2 is greater than seven, the mass constraint is not applied. The choice of $\chi_{min}^2 < 7$ is found by scanning values of χ^2 and calculating the acceptance for the $\mu\mu\gamma$ final state. This requirement ensures that Drell-Yan events will only be moved to the Z boson mass if they are consistent with that mass. This technique results in a substantial improvement of the $M_{\mu\mu\gamma}$ resolution, as shown in Table 7.2.

7.3.3 High mass inefficiency

An unusual source of inefficiency appears at high resonance masses: the leptons from the Z boson decay are spatially more collinear, and eventually can become indistinguishable. This effect becomes important at resonance masses above $600 \text{ GeV}/c^2$. In case of the muon channel this effect is easy to model. However, in the electron case the parameterized MC is not sufficient to model this effect. For this reason, we require the electron pair to be separated by $\Delta R_{ee} > 0.6$, while the muon pair separation $\Delta R_{\mu\mu}$ is above 0.5.

Table 7.2: *Dilepton plus photon invariant mass resolution. The fourth column shows an improvement in the dimuon plus photon invariant mass resolution after the Z mass constraint has been applied.*

Mass (GeV/ c^2)	$M_{ee\gamma}$ resolution (%)	$M_{\mu\mu\gamma}$ uncorrected resolution (%)	$M_{\mu\mu\gamma}$ corrected resolution (%)
100	4.1	8.3	4.6
200	4.4	8.0	4.7
300	4.8	9.9	5.2
400	4.9	11.7	5.5
500	4.9	11.8	5.8
600	4.9	13.6	6.1
700	4.9	14.6	6.4
800	5.2	16.8	7.2
900	5.3	17.6	7.8

7.4 Acceptance and Efficiencies

The total efficiency to reconstruct a $Z\gamma \rightarrow \ell\ell\gamma$ event can be calculated as a product of the following terms: fiducial and kinematic acceptance, trigger efficiency, lepton identification efficiency, and photon reconstruction efficiency. As the selection criteria, reconstruction methods, trigger sets, *etc.*, are inherited from the $Z\gamma \rightarrow \ell\ell\gamma$ cross section analysis, we will not discuss the acceptance and efficiency measurements in this Section, but refer to Sections 5.1.4–5.1.6.3 instead. The total efficiencies of the event selection criteria as functions of vector or scalar resonance mass are shown in Fig. 7.2. The reduction in acceptance due to the $\Delta R_{\ell\ell}$ cut described in Sec. 7.3.3 can also be seen in Fig. 7.2.

7.5 Backgrounds

The two main backgrounds to the process under study are the SM $Z\gamma$ production and the Z +jet production, where a jet is misidentified as a photon.

The Z +jet background determination in both electron and muon channels has been described in details in Section 5.1.7. We can readily use those results taking into account two modified cuts: dilepton invariant mass $M_{\ell\ell} > 80$ GeV/ c^2 and photon $E_T > 20$ GeV.

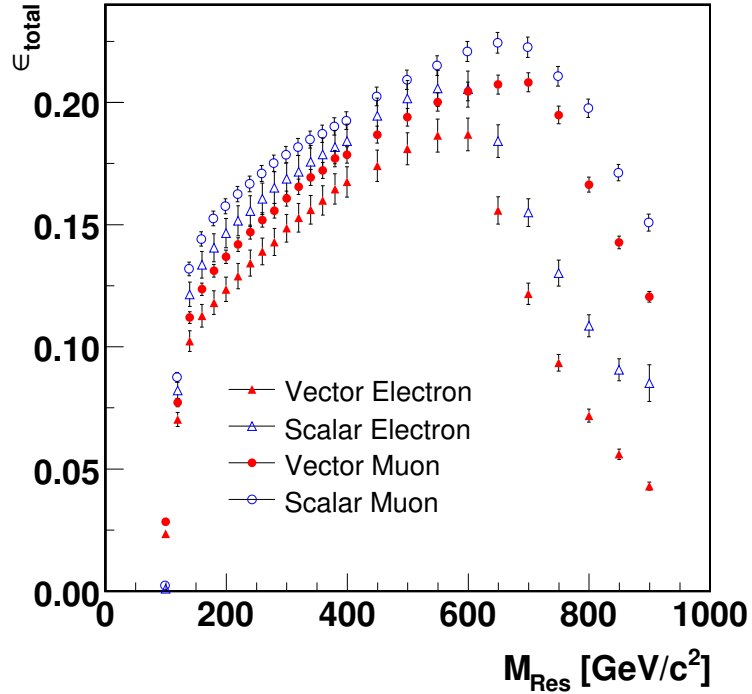


Figure 7.2: Total efficiencies of the $X \rightarrow Z\gamma$ process as a function of the resonance mass. Here, X denotes either a vector or a scalar resonance.

We obtain $4.5 \pm 0.7(\text{stat.}) \pm 0.6(\text{syst.})$ Z +jet background events in the electron channel and $4.4 \pm 0.7(\text{stat.}) \pm 0.6(\text{syst.})$ events in the muon channel.

The number of the SM $Z\gamma$ background events is estimated from the $Z\gamma$ MC sample described in Section 5.1.2 with the SM values (zero) of the trilinear $Z\gamma\gamma$ and $ZZ\gamma$ couplings. We take the NLO QCD corrections (see Section 5.1.2.1) into account when we estimate the generator level cross section of the SM $Z\gamma$ process, $\sigma_{\text{SM}}(Z\gamma)$. The PMCS [62] is used to estimate the total efficiency of the selection criteria, ϵ_{tot} . Then, the number of the SM $Z\gamma$ background events is calculated as:

$$N_{\text{SM}}(Z\gamma \rightarrow \ell\ell\gamma) = \epsilon_{\text{tot}} \cdot \sigma_{\text{SM}}(Z\gamma) \cdot \int \mathcal{L}dt, \quad (7.7)$$

where $\int \mathcal{L}dt$ is the integrated luminosity of the corresponding data sample. We summarize the values of the components of Eq. 7.7 in Table 7.3.

Table 7.3: Summary of the components used to estimate number of SM $Z\gamma$ background events.

Parameter	Electron channel	Muon channel
Total efficiency, ϵ_{tot}	0.0026 ± 0.0002	0.0032 ± 0.0002
$\sigma_{SM}(Z\gamma)$, pb	12.85 ± 0.60	12.85 ± 0.60
$\int \mathcal{L} dt$, pb $^{-1}$	1110 ± 70	1010 ± 60

Table 7.4: Summary of background events.

Background	Events, electron channel	Events, muon channel
Z +jet	$4.5 \pm 0.7(\text{stat.}) \pm 0.6(\text{syst.})$	$4.4 \pm 0.7(\text{stat.}) \pm 0.6(\text{syst.})$
SM $Z\gamma$	$37.4 \pm 6.1(\text{stat.}) \pm 2.6(\text{syst.})$	$41.6 \pm 6.5(\text{stat.}) \pm 2.2(\text{syst.})$
Total	$41.9 \pm 6.2(\text{stat.}) \pm 2.7(\text{syst.})$	$46.0 \pm 6.6(\text{stat.}) \pm 2.3(\text{syst.})$

Table 7.4 summarizes the number of background events in the electron and muon channels. Other background sources, such as Drell-Yan events, $b\bar{b} \rightarrow \mu\mu$, jets faking electrons, and WZ events are estimated to be small, and are neglected in this analysis.

7.5.1 Interferences

The SM $Z\gamma$ and the production of a scalar or vector resonance have the same final state. Interference can only happen if both amplitudes are large at the same point in phase space. In the SM, the $Z\gamma$ process cannot proceed through the s -channel, because a Z boson and a photon do not couple at the tree level. In the scalar or vector models proposed, signal processes go through the s -channel. Since it is a 2-to-2 process, the two kinematic invariants are: \hat{s} (the squared invariant mass of the $Z\gamma$ system) and \hat{t} (the difference between the incoming quark and the Z boson momentum, squared). We plot the vector resonance production phase space (\hat{s}, \hat{t}) divided by the SM $Z\gamma$ process phase space in Fig. 7.3. Each phase space is normalized to its cross section. In this analysis, we are only sensitive to a narrow resonance, so if the resonance is narrow enough, the interference of the resonance with the Z boson and photon can be neglected [106].

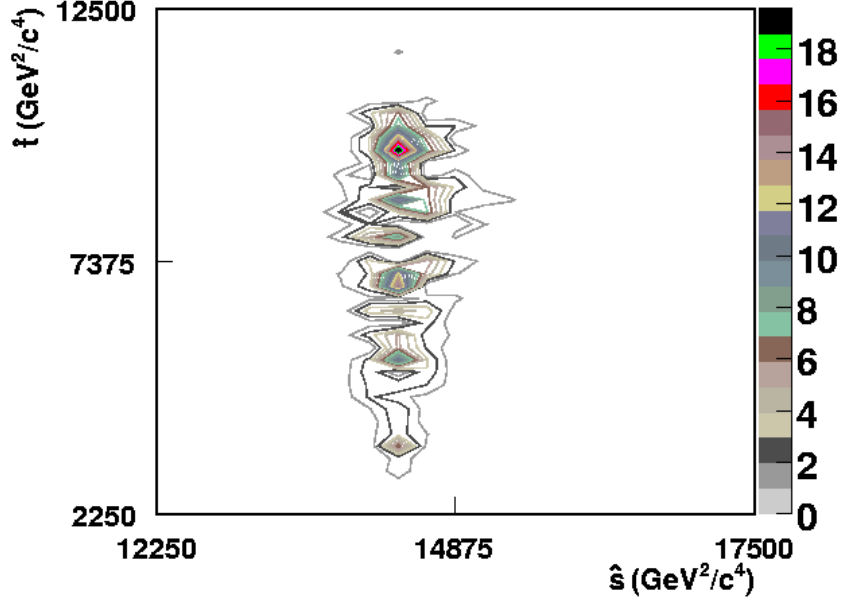


Figure 7.3: Ratio of the vector resonance production phase space (\hat{s}, \hat{t}) and the SM $Z\gamma$ process phase space. Each phase space is normalized to its cross section.

7.6 Analysis

7.6.1 Observed data

The selection criteria yield 49 candidates in the electron channel and 50 candidates in the muon channel. The dilepton plus photon invariant mass *vs.* dilepton invariant mass distribution is shown in Fig. 7.4. The vertical band is populated by the ISR events where the radiated photon originates from one of the initial partons, and an on-shell Z boson decays into two leptons. The Drell-Yan events cluster along the diagonal band. Most of the FSR events, which would populate the horizontal band centered at $M_{\ell\ell\gamma} \approx M_Z$, are removed by the $M_{\ell\ell} > 80 \text{ GeV}/c^2$ cut. The combined SM $Z\gamma$ and Z +jet background is $41.9 \pm 6.2(\text{stat.}) \pm 2.6(\text{syst.})$ in the electron channel and $46.0 \pm 6.6(\text{stat.}) \pm 2.3(\text{syst.})$ in the muon channel.

The dilepton plus photon invariant mass distribution in data, backgrounds, and two MC samples with resonance masses of $200 \text{ GeV}/c^2$ and $300 \text{ GeV}/c^2$ are shown in Fig. 7.5

and Fig. 7.6 for the scalar and vector resonance, respectively. The values of the cross section times branching fraction are 2.9 pb and 3.5 pb, and 4.0 pb and 4.6 pb, respectively. The signal coupling constants for a vector resonance decaying into $Z\gamma$ are taken to be $C_{qq} = C_{Z\gamma} = 0.1$.

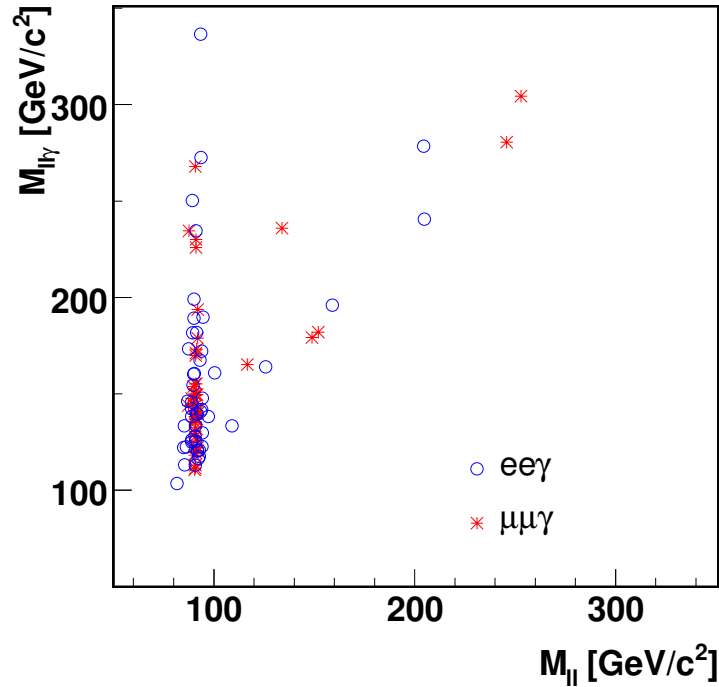


Figure 7.4: *Invariant mass of the dilepton system vs. invariant mass of dilepton and a photon candidates.*

We find no region in the $M_{\ell\ell\gamma}$ mass spectrum with the equivalent of a 3 s.d. or larger over the SM expectations, hence we set limits on the cross section times branching fraction (both vector and scalar modes) and $C_{qq}^2 \cdot C_{Z\gamma}^2$ (vector mode only) as functions of the resonance mass.

7.6.2 Limits setting software

A modified frequentist method [107] is used to examine the data for discrepancies with respect to the SM sources. A negative Poisson log-likelihood ratio test statistic (LLR) [108]

is used to compare the SM-only background hypothesis to one that incorporates a possible $Z\gamma$ resonance signal.

$$Q = \prod_{i=1}^{N_{bins}} \frac{(s_i + b_i)^{d_i} e^{-(s_i + b_i)}}{d_i!} / \frac{b_i^{d_i} e^{-b_i}}{d_i!}. \quad (7.8)$$

In this equation, d_i is the number of observed events in bin i , b_i is the number of background events, and s_i is the number of signal events. The LLR is then calculated as:

$$LLR = -2\ln Q = 2 \sum_{i=1}^{N_{bins}} s_i - 2 \sum_{i=1}^{N_{bins}} d_i \ln(1 + s_i/b_i). \quad (7.9)$$

The confidence levels (C.L.) for the probability that the background-only or the signal-plus-background hypotheses are consistent with the data are:

$$CL_b = P_b(Q \leq Q_{obs}), CL_{s+b} = P_{s+b}(Q \leq Q_{obs}). \quad (7.10)$$

Then the modified frequentist C.L. is defined as $CL_s = CL_{s+b}/CL_b$. The LLR incorporates systematic errors in the form of nuisance parameters that are integrated out assuming a Gaussian prior, and a relative contribution to the signal and background uncertainties that is independent of the dilepton plus photon invariant mass. The reconstruction efficiency systematic uncertainty in signal and backgrounds is 6%. A 6.1% luminosity systematic uncertainty is applied to the signal. The systematic uncertainties on the SM Z +jet and $Z\gamma$ contributions are taken to be 9% and 6%, respectively.

7.6.2.1 Results

Due to the fact that the total efficiencies of the selection criteria in vector and scalar mode differ by a fair amount (see Fig. 7.2), we set limits in two modes using the same software, but separately from each other. Limits on the cross section times branching fraction $X \rightarrow Z\gamma$ are set by comparing the observed three body mass spectrum from data with Monte Carlo $M_{\ell\ell\gamma}$ distributions with the combined background component overlaid (Figs. 7.5, 7.6). The confidence level is calculated at each mass point assuming flat Gaussian systematic

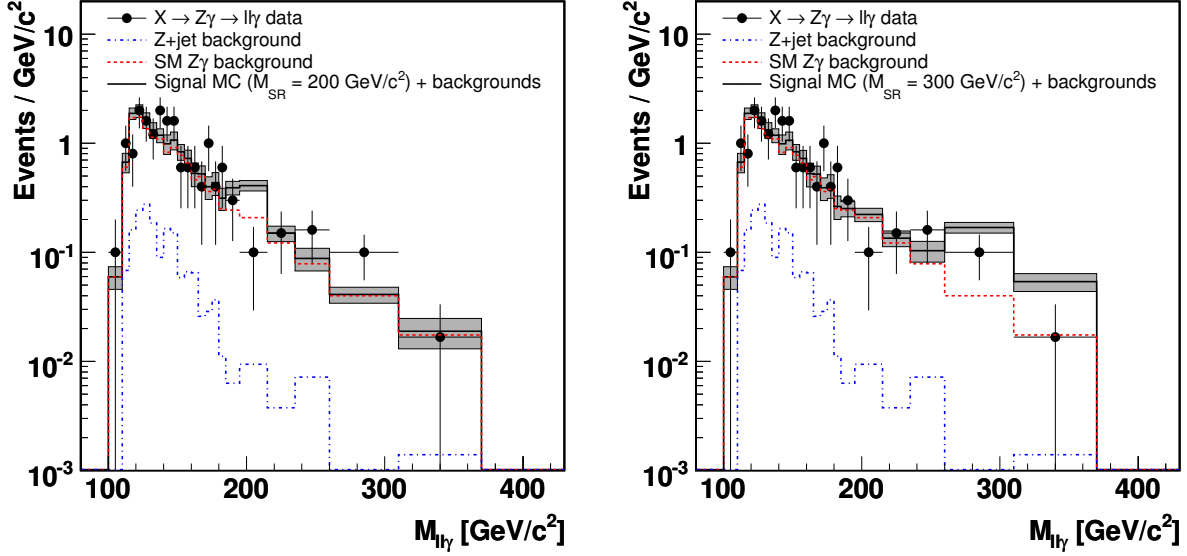


Figure 7.5: Invariant dilepton plus photon mass spectrum for $\ell\ell\gamma$ data (dots), SM $Z\gamma$ background (dashed line histogram), Z +jet background (dash-dot line histogram) and Monte Carlo signal plus background associated with a scalar particle of $200 \text{ GeV}/c^2$ (left) and $300 \text{ GeV}/c^2$ (right) decaying into $Z\gamma$ (solid line). The shaded band represents the 1 s.d. systematic and statistical uncertainty on the Monte Carlo signal plus background.

uncertainties for the background, luminosity, and efficiencies. The statistical uncertainty dominates over the systematic uncertainties.

The 95% C.L. observed upper limits on cross section times branching fraction for a vector (scalar) resonance decaying into $Z\gamma$ are shown as functions of $M_{\ell\ell\gamma}$ mass in Fig. 7.7 (Fig. 7.8), respectively. Resonances with the cross section times branching fraction values in the region above the lines in these figures are excluded.

Using the definitions of couplings associated with the diagram Fig. 7.1(c) (see Section 7.1), the amplitude A of the process is proportional to $C_{qq} \cdot C_{Z\gamma}$. As the cross section is proportional to $|A|^2$, we conclude that the cross section associated with a vector resonance decaying into $Z\gamma$ is proportional to $C_{qq}^2 \cdot C_{Z\gamma}^2$. Therefore, we can also extract limits on $C_{qq}^2 \cdot C_{Z\gamma}^2$ as functions of $M_{\ell\ell\gamma}$ as shown in Fig. 7.9.

The number of signal events for a vector (scalar) resonance decaying into $Z\gamma$, if the cross

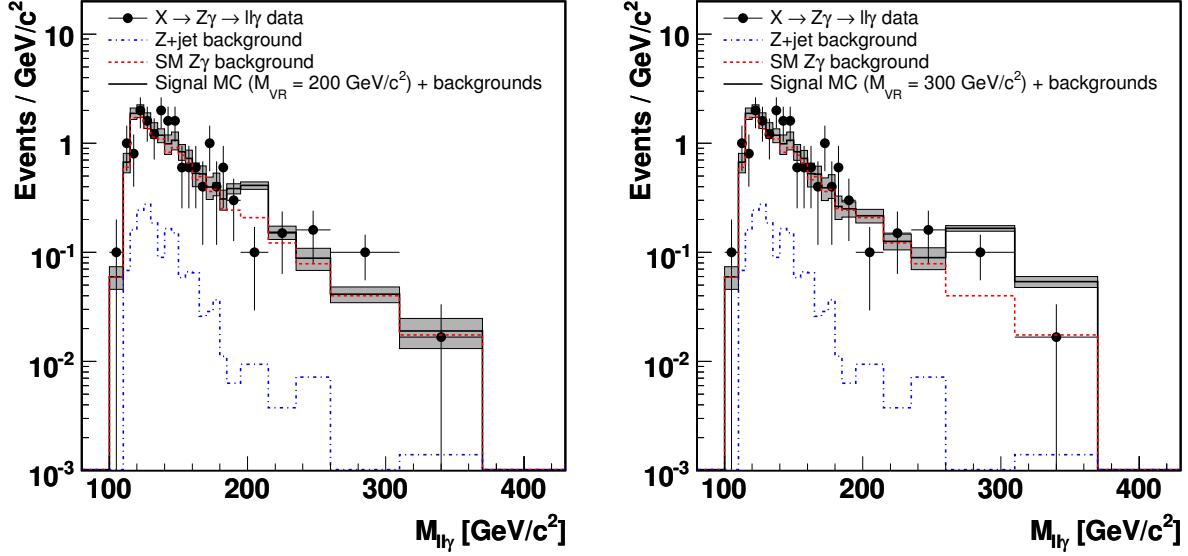


Figure 7.6: Invariant dilepton plus photon mass spectrum for $\ell\ell\gamma$ data (dots), SM $Z\gamma$ background (dashed line histogram), Z +jet background (dash-dot line histogram) and Monte Carlo signal plus background associated with a vector particle of $200 \text{ GeV}/c^2$ (left) and $300 \text{ GeV}/c^2$ (right) decaying into $Z\gamma$ (solid line). The shaded band represents the 1 s.d. systematic and statistical uncertainty on the Monte Carlo signal plus background.

section times branching fraction is right below our 95% C.L. limit, are shown as a function of the $M_{\ell\ell\gamma}$ mass in Fig. 7.10 (Fig. 7.11), respectively.

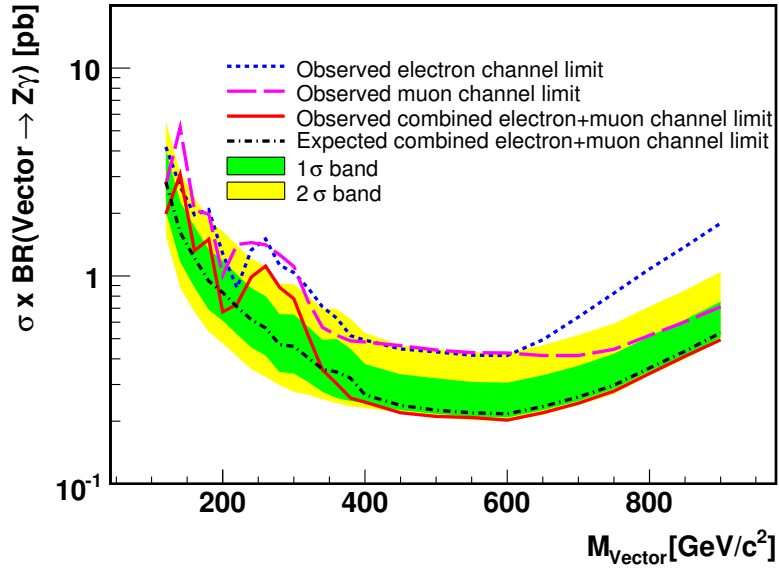


Figure 7.7: The cross section times branching fraction at 95% C.L. limit for a vector particle that decays into $Z\gamma$ as a function of the vector resonance mass. The two shaded bands represents the 1 s.d. (dark) and 2 s.d. (light) uncertainties on the expected limit.

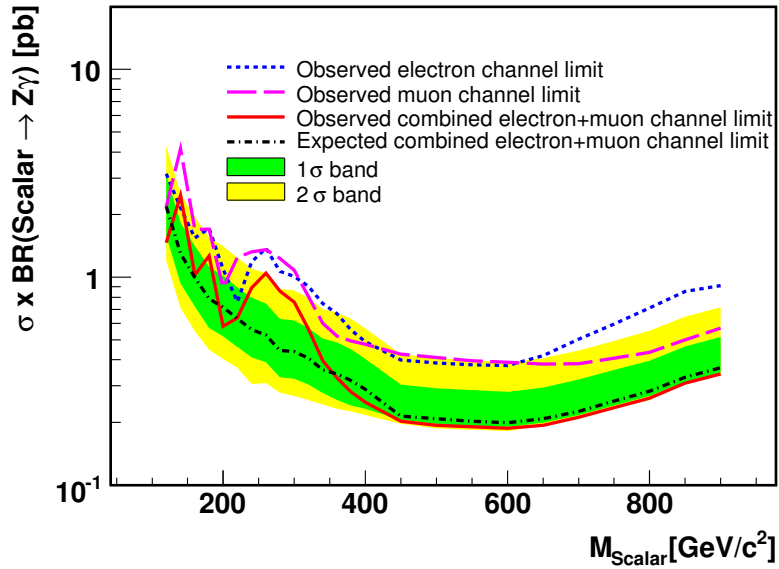


Figure 7.8: The cross section times branching fraction at 95% confidence level limit for a scalar particle that decays into $Z\gamma$ as a function of the scalar particle mass. The two shaded bands represents the 1 s.d. (dark) and 2 s.d. (light) uncertainties on the expected limit.

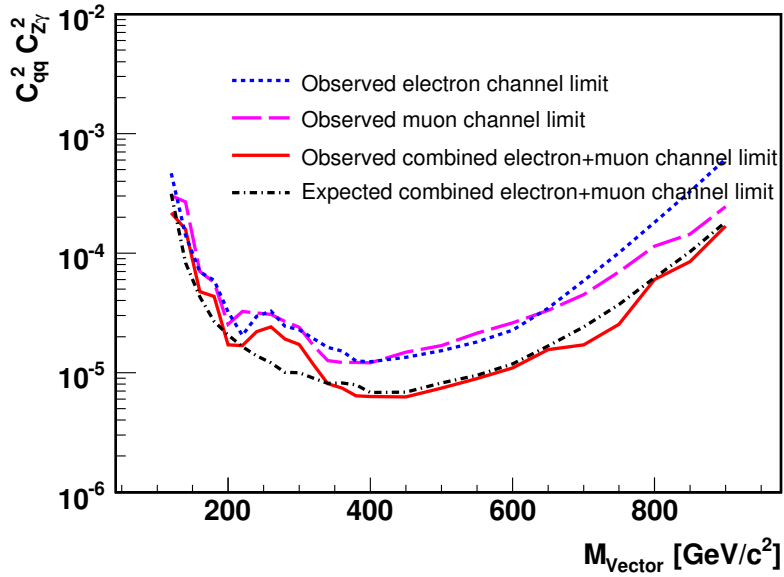


Figure 7.9: $C_{qq}^2 \cdot C_{Z\gamma}^2$ at 95% C.L. limit for a vector particle that decays into $Z\gamma$ as a function of the vector particle mass.

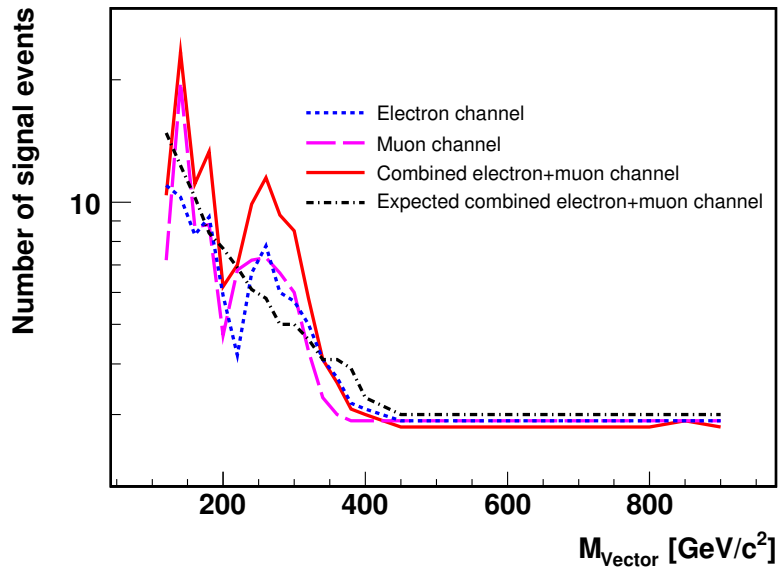


Figure 7.10: Signal events for a vector particle that decays into $Z\gamma$ if the cross section times branching fraction is right below our 95% C.L. limit as a function of the vector particle mass.

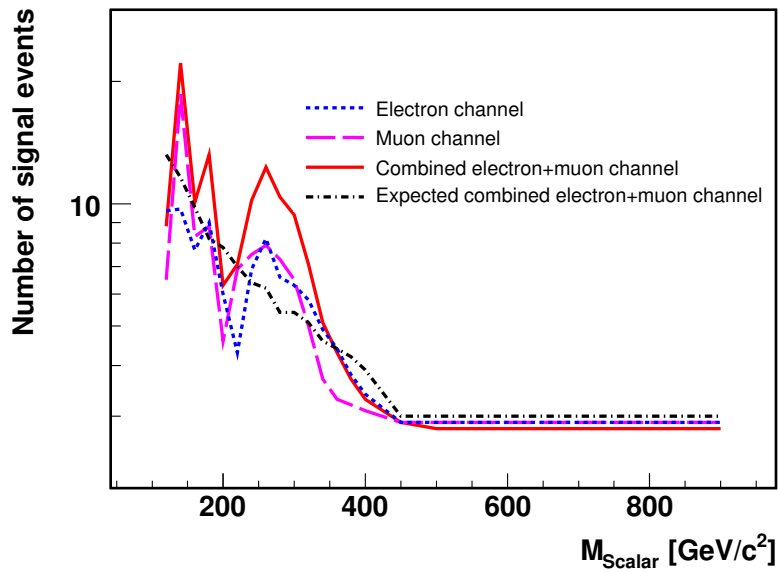


Figure 7.11: *Signal events for a scalar particle that decays into $Z\gamma$ if the cross section times branching fraction is right below our 95% C.L. limit as a function of the scalar particle mass.*

Chapter 8

Summary

We have performed a comprehensive study of the $Z\gamma \rightarrow \ell\ell\gamma$ ($\ell = e$ or μ) and $Z\gamma \rightarrow \nu\bar{\nu}\gamma$ final states with up to 3.6 fb^{-1} of integrated luminosity searching for either anomalous $Z\gamma$ production or new physics resonances that decay to $Z\gamma$. The most important results are summarized below.

- Using more than 1 fb^{-1} of data, we measure the most precise $Z\gamma$ cross section at hadron colliders of $4.96 \pm 0.30(\text{stat.} + \text{syst.}) \pm 0.30(\text{lumi.}) \text{ pb}$ for the photon $E_T > 7 \text{ GeV}$, dilepton mass above $30 \text{ GeV}/c^2$, and separation of the photon from leptons $\Delta R > 0.7$ in the charged leptons channel (e and μ). It is in a good agreement with the SM NLO prediction of $4.74 \pm 0.22 \text{ pb}$. All kinematic distributions agree with the predicted shapes.
- With roughly 3.6 fb^{-1} of data, we measure the most precise $Z\gamma$ cross section at hadron colliders of $0.032 \pm 0.009(\text{stat.} + \text{syst.}) \pm 0.002(\text{lumi.}) \text{ pb}$ for the photon $E_T > 90 \text{ GeV}$ in the neutrino channel. It also is in agreement with the theoretical prediction of $0.039 \pm 0.004 \text{ pb}$. The probability of the estimated background to fluctuate into the number of events that we observed is 3.1×10^{-7} , which corresponds to a statistical significance of 5.1 standard deviations. Thus, we claim a first definitive observation of the $Z\gamma \rightarrow \nu\bar{\nu}\gamma$ process at the Tevatron collider.
- We found no evidence for the anomalous $Z\gamma$ production in either of the channels,

hence we set limits on anomalous trilinear gauge boson $Z\gamma\gamma$ and $ZZ\gamma$ couplings. The combined neutrino and charged lepton one-dimensional 95% C.L. limits on the CP-conserving couplings are: $|h_{30}^\gamma| < 0.033$, $|h_{40}^\gamma| < 0.0017$, $|h_{30}^Z| < 0.033$, and $|h_{40}^Z| < 0.0017$ for the form-factor scale $\Lambda = 1.5$ TeV. These limits are roughly three times more restrictive compared to the most recent limits set at the Tevatron [95], published as a part of this dissertation, and are the tightest limits on the anomalous couplings set at hadron colliders to date. Three of these limits (h_{30}^Z , h_{40}^Z , and h_{40}^γ) improve on the limits set at LEP [30, 31]. The limits on the CP-violating couplings are expected to be the same as the limits on the corresponding CP-conserving couplings.

- Using more than 1 fb^{-1} of data in the charged leptons channel, we searched for a narrow scalar or vector resonance that decay into $Z\gamma$. We found no significant deviation of the observed kinematic distributions from the SM expectations, thus we set the upper limit on the resonance production cross section multiplied by the branching fraction of $X \rightarrow Z\gamma$. These limits vary from 2.5 pb (3.1 pb) for the scalar (vector) resonance with $M_{Res} = 140 \text{ GeV}/c^2$ to roughly 0.2 pb for both types of resonances with $M_{Res} = 600 \text{ GeV}/c^2$.

The results of the measurements and searches described in this dissertation have either been published in Refs. [95, 109] (Sections 5.1, 6.1, 7) or submitted to the Physics Review Letters (PRL) journal (Sections 5.2, 6.2–6.5).

8.1 Large Extra Dimensions

It is worth mentioning, that the $\gamma + \cancel{E}_T$ final state with a signature identical to that of the $\nu\bar{\nu}\gamma$ final state (see Section 5.2) can be used for a search for large extra dimensions [110, 111]. The $\gamma + \cancel{E}_T$ signature arises from the process $q\bar{q} \rightarrow \gamma G_{KK}$. Here, G_{KK} is a Kaluza-Klein graviton - a stable particle, which represents the quantized energy states of the gravitational field in the $4+n$ -dimensional space-time. The search of this kind has been performed by the

CDF [112] and DØ [91] collaborations, and at the CERN LEP collider [113]. Having found no evidence for large extra dimensions, all experiments set lower limits on the fundamental Planck mass, M_D , for number of extra dimensions, n , from 2 to 6 (CDF and LEP) or 8 (DØ).

8.2 Future Prospects

At the time of writing this dissertation, the Tevatron collider has delivered 6.2 fb^{-1} of data and the DØ detector has written to tapes roughly 5.5 fb^{-1} of integrated luminosity. The Tevatron is expected to run through 2010 and deliver up to 10 fb^{-1} of data by the end of 2010. The 95% C.L. limits on ATGC improve as the fourth root of integrated luminosity. Thus, we expect the limits to improve by $\approx 50\%$ in the charged leptons channel alone, and by $\approx 15\%$ in the neutrino channel for the same form-factor scales used in this work, thus leading to an even larger (than 15%) improvement of the combined limits. Further, a significant increase in the size of the samples will allow one to study the sensitive kinematic distributions in more details. This will not only lead to a reduction of the statistical uncertainties on the measured $Z\gamma$ cross sections, but possibly lead to an observation of a significant excess of the data over the SM predictions. Ultimately, combining the DØ results with those from the CDF will further increase the statistical significance of the observations.

We are living in a very exciting time for the High Energy Physics. The current experimental data from the laboratories all around the world confirm that the standard model describes the interactions between particles very well at currently available energies. With the Large Hadron Collider (LHC) about to start colliding proton beams with the center-of-mass energies of $\sqrt{s} = 14 \text{ TeV}$, we expect to find answers to many of the fundamental questions (see Chapter 1). At such high energies and with a much larger data sets provided by the LHC, we will test all known sectors of the SM, and possibly find an evidence of the new phenomena described in this work.

Bibliography

- [1] G. Glashow, Nucl. Phys. **20**, 579 (1961).
- [2] S. Weinberg, Phys. Rev. Lett. **19**, 1264 (1967).
- [3] F. J. Hasert et al., Phys. Lett. B **46**, 138 (1973).
- [4] G. Arnison et al., Phys. Lett. B **126**, 398 (1983), (UA1 Collaboration).
- [5] G. Arnison et al., Phys. Lett. B **129**, 273 (1983), (UA1 Collaboration).
- [6] P. Bagnaia et al., Phys. Lett. B **129**, 310 (1983), (UA2 Collaboration).
- [7] P. Bagnaia et al., Z Phys. **24C**, 1 (1984), (UA2 Collaboration).
- [8] C. Amsler et al., Phys. Lett. B **667**, 1 (2008).
- [9] P. W. Higgs, Phys. Rev. Lett. **12**, 132 (1964).
- [10] ALEPH, DELPHI, L3, OPAL, and the LEP working group for Higgs Boson Searches, Phys. Lett. B **565**, 61 (2003).
- [11] CDF, DØ, and the TEVNPH Working Group, arXiv:hep-ex/0808.0534v1 (2008), FERMILAB-PUB-08-270-E.
- [12] U. Baur and E. L. Berger, Phys. Rev. D **47**, 4889 (1993).
- [13] U. Baur, T. Han, and J. Ohnemus, Phys. Rev. D **57**, 2823 (1998).
- [14] H. E. Haber and G. L. Kane, Phys. Rep. **117**, 75 (1985), and references therein.
- [15] O. W. Greenberg and J. Sucher, Phys. Lett. B **99**, 339 (1981), and references therein.

- [16] R. Barbieri and R. N. Mohapatra, Phys. Rev. D **25**, 2419 (1982), and references therein.
- [17] Private communication with Ulrich Baur.
- [18] F. Abe et al., Phys. Rev. Lett. **74**, 1941 (1995), (CDF Collaboration).
- [19] D. Acosta et al., Phys. Rev. Lett. **94**, 041803 (2005), (CDF Collaboration).
- [20] A. Lyon, arXiv:hep-ex/0810.3766v1 (2009).
- [21] S. Abachi et al., Phys. Rev. Lett. **75**, 1028 (1995), (DØ Collaboration).
- [22] S. Abachi et al., Phys. Rev. Lett. **78**, 3640 (1997), (DØ Collaboration).
- [23] B. Abbott et al., Phys. Rev. D **57**, 3817 (1998), (DØ Collaboration).
- [24] V. Abazov et al., Phys. Rev. Lett. **95**, 051802 (2005), (DØ Collaboration).
- [25] ALEPH, ALEPH 2001-061, CERN-CONF-2001-041 (2001).
- [26] P. Abreu et al., Phys. Lett. B **380**, 471 (1996), (DELPHI Collaboration).
- [27] P. Acciarri et al., Phys. Lett. B **346**, 190 (1995), (L3 Collaboration).
- [28] P. Achard et al., Phys. Lett. B **597**, 119 (2004), (L3 Collaboration).
- [29] G. Abbiendi et al., Eur. Phys. J **C32**, 303 (2004), (OPAL Collaboration).
- [30] W.-M. Yao et al., J. Phys. G: Nucl. Part. Phys. **33** (2006).
- [31] L. E. W. Group, LEPEWWG/TGC/2003-01 .
- [32] J. Abdallah et al., Eur. Phys. J **C51**, 525 (2007), (DELPHI Collaboration).
- [33] Cole, Frank, Goldwasser, Edwin, and Wilson, *National Accelerator Laboratory design report*, FERMILAB-DESIGN-1986-01, 1968.

- [34] F. A. Division, *Operations Rookie Book*, 2006-2008.
- [35] V. M. Abazov et al., Nucl. Inst. Meth. **A565**, 463 (2006).
- [36] G. Borissov, *Ordering a Chaos or... Technical Details of AA Tracking*, All DØ Meeting, 2005.
- [37] A. Khanov, *HTF: histogramming method for finding tracks. The algorithm description*, DØNote 3778, 2000.
- [38] F. Fleuret, *The DØ Electron/Photon Analysis Package EMAnalyze*, DØNote 3888, 2001.
- [39] G. Steinbrueck, *Measurement of the angular distribution of electrons from W boson decays at DØ*, PhD thesis, University of Oklahoma, 1999, FERMILAB-THESIS-1999-24.
- [40] O. Atramentov and Y. Maravin, *Utilizing CFT and SMT hits count for photon and electron reconstruction*, DØNote 4444, 2004.
- [41] E. Busato and A. Bernard, *Jet Algorithms in DØ Run II Software: Description and User's Guide*, DØNote 4457, 2004.
- [42] B. Oliver, U. Bassler, and G. Bernardi, *NADA: A new Event by Event Hot Cell Killer*, DØNote 3687, 2000.
- [43] O. Peters, Muon segment reconstruction - linked list algorithm, http://www-d0.fnal.gov/nikhef/muon_reco/segmentreco/MuonSegmentReconstruction.pdf, 2001.
- [44] P. Calfayan et al., *Muon Identification Certification for p17 data*, DØNote 5157, 2006.
- [45] G. Hesketh, *Content of the p17 Muon Thumbnail*, DØNote 4735, 2005.
- [46] A. Garcia-Bellido, S. Lager, F. Rizatdinova, A. Schwartzman, and G. Watts, *Primary Vertex certification in p14*, DØNote 4320, 2004.

- [47] A. Schwartzman, Y. Peters, and H. Greenlee, *Adaptive Primary Vertex Certification in p17*, DØNote 5192, 2006.
- [48] A. Schwartzman and C. Tully, *Primary Vertex Reconstruction by Means of Adaptive Vertex Fitting*, DØNote 4918, 2005.
- [49] L. Sawyer and A. L. Stone, *Missing ET Reconstruction: Variable and Methods*, DØNote 3957, 2002.
- [50] Common samples group, <http://www-d0.fnal.gov/Run2Physics/cs/index.html>.
- [51] Common analysis framework, <http://www-d0.fnal.gov/Run2Physics/cs/caf>.
- [52] A. Bellavance et al., *Measurement of $p\bar{p} \rightarrow \mu\mu$ yield in the Z mass region for DØ Run 2A data*, DØNote 5269, 2006.
- [53] G. Snow, *Lumi Determination Status*, Joint Algorithm/Physics Conveners Meeting, June 2nd, 2006.
- [54] H. Schellman et al., *Luminosity Calculation for the Run IIa Blinded Z cross sections*, DØNote 5243, 2006.
- [55] T. Sjöstrand et al., *Comp. Phys. Commun.* **135**, 238 (2001).
- [56] J. M. Campbell and R. K. Ellis, *Phys. Rev. D* **60**, 113006 (1999).
- [57] J. Pumplin et al., *JHEP* **0207**, 012 (2002).
- [58] D. Stump et al., *JHEP* **0310**, 046 (2003).
- [59] To estimate the K -factor, we run the NLO $Z\gamma$ Baur Monte Carlo generator twice: first with the NLO PDF (CTEQ6M group), then with the LO PDF (CTEQ6L1 group). The K -factor is then measured as the ratio of the NLO photon E_T distribution obtained from the first run and the LO photon E_T distribution obtained from the second run.

- [60] The NLO corrections to the photon E_T depend on the values of the anomalous couplings. However, this K -factor dependence results in a negligible effect (less than 1%) on the values of the limits, and therefore is not considered in this analysis.
- [61] R. Brun and F. Carminati, *CERN Program Library Long Writeup W5013*, unpublished.
- [62] S. Eno and M. Verzocchi, *Status of the Fast Simulation PMCS, v01-98-00*, DØNote 4165, 2003.
- [63] J. Hays, J. Mitrevski, C. Schwanenberger, and T. Toole, *Single Electron Efficiencies in p17 Data and Monte-Carlo Using p18.05.00 d0correct*, DØNote 5105, 2006.
- [64] O. Atramentov et al., *Electron and Photon Identification with p20 data*, DØNote 5761, 2008.
- [65] D. Whiteson and M. Kado, *Muon Isolation Studies*, DØNote 4070, 2002.
- [66] The distance of the closest approach, DCA , is defined as the shortest distance of the track projection in the x-y plane with respect to the beam position in the same plane.
- [67] O. Atramentov et al., *Photon Identification in P17 Data*, DØNote 4976, 2005.
- [68] We use the following definition of the $fmod$ function: $fmod$ is the function that returns the floating point remainder (modulo) of dividing the dividend (x) by the divisor (y). The remainder (r) is defined as: $x = i \cdot y + r$, for some integer i . If y is non-zero, r has the same sign as x and a magnitude less than the magnitude of y .
- [69] The DØ calorimeter is divided into towers. Units of “phimod”, defined as $(\phi_{det} \times 16/\pi) \bmod 1.0$, are used. In phimod units, 0.0 is at one calorimeter tower boundary and 1.0 is at the other. Standard ϕ fiducial cuts are made if $phimod < 0.1$ or $phimod > 0.9$.

- [70] J. Hays, J. Mitrevski, and C. Schwanenberger, *The Program Package em_cert: Version p18-br-20*, DØNote 5070, 2006.
- [71] Private communication with J. Zhu and L. Wang.
- [72] J. Hays, J. Mitrevski, C. Schwanenberger, and T. Toole, *Single Electron Efficiencies in p17 Data and Monte-Carlo*, DØNote 5025, 2006.
- [73] M. Owen and M. Hohlfeld, *Trigger Efficiencies for the OR of Single Electron Triggers in p17 Data*, DØNote 5409, 2007, and references therein.
- [74] A. Baden, C. Jarvis, J. Mans, T. Toole, and M. Yan, *Measurement of $\Delta\sigma(Z \rightarrow ee)/dY$ at the Tevatron*, DØNote 4872, 2005.
- [75] http://www-clued0.fnal.gov/~venkat/TriggerStudy/Parameterization_Sqrt2.ps.
- [76] A. Alton, A. Askew, and Y. Maravin, *Analysis of $Z\gamma$ events in DØ RunII Data*, DØNote 4488, 2004.
- [77] Private communication with Carsten Hensel and Kristian Harder.
- [78] O. Atramentov, D. Bandurin, and Y. Maravin, *Photon energy scale for jet energy scale setting*, DØNote 4974, 2005.
- [79] Private communication with Dmitri Bandurin.
- [80] E. Barberis et al., *The Matrix Method and its Error Calculation*, DØNote 4564, 2004.
- [81] L. Lyons, D. Gibaut, and P. Clifford, Nucl. Inst. Meth. **A270**, 110 (1988).
- [82] K. DeVaughan et al., *Jet Energy Scale Determination for DØ Run Iib*, DØNote 5801, 2008.
- [83] Private communication with D. Bandurin and G. Golovanov.
- [84] W. K. Tung et al., JHEP **0702**, 053 (2007).

- [85] P. Nadolsky et al., Phys. Rev. D **78**, 013004 (2008).
- [86] E. Carrera, A. Ferapontov, Y. Gershtein, and Y. Maravin, *Search for Large Extra Dimensions in the Mono-Photon Final State at $\sqrt{s} = 1.96$ TeV*, DØNote 5617, 2008.
- [87] E. Carrera, A. Ferapontov, Y. Gershtein, and Y. Maravin, *Search for Large Extra Dimensions in the Mono-Photon Final State at $\sqrt{s} = 1.96$ TeV*, DØNote 5731, 2008.
- [88] Y. Gershtein and Y. Maravin, *Search for GMSB in Diphoton Events with Large Missing Transverse Energy*, DØNote 5425, 2007.
- [89] O. Atramentov, X. Bu, and J. Zhu, *P20 hits on the road study*, CALGO meeting, May 13th, 2008.
- [90] S. I. Kesisoglou, *Search for gauge mediated supersymmetry in the $\gamma\gamma+MET$ channel*, PhD thesis, Brown University, 2004, FERMILAB-THESIS-2004-44.
- [91] V. Abazov et al., Phys. Rev. Lett. **101**, 011601 (2008).
- [92] The purpose of the muon-stub veto tool is to reject events that have activity in the muon chambers and the calorimeter that is consistent with a cosmic muon undergoing bremsstrahlung, *i.e.* if two of the muon A-segments align with the selected photon EM cluster. The vectors from all the muon A-segments to the location of the EM cluster are calculated, and the angle (θ) between these vectors is then computed. We veto on the events containing a best aligning trio with $|\cos(\theta)| > 0.9$. For more information, please see: J. Lazoflores, DØ Note 5112.
- [93] J. Lazoflores, *Tagging of Bremsstrahlung Muons that Deposit Energy in the Electromagnetic Calorimeter Faking a Photon Signal*, DØNote 5112, 2006.
- [94] S. Abachi et al., Phys. Rev. D **56**, 6742 (1997).
- [95] V. Abazov et al., Phys. Lett. B **653**, 378 (2007).

- [96] V. Abazov et al., Phys. Rev. D **57**, 3817 (1998).
- [97] V. Buescher and K. Jakobs, Int. J. Mod. Phys. A **20**, 2523 (2005).
- [98] A. Djouadi, J. Kalinowski, and M. Spira, Comput. Phys. Commun **108**, 56 (1998).
- [99] G. A. Kozlov, Phys. Rev. D **72**, 075015 (2005).
- [100] S. Ono, Acta Phys. Polon. B **15**, 201 (1984).
- [101] O. Cakir, R. Ciftci, E. Recepoglu, and S. Sultansoy, Acta Phys. Polon. B **35**, 2103 (2004).
- [102] C. Hill and E. Simmons, Phys. Rept. **381**, 235 (2003; Erratum-ibid. **390**, 553 (2004)).
- [103] V. Abazov et al., Phys. Lett. B **641**, 415 (2006; Erratum-ibid. **XXXXXX**).
- [104] F. Maltoni and T. Stelzer, JHEP **0302**, 027 (2003).
- [105] Private communication with Steve Mrenna.
- [106] M. Carena, A. Daleo, B. A. Dobrescu, and T. M. P. Tait, arXiv:hep-ph/0408098v1 (2004), FERMILAB-PUB-04/129-T.
- [107] W. Fisher, *Systematics and Limit Calculations*, FERMILAB-TM-2386-E, 2006.
- [108] T. Junk, Nucl. Inst. Meth. **A434**, 435 (1999).
- [109] V. Abazov et al., Phys. Lett. B **671**, 349 (2009).
- [110] N. Arkani-Hamed, S. Dimopoulos, and G. R. Dvali, Phys. Rev. Lett. **429**, 263 (1998).
- [111] N. Arkani-Hamed, S. Dimopoulos, and G. R. Dvali, Phys. Rev. D **59** (1999).
- [112] T. Aaltonen et al., Search for large extra dimensions in final states containing one photon or jet and large missing transverse energy produced in $p\bar{p}$ collisions at $\sqrt{s} = 1.96$ TeV, 2008.

[113] LEP Exotica Working Group. Combination of LEP Results on Direct Searches for Large Extra Dimensions: http://lepexotica.web.cern.ch/LEPEXOTICA/notes/2004-03/ed_note_final.ps.gz .